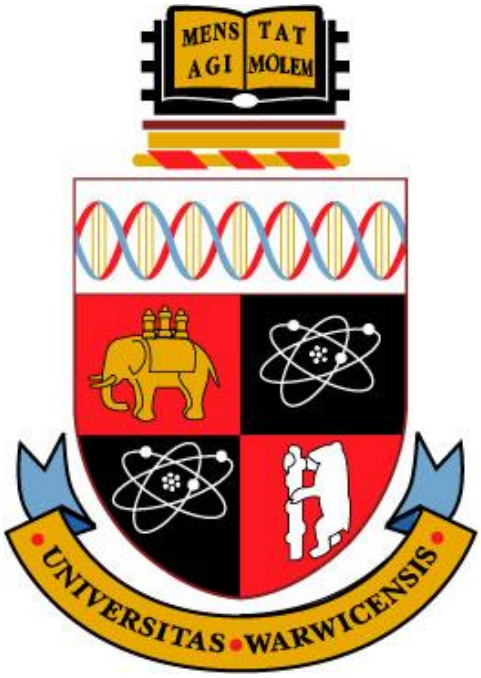

Electrocatalysis at the Nanoscale: From Polycrystalline Platinum to Nanoparticles

Changhui Chen

Submitted to the University of Warwick
for the degree of

Doctor of Philosophy

Department of Chemistry

September 2015

For my parents, Qingyin Chen and Ruiling Zhu

In loving memory of Grandma

Table of Contents

List of Figures

List of Tables

Acknowledgements

First and foremost, I would like to express my sincere thanks to my supervisor, Prof. Patrick Unwin, for giving me the opportunity to work at Warwick. Without the encouragement and support he has provided during my PhD application, I would never be able to come here. I am truly grateful for all the guidance, encouragement and advice he has provided throughout every step of my PhD, especially the patience and support during frustrating times. His enthusiasm for science and incredible source of knowledge has guided me and will keep inspiring me in the future. I would also like to thank Prof. Julie Macpherson for her insightful scientific advices, patient guidance and helpful career suggestions.

A huge acknowledgement goes to all the people I have collaborated during my PhD. I would like to thank Prof. Marc Koper for his valuable advice and support, especially on chapter three and five. I want to thank Barak Aaronson for working with me and 'Baraking' me during the first year. It was difficult for me at the beginning and he encouraged me a lot, both academically and socially. I also want to thank Leon Jacobse, for his contribution in voltammetric SECCM. He is a great person to work with and have taught me a lot. My gratitude also goes to Kim McKelvey and Yangrae Kim, for their help in LabVIEW programming and data analysis; Anatolii Cuharuc, Kate Meadows and Dmitry Momotenko for building the simulations; Emma Ravenhill for helping me in AFM force measurement and Hongjiao Li for the single-crystal experiments.

I also thank Joshua Byers, David Perry, Aleix Güell, Lingcong Meng, Sharel E. Pei and Guohui Zhang for their advice and support in different techniques. Thanks Binoy Nadappuram for sharing the experience with me of starting a PhD in a strange country. Thanks Rob Lazenby, for helping me in SEM and TEM. He is a wonderful office mate and is always there to offer help whenever I ask. I will miss the office tea time a lot.

I would like to thank Lee Butcher, Marcus Grant and Rod Wesson in the mechanical and electronics workshops for making specific components for my experiments. Thanks Dr. Alexander Colburn for his amazing electronic instrumentation, and for teaching me about electronics.

I also thank the Warwick chancellor's international scholarships and European Research Council grant for funding my PhD.

Over the last four years, there have been a lot of ups and downs. I am extremely lucky to be in a fantastic group and have wonderful colleagues who I could always turn to for help and support. Thanks everyone, previous and present, in the Warwick Electrochemistry and Interface group, for being so friendly and helpful. I have enjoyed working with you and I have learned so much from all of you.

Furthermore, I want to thank all my friends in UK for their great support and friendship. I will remember all happy times we have spent together. Especially, I want to thank my friend Juan Wei, for listening to me and comforting me during tough times.

There is one more important person I want to acknowledge separately. A special thanks goes to Stanley Lai, my best teacher and friend. Thank you for teaching and supporting me over the last four years. Without the effort you have put into every aspect of the research, this thesis would be impossible. Thank you for encouraging me and believing in me. You are always there whenever I need you. Knowing you is the best thing that happened at Warwick and in my life.

Finally, nothing can be achieved without the support from my family. I am truly grateful for the love, care and support from my parents and my brothers. I would like to acknowledge them in Chinese:

爸爸妈妈，感谢你们给我生命，含辛茹苦将我养育成人。感谢你们在最困难的时候，依然坚持让我读书，求学，尽己所能给我接受最好的教育。你们总是宽人严己，勤勉努力。是你们的言传身教，让我懂得如何做人，做事。感谢你们给我自由，从不阻拦我做自己想做的事。女儿的点滴成长，进步，都是因为有你们的鼓励，爱护和支持。多年在外求学，羞愧很少陪伴你们，感谢你们一直以来的理解。这本论文，是献给你们的礼物。希望这点小小的成绩，能让你们感到开心和骄傲。感谢我的哥哥长波和长运，弟弟长星。感谢你们这么多年一直宠爱，关心和支持着我。家人永远是我工作的动力和最温暖的港湾。我爱你们。

Declaration

This thesis is submitted to the University of Warwick in support of my application for the degree of Doctor of Philosophy. It has been composed by myself and has not been submitted in any previous application for any degree.

All work contained is entirely my own, except for the following contributions:

(i) Chapter 3: The single-crystal measurements were performed Dr. Hongjiao Li at Leiden University.

(ii) Chapter 4: The finite element method modelling was developed by Anatolii Cuharuc and Dr. Katherine E. Meadows.

(iii) Chapter 5: Data analysis of voltammetric scanning electrochemical cell microscopy (SECCM) was done by Leon Jacobse at Leiden University. The focused ion beam marking of Pt foils was made by Dr. Robert Lazenby.

(iv) Chapter 6: The finite element method modelling was made by Dr. Dmitry Momotenko. The TEM image of nanoparticles was recorded by Dr. Robert Lazenby.

Parts of the thesis have been published, as listed below:

Chapter 3: B. D. B. Aaronson, C.-H. Chen (joint first author), H. Li, M.T.M. Koper, S.C.S. Lai, P.R. Unwin, *Pseudo-single-crystal electrochemistry on polycrystalline electrodes: Visualizing activity at grains and grain boundaries on platinum for the* Fe^{2+}/Fe^{3+} *redox reaction*, *J. Am. Chem. Soc.* 2013, *135*, 3873-3880. This work was performed with conjunction of Barak D. B. Aaronson and it will also be part of his PhD thesis.

Chapter 4: C.-H. Chen, K.E. Meadows, A. Cuharuc, S.C.S. Lai, P.R. Unwin, *High resolution mapping of oxygen reduction reaction kinetics at polycrystalline platinum electrodes , Phys. Chem. Chem. Phys.* 2014, *15*, 18545-18552.

Chapter 5: C.-H. Chen, L Jacobse., K. McKelvey, S.C.S Lai, M.T.M. Koper, P.R. Unwin, *Voltammetric scanning electrochemical cell microscopy: dynamic imaging of hydrazine electro-oxidation on platinum electrodes*, *Anal. Chem.* 2015. 87, 5782–5789. This work was performed with conjunction of Leon Jacobse.

Chapter 6: C-H Chen, E. Ravenhill, D. Momotenko, Y.-R. Kim, S. C. S. Lai, P. R. Unwin, *Nanoparticle-Substrate Interactions in the Electrochemical Detection of Nanoparticle Collisions*, *Langmuir*, 2015, 31, 11932–11942.

Abstract

The influence of the electrode surface structure on its activity is a major theme in electrochemical research, especially in electrocatalysis. To obtain a truly fundamental understanding of the structure-activity relationship requires probing electrochemistry locally, as most electrode surfaces are inherently heterogeneous. The main concern of this thesis is studying the effect of the electrode surface structure on the activity of electrocatalytic reactions. This is attained by utilising scanning probe techniques as well as traditional macroscopic electrochemical methods, coupled with a number of structure characterisation techniques. A new approach, termed the 'pseudo-single-crystal approach', was introduced. It utilises scanning electrochemical cell microscopy and electron backscatter diffraction to obtain electrochemical activity and crystallographic orientation information across a surface of interest, providing a novel platform for understanding structure-reactivity relationship of complex electrode materials. Platinum electrodes are the main focus. The principle of the approach was first demonstrated by studying a simple one-electron transfer reaction, Fe^{2+} oxidation to Fe^{3+} in aqueous acid solution. Results showed clear grain dependent activity for Fe^{2+} oxidation in perchloric acid but grain boundary controlled activity in sulfuric acid, showing how electrolyte species can significantly alter the patterns of reactivity. These results are consistent with data obtained by single-crystal approaches. Then, this approach was employed to study the oxygen reduction reaction. Significantly, for this reaction, SECCM provides a three-phase boundary configuration, which allows the ORR to be studied under high mass transport conditions. Clear grain-dependent activity of the ORR on high-index Pt surfaces was visualised and the possible effect of differential mass transport of the reactants and products was discussed. This feature of SECCM (high mass transport of oxygen) allowed us to study the effect of oxygen on the electrochemical oxidation of hydrazine. Hydrazine oxidation in air and in deaerated environment showed activity that was strongly grain dependent, but the magnitude of the current decreased dramatically in air. For this study, CVs at each pixel of a scan were recorded, providing potentiodynamic information at high resolution. Electrochemistry at single nanoparticles and their interaction with support electrode is a topic of considerable interest. In the last results chapter, the electron transfer properties of single Au nanoparticles and the interaction of these particles with self-assembled monolayer-modified gold substrates was investigated. Results showed that surface functionality plays an important role in this interaction. By comparing the results with atomic force microscopy measurements, it is shown that SECCM can detect subtle variations in the interactions, confirming it be a good tool for detecting surface chemistry at the nanoscale.

Abbreviations

Symbol	Abbreviation
AFM	Atomic force microscopy
CCD	Charge-coupled device
CFM	Chemical force microscopy
$CH_{3,SAM}$	Self-assembled monolayer formed from dodecanethiol
CNT	Carbon nanotube
$COOH_{SAM}$	Self-assembled monolayer formed from 11-mercaptoundecanoic acid
CV	Cyclic voltammogram/Cyclic voltammetry
D.L.	Double layer
DAFCs	Direct alcohol fuel cells
EBSD	Electron backscatter diffraction
ET	Electron transfer
$FcTMA^+$	(Trimethylammonio)methyl ferrocene$^+$
FEM	Finite element method
FIB	Focussed ion beam
FPGA	Field-programmable gate array
HER	Hydrogen evolution reaction
HOR	Hydrogen oxidation reaction
H_{upd}	Hydrogen underpotential deposition
ICP-MS	Inductively coupled plasma mass spectrometry
IHP	Inner-Helmholtz plane
NHE	Normal hydrogen electrode
NP	Nanoparticle
OER	Oxygen evolution reaction
OHP	Outer-Helmholtz plane
OH_{SAM}	Self-assembled monolayer formed from 11-mercapto-1-undecanol

OIM	Orientation imaging microscopy
OLEMS	On-line electrochemical mass spectroscopy
ORR	Oxygen reduction reaction
O_{upd}	Oxygen underpotential deposition
Pd-H_2	Palladium-hydrogen electrode
PEMFC	Proton exchange membrane fuel cells
pztc	Potential of zero total charge
QRCE	Quasi-reference counter electrode
RE	Reference electrode
RHE	Reversible hydrogen electrode
SAM	Self-assembled monolayer
SECCM	Scanning electrochemical cell microscopy
SECM	Scanning electrochemical microscopy
SEM	Scanning electron microscopy
SHE	Standard hydrogen electrode
SMCM	Scanning micropipette contact method
TEM	Transmission electron microscopy
TG-SC	Tip generation-substrate collection
UME	Ultramicroelectrode

Glossary of Symbols

Symbol	Definition
A	Area of the electrode
b	Tafel slope
c	Concentration
c^0	Bulk concentration
c_S	Concentration at an electrode surface
D	Diffusion coefficient
d	Alkyl carbon chain thickness
E	Electrode potential
E^0	Standard potential of a redox couple
$E^{0'}$	Formal potential
E_e	Equilibrium potential
E_F	Fermi level
E_O	Energy level for oxidised species
E_R	Energy level for reduced species
E_p	Peak potential in cyclic voltammetry
$E_{p,ox}$	Peak potential of oxidation reaction
$E_{p.red}$	Peak potential of reduction reaction
E_s	Potential of an working electrode in scanning electrochemical cell microscopy (SECCM)
F	Faraday constant
f_{NP}	Collision frequency of nanoparticles
i	Current
i_0	Exchange current
i_{AC}	Alternating current in SECCM
i_{bias}	Current measured between QRCEs in SECCM
i_{DC}	Ionic conductance current

i_{lim}	Mass transport limited current
i_{ox}	Current during an oxidation
i_p	Peak current due to nanoparticle collisions
$i_{p,c}$	Corrected i_p by taking into account of an instrument response effect
i_{red}	Current during a reduction
i_s	Current flowing through a working electrode in SECCM
J	Flux
j	Current density
j_0	Exchange current density
j_d	Diffusion-limited current density
j_k	Kinetically-limited current density
$j_{M\text{-}M}$	Exchange current density between two metals
$j_{M\text{-}redox}$	Exchange current density between a redox species and a metal
j_t	Mass transport-limited current density
k^0	Standard heterogeneous rate constant
k^A	Electron transfer rate constant in the absence of SAM
k_B	Boltzmann constant
k_{ET}	Electron transfer rate constant of redox species in the presence of SAM
k_{ox}	Reaction rate constant of an oxidation
k_r	Electron transfer rate constant
k_{red}	Reaction rate constant of a reduction
k_t	Mass transport coefficient
L	Diffusion length
m_h	Height of a meniscus
n	Number of electrons
N_A	Avogadro constant
O	Oxidised form of a redox species
P_{H2}	Pressure of hydrogen
pK_a	Acid dissociation constant
Q	Charge

R	Reduced form of a redox species
R	Gas constant
r	Radius of electrodes/meniscus /nanoparticles
r_{a}	Major inner radius of a pipette
R_a	Surface roughness
r_{b}	Minor inner radius of a pipette
$r_{m\mathrm{a}}$	Major inner radius of a meniscus
$r_{m\mathrm{b}}$	Minor inner radius of a meniscus
T	Temperature
t	Time
V_1	Potential applied to one of the QRCEs in SECCM
V_2	Potential applied between the two QRCEs in SECCM
Λ	Ion conductivity
η	Overpotential/ dynamic viscosity
α	Transfer coefficient
α_{H^+}	Activity of protons
β	Tunneling constant
δ	Cantilever deflection
θ	Taper angle of a pipette
κ	Spring constant
σ	Standard deviation
τ	Time constant of a current amplifier
τ_{D}	Diffusion time of a nanoparticle
τ_{p}	Residence time of nanoparticles on an electrode surface
φ	Rotation angle of the carbon chain of self-assembled monolayers
χ	Geometry dependent factor of a UME
ω	Tilt angle of self-assembled monolayers
[O]	Surface concentration of oxidised species
[R]	Surface concentration of reduced species

Chapter One

Introduction

Abstract

This thesis focuses on studying electrocatalysis at the nanoscale using electrochemical scanning probe techniques, especially scanning electrochemical cell microscopy. A new approach for studying structure-reactivity relationships is developed combining scanning electrochemical cell microscopy and electron backscatter diffraction, and used to study exemplar electrochemical reactions, ranging from a simple, inner-sphere redox couple to complex catalytic reactions. In addition, the electron transfer properties at single nanoparticles (NPs) and their interaction with alkanethiol modified electrodes are also studied. This introduction provides a brief view of the basic principles of dynamic electrochemistry and electrocatalysis, as well as of the structure of polycrystalline platinum and scanning probe approaches used in electrocatalytic studies.

Chapter 1

1.1 Dynamic electrochemistry

Dynamic electrochemistry involves the study of electron transfer across an interface, often between a solid electrode and a molecular species in a solution.[1,2] In a typical experiment, a working electrode is inserted into a solution containing a redox species of interest, with sufficient supporting electrolyte, and an electric potential is applied to the working electrode which drives either the oxidation or the reduction of the redox species at the electrode surface.

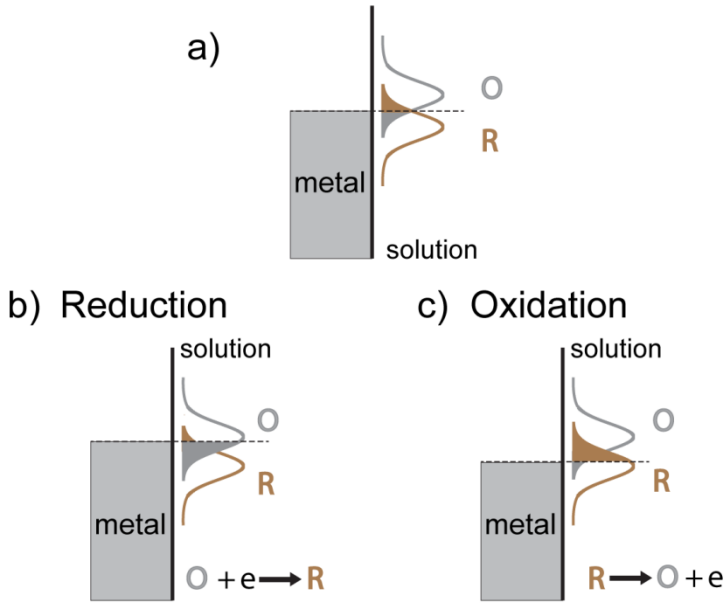

Figure 1.1 Schematic illustration of electron transfer at an interface between a metal electrode and solution containing oxidised (O) and reduced (R) species. The Fermi level of the electrode is marked by dashed lines. On the solution side, the energy levels for species O (grey line) and R (brown line) are shown as Gaussian distributions. The integral of the Fermi junction in the metal and the energy levels for the O and R species are denoted as grey and brown shading, respectively. Electrode states are given for three representative electrode potentials: **a)** $E = E_0$; **b)** $E < E_0$; and **c)** $E > E_0$. Herein, E_0 is the equilibrium potential of the redox couple in solution.

The physical basis for the inducing electron transfer processes by applying an electronic potential is illustrated in Figure 1.1. Metals possess closely packed energy levels and electrons occupy an effective continuum of energy states up until a level termed the Fermi level (E_F). E_F can be adjusted by applying an electric potential. The energy levels for oxidised species O and reduced species R in solution are denoted as E_O and E_R, respectively. For the reduction half reaction, the cathodic current density, j_c, is proportional to the overlap of filled electronic states of the electrode with E_O (grey shading). For the oxidation half reaction, the anodic current density, j_a, is proportional to the overlap integral of the empty states with E_R (brown shading). As shown in Figure 1.1a, at equilibrium potential, both overlap integrals have the same magnitude. Therefore j_c and j_a have the same values but opposite signs, resulting in a zero net current density. In Figure 1.1b, a negative potential is applied ($E < E_0$), the Fermi level at the electrode is raised and the overlap integral with E_O is higher than with E_R. Thus, j_c is higher than j_a, and a net reduction reaction occurs. Conversely (Figure 1.1c), when a positive potential applied ($E > E_0$), j_a is higher than j_c and oxidation reaction occurs.

1.1.1 Overpotential

From the above description, it can be seen intuitively that the more positive (negative) potential applied to the electrode, the easier the oxidation (reduction) reaction will proceed. Thus, electrode potential, or more specifically, the overpotential, η, is the key 'driving force' in electrochemical reactions. Overpotential is the deviation of the potential (E) applied to an electrode from the thermodynamic equilibrium potential (E_e) for a redox species.

$$\eta = E - E_e \tag{1-1}$$

For a general electrochemical reaction in which *n* electrons are transferred, the equilibrium potential is given by the Nernst equation,

$$E_e = E^0 + \frac{RT}{nF}\ln\frac{[\mathrm{O}]}{[\mathrm{R}]} \tag{1-2}$$

where E^0 is the standard potential of a reaction, *R* is the ideal gas constant (8.14 J K^{-1} mol^{-1}), *T* is the temperature, F is the Faraday constant (96,485 C mol^{-1}), and [O] and [R] are the surface concentration of oxidised and reduced species respectively.

1.1.2 Electrode kinetics

For a general electrochemical reaction in which *n* electrons are transferred,

$$\mathrm{O(aq)} + ne^- \underset{k_{ox}}{\overset{k_{red}}{\rightleftharpoons}} \mathrm{R(aq)} \tag{1-3}$$

the electron transfer rate constants (k_{red} and k_{ox}) at the surfaces show an exponential dependence on the overpotential:

$$k_{ox} = k^0 e^{\left((1-\alpha)nF\eta/RT\right)} \tag{1-4}$$

$$k_{red} = k^0 e^{\left(-\alpha nF\eta/RT\right)} \tag{1-5}$$

where k^0 is the intrinsic heterogeneous electron transfer rate constant and α is the transfer coefficient. The electron transfer rate constants are directly proportional to the currents of the half reactions following Faraday's law, such that:

$$i_{red} = nFAk_{red}\left[\mathrm{O}\right] \tag{1-6}$$

$$i_{ox} = nFAk_{ox}\left[\mathrm{R}\right] \tag{1-7}$$

where i_{red} and i_{ox} are the currents of the reduction and oxidation reaction, respectively. A is area of an electrode. Adding the currents of the half-reactions together and combining equations (1-6) to (1-7) gives an expression for the total current i:

$$i = i_{ox} - i_{red} = nFA\left(k_{ox}\left[\mathrm{R}\right] - k_{red}\left[\mathrm{O}\right]\right) \tag{1-8}$$

$$i = nFAk^0\left\{\left[\mathrm{R}\right]e^{\left((1-\alpha)nF\eta/RT\right)} - \left[\mathrm{O}\right]e^{\left(-\alpha nF\eta/RT\right)}\right\} \tag{1-9}$$

Equation (1-9) is known as the Butler-Volmer equation, and gives the current as function of applied potential (in the absence of mass transport limitations).

Two limiting cases can be distinguished for the Butler-Volmer equation. At low overpotential, where [R] ≈ [O] = c^0 (and c^0 is the bulk concentration of the redox species) and $\eta = (E - E_e) \approx 0$, equation (1-9) linearizes to:

$$i = nFAk^0c^0\left(e^{\left((1-\alpha)nF\eta/RT\right)} - e^{\left(-\alpha nF\eta/RT\right)}\right) = i_0c^0\,\frac{nF}{RT}\eta \tag{1-10}$$

where i_0 is the exchange current. At high overpotentials (or for irreversible reactions, such as most electrocatalytic reactions), one of the exponents in equation (1-9) goes to zero, and equation (1-9) simplifies to:

$$\ln i = \ln\left(nFAk^0\left[\mathrm{R}\right]\right) + \frac{(1-\alpha)nF}{RT}\eta \qquad \text{for } E >> E_e \text{ (anodic limit)} \tag{1-11}$$

$$\ln i = \ln\left(nFAk^0\left[\mathrm{O}\right]\right) - \frac{\alpha nF}{RT}\eta \qquad \text{for } E << E_e \text{ (cathodic limit)} \tag{1-12}$$

Equations (1-11) and (1-12) are termed the Tafel equations, and describe the current/voltage characteristics for an irreversible reaction. Importantly, it can be seen that, for a reaction under electrochemical control in the absence of mass transport limitations, the current is exponentially proportional to the applied potential.

1.1.3 Mass transport

Prior to the electron transfer reaction, a solution species needs to be transported from bulk solution to the electrode surface. Figure 1.2 summarizes this process.[1] The mass transport coefficient, k_t, determines the rate movement of reactants species from a bulk solution to the electrode surface, whereas k_r, the electron transfer rate constant, determines the reaction rate at the electrode surface. Depending on the conditions, the overall rate of an electrochemical reaction may be dominated by the electron transfer kinetics ($k_r << k_t$), by the mass transport towards the electrode surface ($k_r >> k_t$), or it can be under mixed control ($k_r \approx k_t$).

There are three modes of mass transport in an electrochemical system, namely convection, migration and diffusion.[1,2]

Convection is the forced movement of solution species by mechanical or other means. Two examples of 'force convection' can be found in rotating disk electrode and 'flow electrodes', in which mechanical stirring or pumping is applied to enforce an electrolyte flow to the electrode surface.[1,3] For typical electrochemical measurements under quiescent conditions, the contribution of convective mass transport is minimal and can be neglected at short timescales.

Migration is the movement of charged species under the electric field gradient. As an electrochemical reaction changes the charge on the redox species, migration could give rise to differential mass transport of the reduced and the

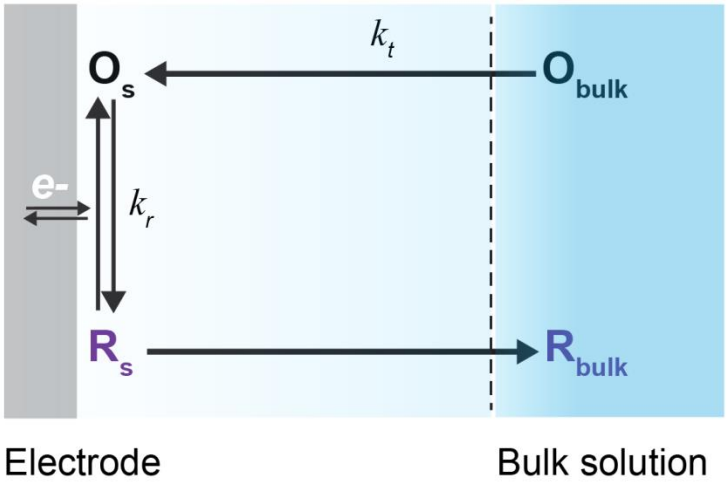

Figure 1.2 Dynamic electrochemistry of a general electrochemical (reduction) reaction. k_t is the mass transport coefficient and k_r is the surface electron transfer rate constant. O_{bulk} and R_{bulk}, represent the oxidised and reduced species in bulk solution; whereas O_s and R_s represent the same species in close vicinity of the electrode surface.

oxidised species, leading to complex mass transport. Thus, in most electrochemical measurements, 'background' supporting electrolyte is added to confine the electric field gradient to the near-electrode region to suppress these effects. The supporting electrolyte maintains the electroneutrality near the electrode-electrolyte interface and ensures that no extra electric field gradient builds up due to the reaction. A rule of thumb is that about 100 times the concentration of background electrolyte relative to that of the reactant is required to avoid significant migration.[2] Additionally, sufficient supporting electrolyte ensures the conductivity of the electrolyte to prevent potential drop (Ohmic drop) in the bulk electrolyte.

Diffusion arises from concentration gradients in a system. For example, consider an electrode placed in a solution, initially only containing species O. Upon applying a potential to electrochemical convert O to R, the concentration of O at the electrode surface decreases, while the concentration of R increases. The differential

concentration of O at the surface and the bulk acts to force a flux of O diffusing to the surface, with the resulting concentration profile dependent on the electrode size and geometry. In particular, this diffusion profile is different at a macroscale electrode and a microscale electrode. Importantly, the rate of diffusion towards a microscopic electrode is much higher than that towards a macroscopic electrode.

1.1.4 Microelectrode

Microelectrodes,[1,4,5] also known as ultramicroelectrodes (UMEs), are electrodes whose critical dimensions are in the micrometre range or lower. In practice, the dimension is generally in the range of 100 nm to 25 μm. Microelectrodes have a few important features compared to macroscale electrodes, including much enhanced mass transport rates due to a spherical rather than planar diffusion profile, reduced capacitances due to smaller electrode areas, and reduced Ohmic drop due to smaller currents. Thus, they are used widely for measuring ultra-fast electron transfer kinetics and electroanalysis in unusual biology systems. Furthermore, they are often employed as probes in the scanning electrochemical microscopy. [3,4,6]

Microelectrodes can be fabricated with different geometries, such as spherical, hemispherical, inlaid disk electrode, and a sphere supported on a plane as shown in Figure 1.3.[4,5] The current-time profile for a UME placed in a solution which initially only contains a redox-active species with a bulk concentration c^0 can be given by the following general form[1,4,5]:

$$i(t) = \frac{nFAD^{1/2}c^0}{\pi^{1/2}t^{1/2}} + nFAk_t c^0 = \frac{nFAD^{1/2}c^0}{\pi^{1/2}t^{1/2}} + nFA\chi D\, c^0 \qquad (1\text{-}13)$$

where D is the diffusion coefficient, t is time, χ (Table 1-1) is a geometry dependent factor with the dimensions of length^{-1}, and all other symbols have their meanings as described above. It can be seen that the current-time behaviour consists of two terms. The first term, which dominates at short time-scales, shows a transient, Cottrellian behaviour.[1] The magnitude of this term decays with $t^{-1/2}$, characteristic for planar diffusion (similar for macroscopic electrodes). The second term, which dominates at 'long' time-scales, is a time-independent steady-state current. This steady state current is characteristic for radial diffusion, in which the growing diffusion field draws material from an ever-increasing area of the outer limit until the electrolysis rate is equal to the rate at which molecules are transported to the electrode surface.

For the geometry employed in scanning electrochemical cell microscopy (SECCM), a microscale pipette contacts an electrode and form an electrochemical cell of micrometre size, and the diffusion profile have both a planar and a spherical described above. It can be seen that the current-time behaviour consists of two terms. The first term, which dominates at short time-scales, shows a transient, Cottrellian behaviour.[1] The magnitude of this term decays with $t^{-1/2}$, characteristic for planar

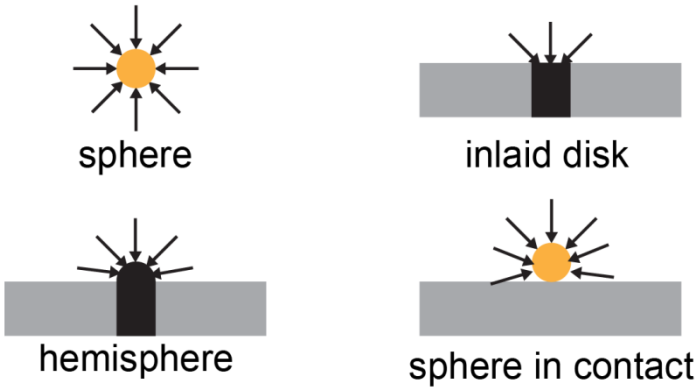

Figure 1.3 Schematic views of microelectrodes with different geometries and the corresponding diffusion profiles.

Table 1-1: Functional form of χ for microelectrodes of different geometries

Spherical	Hemispherical	Inlaid disk	Supported sphere	SECCM
$\frac{1}{r}$	$\frac{1}{r}$	$\frac{4}{\pi r}$	$\frac{4\ln 2}{\pi r}$	$\frac{0.2}{\pi r}$ to $\frac{0.4}{\pi r}$

r: UME radius

diffusion (similar for macroscopic electrodes). The second term, which dominates at 'long' time-scales, is a time-independent steady-state current. This steady state current is characteristic for radial diffusion, in which the growing diffusion field draws material from an ever-increasing area of the outer limit until the electrolysis rate is equal to the rate at which molecules are transported to the electrode surface. For the geometry employed in scanning electrochemical cell microscopy (SECCM), a microscale pipette contacts an electrode and form an electrochemical cell of micrometre size, and the diffusion profile have both a planar and a spherical component. As a rule of thumb, the (quasi) steady-state currents for the micropipettes employed in this thesis are 5-10 % (depending on the precise geometry of the pipette) of the value of the steady-state current for an inlaid disk UME of the same size.[7,8]

1.1.5 Outer-sphere and inner-sphere electron transfer

For heterogeneous electrochemical reactions, the electron transfer at an electrode-electrolyte interface can occur through an 'outer-sphere' or 'inner-sphere' mechanism.[1,9-11] Schematic illustrations the two mechanisms are shown in Figure 1.4. A double layer model is often used to describe the electrode-electrolyte interface. For an electrode placed in solution, its charge is balanced by the opposite charges in

the solution to maintain electrical neutrality in the interface region. At a region very close to the electrode, some solvated redox species are attracted and can approach to the surface, but only at a distance limited by the solvent shell. The centre of these species forms an Outer-Helmholtz plane (OHP). Upon approach, some ions may lose their solvent shell and adsorb on the electrode. These ions, named 'specifically absorbed' ions, can directly interact with the electrode and the centre of these ions defines the Inner-Helmholtz plane (IHP). The OHP and IHP planes together are called the 'compact layer' or Stern layer. In addition to the 'compact layer', excess balancing charges extend out into the solution with some thickness, forming a diffuse (Gouy-Chapman) layer.[1]

For outer-sphere reactions (Figure 1.4), the closest plane that the redox species can approach is the OHP and electrons transfer through electron tunnelling across at least one layer of solvent. Consequently, there is minimal interaction between the electrode and the redox mediator. In other words, the reaction is electrode insensitive. In addition, in an outer-sphere reaction, the redox mediators are often bulky molecules. This allows the charge (in the transition state) to be stabilized by delocalizing it on the ligands. As the charge is delocalized, there is very little nuclear rearrangement needed to go to the transition state, neither of the redox mediator nor the solvating water molecules. This makes the reaction fast, as electron transfer is fast (~10^{-13} s) compared to nuclear motion (~10^{-8} s) based on Franck-Condon principle. Examples of redox couples following outer-sphere reaction mechanism include $[Fe(CN)_6]^{3-}/[Fe(CN)_6]^{4-}$, $[Ru(NH_3)_6]^{2+}/[Ru(NH_3)_6]^{3+}$ and various ferrocene derivatives. Conversely, for inner-sphere reactions, at least the electrode or the redox mediator has to shed part of its solvation shell as illustrated in Figure 1.4b.

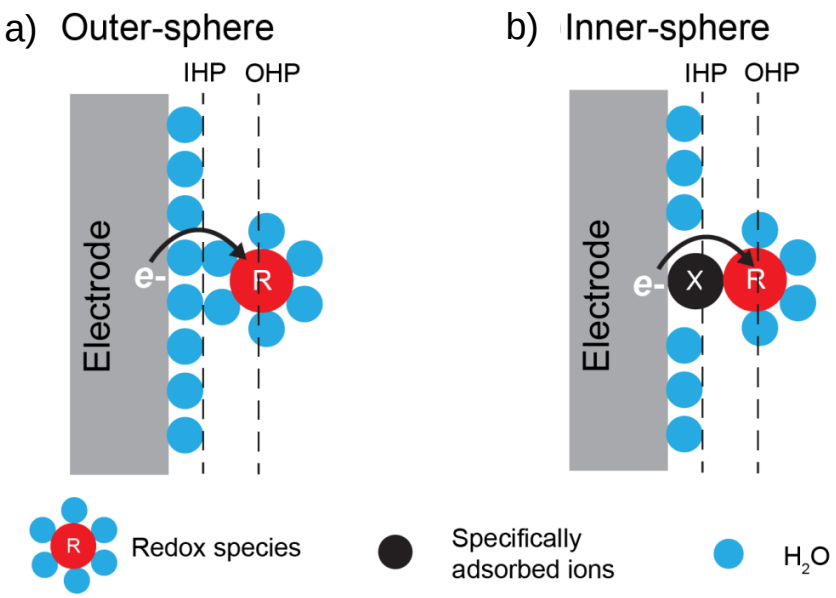

Figure 1.4 Schematic illustration of the metal-electrolyte interface and the reaction site of **a)** an outer-sphere reaction and **b)** an inner-sphere (right) reaction. IHP and OHP are the inner- and outer- Helmholtz planes, respectively separately.

The redox species either directly adsorbs on the electrode or interacts with the 'specifically absorbed' ions. In both cases, the adsorption depends on the electrode surface. Thus the kinetics of inner-sphere reactions is strongly electrode structure dependent, which makes steering the reaction possible by controlling the surface structure. Heterogeneous inner-sphere reaction is also called electrocatalytic reaction.[10]

1.2 Electrocatalysis

Electrocatalysis is an important fundamental research field, with applications in a vast array of technologies, including: fuel cells, [12-14] battery technologies[15-17] and electroanalytical sensors.[18,19] The first use of 'electrocatalysis' in English scientific

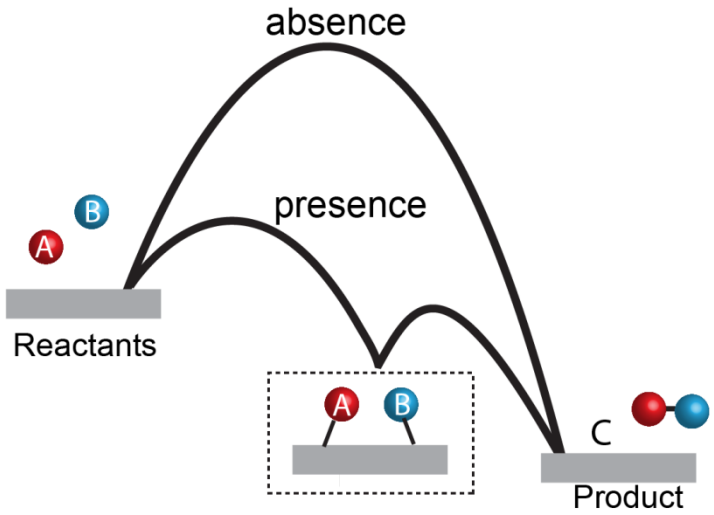

Figure 1.5 An illustration view of the electrocatalysis mechanism in the absence (top) and presence (bottom) of an electrocatalyst.

literature was by Grubb, in which it was defined as 'Electrocatalysis may be the enhancement of the rate of an electrochemical reaction by a substance, not consumed in the reaction, called the electrocatalyst'. [12]

Similar to the study of general heterogeneous catalysis, classical transition state theory can be used to understand the electrocatalysis reactions. Figure 1.5 provides a schematic illustration for an electrocatalytical reaction pathway. In the course of a reaction, in order to convert reactants A and B to product C, a significant energy barrier needs to be overcome. In the absence of an electrocatalyst (top), the transition barrier is high and the system does not have sufficient enough energy to pass it, resulting in low reaction rate. With the presence of an electrocatalytic active material, an alternative pathway is provided (for example, by forming adsorbed intermediates) with lower energy barriers, thereby the reaction is accelerated.

Electrocatalytical reactions have a lot in common with general heterogeneous catalytical reactions. For both, the reaction kinetics can be affected by the

reactant/product concentration, pressure and temperature. Importantly, electrocatalytical reactions are electrochemical reactions in nature and can be further steered by the electrode potential. Additionally, as heterogeneous inner-sphere electron transfer reactions (section 1.1.5), electrode structure plays an important role in the reaction kinetics and mechanism. An important goal in electrocatalytic research is gaining understanding in the role of the electrode surface on the reaction rate, and allowing optimization of electrocatalysts. The performance of an electrocatalyst is often evaluated by comparing the current at a fixed driving potential or the required potential for a certain current value.

For a given electrocatalyst, the rate of an electrocatalysis reaction typically depends on the structure of this electrocatalyst, which relates to the geometric and electronic properties of the catalyst.[20] Geometric effect relates to surface features of an electrocatalyst, such as the local arrangement of surface atoms. Surfaces with different crystalline orientations have different atomic coordination and densities and thus different geometry. This can affect the activity of an electrocatalyst through the bond length (energy) between a reactant and the electrocatalyst, leading to different reaction rates. For example, it is known that the bonding energy of hydrogen at Pt surfaces varies significantly with different crystal orientations, leading to different peaks in a cyclic voltammogram. Another important property of an electrocatalyst is the electronic structure, in particular the electronic density of states near the Fermi level. Again, the electronic structure also relates to the crystallographic orientation of a surface. Therefore, studying the structure effect on electrocatalyst, especially the crystallographic orientation effect, is important for understanding the fundamentals of an electrocatalytic reaction and for improving the reactivity.

1.3 Platinum electrodes

1.3.1 Pt structure

Pt (and some Pt based alloys) has been investigated extensively due to its importance in energy storage application, such as proton exchange membrane fuel cells (PEMFCs)[21-23] and direct alcohol fuel cells (DAFCs) technologies.[24-26] Hitherto, platinum-based electrocatalyst materials are found to be the best catalysts for the cathode oxygen reduction reactions (ORRs) and various anode fuel oxidation reactions.

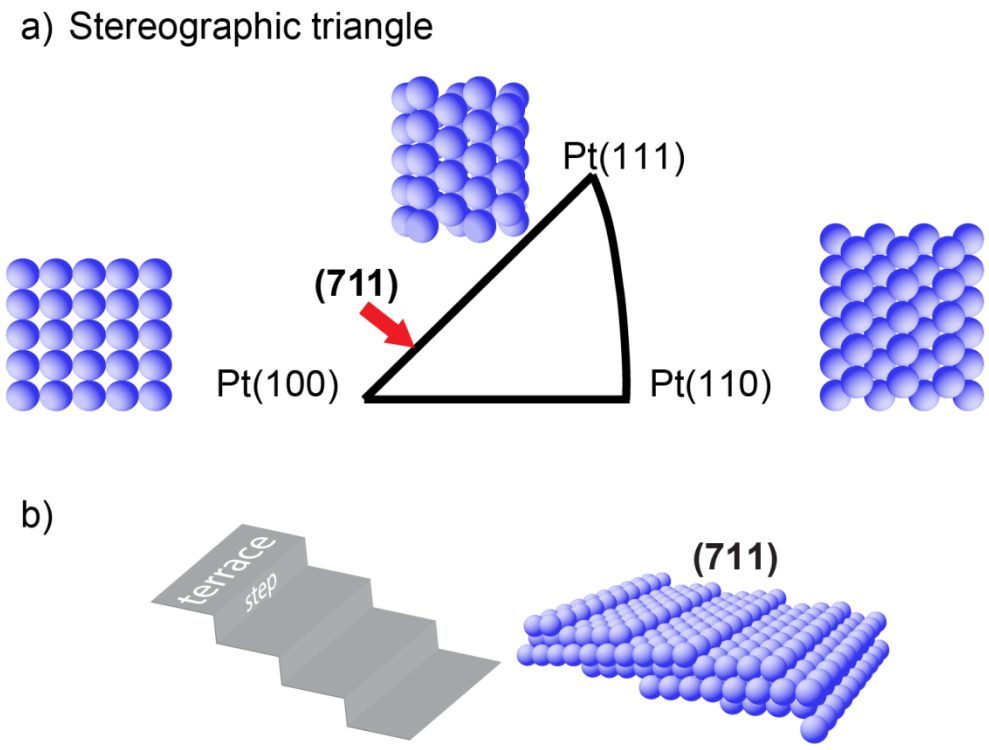

Figure 1.6 a) Stereographic triangle and the atomic structure of three basal planes for Pt. **b)** Schematic illustration of the structure of a high-index surface and the atomic structure of a Pt (711) surface. The location of Pt (711) surface in a stereographic triangle is marked by a red arrow.

Pt has a face-centred cubic crystal structure. By cutting the Pt unit cell along different directions, single-crystal facets with different structures can be obtained. The three basal facets of platinum crystals are Pt (111), Pt (110) and Pt (100). Among the three basal planes, Pt (111) has the lowest surface energy and is the most thermodynamically stable surface.[27] High-index surfaces can be obtained by cutting between these three basal planes at different angles, resulting in stepped and kinked surface structures.[27] The orientation of Pt surfaces can be represented with a stereographic triangle, as show in Figure 1.6.[9,28] The three corners represent the basal planes, while orientations along the edges represent stepped surface. The surfaces inside the triangle are the high-index surfaces, which combines basal planes with steps and kinks. For example, a Pt (711) surface contains (100) terraces of 4 atoms wide separated by mono-atomic (111) steps.[29] An illustrative view of this high-index surface is shown in Figure 1.6b.

It is known that the crystallographic orientation of platinum affects its activity towards catalytic reactions greatly. This 'structure sensitivity' has been investigated extensively using single-crystal approaches at gas-solid or liquid-solid interfaces.[30-32] These single-crystals, having well-defined surfaces at atomic level, provide a relatively simple system, which can be used as models for interpreting more complicated systems in applied systems.

1.3.2 Polycrystalline Pt foil

Commercially available Pt materials, including macroscopic Pt wires, foils and Pt nanoparticles (NPs), are often structurally heterogeneous, consisting of many grains of different orientations. Figure 1.7a shows a scanning electron microscopy

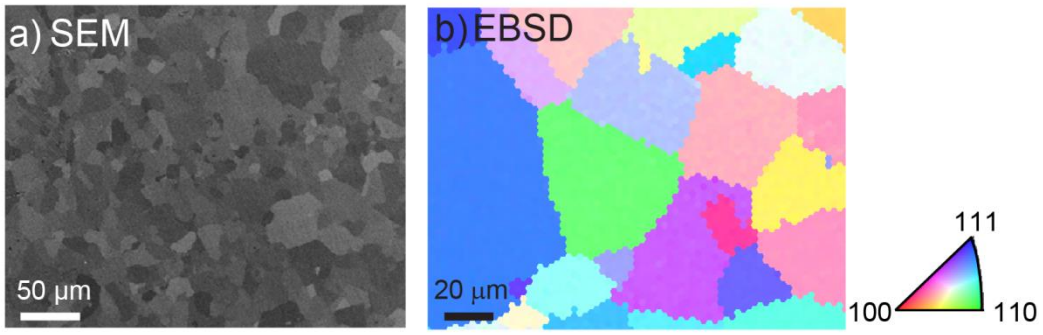

Figure 1.7 A typical **a)** SEM and **b)** EBSD image (does not correspond) of polycrystalline Pt foils. The triangle colour coded map indicates the crystallographic orientation of the grains.

(SEM) image obtained from a piece of (polycrystalline) Pt foil. This image clearly shows the surface is heterogeneous, containing grains of various sizes and shapes. The crystallographic orientation of individual grains of a platinum foil can be obtained using electron backscatter diffraction (EBSD). Further detail of this technique can be found in Chapter 2. Figure 1.7b is an EBSD image recorded at an area of a polycrystalline Pt foil. Most of the grains in this EBSD image are located in the middle of a colour coded map, suggesting they are high-index surfaces. Notably, clear boundaries between the grains can be observed in both the SEM and EBSD images.

As discussed above, single-crystal approaches are immensely powerful in fundamental electrocatalysis research. However, preparing and maintaining a well-defined single-crystal surface (especially for high-index surfaces) is challenging. Besides, multiple surfaces with different orientations are needed to reveal a systematic structural dependency of the reactivity.

Polycrystalline Pt material, such as Pt foils, can also provide surfaces with different crystal orientations, especially high-index surfaces. Thus, it is an interesting

material to study the structure-activity relationship in electrocatalysis. Especially, electrocatalytical activity of grain boundaries, which cannot be probed by single-crystal approaches, can be studied using polycrystalline materials. In this thesis, polycrystalline platinum foils were employed as the substrates of interest. By combining electrochemical imaging and material characterization methods, a 'pseudo-single-crystal' approach is developed and is used to study a few reactions of interest. This is discussed in detail in section 1.4.

1.3.3 Macroscale electrochemical characterization of polycrystalline Pt electrodes

It has been known since the 1970s that well-defined characteristic cyclic voltammograms (CVs) of polycrystalline Pt electrodes can be obtained by continuous CV cycling, between the onset of hydrogen evolution reaction (HER) and oxygen evolution reaction (OER) in acidic solutions.[33-37] However, extremely careful handling of Pt electrodes is needed to ensure a clean Pt surface. In 1979, Clavilier introduced a flame annealing method to reproducibly produce high quality single crystal surfaces.[38-41] In this method, well-ordered single-crystal platinum electrodes were flamed annealed in gas/hydrogen-oxygen flames at a high temperature (1100 °C ~ 1300 °C), left to cool in an inert atmosphere, quenched with water and then carefully transferred to an electrochemical cell protected by a thin layer of water. Using this method, clean single-crystal surfaces with protected crystallographic orientations were obtained and reproducible electrochemical measurements were achieved. In this thesis, the flame annealing method is used to prepare the polycrystalline platinum foil and single-crystal electrodes.

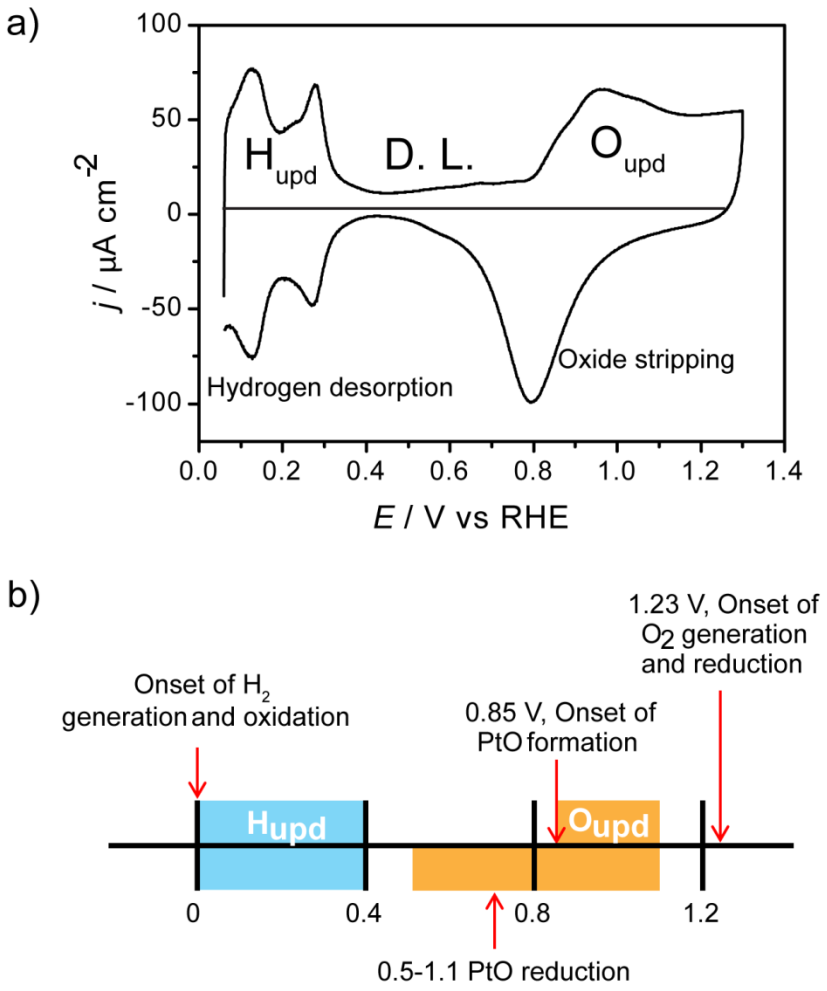

Figure 1.8 a) Cyclic voltammograms of polycrystalline platinum in nitrogen purged 50 mM H_2SO_4 at a scan speed of 50 mV s^{-1}.Three regions, hydrogen underpotential deposition (H_{upd}), double layer charging (D.L.) and oxygen underpotential deposition (H_{opd}) are marked in the figure. **b)** Potential diagram showing the regions of main reactions on a polycrystalline Pt electrode. It should be mentioned that the potentials for H_2 generation/oxidation and O_2 generation/reduction are standard electrode potentials for these reactions, and an overpotential is required to drive these reactions.

Figure 1.8a shows a CV of a polycrystalline Pt wire electrode recorded in an deaerated electrolyte solution containing 50 mM H_2SO_4 prepared by the flame-annealing method.[37] This characteristic CV includes a few main potential regions as marked with different colours in Figure 1.8b. First, in the potential range between 0

V (start of the HER) and 0.4 V, two couples of reversible peaks can be seen, which are assigned to the underpotential deposition of a hydrogen monolayer (H_{upd}) on the surface. The peak at ~ 0.12 V corresponds to adsorbed hydrogen on the (110) and (111) orientations. The more positive peak, at ~0.25 V, corresponds to adsorbed hydrogen at (100) orientations. At potentials between 0.4 V to 0.85 V on the anodic sweep, the featureless region is assigned to double layer (D.L.) charging. At potentials above 0.9 V until the onset of oxygen evolution (1.23 V), a broad peak in the forward scan can be observed. This peak is attributed to the formation of an adsorbed oxygen species before oxygen evolution.[33,34] Similarly with H_{upd}, this potential region is termed the oxygen underpotential deposition (O_{upd}) region. Correspondingly, in the reverse scan, a peak between 0.5-1.1 V is the reduction of the adsorbed surface oxygen.

The characteristic features of a Pt surface shown in Figure 1.8 are important to evaluate the cleanliness of a polycrystalline Pt surface. Especially, the H_{upd} features (210 $\mu C\ cm^{-2}$ [42]) are considered as a fingerprint of the clean polycrystalline Pt/sulfuric acid electrolyte interface as these features are highly sensitive to surface cleanliness. Contaminations from electrolyte solution or air can block surface sites, leading to a diminished charge in the H_{upd} and O_{upd} regions. Flame annealing, combined with CV cycling, is a widely accepted method to obtain reproducible and clean Pt surfaces.[30]

1.4 Structure-sensitive reactions

In this thesis, structural effects on activity for a few reactions are investigated. The study starts with an ostensibly simple redox couple, Fe^{2+}/Fe^{3+} to study electrolyte effects on an inner-sphere redox reaction. Then, the oxygen reduction

reaction and hydrazine oxidation were considered, two reactions which are of interests for the development of low-temperature fuel cells. Brief introductions to each reaction are provided to provide a view of the previous investigations.

1.4.1 Fe^{2+}/Fe^{3+} redox couple

The $Fe^{2+/}Fe^{3+}$ redox couple is a classical redox couple in electrochemistry. In the absence of a ligand to a complex with the ions, the reaction is expected to be a simple outer-sphere reaction:

$$Fe\,(H_2O)_6^{3+} + e^- \rightarrow Fe\,(H_2O)_6^{2+} \qquad (1\text{-}14)$$

In early studies, this reaction is treated as a simple charge transfer reaction and is used for testing electrochemical techniques and characterizing electrodes.[43,44] However, researchers found the rate constant for this reaction varies with the supporting electrolytes and electrode materials employed. [45,46] In solutions with chloride, bromide, and sulfate ions present, there is a strongly correlation of reaction rate with ion concentration.[47] One explanation for the catalytic effects of these ions is that they form complexes with the iron ions, leading to the change in the charge of the species and the double layer structure and an apparent improvement in kinetics.[48,49] For example, Weber found the apparent rate constant of ferrous/ferric reaction at polycrystalline Pt and Au electrodes increases linearly with the concentration of chloride ions from 10^{-6} to 10^{-4} mol L^{-1}.[46] To avoid the complexity of strongly adsorbed ions, researchers have turned to use $HClO_4$, a weakly adsorbed medium, as the supporting electrolyte.[43,48] However, even for the perchloric acid electrolyte, there are reports that there is a dependence of activity on crystallographic

orientation.[49] These contradictory results make the $Fe^{2+/3+}$ an interesting reaction to study and raise the question of the role of localized effects. Chapter 3 studied the structure effects on the activity of ferrous oxidation at a polycrystalline Pt foil in both perchloric and sulfuric acid media, to explore both electrode surface structure and electrolyte effects on this reaction.

1.4.2 Oxygen reduction reaction

The electroreduction of oxygen is one of the most important electrocatalysis reactions as it is critical to electrochemical energy conversion applications.[13,50-52,53] However, even on the most active single element catalyst, Pt, the oxygen reduction reaction (ORR) has sluggish kinetics and a sizeable current is only observed at potentials below 0.9 V, significantly below the thermodynamic potential of 1.23 V.[54] Electronic structure calculations have found that the stability of reaction intermediates of electrochemical processes plays key role on the ORR kinetics.[55,56 57]

The ORR is a multi-electron reaction which includes a number of elementary steps and reaction intermediates. Among the various ORR reaction mechanisms proposed,[58-64] the most widely accepted mechanism was given by Wroblowa in 1976 and is shown in Figure 1.9.[64]

As shown, the ORR can occur through two pathways. In both pathways, the first step is the adsorption of oxygen onto the surface, which was confirmed later as the rate determining step. After adsorption, O_2^* can react through a 'direct' pathway or an 'indirect pathway'. In the direct pathway, O_2^* is directly reduced to H_2O in a four electron reaction. In the indirect pathway, the O_2^* is converted to an adsorbed

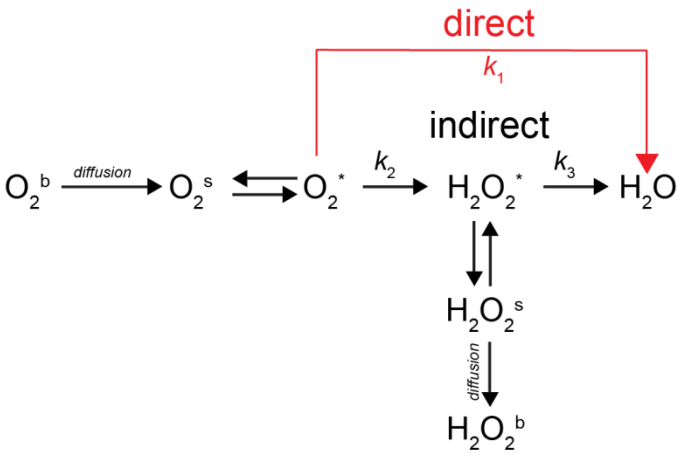

Figure 1.9 A proposed mechanism for the oxygen reduction reaction at a Pt electrode.[64] b, s and * designates to the bulk, vicinity of the electrode, and adsorbed species, respectively.

$H_2O_2^*$ intermediate in a two electron reaction. This adsorbed $H_2O_2^*$ can subsequently undergo another two electron step to form H_2O, or desorb from the surface and diffuse into the bulk of the solution. Finally, in solution phase, it can also undergo the non-Faradaic, homogeneous decomposition reaction to O_2.

The structural sensitivity of ORR has been investigated extensively, mainly using single-crystal electrodes, originally on low-index surfaces[65-68] and later on stepped-surfaces.[69-71] Generally, the structure sensitivity of ORR arises from two aspects: i) the sensitivity of the adsorption energy of the reactive intermediates at different facets and ii) the structure sensitive adsorption of electrolyte species.[28,66,72] For the latter, it is known that solutions containing SO_4^{2-}/HSO_4^-, Cl^- and Br^- adsorb strongly on the Pt surface, whereas ClO_4^- and F^- show minimal adsorption. $HClO_4$ and H_2SO_4 are the two most widely employed acidic electrolytes in fundamental studies. In $HClO_4$, the ORR activity for all the three basal planes (considering half-wave potentials) decreases in the order of Pt(110) > Pt(111) > Pt(100).[66] In H_2SO_4, the ORR activity for all three basal planes is decreased, and the order of activity for the three basal planes is Pt(110) > Pt(100) > Pt(111). The much decreased ORR

activity for all the three planes, especially at Pt(111), illustrates the strong anion adsorption effects for this medium. This (bi)sulfate adsorption was confirmed by spectroscopic evidence[73] and STM data.[74,75] Results indicate sulfate adsorbs on Pt surface through the three oxygen atoms and forming a C3v symmetry. However, (bi)sulfate interacts more weakly with Pt(100) and Pt(110) surface, leading to different structure and much lower coverage. [73,76]

1.4.3 Hydrazine oxidation

Hydrazine (N_2H_4) is of practical interest due to its wide application in the fields of electrocatalysis and electroanalysis.[77-79] For example, it is considered as a possible fuel in low temperature fuel cells.[80,81] Hydrazine is also important in the pharmaceutical industry as it is a common starting material in the synthesis of many pharmaceutical compounds.[82-85]

The mechanism and kinetics of hydrazine oxidation on Pt have been studied in detail[86-89] and a good summary can be found in a review.[90] The overall reaction oxidises hydrazine to molecular nitrogen and depends on the pH:

$$N_2H_5 \rightarrow N_2 + 5H^+ + 4e^- \qquad E^0 = -0.23 \text{ V (vs NHE)} \quad (1\text{-}15)$$

$$N_2H_4 + 4OH^- \rightarrow N_2 + 4H_2O + 4e^- \quad E^0 = -0.33\text{V (vs RHE)} \quad (1\text{-}16)$$

In acidic solution, hydrazine oxidation takes place step-wisely with nitrogen as the final product. The mechanism suggested by Harrison and Khan contains multiple steps:[86]

$$N_2H_5^+ \rightarrow N_2H_4^* + H^+ \quad (1\text{-}17)$$

$$N_2H_4^* \rightarrow N_2H_4^+ + e^- \quad \text{(slow)} \qquad (1\text{-}18)$$

$$N_2H_4^+ \rightarrow N_2 + 4H^+ + 3e^- \quad \text{(fast)} \qquad (1\text{-}19)$$

The first electron transfer step of N_2H_4 on the surface is found to be the rate determining step. The role of the surface structure on the reactivity of hydrazine oxidation has been investigated in different electrolyte at different pH conditions with single-crystal electrodes.[91-96] Feliu *et al.* studied hydrazine oxidation in acidic media on the three basal planes of Pt, Au, and Rh electrodes.[95] For platinum in $HClO_4$, the reactivity (in terms of peak potential) for the basal planes decreases in the order of Pt(100) > Pt(111) > Pt(110). In alkaline solution, the reaction mechanism is different, resulting in a different electrocatalytic activity order: Pt(110) > Pt(100) > Pt(111).[96]

Hydrazine is also interest as it is extensively used in industry as an 'oxygen scavenger' to prevent corrosion, for example of boilers.[97,98] The reaction of hydrazine with oxygen forms the harmless products nitrogen and water, which does not further contribute to corrosion.

$$N_2H_4 + O_2 \rightarrow 2H_2O + N_2 \qquad (1\text{-}20)$$

This reaction, although mainly used at high temperatures and pressure, is reported to occur slowly at room temperature, and can be catalysed by a high solution pH or by some metals, such as Pt and Cu.[82,99,100] Due to the importance of hydrazine in pharmaceutical industry and energy related fields, the detection of hydrazine attracts ample attention, mainly using functionalized electrodes.[101-103] Typically, this detection is carried out in an aerated environment and the effect of oxygen on hydrazine sensors is seldom reported and may not be negligible. In

Chapter 5, the effect of oxygen on hydrazine oxidation at high mass transport conditions was studied.

1.5 Scanning electrochemical probes for electrocatalysis

Traditional macroscopic electrochemical measurements provide important information on structure-activity relationships. However, the information obtained is necessarily an average across an electrode surface, and can only be directly correlated to electrode surface structure if the electrode is homogenous across the probed surface. For polycrystalline metals, which typically heterogeneous features (grains of different sizes and structure), localized measurements are required. In this section, a brief introduction of the application of scanning electrochemical probes in electrocatalysis is outlined.

1.5.1 Scanning electrochemical microscopy (SECM)

Scanning electrochemical microscopy (SECM), developed in the late 1980s, is one of the best known scanning electrochemical probe techniques.[104,105] SECM employs a UME to probe the substrate closely, and scan across the substrate to produce a reactivity map.[1,3,106] The UME is typically an inlaid disk UME, which can be fabricated by sheathing a metal microwire (typically 25 μm or smaller) in an insulating material, such as glass. Depending on the operating mode, the electrochemical current can be recorded at either the UME tip or the substrate to obtain reactivity information.[106] The spatial resolution of SECM depends strongly on the UME size and the UME-to-substrate distance.

SECM has been employed as a quick method to screen libraries of electrocatalysts with different structures and compositions, to provide a guideline for material synthesis.[10,106-111] The ability of SECM in electrocatalysis has been investigated widely by different research groups.[112-115] To date, it has mostly been used to study hydrogen oxidation reaction (HOR)[115-117] and the oxygen reduction reaction (ORR).[108,109,118-121] The studies were summarized in a few reviews.[112,122-124] Herein, only SECM studies for the ORR catalyst screening are discussed. For the ORR, two operation modes, tip generation-substrate collection (TG-SC) and redox competition mode, are used.[107-109] In the TG-SC mode, the SECM tip is held to generate oxygen from water at a constant current. Importantly, oxygen is only generated locally at the tip, with no dissolved oxygen in the bulk of the solution. The generated oxygen can then be reduced at the substrate. By scanning the tip across the substrate, higher substrate currents are observed when the tip passes over the more active spots. Therefore, the magnitude of the substrate current is used as a direct measure of the electrocatalytic activity. In this mode, the magnitude of the substrate current is dominated by the local activity of electrocatalyst spot, with relatively little influence form the tip-to-substrate distance. Bard *et al.* employed this mode to screen the ORR activity of Pd-Co-Au catalysts (of various compositions) supported on carbon.[109]

Figure 1.10 shows the principles of TG-SC mode for ORR and the screening results. It was found spots with a high Pd can efficient reduce oxygen while spots with a high Co content show negligible current towards the ORR. At a low driving force, the catalysts containing 70% Pd, 10% Co and 20% Au have the highest activity towards the ORR.

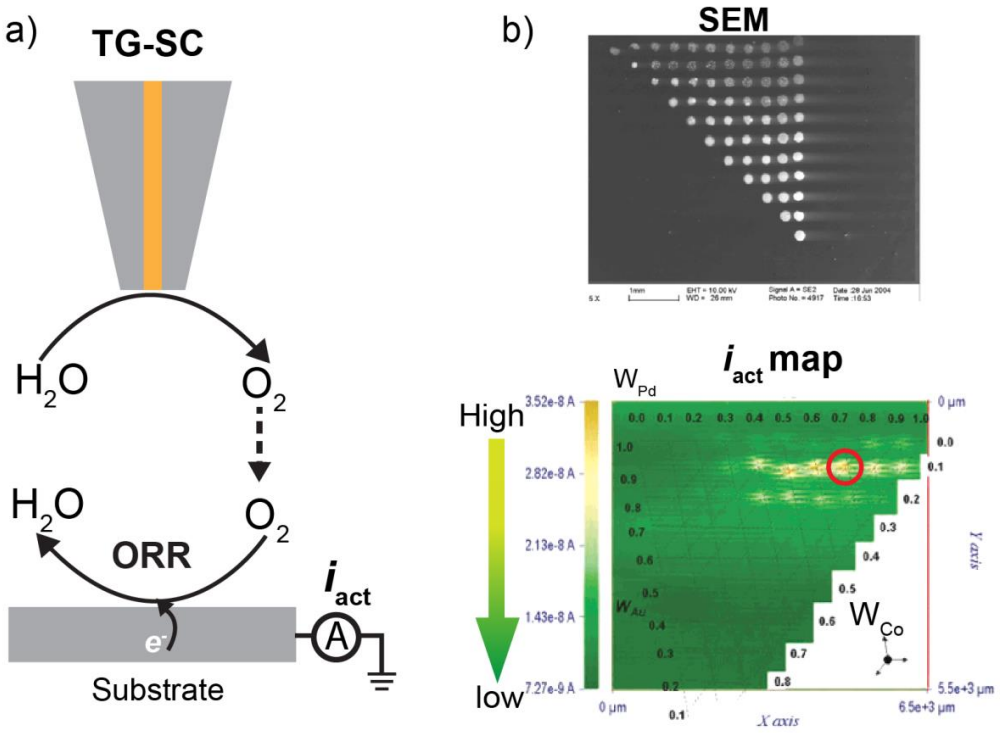

Figure 1.10 a) An illustrative image of TG-SC mode in SECM. **b)** Top, a typical SEM image of a Pd-Au-Co catalyst array. Bottom, a TG-SC SECM image of the ORR activity measured on the array in 0.5 M H_2SO_4 at a substrate potential of 0.75 V versus RHE. The most active spot is marked by a red circle. Reproduced from reference [109].

The main drawback of this technique is that the ORR current is measured at the entire substrate with all the different catalysts, which can lead to a high background current and a lowered resolution. To overcome this, a redox competition mode was introduced.[125-127] A schematic figure is shown in Figure 1.11 in which a potential is applied to both the tip and substrate to reduce dissolved oxygen, while the current at the tip is continuously monitored. As the tip passes over an active area at the substrate, the oxygen flux to the tip is decreased, leading to a decreasing tip current. Conversely, a less active region of the substrate leads to a higher tip current.

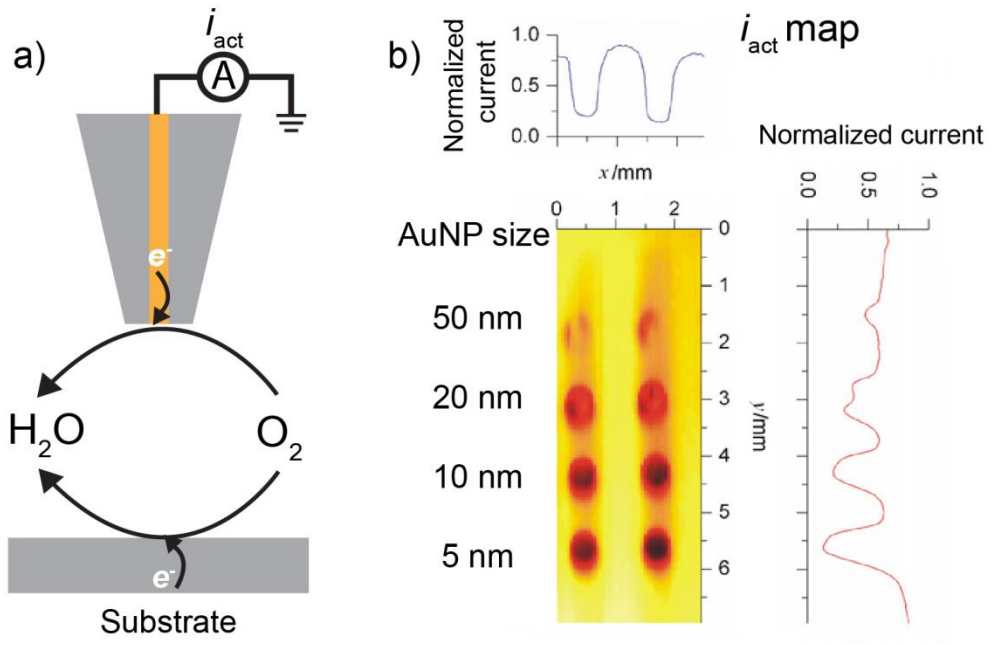

Figure 1.11 a) Schematic illustration of SECM redox competition mode for measuring the ORR activity. **b)** Redox competition SECM image of the ORR activity on Au NP spots of varying particle size ranging from 5 to 50 nm. Electrolyte solution, 0.1 M H_2SO_4. Both tip and substrate potentials were held at -0.2 V versus Ag/AgCl. The current is normalised with bulk current and dark red indicates high activity. Adopted from reference [128].

Thus, compared to the TG-SC mode, redox competition mode shows two key differences. First, the bulk concentration of oxygen is non-zero, and the entire substrate is continuously turning over oxygen. Second, the activity is inferred from the current at the tip rather than from the substrate. As the tip is typically much smaller than the substrate, this leads to lower background currents and therefore an enhanced spatial resolution and sensitivity. Figure 1.11 shows an example of using the SECM redox competition mode to image the electrocatalytic activity of Au NP arrays towards the ORR in H_2SO_4 solution.[128] Spots of varying Au NP sizes were prepared by dispersing Au NP colloid solution on a glassy carbon substrate. It is

found for Au NPs diameter in the range 5–50 nm, the electrocatalytic activity towards the ORR increased with decreasing particle size.

1.5.2 Scanning droplet cell

Although SECM is a powerful technique for investigating electrocatalysis locally, the spatial resolution is limited by the fact that it relies on probing diffusion fields. Consequently, only reactions with a reaction rate sufficiently high to induce concentration gradients can be probed. Furthermore, when performing SECM experiments, the substrate has to be immersed in the electrolyte solution during acquisition of the electrochemical image, which could result in unwanted fouling of or corrosion of the surface. Additionally, SECM measurements require the redox species to have a reversible reaction mechanism, which makes it less suitable for studying more complicated reactions. To circumvent these issues, pipette-based electrochemical scanning probe methods were used as an alternative approach to study electrocatalysis.

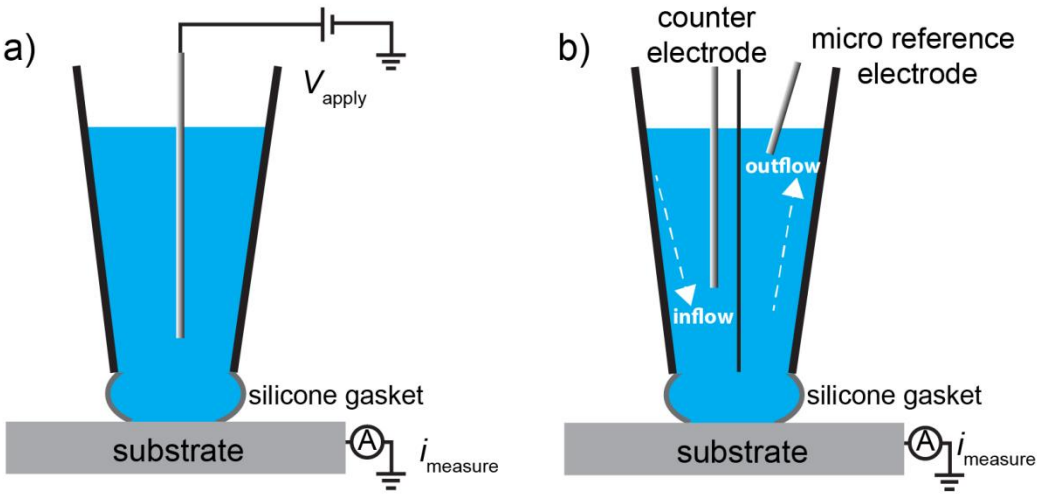

Figure 1.12 Schematic illustration of scanning droplet cells. **a)** A single barrel cell; **b)** a double channel flow cell.

One of such pipette-based electrochemical scanning probe methods is the scanning droplet cell (schematically shown in Figure 1.12), which was originally developed by Bohni, Suter and Lohrengel for high resolution corrosion studies.[129-131] A scanning droplet cell consists of three main components: i) a (mobile) pipette probe, made of glass, plastic or metal, filled with electrolyte solution; ii) a reference and/or counter electrode placed in the pipette; iii) a substrate of interest as a working electrode. By bringing the droplet at the end of the probe in contact with a substrate, a small electrochemical cell is formed in which the contact area of the substrate defines the working electrode. Consequently, any electrochemical response at the substrate can wholly be attributed to only the contact area. Initially, scanning droplet cells employed relatively large pipettes, with diameters ranging from 100 μm to 1000 μm, and a silicone rubber gasket was required to confine the droplet at the end of the pipette.[129,130] This setup allowed measurement of localized corrosion process on various stainless steels. Researchers later introduced automated probe-positioning system to monitor pipette landing and electrolyte flow cells to reduce the risk of pipette blocking and to refresh the electrolyte solution (Figure 1.12b). [132-135]

A key application of scanning droplet cells is to isolate a single surface site on a (heterogeneous) surface. This property has, for example, been exploited to investigate oxide film growth on polycrystalline electrodes.[136,137] For instance, Lohrengel studied the crystallographic orientation dependent metal oxide growth at Zr and Ta electrodes by placing the droplet cell on a grain or at a grain boundary of interest (as schematically shown in Figure 1.13).[137] Then, CV measurements were performed. EBSD experiments provide further information of the grain crystallographic orientation. In this study, due to the size of the pipette, only grains

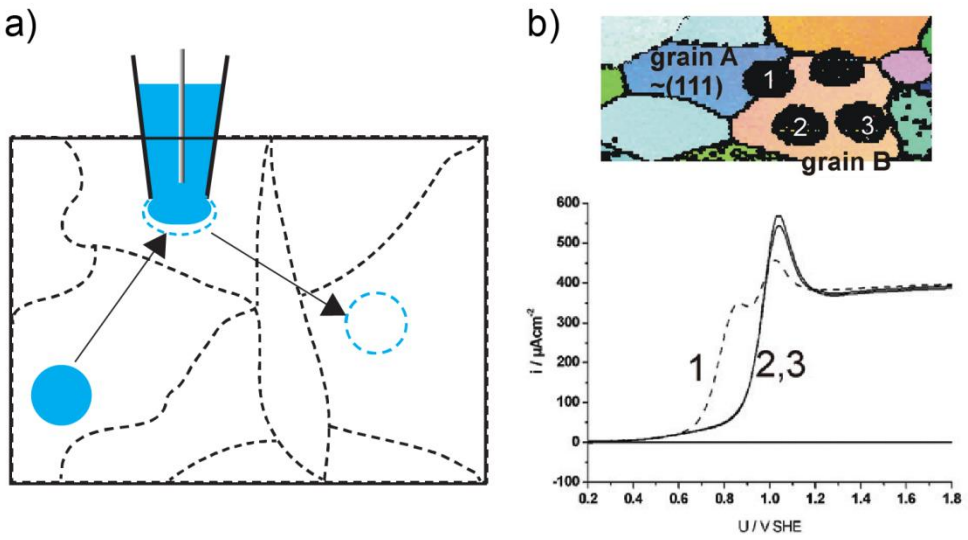

Figure 1.13 a) Illustration of the movement of a scanning droplet cell at a polycrystalline material. Solid dot: a measured spot. Dash dot: an aiming spot. **b)** Using scanning droplet cell to locate (top) and record CVs (bottom) at different grains to study oxide formation at an electropolished Nb substrate. Reproduced from reference [137].

larger than 100 μm could be studied. Besides, due to the pipette operation mode, the measurements could only be performed at a limit number of isolated areas. Thus, the spatial resolution is rather low and the activity of the grain boundary cannot be easily deconvoluted from that of the neighbouring grains.

Another interesting application of scanning droplet cells in electrocatalysis is combining this technique with other analytical methods, to achieve real time detection of the reaction intermediates and products. For example, Mayrhofer's group combined an electrochemical scanning flow cell with an inductively coupled plasma mass spectrometer (ICP-MS), to study the stability of electrocatalysts, especially Pt-based catalysts, during voltammetric cycling.[138,139] A schematic of the instrument setup and the results is shown in Figure 1.14. The electrolyte flows in

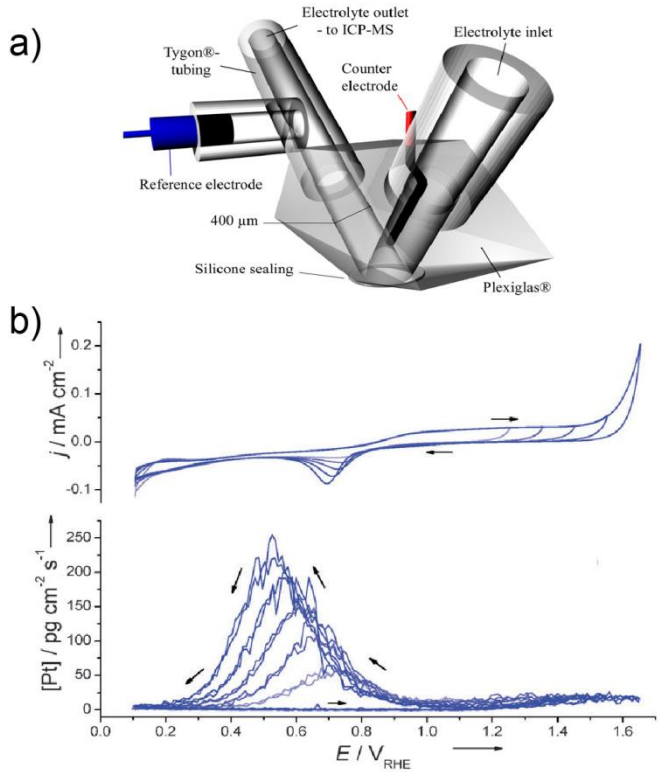

Figure 1.14 a) Experiment setup of a scanning flow cell coupled with ICP-MS. **b)** Representative cyclic voltammograms (top) of a Pt foil in an electrolyte solution of 0.1 M $HClO_4$ at a scan rate of 10 mV s^{-1} and their corresponding mass-spectrometric voltammograms (bottom). Figures are reproduced from references [138] and [139].

from one channel, participates in the surface reaction, and flows out from the other, containing species produced at the surface and analysed immediately with a ICP-MS.

Figure 1.14b shows one result obtained on a platinum electrode.[139] The top figure is the CVs starting at 0.1 V and ending at different anodic potentials, ranging from 1.2 to 1.6 V. The bottom figure shows the detected amount of dissolved Pt with the change in applied potentials. Clearly, Pt dissolution occurs during both the anodic and cathodic cycling although it is much more pronounced in the cathodic scan. Furthermore, results indicate that the loss of Pt during cycling increases with the increased upper-limit potential.

1.5.3 Scanning micropipette contact methods (SMCM)

The scanning micropipette contact methods (SMCM) advances the pipette cell techniques with an automated probe-positioning system, allowing the use of (sub-) micrometre-sized pipettes.[140] In SMCM, a single-barrelled pipette is mounted on a *x*,*y*,*z*-piezoelectric positioner, allowing lateral and vertical movement of the cell. A bias potential is applied between the substrate (working electrode) and the reference electrode. The pipette was automatically halted when a non-zero electrochemical current at the surface was measured, indicative of contact of the droplet. By holding the potential at a fixed value, the electrochemical measurement is performed at a fixed area or through scanning with a point to point movement. One of the applications of SMCM in electrocatalysis is the NP deposition.[141,142] One example is using SMCM to deposit Pt NPs at carbon nanotube networks.[142] The well separated Pt NP arrays with different densities were prepared by varying the number of deposition cycles. These arrays were used to study the surface coverage effect on the ORR and the oxidation of methanol. For the ORR, it is found once the diffusion profile of NPs overlaps with each other, further increasing the NP coverage has little effect on the ORR activity. For the methanol oxidation reaction, the activity increases linearly with the active area of the NP array. In SMCM, importantly, as the current at the substrate is used for monitoring electrolyte contact, this method is limited to (semi-) conductive substrates. The main challenge in SMCM measurement is the lack of control over the tip-to-substrate separation, requiring a new approach for each surface site, thereby building an image one spot at a time.

1.5.4 Scanning electrochemical cell microscopy (SECCM)

Scanning electrochemical cell microscopy (SECCM), developed in 2010 in the Warwick Electrochemistry and Interface Group,[7,143-148] further advances on the micropipette concept by implementing a feedback protocol. As a result, electron transfers at a working electrode and the topography of the substrate can be recorded simultaneously in SECCM. It is particularly powerful in imaging heterogeneous surfaces and studying electrocatalysis at these surfaces.

The working principle of SECCM is briefly shown in Figure 1.15, and discussed in detail in Chapter 2. One of the applications of SECCM in

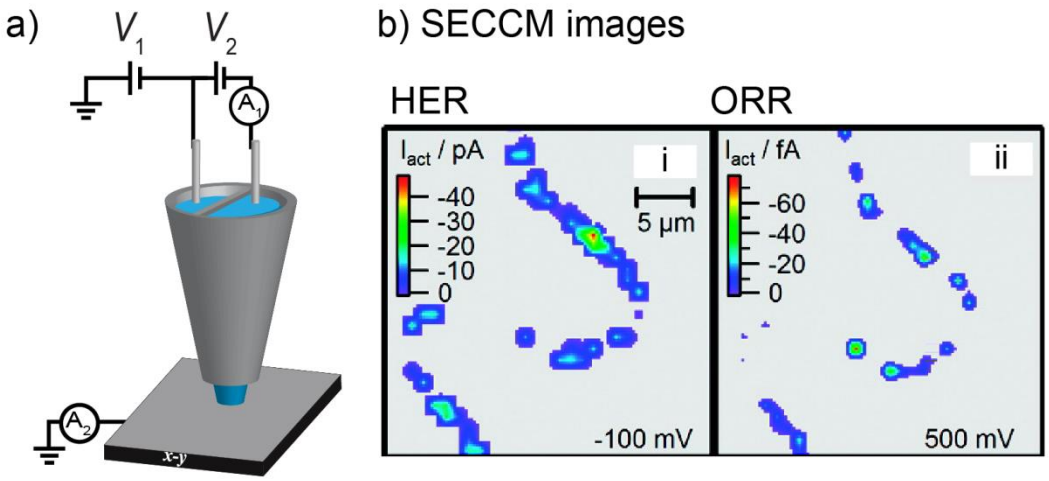

Figure 1.15 a) A schematic representation of SECCM setup and SECCM imaging of Pt nanoparticles. A bias potential (V_2) is applied between two quasi-reference counter electrodes (QRCEs), allowing for positional feedback. Surface potential (E_s) is applied to the substrate (working electrode). $E_s = -(V_1 + 0.5V_2)$. While the tip scans in the *xy*-plane, images of the ion conductivity across the meniscus, feedback quality, topography, and surface activity are obtained simultaneously. **b)** Electrochemical activity image of the Pt NPs deposited on a carbon nanotube for the HER (i), and the ORR (ii). Figure 1.15b is adapted from reference [149].

electrocatalysis was studying the electrocatalytic activity of Pt NPs toward the HER and ORR in acidic solution.[149] Well-separated Pt NPs were prepared by electrodeposition on a single-walled carbon nanotube. The carbon nanotube served as a template for electrodeposition as well as a conductive support to connect all the NPs. By scanning the Pt NPs with a pipette of ~ 1 μm, which is smaller than the typical separation between the NPs, surface activity maps at different driving potentials (from - 0.1 to 0.6 vs RHE) showing single NPs were obtained. The electrocatalytic response of individual Pt NPs obtained with SECCM could be correlated with atomic force microscopy (AFM) and SEM images of the same area. SECCM surface current images showed highly non-uniform catalytic activity of these NPs for both the ORR and HER. Subtle changes in NP sizes and shapes leads to significant difference in activity, highlighting the strength of single NP measurement.

1.6 Towards 'real' nanoparticle catalysis

1.6.1 Single nanoparticle collision experiment

Electrocatalysts in technical applications often employ nanoparticles (NPs).[27,150-152] These NPs, due to their small size, have physical and chemical properties which can differ greatly from those of bulk materials.[153,154] In addition, NPs possess a high surface-to-volume ratio, allowing for maximum material utilisation. Typical electrochemical approaches for studying NP properties are carried out on NP ensembles, which are immobilized on a support electrode. In addition to NP size and shape effects, the local interactions between NPs and the supporting

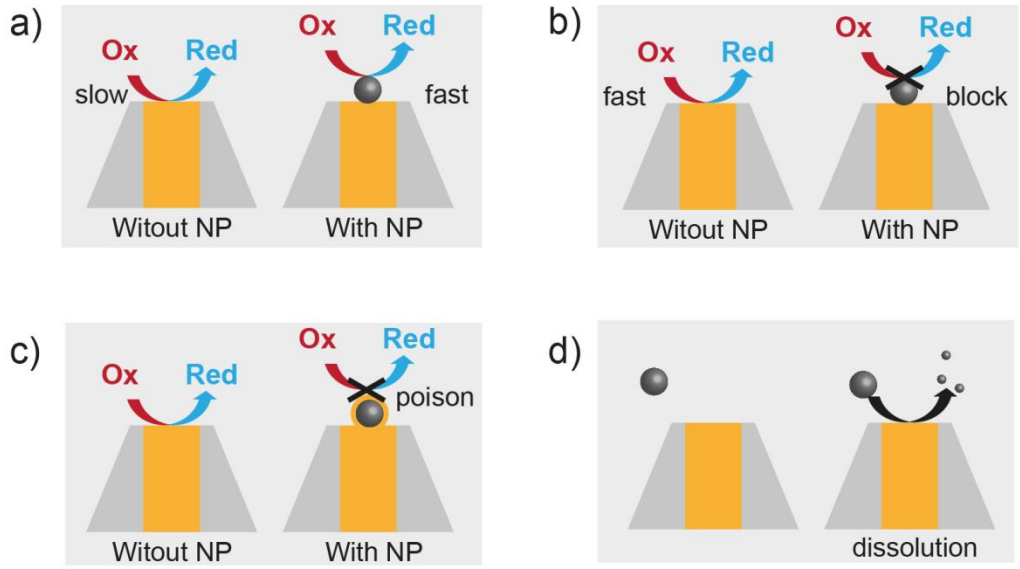

Figure 1.16 Schematic illustration of different methods for NP-impact experiment. **a)** NPs boost electron transfer of a solution species. **b)** Insulating NPs block electron transfer of a solution species **c)** NPs were poisoned at an (Hg) UME. **d)** NP dissolution at an UME.

electrode also have influence on the electrocatalytic performance of NPs. To fully understand these (coupled) effects and to avoid ensemble averaging of the electrocatalytic response, single NP electrochemical measurements need to be performed. [155]

To study single NP electrochemistry, one can separate NPs spatially or temporally. The SECCM study discussed above (section 1.5.4) is one of the examples of studying single NPs by separating them on a supporting material. Another strategy is reported by Bard's group in 2007, in which they studied the electron transfer properties of NPs by performing NP collision experiments.[156] In this strategy, a non-catalytic UME is immersed into solutions containing both redox species and electrocatalytically active colloidal NPs. The UME is held at a potential at which the reaction would occur on the NPs, but not at the bare UME. Consequently, the arrival of a NP at the UME 'switches on' the electrocatalytic

reaction and produces an electrochemical signal which can be detected and directly related to that particular single NP. Various combinations of electrocatalytic reactions, NPs and UMEs have been studied, including the HER at Pt NPs on carbon UMEs,[156] hydrazine oxidation at Pt- or Au- NPs on carbon,[148] diamond,[157] and Hg UMEs,[158-160] and the ORR at IrOx NPs on PtO UMEs.[161] This NP collision method has shown great promise in particle sizing, detecting and studying ET kinetics at a single NP level.

So far, most of the NP-impact experiments were performed at sealed-microwire UMEs. Figure 1.16 summarized four different types NP collision experiments. These include (i) NP mediated electrochemical reactions at 'inert' UMEs; (ii) insulating NPs blocked electrochemical reactions at 'active' UMEs; (iii) detecting NPs by poisoning them with mercury electrodes and (iv) NP dissolution. Although various types of reactions can occur at the NP (or electrode) surface, in general terms, two types of responses have been observed: if the catalytic reaction on the NP only occurs for a short time (due to, e.g., elastic collision of the NP, NP deactivation or NP dissolution), the resulting signal has a transient nature, which is termed a 'spike' signal. Conversely, if the catalytic reaction on the NP is permanent, the resulting current-time trace shows a stepwise increase, termed a 'staircase' signal.[162-164]

1.6.2 Self-assembled monolayers (SAMs)

To investigate the surface chemistry effects on NPs, an (electrode) surface on a fundamental level, well-defined and thoroughly characterized model systems would be greatly beneficial. SAMs present such a system. An exemplar class of

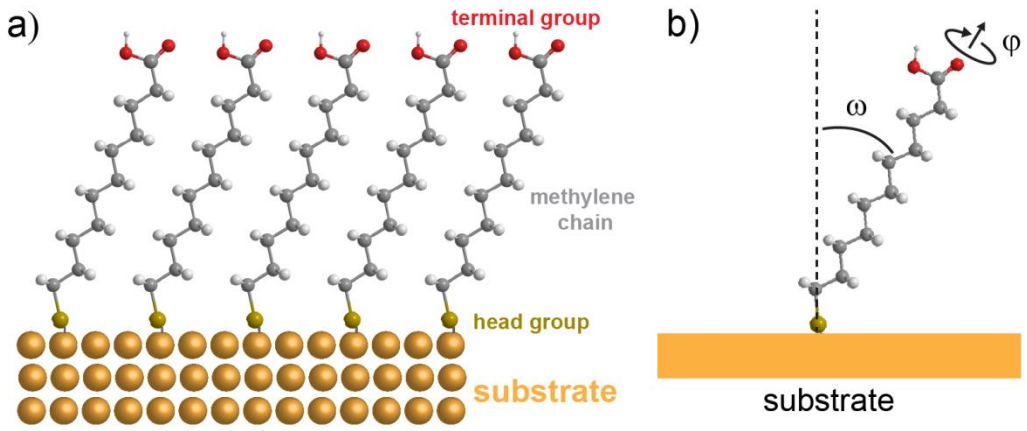

Figure 1.17 a) Structure of a SAM formed by HS-$(CH_2)_{10}$COOH at a Au (111) substrate. **b)** Illustration of tilted angles of alkanethiols adsorbed on a surface: ω : tilt angle with respect to the surface normal direction; φ : rotation angle of the carbon bond plane relative to the plane of the surface normal. For alkanethiols at a Au(111) surface, ω and φ value are ~30° and 50° respectively.[167]

SAM systems is a monolayer of (functionalised) alkanethiols at metal surfaces.[165,166] Alkanethiolate SAMs offer a number of key advantages as a model substrate, including i) the ease of monolayer fabrication, ii) a wide understanding of the behaviour of alkanethiol SAMs, providing a useful frame of reference, iii) a wide range of accessible chemical functionalities of the terminating group, and iv) high control over monolayer thickness, (within ~ 1 Å, one CH_2 group), by varying the length of the carbon chain.[167] [168] In this thesis, unless specified, the SAMs denotes to SAMs formed by alkanethiols.

The general structure of an alkanethiol can be given by $HS(CH_2)_nX$ (Figure 1.17), in which HS is the thiol head group, *n* gives the number of methylene units and X represents the terminal group. The generally accepted structure of high-coverage alkanethiols formed at Au(111) surfaces is a 2 dimensional structure

featuring a $(\sqrt{3}\times\sqrt{3})$ R30° lattice (R = rotated).[169-173] Figure 1.17 illustrates the SAM structure on an Au substrate, in which ω is the tilt angle of the carbon chain with respect to the surface normal direction and φ is the twist of the carbon chain plane with respect to its long axis. [167,173]

Among all the substrates reported for preparing SAMs, Au (especially Au(111)) is the most well understood and intensively studied substrate. The main reason arises from (i) it is relatively 'inert' to most chemicals; (ii) it has a high affinity with thiols. The formation of alkanethiol SAMs at Au surfaces is presumed to occur through the oxidative addition of the S-H bond to the Au surface, as described in the following reaction:[174]

$$\text{RS-H} + \text{Au} \rightarrow \text{RS-Au} + \text{H}^+ + \text{e}^- \qquad (1\text{-}21)$$

A standard procedure for preparing SAMs is by immersing a clean Au substrate into a solution containing a mM concentration of the thiol of interest in ethanol for ~ 12 to 24 hours.[166,173] The initial attachment of thiols on the surface is quick, but a long time is needed to form a close-packed structure. During the formation, various factors can affect SAM quality, including substrate roughness, alkanethiol length, temperature, and immersion time. In terms alkanethiol length, it is found that thiols with long carbon chains can form better ordered SAM with relatively low defects as the Van der Waals interaction between the individual molecules increase proportionally with the length of the alkyl chain. In Chapter 6, all thiols used have alkane chains more than ten carbons long.

1.6.3 Electrochemistry at SAMs

Chemical modification of an electrode surface with an insulating (SAM) layer effects the electron transfer rate at the surface, as an electron needs to tunnel through the layer. Specifically, the electron transfer rate has been found to follow the following relation with the thickness of the insulating layer.[175-178]

$$k_{ET} = k^{A} e^{-\beta d} \tag{1-22}$$

in which k_{ET} is the rate of electron transfer, k^{A} is a pre-exponential factor, (electron transfer rate of a redox species in the absence of the SAM), d is the alkyl chain length and β is the tunnelling constant which is determined by the SAM structure.

The tunnelling constant, β, can be determined by comparing the electron transfer rate at the SAM modified electrode and bare electrode, either through studying electron transfer of solution redox species[165] or examining the ET property of redox couples covalently bounded to the thiol.[175,179,180] It is found typical β values for saturated hydrocarbon chain are in the range of 0.9 to 1.3 $Å^{-1}$.[176,177,181] Consequently, for a β value of 1.0 $Å^{-1}$ and a SAM with a carbon chain of 12 carbon lengths (~12 Å), the calculated k_{ET} is approximately one million times smaller than k^{A}. This illustrates SAMs thicker than 1 nm can effectively block ET between a species in solution and the electrode surface, with negligible Faradaic electrochemistry taking place.

1.6.4 NP mediated electron transfer

Although the electron transfer can be blocked by SAM layer, it has been found recently that by assembling metal nanostructures on top of a SAM modified

surface, the electron transfer can be restored.[182-192] The first example might be experiments reported by Natan, in which they found the cyclic voltammetry of p-nitrosodimethylaniline on Au/In-SnO_2/Au surface is the same as that on unmodified Au surface.[193] More recent work has been reported by the Fermín[182] and Gooding[192] groups by studying electron transfer of simple redox species in the solution. For example, the Fermín group studied the electron transfer of $[Fe(CN)_6]^{4-}/[Fe(CN)_6]^{3-}$ at Au electrodes modified by a self-assembled monolayer of 11-mercaptoundecanoic acid, followed by alternate adsorption of poly-L-lysine and poly-L-glutamic acid layers.[185] In the absence of Au NPs, the electron transfer was efficiently blocked. With Au NPs adsorbed on top of the polymer modified surface, effective electron-transfer kinetics was observed for film thicknesses up to 6.5 nm. The results were interpreted in terms of increased tunnelling probability between the electrode and the high density of states of the adsorbed NPs. The NP mediated electron transfer at SAM modified metal electrodes has been confirmed by the two groups at a variety of modified surfaces with NPs of various sizes and compositions.[182-191,194]

The principle of NP-mediated electron transfer can be illustrated by Figure 1.18 and the experimental results for can be summarized as a few key observations.[184,195] (i) The absence of NPs, electron transfer to the metal electrode is blocked by the insulating SAM layer. In the presence of NPs, CVs obtained were nearly identical to those on bare metal electrodes. (ii) No length effect was found for CH_2 unit ranging from two to ten. (iii) The limiting step is the electron transfer between redox species in the solution and the NP.

A theoretical framework for this phenomenon was proposed by Chazalviel and Allongue.[196] In brief, the electron transfer rate between two objects is essentially

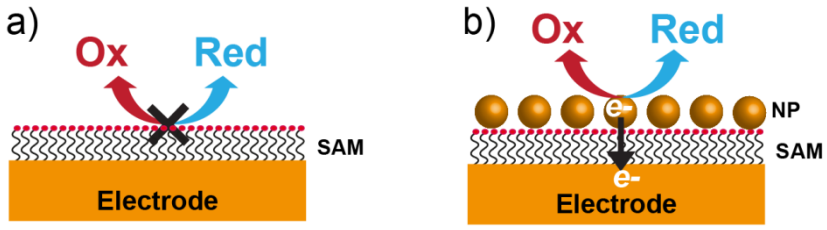

Figure 1.18 Principle of NP mediated charge transfer across insulating monolayers. **a)** In the absence NPs, electron transfer from solution species to the underlying electrode is hindered by the SAM layer. **b)** In the presence of NPs, the electron transfer can occur with the mediation of NPs.

the probability of electron tunneling: $k_{ET} \sim j_0 \cdot \exp(-\beta d)$. The pre-exponential factor, expressed as an exchange current density, depends on the coupling of the electronic state between the two objects. For two metallic phases, such as a NP and a metal electrode, the exchange current density ($j_{M\text{-}M}$) is much larger (about 10^{12} times) than that for a redox species to a metal electrode ($j_{M\text{-redox}}$). The introduction of a SAM causes a decrease in the k_{ET} rate proportional to $\exp(-\beta d)$. However, due to the large $j_{M\text{-}M}$, electron transfer between two metals (such as a NP and a supporting electrode) across an insulating layer ($\sim j_{M\text{-}M} \exp(-\beta d)$) remains much larger than that between a redox species and a metal (such as the Faradaic reaction at a NP, $\sim j_{M\text{-redox}}$). Thus, the overall electron transfer rate is limited by the slower process, which is the electron transfer between the redox species and the NP. Figure 1.19a is the theoretical predication of the critical SAM thickness versus NP diameter to lead to a change in voltammograms of a reversible redox species compared to a bare electrode. As shown, this model[196] predicts that electron tunneling from a NP to a metal electrode is more efficient when the NP size relative to the SAM thickness increases.

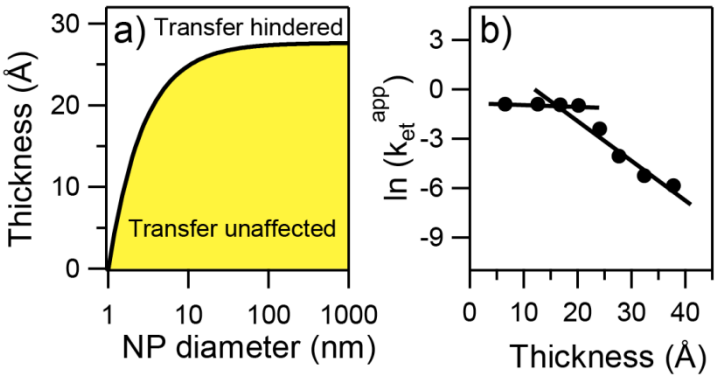

Figure 1.19 a) Theoretical prediction of critical SAM thickness versus NP diameter to lead to a change in the k_{ET} of a reversible redox species. Yellow area, transfer unaffected. White area, transfer hindered. **b)** Experimental data of the apparent k_{ET} for $[Ru(NH_3)_6]^{3+}/[Ru(NH_3)_6]^{2+}$ on 27 nm Au NPs with the thickness of an insulating poly(ethylenediame) layer. Figures are adopted from references [164], [196], and [197].

Experimental data from Gooding's group supported this theory and is summarized in Figure 1.19b. They studied electron transfer of $[Ru(NH_3)_6]^{3+}/[Ru(NH_3)_6]^{2+}$ redox couple on a poly(ethylenediame)-glassy carbon electrode modified with 27 nm diameter Au NPs. The apparent rate constant showed a change from thickness independent to thickness dependent as the organic layer exceeded an average thickness of 20 Å.

Recently, Bard and co-workers proposed a model to understand the effects of film thickness and NP size on the electrochemical current densities in a NP-insulating film-metal system by treating mass transfer, electron transfer from redox species to an NP, and the electron tunnelling between a NP and the metal substrate as separate steps. For a system that is mass transport controlled, the critical film thickness to change the reaction from tunnelling control to electrochemistry control is about 1 to 2 nm. For a reaction that is under kinetic control, the dependence of the

film thickness is similar with the previous case, with the role of electron tunnelling becoming more prominent with increasing NP size.[198]

1.6.5 Atomic Force Microscopy (AFM) force measurement

Force-distance measurements with an AFM can provide valuable information on local material properties and molecular interactions.[199-201] As shown from the schematic in Figure 1.20a, it employs a conventional AFM setup, in which the sample, or the AFM cantilever tip is mounted on a piezoelectric translator. The deflection of the AFM cantilever is monitored continuously through the reflection of a laser beam on the back of the cantilever, onto a photodiode, while the tip is brought towards the surface. As a result, the cantilever deflection (δ) as a function of the tip position is obtained.

To convert the cantilever deflection to forces, Hooke's law is applied to the cantilever deflection:

$$F = \kappa\delta \tag{1-23}$$

where, κ is the spring constant of the cantilever. The spring constant can be obtained by measuring its deflection in response to thermal noise.

A schematic of a typical force-distance (or, more specifically, a force-displacement) curve is shown in Figure 1.20b, and multiple regions in the response can be observed. In region i), the tip is far away from the surface and no force is detected; ii) a contact is made between the tip and the substrate; iii) further movement bends the cantilever and a repulsive interaction is observed; iv) after

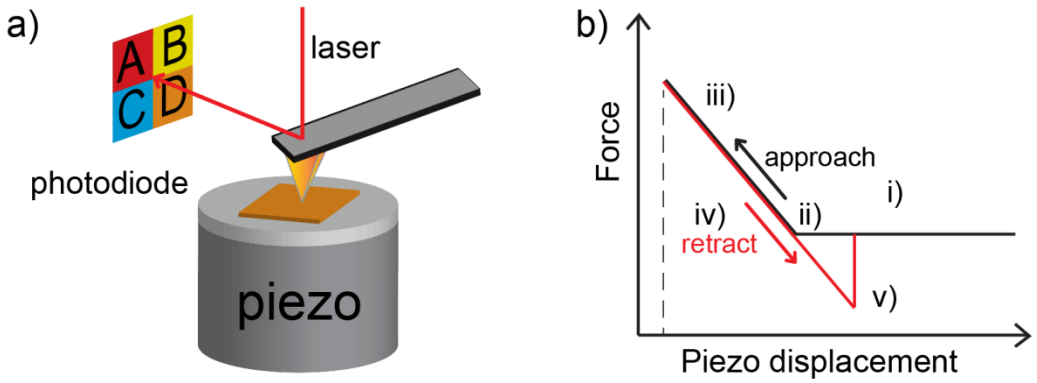

Figure 1.20 a) Schematic of an atomic force microscope and **b)** a typical force versus piezo displacement curve. Five different regions of piezo positions are marked in the force curve.

reaching a user-defined deflection threshold, the piezo movement is reversed and the cantilever is retracted. In this stage, withdrawing of the tip can lead to hysteretic behaviour of the curve; v) continuous withdrawal overcomes the adhesion force and leads to a 'snap-off'. The adhesion force measured during cantilever withdrawal provides information of the interaction between tip and the substrate.

One important application of AFM force measurement is probing inter-molecular forces and the measurement of surface energetics. To do this, the Lieber group introduced chemical force microscopy (CFM).[200,202,203] In CFM, AFM probes are modified with organic molecules or strongly adsorbed ions. By measuring the force curve of the tip approaching a substrate of interest, the molecular interactions can be probed directly and imaging with chemical sensitivity can be achieved. CFM has found applications in a lot of area, including study of intermolecular forces between different molecular groups,[203,204] determining surface pK_a values,[205,206] and measuring surface energetics. In this thesis, CFM was used to study the interaction between NP and alkanethiol modified Au electrodes with different terminating groups.

1.7 Aims of study

A fundamental understanding of the role of the morphology (e.g. crystallographic orientation) of an electrode surface on its electrochemical activity is a key topic in electrochemical research, and of crucial importance to the development of electrochemical technologies. A true understanding of this relation between electrode structure and reactivity requires investigations at the level at which only a single surface feature is probed, necessitating approaches that allow probing electrochemical responses locally. The work described in this thesis focuses on performing localised electrochemical measurements at polycrystalline platinum surfaces using SECCM. SECCM allows measurements at (sub-)micrometer scale, thereby isolating the response of a single type of surface site or feature, rather than measuring at the macroscale, where the reactivity of a single site may be obscured. In addition to elucidating the role of surface properties on the activity, a number of other interesting issues, such as electrolyte effects on the reaction, the role of (enhanced) mass transport and the effect of parasitic reactions were also studied through investigating different electrochemical systems.

Chapter 2 describes the procedures and techniques used throughout this thesis. In particular, the SECCM setup and imaging procedures are discussed in detail in this chapter.

Chapter 3 introduces a 'pseudo-single crystal' method to study structure-activity relationship for polycrystalline platinum electrodes. $Fe^{2+/3+}$, an ostensibly simple one-electron transfer redox couple is used as an illustrative case. While the ubiquity of this redox couple in electroanalysis has caused it to be studied extensively, the role of electrode structure and electrolyte composition on its activity is still under debate. In particular, there is no consensus on the very basic issue of

whether this couple should be treated an outer-sphere reaction or as a structure-sensitive inner-sphere reaction. So far, most of the previous research was carried out at macroscopic electrodes, which are heterogeneous in structure. To truly understand this reaction, one needs to study the features and sites present on the surfaces and the local electrochemical responses of these sites. In this chapter, $Fe^{2+/3+}$ is studied at a polycrystalline Pt electrode using a SECCM. The small size of the probe allows investigating the electrochemistry of $Fe^{2+/3+}$ at single grains and grain boundaries. High resolution maps of the electrochemical activity across the surface demonstrate that the activity of this redox couple relates to local electrode structure. Additionally, the effect of specific ion adsorption was studied by comparing two different electrolytes, namely perchloric acid and sulfuric acid, and we show that the pattern of reactivity can change completely depending on the anion adsorption strength.

Chapter 4 employs the 'pseudo-single crystal method' to study the single grain activity of the ORR at polycrystalline platinum electrode in sulfuric acid medium. The ORR is one of the most important electrocatalysis reactions and its slow kinetics is one of the main (scientific) limitations to the widespread adoption of commercially viable fuel cell devices. Most fuel cells operate with gaseous oxygen from air rather than dissolved oxygen, and the reaction occurs mainly at the (electrode-electrolyte-air) three-phase boundary. SECCM mimics this configuration, as it provides a three-phase boundary between Pt electrode, aqueous electrolyte and air. This chapter aims to study the ORR under differential mass transport conditions, where oxygen can be supplied across the electrolyte-air interface, but other reactant and products species can only be supplied or removed through the electrolyte. By employing the pseudo-single crystal method introduced in Chapter 3, we mapped the ORR activity at high-index Pt surfaces. The effects of electrode structure and

differential mass transport on the activity of ORR at a polycrystalline Pt electrode are discussed.

Chapter 5 introduces voltammetric scanning electrochemical cell microscopy (SECCM). The work discussed in Chapters 3 and 4 were performed by scanning a substrate of interest by holding it at a constant potential. Although this constant potential mode is powerful, only one potential of interest can be applied during the scanning thus only electrostatic information can be obtained. Furthermore, as the probe is continuously in contact with the surface, it is limited to relatively flat surfaces. To overcome the difficulty in the application of SECCM scanning on rough surfaces, as well as to obtain electrodynamic information of a reaction, voltammetric SECCM is developed in Chapter 5. This approach advances electrochemical imaging by incorporating a hopping voltammetric scanning mode. The approach was exemplified by studying surface structure effects on the oxidation of hydrazine, both in air and under deoxygenated conditions at a polycrystalline platinum electrode.

In Chapter 6, the electron transfer of single nanoparticles and their interaction with the substrate is studied. The fundamental electron transfer properties between an NP and a redox species in solution, as well as between the NP and substrate is of great importance. Although the detection of single NP through collisions with an UME has provided significant insights in single NP electrochemistry, the effect of the properties of the supporting surface on its interaction with a NP has often been overlooked. In addition, the effect of the instrument response on the electrochemical measurement of single NP collisions (and in small, transient electrochemical signals in general), is rarely discussed. In this chapter, a pipette based approach is used to detect electron transfer of a redox couple at single NPs and to probe their interactions with self-assembled monolayers with different functionalities. The result was

supported by AFM force measurements. Results showed that the chemical functionality of the substrate plays an important role in NP interaction with the substrate.

Chapter 7 provides a summary of the work undertaken, draws some general conclusions and provides an outlook for future developments and research.

1.8 References

(1) Bard, A. J.; Faulkner, L. R. *Electrochemical Methods: Fundamentals and Applications*; Wiley, 2000.

(2) Fisher, A. C. *Electrode Dynamics*; Oxford University Press, 1996.

(3) Amemiya, S.; Bard, A. J.; Fan, F. R. F.; Mirkin, M. V.; Unwin, P. R. *Annu. Rev. Anal. Chem.* **2008**, *1*, 95.

(4) Forster, R. J. *Chem. Soc. Rev.* **1994**, *23*, 289.

(5) Montenegro, I.; Queirós, A.; Daschbach, J. L.; Division, N. A. T. O. S. A. *Microelectrodes: Theory and Applications: Theory and Applications*; Springer Netherlands, 1991.

(6) Bard, A. J.; Mirkin, M. V. *Scanning Electrochemical Microscopy*; Marcel Dekker: New York, 2001.

(7) Snowden, M. E.; Güell, A. G.; Lai, S. C. S.; McKelvey, K.; Ebejer, N.; O'Connell, M. A.; Colburn, A. W.; Unwin, P. R. *Anal. Chem.* **2012**, *84*, 2483.

(8) Mirkin, M. V.; Amemiya, S. *Nanoelectrochemistry*; CRC Press, 2015.

(9) Schmickler, W.; Santos, E. *Interfacial Electrochemistry*; Springer Berlin Heidelberg, 2010.

(10) Bard, A. J. *J. Am. Chem. Soc.* **2010**, *132*, 7559.

(11) Taube, H. *Electron transfer reactions of complex ions in solution*; Academic Press, 1970.

(12) Grubb, W. T. *Nature* **1963**, *198*, 883.

(13) Appleby, A. *Catalysis Reviews* **1971**, *4*, 221.

(14) Carrette, L.; Friedrich, K. A.; Stimming, U. *Fuel Cells* **2001**, *1*, 5.

(15) Girishkumar, G.; McCloskey, B.; Luntz, A. C.; Swanson, S.; Wilcke, W. *J. Phys. Chem. Lett.* **2010**, *1*, 2193.

(16) McCloskey, B. D.; Scheffler, R.; Speidel, A.; Bethune, D. S.; Shelby, R. M.; Luntz, A. C. *J. Am. Chem. Soc.* **2011**, *133*, 18038.

(17) Shao, Y.; Park, S.; Xiao, J.; Zhang, J.-G.; Wang, Y.; Liu, J. *ACS Catal.* **2012**, *2*, 844.

(18) Walcarius, A. *TrAC, Trends Anal. Chem.* **2012**, *38*, 79.

(19) Sherigara, B. S.; Kutner, W.; D'Souza, F. *Electroanalysis* **2003**, *15*, 753.

(20) Srinivasan, S. *Fuel cells: from fundamentals to applications*; Springer Science & Business media, 2006.

(21) Mehta, V.; Cooper, J. S. *J. Power Sources* **2003**, *114*, 32.

(22) Zhang, S.; Yuan, X.-Z.; Hin, J. N. C.; Wang, H.; Friedrich, K. A.; Schulze, M. *J. Power Sources* **2009**, *194*, 588.

(23) Srinivasan, S.; Mosdale, R.; Stevens, P.; Yang, C. *Annu. Rev. Energy* **1999**, *24*, 281.

(24) Liu, H.; Song, C.; Zhang, L.; Zhang, J.; Wang, H.; Wilkinson, D. P. *J. Power Sources* **2006**, *155*, 95.

(25) Kua, J.; Goddard, W. A. *J. Am. Chem. Soc.* **1999**, *121*, 10928.

(26) Aricò, A. S.; Srinivasan, S.; Antonucci, V. *Fuel Cells* **2001**, *1*, 133.

(27) Koper, M. T. M. *Nanoscale* **2011**, *3*, 2054.

(28) Marković, N. M.; Ross, P. N., Jr *Surf. Sci. Rep.* **2002**, *45*, 117.

(29) Tian, N.; Zhou, Z.-Y.; Sun, S.-G. *J. Phys. Chem. C* **2008**, *112*, 19801.

(30) Climent, V.; Feliu, J. M. *J. Solid State Electrochem.* **2011**, *15*, 1297.

(31) Marković, N. M.; Schmidt, T. J.; Stamenković, V.; Ross, P. N. *Fuel Cells* **2001**, *1*, 105.

(32) Koper, M.; Wieckowski, A. *Fuel Cell Catalysis: A Surface Science Approach*; Wiley, 2009.

(33) Conway, B. E. *Prog. Surf. Sci.* **1995**, *49*, 331.

(34) Angerstein-Kozlowska, H.; Conway, B. E.; Sharp, W. B. A. *J. Electroanal. Chem. Interfacial Electrochem.* **1973**, *43*, 9.

(35) Woods, R. *J. Electroanal. Chem. Interfacial Electrochem.* **1974**, *49*, 217.

(36) Breiter, M. W. *Electrochim. Acta* **1962**, *8*, 925.

(37) Conway, B. E.; Angerstein-Kozlowska, H.; Sharp, W. B. A.; Criddle, E. E. *Anal. Chem.* **1973**, *45*, 1331.

(38) Clavilier, J.; Faure, R.; Guinet, G.; Durand, R. *J. Electroanal. Chem.* **1980**, *107*, 205.

(39) Clavilier, J.; Durand, R.; Guinet, G.; Faure, R. *J. Electroanal. Chem.* **1981**, *127*, 281.

(40) Clavilier, J. *J. Electroanal. Chem. Interfacial Electrochem.* **1979**, *107*, 211.

(41) Clavilier, J.; Faure, R.; Guinet, G.; Durand, R. *J. Electroanal. Chem. Interfacial Electrochem.* **1979**, *107*, 205.

(42) Trasatti, S.; Petrii, O. A. *J. Electroanal. Chem.* **1992**, *327*, 353.

(43) Agarwal, H. P.; Qureshi, S. *Electrochim. Acta* **1974**, *19*, 607.

(44) Angell, D. H.; Dickinson, T. *J. Electroanal. Chem. Interfacial Electrochem.* **1972**, *35*, 55.

(45) Anson, F. C. *Anal. Chem.* **1961**, *33*, 939.

(46) Weber, J.; Samec, Z.; Mareček, V. *J. Electroanal. Chem. Interfacial Electrochem.* **1978**, *89*, 271.

(47) *Trace-Anion Catalysis of Outer-Sphere Heterogeneous Charge-Transfer Reactions*; White, R.; Conway, B. E.; Vayenas, C. G.; Gamboa-Adelco, M., Eds.; Springer US, 2004; Vol. 37.

(48) Hung, N. G.; Nagy, Z. *J. Electrochem. Soc.* **1987**, *134*, 2215.

(49) Samec, Z. *J. Electrochem. Soc.* **1999**, *146*, 3349.

(50) Lu, Y.-C.; Gasteiger, H. A.; Shao-Horn, Y. *J. Am. Chem. Soc.* **2011**, *133*, 19048.

(51) Jeon, M. K.; Lee, C. H.; Park, G. I.; Kang, K. H. *J. Power Sources* **2012**, *216*, 400.

(52) Neyerlin, K. C.; Gu, W. B.; Jorne, J.; Gasteiger, H. A. *J. Electrochem. Soc.* **2006**, *153*, A1955.

(53) Watanabe, M.; Tryk, D. A.; Wakisaka, M.; Yano, H.; Uchida, H. *Electrochim. Acta* **2012**, *84*, 187.

(54) Stamenkovic, V. R.; Fowler, B.; Mun, B. S.; Wang, G.; Ross, P. N.; Lucas, C. A.; Marković, N. M. *Science* **2007**, *315*, 493.

(55) Nørskov, J. K.; Rossmeisl, J.; Logadottir, A.; Lindqvist, L.; Kitchin, J. R.; Bligaard, T.; Jónsson, H. *J. Phys. Chem. B* **2004**, *108*, 17886.

(56) Norskov, J. K.; Bligaard, T.; Rossmeisl, J.; Christensen, C. H. *Nat Chem* **2009**, *1*, 37.

(57) Yue, J.; Du, Z.; Shao, M. *J. Phys. Chem. Lett.* **2015**, 3346.

(58) Damjanovic, A.; Dey, A.; Bockris, J. M. *Electrochim. Acta* **1966**, *11*, 791.

(59) Damjanovic, A.; Genshaw, M.; Bockris, J. M. *J. Chem. Phys.* **1966**, *45*, 4057.

(60) Sepa, D.; Vojnovic, M.; Damjanovic, A. *Electrochim. Acta* **1980**, *25*, 1491.

(61) Sepa, D.; Vojnovic, M.; Vracar, L. M.; Damjanovic, A. *Electrochim. Acta* **1987**, *32*, 129.

(62) Anastasijević, N.; Vesović, V.; Adžić, R. *J. Electroanal. Chem. Interfacial Electrochem.* **1987**, *229*, 305.

(63) Anastasijević, N.; Vesović, V.; Adžić, R. *J. Electroanal. Chem. Interfacial Electrochem.* **1987**, *229*, 317.

(64) Wroblowa, H. S.; Yen Chi, P.; Razumney, G. *J. Electroanal. Chem.* **1976**, *69*, 195.

(65) Ross, P. N. *J. Electrochem. Soc.* **1979**, *126*, 78.

(66) Marković, N. M.; Adžić, R. R.; Cahan, B. D.; Yeager, E. B. *J. Electroanal. Chem.* **1994**, *377*, 249.

(67) Marković, N. M.; Gasteiger, H. A.; Ross, P. N. *J. Phys. Chem.* **1996**, *100*, 6715.

(68) Marković, N. M.; Gasteiger, H. A.; Ross, P. N. *J. Phys. Chem.* **1995**, *99*, 3411.

(69) Maciá, M. D.; Campiña, J. M.; Herrero, E.; Feliu, J. M. *J. Electroanal. Chem.* **2004**, *564*, 141.

(70) Kuzume, A.; Herrero, E.; Feliu, J. M. *J. Electroanal. Chem.* **2007**, *599*, 333.

(71) Bandarenka, A.; Hansen, H. A.; Rossmeisl, J.; Stephens, I. *Phys. Chem. Chem. Phys.* **2014**, 13625.

(72) El Kadiri, F.; Faure, R.; Durand, R. *J. Electroanal. Chem. Interfacial Electrochem.* **1991**, *301*, 177.

(73) Faguy, P. W.; Markovic, N.; Adzic, R. R.; Fierro, C. A.; Yeager, E. B. *J. Electroanal. Chem. Interfacial Electrochem.* **1990**, *289*, 245.

(74) Funtikov, A. M.; Stimming, U.; Vogel, R. *J. Electroanal. Chem.* **1997**, *428*, 147.

(75) Funtikov, A. M.; Linke, U.; Stimming, U.; Vogel, R. *Surf. Sci.* **1995**, *324*, L343.

(76) Faguy, P. W.; Markovic, N.; Ross, P. N. *J. Electrochem. Soc.* **1993**, *140*, 1638.

(77) Kohnke, H. In *Handbook of Fuel Cells*; John Wiley & Sons, Ltd: 2010.

(78) Serov, A.; Padilla, M.; Roy, A. J.; Atanassov, P.; Sakamoto, T.; Asazawa, K.; Tanaka, H. *Angew. Chem.* **2014**, *126*, 10504.

(79) Lan, R.; Irvine, J. T. S.; Tao, S. *Int. J. Hydrogen Energy* **2012**, *37*, 1482.

(80) Serov, A.; Kwak, C. *Appl. Catal., B* **2010**, *98*, 1.

(81) Yamada, K.; Asazawa, K.; Yasuda, K.; Ioroi, T.; Tanaka, H.; Miyazaki, Y.; Kobayashi, T. *J. Power Sources* **2003**, *115*, 236.

(82) Andries, V.; Couturier, D. *Mater. Perform.* **2000**, *39*, 58.

(83) Kean, T.; Miller, J. H.; Skellern, G. G.; Snodin, D. *Pharmeur. Sci. Notes* **2006**, *2006*, 23.

(84) Elder, D. P.; Snodin, D.; Teasdale, A. *J. Pharm. Biomed. Anal.* **2011**, *54*, 900.

(85) Channon, R. B.; Newland, J. C.; Bristow, A. W. T.; Ray, A. D.; Macpherson, J. V. *Electroanalysis* **2013**, *25*, 2613.

(86) Harrison, J. A.; Khan, Z. A. *J. Electroanal. Chem. Interfacial Electrochem.* **1970**, *28*, 131.

(87) Metters, J. P.; Tan, F.; Kadara, R. O.; Banks, C. E. *Anal. Methods* **2012**, *4*, 1272.

(88) Aldous, L.; Compton, R. G. *Phys. Chem. Chem. Phys.* **2011**, *13*, 5279.

(89) Bard, A. J. *Anal. Chem.* **1963**, *35*, 1602.

(90) Rosca, V.; Duca, M.; de Groot, M. T.; Koper, M. T. M. *Chem. Rev.* **2009**, *109*, 2209.

(91) García Azorero, M. D.; Marcos, M. L.; González Velasco, J. *Electrochim. Acta* **1994**, *39*, 1909.

(92) García, M. D.; Marcos, M. L.; Velasco, J. G. *Electroanalysis* **1996**, *8*, 267.

(93) Nishihara, C.; Raspini, I. A.; Kondoh, H.; Shindo, H.; Kaise, M.; Nozoye, H. *J. Electroanal. Chem.* **1992**, *338*, 299.

(94) Gómez, R.; Orts, J. M.; Rodes, A.; Feliu, J. M.; Aldaz, A. *J. Electroanal. Chem.* **1993**, *358*, 287.

(95) Álvarez-Ruiz, B.; Gómez, R.; Orts, J. M.; Feliu, J. M. *J. Electrochem. Soc.* **2002**, *149*, D35.

(96) Rosca, V.; Koper, M. T. M. *Electrochim. Acta* **2008**, *53*, 5199.

(97) Khaled, K. *Appl. Surf. Sci.* **2006**, *252*, 4120.

(98) Moussa, M.; Taha, F.; Gouda, M.; Singab, G. *Corros. Sci.* **1976**, *16*, 379.

(99) Cuy, E.; Bray, W. *J. Am. Chem. Soc.* **1924**, *46*, 1786.

(100) Gaunt, H.; Wetton, E. A. M. *J. Appl. Chem.* **1966**, *16*, 171.

(101) Ding, Y.; Wang, Y.; Zhang, L.; Zhang, H.; Li, C. M.; Lei, Y. *Nanoscale* **2011**, *3*, 1149.

(102) Azad, U. P.; Ganesan, V. *Electrochim. Acta* **2011**, *56*, 5766.

(103) Sultana, W.; Ghosh, S.; Eraiah, B. *Electroanalysis* **2012**, *24*, 1869.

(104) Bard, A. J.; Fan, F. R. F.; Kwak, J.; Lev, O. *Anal. Chem.* **1989**, *61*, 132.

(105) Kwak, J.; Bard, A. J. *Anal. Chem.* **1989**, *61*, 1794.

(106) Bard, A. J.; Mirkin, M. V. *Scanning electrochemical microscopy*; CRC Press, 2012.

(107) Fernández, J. L.; Bard, A. J. *Anal. Chem.* **2003**, *75*, 2967.

(108) Fernández, J. L.; Raghuveer, V.; Manthiram, A.; Bard, A. J. *J. Am. Chem. Soc.* **2005**, *127*, 13100.

(109) Fernández, J. L.; Walsh, D. A.; Bard, A. J. *J. Am. Chem. Soc.* **2005**, *127*, 357.

(110) Fernández, J. L.; White, J. M.; Sun, Y.; Tang, W.; Henkelman, G.; Bard, A. J. *Langmuir* **2006**, *22*, 10426.

(111) Zhang, F.; Roznyatovskiy, V.; Fan, F.-R. F.; Lynch, V.; Sessler, J. L.; Bard, A. J. *J. Phys. Chem. C* **2011**, *115*, 2592.

(112) Wain, A. J. *Electrochem. Commun.* **2014**, *46*, 9.

(113) Jambunathan, K.; Shah, B. C.; Hudson, J. L.; Hillier, A. C. *J. Electroanal. Chem.* **2001**, *500*, 279.

(114) Zhou, J.; Zu, Y.; Bard, A. J. *J. Electroanal. Chem.* **2000**, *491*, 22.

(115) Jayaraman, S.; Hillier, A. C. *J. Phys. Chem. B* **2003**, *107*, 5221.

(116) Black, M.; Cooper, J.; McGinn, P. *Meas. Sci. Technol.* **2005**, *16*, 174.

(117) Lu, G.; Cooper, J. S.; McGinn, P. J. *J. Power Sources* **2006**, *161*, 106.

(118) Liu, B.; Bard, A. J. *J. Phys. Chem. B* **2002**, *106*, 12801.

(119) Sanchez-Sanchez, C. M.; Solla-Gullon, J.; Vidal-Iglesias, F. J.; Aldaz, A.; Montiel, V.; Herrero, E. *J. Am. Chem. Soc.* **2010**, *132*, 5622.

(120) Sanchez-Sanchez, C. M.; Bard, A. J. *Anal. Chem.* **2009**, *81*, 8094.

(121) Sanchez-Sanchez, C. M.; Rodiriguez-Lopez, J.; Bard, A. J. *Anal. Chem.* **2008**, *80*, 3254.

(122) Lai, S.; Macpherson, J. V.; Unwin, P. R. *MRS bulletin* **2012**, *37*, 668.

(123) Bandarenka, A. S.; Ventosa, E.; Maljusch, A.; Masa, J.; Schuhmann, W. *Analyst* **2014**, *139*, 1274.

(124) Bertoncello, P. *Energy Environ. Sci.* **2010**, *3*, 1620.

(125) Schäfer, D.; Mardare, C.; Savan, A.; Sanchez, M. D.; Mei, B.; Xia, W.; Muhler, M.; Ludwig, A.; Schuhmann, W. *Anal. Chem.* **2011**, *83*, 1916.

(126) Maljusch, A.; Nagaiah, T. C.; Schwamborn, S.; Bron, M.; Schuhmann, W. *Anal. Chem.* **2010**, *82*, 1890.

(127) Eckhard, K.; Chen, X.; Turcu, F.; Schuhmann, W. *Phys. Chem. Chem. Phys.* **2006**, *8*, 5359.

(128) Wain, A. J. *Electrochim. Acta* **2013**, *92*, 383.

(129) Böhni, H.; Suter, T.; Schreyer, A. *Electrochim. Acta* **1995**, *40*, 1361.

(130) Suter, T.; Bohni, H. *Electrochim. Acta* **1997**, *42*, 3275.

(131) Lohrengel, M. M. *Electrochim. Acta* **1997**, *42*, 3265.

(132) Lohrengel, M. M.; Rosenkranz, C.; Klüppel, I.; Moehring, A.; Bettermann, H.; Bossche, B. V. d.; Deconinck, J. *Electrochim. Acta* **2004**, *49*, 2863.

(133) Klemm, S. O.; Pust, S. E.; Hassel, A. W.; Hupkes, J.; Mayrhofer, K. J. J. *J. Solid State Electrochem.* **2012**, *16*, 283.

(134) Klemm, S. O.; Schauer, J. C.; Schuhmacher, B.; Hassel, A. W. *Electrochim. Acta* **2011**, *56*, 9627.

(135) Klemm, S. O.; Schauer, J.-C.; Schuhmacher, B.; Hassel, A. W. *Electrochim. Acta* **2011**, *56*, 4315.

(136) Schreiber, A.; Schultze, J. W.; Lohrengel, M. M.; Kármán, F.; Kálmán, E. *Electrochim. Acta* **2006**, *51*, 2625.

(137) Schultze, J. W.; Pilaski, M.; Lohrengel, M. M.; Konig, U. *Faraday Discuss.* **2002**, *121*, 211.

(138) Klemm, S. O.; Topalov, A. A.; Laska, C. A.; Mayrhofer, K. J. J. *Electrochem. Commun.* **2011**, *13*, 1533.

(139) Topalov, A. A.; Katsounaros, I.; Auinger, M.; Cherevko, S.; Meier, J. C.; Klemm, S. O.; Mayrhofer, K. J. J. *Angew. Chem. Int. Ed.* **2012**, *51*, 12613.

(140) Williams, C. G.; Edwards, M. A.; Colley, A. L.; Macpherson, J. V.; Unwin, P. R. *Anal. Chem.* **2009**, *81*, 2486.

(141) Dudin, P. V.; Unwin, P. R.; Macpherson, J. V. *J. Phys. Chem. C* **2010**, *114*, 13241.

(142) Miller, T. S.; Sansuk, S.; E, S. P.; Lai, S. C. S.; Macpherson, J. V.; Unwin, P. R. *Catal. Today* **2015**, *244*, 136.

(143) Ebejer, N.; Schnippering, M.; Colburn, A. W.; Edwards, M. A.; Unwin, P. R. *Anal. Chem.* **2010**, *82*, 9141.

(144) Güell, A. G.; Ebejer, N.; Snowden, M. E.; McKelvey, K.; Macpherson, J. V.; Unwin, P. R. *Proc. Natl. Acad. Sci. U. S. A.* **2012**, *109*, 11487.

(145) Ebejer, N.; Güell, A. G.; Lai, S. C. S.; McKelvey, K.; Snowden, M. E.; Unwin, P. R. *Annu. Rev. Anal. Chem.* **2013**, *6*, 329.

(146) Patten, H. V.; Meadows, K. E.; Hutton, L. A.; Iacobini, J. G.; Battistel, D.; McKelvey, K.; Colburn, A. W.; Newton, M. E.; Macpherson, J. V.; Unwin, P. R. *Angew. Chem. Int. Ed.* **2012**, *51*, 7002.

(147) Lai, S. C. S.; Patel, A. N.; McKelvey, K.; Unwin, P. R. *Angew. Chem. Int. Ed.* **2012**, *51*, 5405.

(148) Kleijn, S. E. F.; Lai, S. C. S.; Miller, T. S.; Yanson, A. I.; Koper, M. T. M.; Unwin, P. R. *J. Am. Chem. Soc.* **2012**, *134*, 18558.

(149) Lai, S. C. S.; Dudin, P. V.; Macpherson, J. V.; Unwin, P. R. *J. Am. Chem. Soc.* **2011**, *133*, 10744.

(150) Arvia, A. J.; Salvarezza, R. C.; Triaca, W. E. *J. New Mat.Electrochem. Syst.* **2004**, *7*, 133.

(151) Crooks, R. M.; Zhao, M.; Sun, L.; Chechik, V.; Yeung, L. K. *Acc. Chem. Res.* **2001**, *34*, 181.

(152) Gasteiger, H. A.; Kocha, S. S.; Sompalli, B.; Wagner, F. T. *Appl. Catal., B* **2005**, *56*, 9.

(153) Haruta, M. *Chem. Red.* **2003**, *3*, 75.

(154) Sun, C. Q.; Tay, B. K.; Zeng, X. T.; Li, S.; Chen, T. P.; Zhou, J.; Bai, H. L.; Jiang, E. Y. *J. Phys.: Condens. Matter* **2002**, *14*, 7781.

(155) Sambur, J. B.; Chen, P. *Annu. Rev. Phys. Chem.* **2014**, *65*, 395.

(156) Xiao, X.; Bard, A. J. *J. Am. Chem. Soc.* **2007**, *129*, 9610.

(157) Wakerley, D.; Guell, A. G.; Hutton, L. A.; Miller, T. S.; Bard, A. J.; Macpherson, J. V. *Chem. Commun.* **2013**, *49*, 5657.

(158) Dasari, R.; Robinson, D. A.; Stevenson, K. J. *J. Am. Chem. Soc.* **2013**, *135*, 570.

(159) Dasari, R.; Tai, K.; Robinson, D. A.; Stevenson, K. J. *ACS Nano* **2014**, *8*, 4539.

(160) Dasari, R.; Walther, B.; Robinson, D. A.; Stevenson, K. J. *Langmuir* **2013**, *29*, 15100.

(161) Kwon, S. J.; Fan, F.-R. F.; Bard, A. J. *J. Am. Chem. Soc.* **2010**, *132*, 13165.

(162) Bard, A. J.; Zhou, H.; Kwon, S. J. *Isr. J. Chem.* **2010**, *50*, 267.

(163) Cheng, W.; Compton, R. G. *TrAC, Trends Anal. Chem.* **2014**, *58*, 79.

(164) Kleijn, S. E. F.; Lai, S. C. S.; Koper, M. T. M.; Unwin, P. R. *Angew. Chem. Int. Ed.* **2014**, *53*, 3558.

(165) Porter, M. D.; Bright, T. B.; Allara, D. L.; Chidsey, C. E. D. *J. Am. Chem. Soc.* **1987**, *109*, 3559.

(166) Bain, C. D.; Evall, J.; Whitesides, G. M. *J. Am. Chem. Soc.* **1989**, *111*, 7155.

(167) Love, J. C.; Estroff, L. A.; Kriebel, J. K.; Nuzzo, R. G.; Whitesides, G. M. *Chem. Rev.* **2005**, *105*, 1103.

(168) Ulman, A. *Chem. Rev.* **1996**, *96*, 1533.

(169) Poirier, G. E.; Pylant, E. D. *Science* **1996**, *272*, 1145.

(170) Vericat, C.; Vela, M.; Salvarezza, R. *Phys. Chem. Chem. Phys.* **2005**, *7*, 3258.

(171) Chidsey, C. E. D.; Liu, G. Y.; Rowntree, P.; Scoles, G. *J. Chem. Phys.* **1989**, *91*, 4421.

(172) Dubois, L. H.; Zegarski, B. R.; Nuzzo, R. G. *J. Chem. Phys.* **1993**, *98*, 678.

(173) Schreiber, F. *Prog. Surf. Sci.* **2000**, *65*, 151.

(174) Schwartz, D. K. *Annu. Rev. Phys. Chem.* **2001**, *52*, 107.

(175) Chidsey, C. E. D. *Science* **1991**, *251*, 919.

(176) Adams, D. M.; Brus, L.; Chidsey, C. E. D.; Creager, S.; Creutz, C.; Kagan, C. R.; Kamat, P. V.; Lieberman, M.; Lindsay, S.; Marcus, R. A.; Metzger, R. M.; Michel-Beyerle, M. E.; Miller, J. R.; Newton, M. D.; Rolison, D. R.; Sankey, O.; Schanze, K. S.; Yardley, J.; Zhu, X. *J. Phys. Chem. B* **2003**, *107*, 6668.

(177) Finklea, H. O. *Electroanal. Chem.* **1996**, *19*, 109.

(178) Hsu, C.-P. *J. Electroanal. Chem.* **1997**, *438*, 27.

(179) Chidsey, C. E. D.; Bertozzi, C. R.; Putvinski, T. M.; Mujsce, A. M. *J. Am. Chem. Soc.* **1990**, *112*, 4301.

(180) Tran, E.; Rampi, M. A.; Whitesides, G. M. *Angew. Chem. Int. Ed.* **2004**, *43*, 3835.

(181) Finklea, H. O.; Hanshew, D. D. *J. Am. Chem. Soc.* **1992**, *114*, 3173.

(182) Bradbury, C. R.; Zhao, J.; Fermín, D. J. *J. Phys. Chem. C* **2008**, *112*, 10153.

(183) Hongthani, W.; Patil, A. J.; Mann, S.; Fermin, D. J. *ChemPhysChem* **2012**, *13*, 2956.

(184) Kissling, G. P.; Miles, D. O.; Fermín, D. J. *Phys. Chem. Chem. Phys.* **2011**, *13*, 21175.

(185) Zhao, J.; Bradbury, C. R.; Fermín, D. J. *J. Phys. Chem. C* **2008**, *112*, 6832.

(186) Zhao, J.; Wasem, M.; Bradbury, C. R.; Fermín, D. J. *J. Phys. Chem. C* **2008**, *112*, 7284.

(187) Barfidokht, A.; Ciampi, S.; Luais, E.; Darwish, N.; Gooding, J. J. *Anal. Chem.* **2013**, *85*, 1073.

(188) Chou, A.; Eggers, P. K.; Paddon-Row, M. N.; Gooding, J. J. *J. Phys. Chem. C* **2009**, *113*, 3203.

(189) Dyne, J.; Lin, Y.-S.; Lai, L. M. H.; Ginges, J. Z.; Luais, E.; Peterson, J. R.; Goon, I. Y.; Amal, R.; Gooding, J. J. *ChemPhysChem* **2010**, *11*, 2807.

(190) Gooding, J. J.; Alam, M. T.; Barfidokht, A.; Carter, L. *J. Braz. Chem. Soc.* **2014**, *25*, 418.

(191) Liu, G.; Luais, E.; Gooding, J. J. *Langmuir* **2011**, *27*, 4176.

(192) Shein, J. B.; Lai, L. M. H.; Eggers, P. K.; Paddon-Row, M. N.; Gooding, J. J. *Langmuir* **2009**, *25*, 11121.

(193) Grabar, K. C.; Allison, K. J.; Baker, B. E.; Bright, R. M.; Brown, K. R.; Freeman, R. G.; Fox, A. P.; Keating, C. D.; Musick, M. D.; Natan, M. J. *Langmuir* **1996**, *12*, 2353.

(194) Bradbury, C. R.; Kuster, L.; Fermin, D. J. *J. Electroanal. Chem.* **2010**, *646*, 114.

(195) Dyne, J.; Lin, Y.-S.; Lai, L. M. H.; Ginges, J. Z.; Luais, E.; Peterson, J. R.; Goon, I. Y.; Amal, R.; Gooding, J. J. *ChemPhysChem* **2010**, *11*, 2807.

(196) Chazalviel, J.-N.; Allongue, P. *J. Am. Chem. Soc.* **2010**, *133*, 762.

(197) Barfidokht, A.; Ciampi, S.; Luais, E.; Darwish, N.; Gooding, J. J. *Anal. Chem.* **2012**, *85*, 1073.

(198) Hill, C. M.; Kim, J.; Bard, A. J. *J. Am. Chem. Soc.* **2015**.

(199) Eaton, P.; West, P. *Atomic force microscopy*; Oxford University. Press, 2010.

(200) Butt, H.-J.; Cappella, B.; Kappl, M. *Surf. Sci. Rep.* **2005**, *59*, 1.

(201) Binnig, G.; Quate, C. F.; Gerber, C. *Phys. Rev. Lett.* **1986**, *56*, 930.

(202) Noy, A.; Vezenov, D. V.; Lieber, C. M. *Annu. Rev. Mater. Sci.* **1997**, *27*, 381.

(203) Okabe, Y.; Akiba, U.; Fujihira, M. *Appl. Surf. Sci.* **2000**, *157*, 398.

(204) Ducker, W. A.; Senden, T. J.; Pashley, R. M. *Langmuir* **1992**, *8*, 1831.

(205) Vezenov, D. V.; Noy, A.; Rozsnyai, L. F.; Lieber, C. M. *J. Am. Chem. Soc.* **1997**, *119*, 2006.

(206) Hu, K.; Bard, A. J. *Langmuir* **1997**, *13*, 5114.

Chapter Two

Experimental

This chapter details the chemicals and materials, the sample preparation procedures and the instrumentation used throughout the work described in this thesis.

Chapter 2

2.1 Materials and Chemicals

Table 2-1 Materials and Chemicals used in this thesis

Materials / Chemicals	Details & Supplier
Materials	------
Borosilicate theta capillaries	TG 150-10, Harvard Part No. 30-0114
Chromium coated tungsten bar	99.9 %, Good fellow Cambridge Ltd.
Gold wire for thermal evaporation	99.995 %, MaTecK
Oxidised silicon wafer, SiO_2	n-type, single side polished, 300 nm thermal oxide layer, IDB Technologies Ltd.
Palladium wire, Pd	> 99.95 %, 0.25 mm thickness, MaTeck
Platinum foil, Pt	> 99.95 %, 0.0125 mm thickness, Advent Research Materials
Platinum wire, Pt	0.5 mm diameter, > 99.95 %, MaTeck
Sharp Nitride Lever probes for AFM force measurement	SNL-10, Bruker
Silver wire, Ag	99.9 %, 0.25 mm diameter, MaTecK
Chemicals	------
(Trimethylammonio)methyl ferrocene ($FcTMA^+$) Iodide	> 99 %, Strem Chemicals, Inc.
11-mercapto-1-undecanol, $HS(CH_2)_{11}OH$	97 %, Sigma-Aldrich
11-mercaptoundecanoic acid, $HS(CH_2)_{10}COOH$	95 %, Sigma-Aldrich
1-Dodecanethiol, $CH_3(CH_2)_{11}SH$	≥ 98 %, Sigma-Aldrich
alumina polishing suspension	0.05 μm, Buehler
Au nanoparticles stock solution	10 nm diameter stabilized suspension in citrate buffer, concentration, concentration, 10 nM, Sigma-Aldrich

Dichlorodimethylsilane, $Si(CH_3)_2Cl_2$	> 99 %, Sigma-Aldrich
Hydrazine monohydrate, $N_2H_4 \cdot H_2O$	64 % solution in water, 100 %, Acros Organics
Hydrogen peroxide, H_2O_2 (for piranha cleaning)	30 wt %, A.C.S. Reagent, Sigma-Aldrich
Iron(II) perchlorate hydrate, $Fe(ClO_4)_2 \cdot xH_2O$	98 %, Sigma-Aldrich
Iron(II) sulfate heptahydrate, $FeSO_4 \cdot 7H_2O$	≥ 99.0 %, Sigma-Aldrich
Perchloric acid, $HClO_4$, (for electrolyte solutions)	70 % solution in water, Acros Organics
Potassium chloride, KCl	Reagent Plus, 99 %, Sigma-Aldrich
Potassium ferrocyanide trihydrate, $K_4Fe(CN)_6 \cdot 3H_2O$	Reagent Plus, ≥ 98.5 %, Sigma-Aldrich
Sodium citrate, $Na_3C_6H_5O_7 \cdot 2H_2O$	Sigma-Aldrich
Sulfuric acid, H_2SO_4, (for electrolyte solutions)	99.999 %, Sigma-Aldrich
Sulfuric acid, H_2SO_4, (for piranha cleaning)	Analytical Reagent, > 95 %, Sigma-Aldrich
Solvents	------
ethanol	AnalaR NORMAPUR, VWR
isopropanol	Analytical Reagent, Fisher

2.2 Platinum (Pt) electrode preparation

The work described in this thesis employed three main types of Pt electrodes, namely Pt ultramicroelectrodes (UMEs), macroscopic Pt wire electrodes and Pt foil electrodes. Prior to electrochemical measurements, these electrodes were prepared with different procedures to ensure clean and reproducible surfaces.

2.2.1 Macro-Pt wire and Pt UME preparation

Macro-Pt wires, used either as working electrodes or counter electrodes, were prepared freshly before experiments. Prior to use, a piece of Pt wire was rinsed with copious amount of water, dried under nitrogen flow, and flame-annealed in natural gas flame.[1-3] Immediately after annealing, while the wire was still glowing hot, it was cooled down by immersion in a vial containing 20 mL ultra-pure water before transferring to an electrochemical cell.

The UMEs used in this thesis are Pt discs of 25 μm in diameter. These electrodes were prepared by sealing Pt micro-wires into glass, followed by extensive polishing on a 0.1 μm diamond-lapping disc (PSA, Buehler) until a flat surface was obtained.[4] Before use, the Pt UMEs were cleaned by further mechanical polishing, initially using a alumina suspension followed by polishing on a clean polishing pad without alumina, and rinsed thoroughly with ultra-pure water before use.

2.2.2 Pt foil preparation

Pt foil electrodes were prepared as shown in Figure 2.1. Commercially obtained Pt foils were cut into small pieces as needed, typically *ca.* 0.5 cm × 0.5 cm.

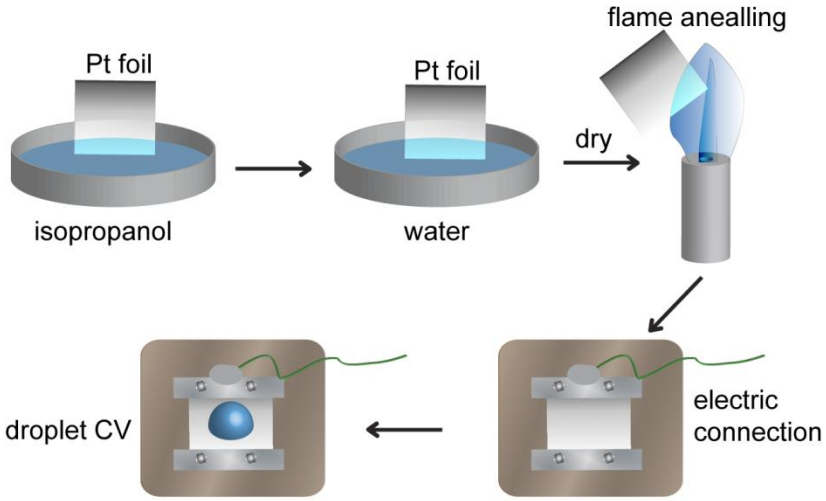

Figure 2.1 Schematic illustration of the preparation of a polycrystalline Pt foil electrode.

First, the freshly cut Pt foils were soaked in isopropanol solution to dissolve organic impurities. Then, they were rinsed with high purity water and dried under a nitrogen flow. Afterwards, they were flame annealed followed by immediate cooling in water. After drying, the sample was mounted on a sample holder. Finally, immediately before performing the electrochemical measurement of interest, repeated cyclic voltammetry (CV) cycling was performed using a droplet cell setup until a stable CV with clear hydrogen underpotential deposition (H_{upd}) features is achieved.

2.3 Reference electrode preparation

2.3.1 Palladium-hydrogen (Pd-H_2) reference electrode

The Pd-H_2 electrode is a widely used reference electrode in electrochemistry study. This reference electrode utilises the intrinsic property of bulk palladium to absorb molecular hydrogen into the atomic lattice. When employed as a reference

electrode, the palladium wire releases the absorb hydrogen to provide a hydrogen containing solution locally. The reference reaction is as follows:

$$2H^+ + 2e^- \rightleftarrows H_2 \qquad (2\text{-}1)$$

The potential of a Pd-H_2 electrode is given by the Nernst equation:

$$E = E^0 + \frac{RT}{F} \ln \frac{a_{H^+}}{(P_{H_2})^{1/2}} \qquad (2\text{-}2)$$

where E^0 is the standard potential, α_{H^+} is the activity of H^+ ions in solution and P_{H_2} is the partial pressure of molecular hydrogen. The Pd-H_2 electrode gives a steady potential of 50 mV (E^0 = + 50 mV) with respect to a reversible hydrogen electrode (RHE) in the same solution.[5] This potential corresponds to the steady state potential normally attributed to the α-β phase transition of palladium-hydrogen alloys.[5] The Pd-H_2 is a pH dependent reference electrode and is sufficiently stable for a few hours in acidic and neutral solutions.

The Pd-H_2 reference electrodes in this thesis were prepared using chronoamperometry in a two-electrode setup in which a Pd wire was used as a working electrode and a Pt wire was used as a reference and counter electrode. The electrolyte solution was H_2SO_4 or $HClO_4$, same as the electrolyte used for later experiments. By applying a potential bias between the two electrodes, normally -3.0 V, the hydrogen evolution reaction (HER) is driven on the Pd surface. The bias was held until a stable current was attained and the palladium wire was fully covered by bubbles, indicating saturated H_2 absorption in the top few atomic layers. After preparation, these Pd-H_2 reference electrodes were kept in the corresponding

experimental electrolyte solution. All the Pd-H_2 electrodes were prepared freshly on the day of experiments.

2.3.2 Silver/silver chloride (Ag/AgCl) reference electrode

Another widely used reference electrode in electrochemical measurements is the silver/silver chloride (Ag/AgCl) electrode, based on the following reaction. The standard potential is 0.230 V vs standard hydrogen electrode (SHE).

$$AgCl + e^- \leftrightarrow Ag + Cl^- \quad (2\text{-}3)$$

The potential of electrode depends on the activity of chloride ions (α_{Cl^-}) in the solution in which it is immersed, as governed by the Nernst equation:

$$E_{Ag/AgCl} = E^0 - \frac{RT}{F} \ln a_{Cl^-} \quad (2\text{-}4)$$

Home-made Ag/AgCl electrodes were used for the work in the thesis. These electrodes were fabricated by immersing a silver wire into a solution containing saturated KCl solution and oxidising the silver wires for a few minutes until a dull greyish-white layer can be observed on the surface of the silver wire. Similar to the Pd-H_2 electrodes, all Ag/AgCl wires were prepared freshly on the day of experiment.

2.4 Electrochemical techniques

2.4.1 Cyclic voltammetry (CV)

Cyclic voltammetry (CV) is a potentiodynamic electrochemical measurement technique. In CV measurements, the potential of a working electrode is varied

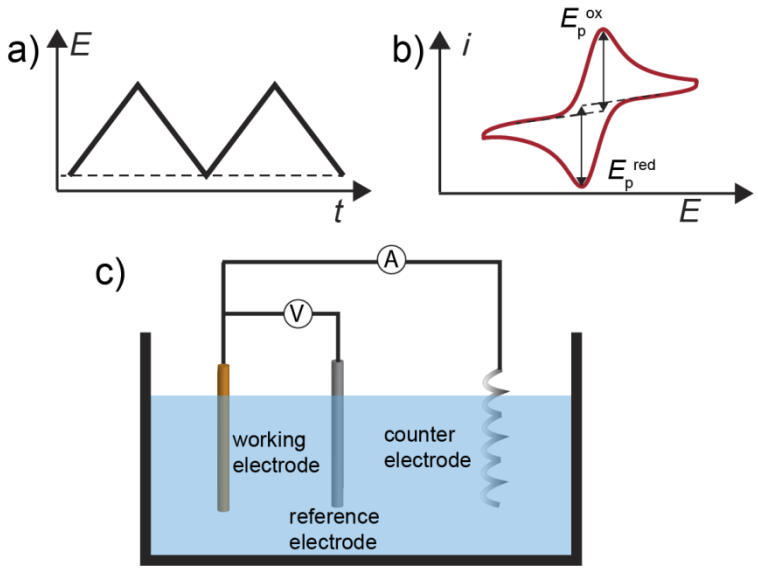

Figure 2.2 a) Potential waveform employed in cyclic voltammetry; **b)** A resulting CV for a reversible electron transfer reaction. **c)** Schematic diagram of a three-electrode setup.

linearly with time at a certain scan speed (V s^{-1}) between two limiting potentials. At the same time, the current flowing through the working electrode is measured and plotted as a function of the applied potential, resulting in current versus potential profiles. A schematic figure of the potential and current profile for a CV is shown in Figure 2.2. For macroscopic electrode (electrode area at the order of mm^2 or bigger), the current passing through a working electrode may be large. If this large current passes through the reference electrode, it can lead to a non-negligible potential drop at the solution/electrode interface or a composition change in the reference electrode, resulting in a non-stable reference potential. To avoid this, typically CVs were carried out in a three-electrode set-up for macro-scale electrochemical measurements, in which the potential is applied between a working electrode and a reference electrode, but current is measured between a working electrode and a counter electrode, as shown in Figure 2.2c.

Figure 2.2b shows a typical CV of an electrochemically reversible redox system. The separation of the two peak potentials, ΔE_p, can be used to determine the electrochemical reversibility of a redox couple,

$$\Delta E_p = E_{p,\,ox} - E_{p,\,red} \tag{2-5}$$

For a fully reversible one-electron reaction at room temperature, ΔE_p is 59 mV.

In this thesis, unless specified, most of the macroscopic CV measurements were performed in three-electrode setups, containing a working electrode, a reference electrode and a counter electrode. All the measurements were performed at room temperature using a computer controlled potentiostat (CH instrument). For experiments under deaerated conditions, the electrolyte solution was flushed with N_2 before and during the measurements.

2.4.2 Chronoamperometry

Whereas cyclic voltammetry is a potentiodynamic measurement, chronoamperometry is a potentiostatic technique. Different from cyclic voltammetry, in chronoamperometry, the potential of a working electrode is not swept but stepped from a starting potential to a potential of interest, as shown in Figure 2.3. Then the

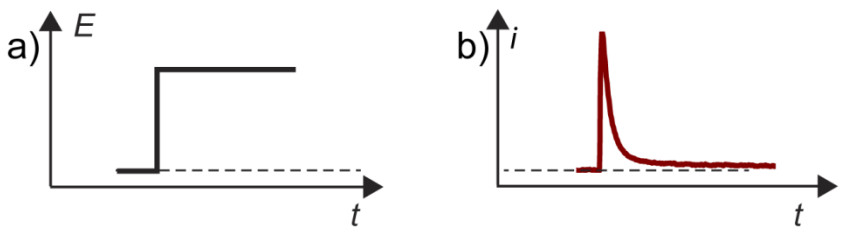

Figure 2.3 Diagrams of **a)** a potential waveform and **b)** a typical current-time response during a chronoamperometric experiment.

potential is held for a pre-determined period of time and the current occurring at the electrode over that time is recorded, results in a current versus time profile. In this thesis, chronoamperometry is mainly used in Chapter 6.

2.5 Non-electrochemical microscopic characterization techniques

2.5.1 Scanning electron microscopy (SEM)

Scanning electron microscopy (SEM) uses a focused electron beam to scan over the surface. The electron beam interacts with surface atoms of a substrate and secondary or backscattered electrons can be generated. By analysing these signals, one can obtain a lot information about the sample, including sample morphology (texture), chemical composition, and crystallographic orientations. In this thesis, SEM is mainly used to characterize polycrystalline platinum foils. All SEM images

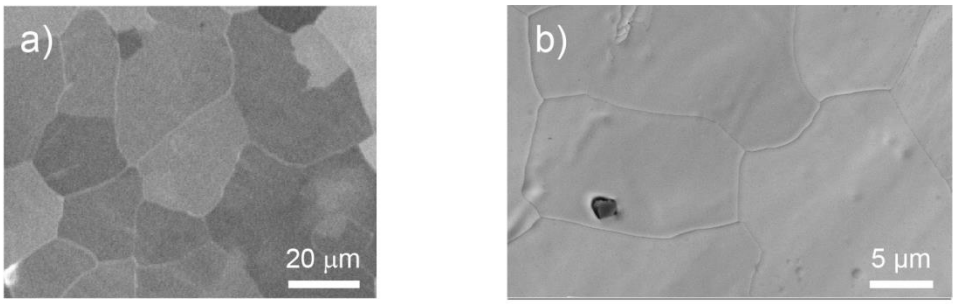

Figure 2.4 a) A SEM image of a Pt polycrystalline foil containing grains of different size and shape. **b)** A higher magnification SEM image showing a few grains and the boundaries between them.

were recorded on a Zeiss SUPRA 55 variable-pressure field emission-SEM. Figure 2.4 gives two typical SEM images of a piece of polycrystalline Pt foil. Both figures show that polycrystalline Pt surfaces are heterogeneous, containing grains of irregular shape and size.

2.5.2 Focused ion beam (FIB)

Focused ion beam (FIB) operates in a similar way with SEM, but instead of using a focused electron beam, it uses a finely focused beam of ions. In FIB, a gallium (Ga^+) primary ion beam hits a substrate and scans across the substrate surface, signals from the sputtered ions or secondary electrons are collected and form images. At a high beam current, FIB can be used to remove a certain amount of material, allowing precisely milling of the substrate with nanometre resolution. FIB was used in Chapter 5 to mark areas of interesting on Pt foils. All the FIB experiments were performed by using a JIB-4500 MultiBeam SEM-FIB system, using a 30 kV ion column with a Ga^+ ion source.

2.5.3 Electron backscatter diffraction (EBSD)

Electron backscatter diffraction (EBSD) is a SEM-based diffraction technique which provides information on the microstructure of materials, such as the crystallographic orientation of a grain, grain size, and grain boundary characteristics.[6,7] A simplified schematic of an EBSD setup is shown in Figure 2.5. The main part of an EBSD contains the hardware of a SEM, a phosphor screen and a sensitive charge-coupled device (CCD) camera. In EBSD, an electron beam strikes

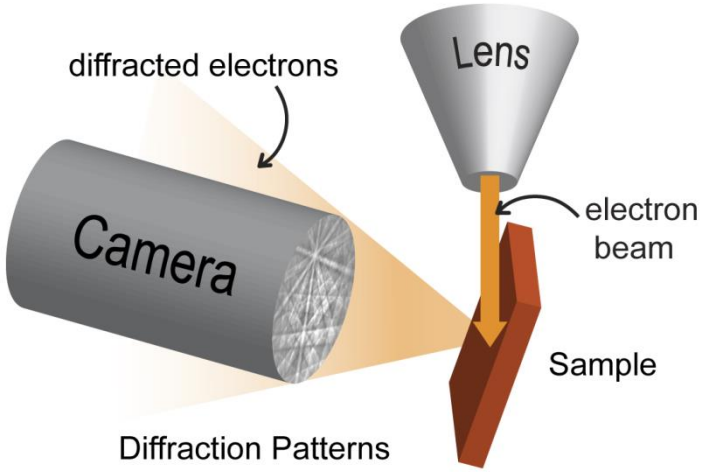

Figure 2.5 The experimental setup for an EBSD. The sample was mounted on a 70° pre-tilted sample holder.

on the surface of a highly tilted crystalline sample with a typical penetration depth of ~ 20 nm. Some of the electrons enter the sample and some backscatter. The backscattered electrons are diffracted due to the atomic lattice of the material. The periodicity of this atomic lattice leads to constructive and destructive interference, giving rise to diffraction patterns. These patterns consist of well-defined Kikuchi lines and can be visualized on a fluorescent phosphor screen, where it is captured by a CCD camera for viewing. The scanned area can be varied from several millimetres to tens of nanometres, with a resolution down to 20 nm for well-polished samples.

Data analysis of EBSD is often carried out by orientation imaging microscopy (OIM) software, which compares the Kikuchi patterns with a pre-defined library of patterns. The inverse pole figure is often used in data analysis to show the orientation information. Compared to other structure characterization techniques, EBSD is a fast and reliable way of obtaining the crystalline structure and orientation of a solid crystalline material.

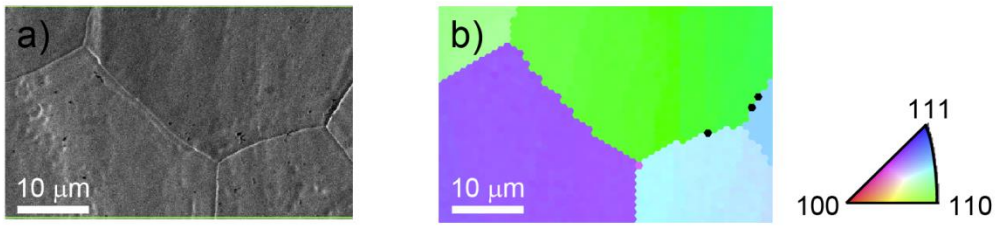

Figure 2.6 a) SEM image and the corresponding EBSD image **b)** of a scanned area on a polycrystalline Pt foil. The triangle colour coded map illustrates the structure of each grain. A few black dots can be seen in the EBSD image, at which the orientation could not be indexed correctly. This indicates that surface cleanliness is vital for crystal structure detection in EBSD.

In this thesis, all EBSD images of polycrystalline platinum foils were recorded on a Zeiss SUPRA 55 variable-pressure field emission SEM at 20 kV on a 70 ° tilted sample holder equipped with an EDAX TSL EBSD system. A typical SEM image and the corresponding EBSD image of a scanned area on a Pt foil are shown in Figure 2.6. The orientation of a specific grain can be identified from a colour coded triangle map, which is a RGB based colour scheme having three corners with full red, green and blue which represent the three basal planes. High-index planes are coloured in a mixture of the above three basal colours. Depending on the size of scanned areas, the resolution of EBSD images in this thesis varies from 1.0 to 3.0 µm.

2.5.4 Transmission electron microscopy (TEM)

Transmission electron microscopy (TEM) images of gold nanoparticles (Au NP) in Chapter 6 were taken using a Jeol 2000FX TEM with 200 kV accelerating voltage. The sample was prepared by depositing Au NPs on a carbon film coated

TEM grids (Agar Scientific). Images were captured using a Gatan ORIUS 11 megapixel digital camera.

2.5.5 Atomic force microscopy (AFM)

The surface roughness of the Pt foil was studied by an AFM. Images were obtained in tapping mode on a Veeco Enviroscope AFM with a Nanoscope IV controller. Images were acquired using standard silicon tapping mode tips (RFESP type, Bruker Probes). Typical AFM images of platinum foils are shown in Chapter 3.

2.6 Scanning electrochemical cell microscopy (SECCM)

SECCM is an electrochemical scanning probe technique developed by the Warwick Electrochemistry and Interfaces Group,[8-13] and is the key electrochemical technique employed in this thesis. The working principles and hardware setup of this technique has been described briefly in Chapter 1 and in detail in literatures. In this part, the details of SECCM pipettes (probes) fabrication, instrumentation setup and the scanning modes employed in this thesis for electrochemical imaging will be discussed.

2.6.1 Pipette fabrication and meniscus size measurement

SECCM double barrel pipettes were pulled from borosilicate theta capillaries using a Sutter P-2000 laser puller (Sutter Instruments, USA). This laser puller contains a sample holder, where a glass capillary (borosilicate or quartz) can be

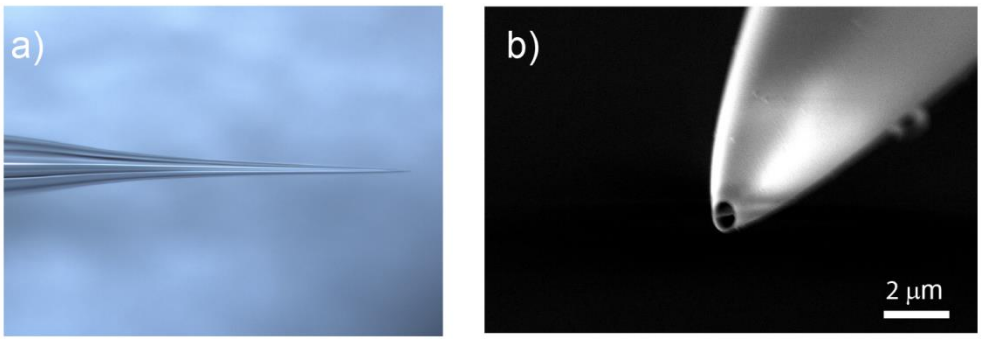

Figure 2.7 a) An optical microscope and **b)** a SEM image of a typical double barrel pipette used in the SECCM experiments described in this thesis.

placed and fixed in a place. A CO_2 laser provides a local heat source to melt the glass. With the heat turned on, a weak pull was applied first to draw out the capillary. Then, a mechanical hard pull was activated (immediately or after a delayed time) to pull the capillary to a pair of pipettes. Pipettes of different sizes and geometries can be obtained easily by adjusting the pulling parameters, such as the heating power, the pull strength and delay time. Each pulled capillary yielded a pair of two near-identical pipettes. This allows using one for electrochemical measurements, while the other half of the pair remained pristine for determining the precise geometry of the pipette.

All SECCM experiments in this thesis were performed with aqueous solutions. To ensure that the electrolyte meniscus was contained at the end of the pipette and remained stable during a SECCM measurement, it was necessary to render the outer walls of the pipette hydrophobic. This was done by using a silanization procedure. In this procedure, the pipettes were immersed in dichlorodimethylsilane ($Si(CH_3)_2Cl_2$) while argon gas was flowed through it, such that small bubbles could be observed by eye. For a pipette with a total diameter of

approximately 1 μm, the pressure was held at ~ 4 bar for one minute, followed by drying in air for another two minutes, while maintaining the argon flow.

The size of pipette opening in this thesis was in the range of 1 to 3 μm diameter. The geometry and size of these pipettes were measured using optical microscopy and SEM. A typical pipette employed in this thesis is shown in Figure 2.7.

2.6.2 SECCM setup

In this section, the SECCM instrumentation and working principles will be discussed in detail.

Figure 2.8 shows a schematic illustration a home-built SECCM setup. It consists of five main parts, namely a scanning probe (a double barrel pipette), a substrate of interest, a bipotentiostat for applying the potentials and measuring the currents, piezoelectric positioners for moving the probe/substrate, and a lock-in amplifier as a feedback system to precisely control the probe position.

A typical SECCM probe is a double barrel pipette. The preparation of SECCM probes has already been described in section 2.6.1. Before placing the probe, it is filled with an electrolyte solution of interest and quasi-reference counter electrodes (QRCEs) are inserted into each channel of the pipette. A bias potential, V_2, is applied between the two identical QRCEs to induce an ion conductance current (i_{DC}) across the meniscus. A potential, V_1, relative to ground, is applied to one of the QRCEs. The effective working electrode potential, E_s, is calculated as - (V_1 + V_2 / 2) relative to ground. During the experiment, V_2 is normally held at a fixed potential

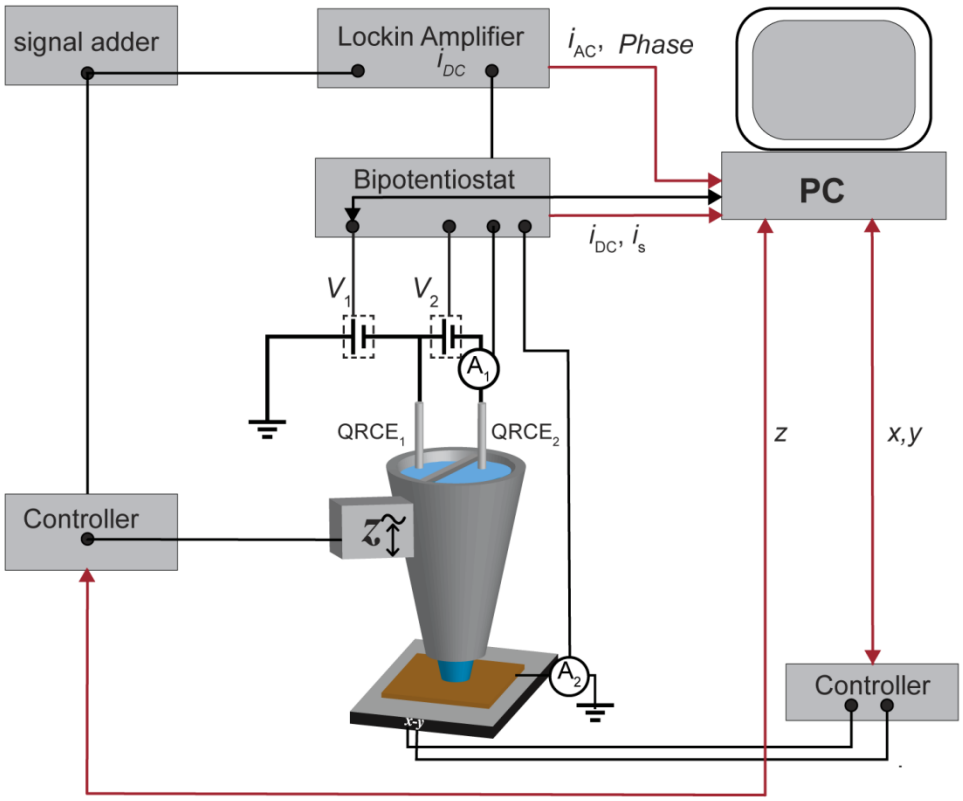

Figure 2.8 Schematic of scanning electrochemical cell microscopy (SECCM). A double barrel pipette was placed on a substrate (working electrode). Quasi-reference counter electrodes (QRCEs) were inserted into each barrel of a pipette, used as an imaging probe. V_1: potential applied to one of the QRCEs (relative to ground); V_2 : potential bias applied between the QRCEs; Current follower A_1 and A_2 measures the ion conductance current (i_{DC}) and the current through the substrate, i_s, respectively. The alternating current signals, i_{AC}, and phase, was measured through a lock-in amplifier. Four parameters, *x*, *y*, *z* piezo positions and V_1 were generated from the PC and seven parameters *x*, *y*, *z*, $i_{DC,}$ $i_{s,}$ i_{AC} and phase were measured through the computer.

while V_1 is adjusted to control the potential of the substrate (which is held at ground) relative to QRCEs. The current flowing through the working electrode is denoted as i_s.

A home-built bipotentiostat is used to apply the potentials (V_2) and measure i_{DC} between the two QRCEs. The substrate current, i_s, was measured either by the bipotentiostat or with high sensitivity current amplifiers.

The pipette and/or the surface are mounted on piezoelectric positioners. In this thesis, two configurations of the instrument were employed, differing in the *x*,*y*-movement of the tip relative to the substrate to control the movement of pipette and substrate. In the first approach, termed the tip scanning configuration, the substrate was fixed in position and only the pipette was allowed to move (in all three dimensions). In this configuration, the pipette was mounted on a three-direction piezoelectric positioner (PI Nanocube P-611.35), allowing 100 μm movement in all *x*, *y* and *z* directions. Figure 2.8 illustrates the second approach, termed the sample scanning configuration, in which the substrate was fixed on a *x*-*y* (P-622.1CD, Physic Instrument) piezoelectric positioner, allows the lateral movement of the substrate. The pipette was on a *z*-piezoelectric positioner, only allowing movement of the tip normal to the substrate. With the exception of Chapter 3 and part of Chapter 5, which was conducted in a tip-scanning configuration, all the other work described in this thesis was performed on a setup employing the sample scanning configuration.

Before an experiment, the pipette is placed close (within ~ 30 μm) to the surface with a micropositioner, either manually or computer-controlled, aided of high magnification CCD-cameras. The final approach of the pipette is controlled by the *z*-piezoelectric positioner. During this approach, a small periodic oscillation was applied to the *z*-piezoelectric positioner holding the pipette by a voltage-wave generator built into an external lock-in amplifier. Upon contact of the electrolyte meniscus with the surface, the oscillation leads to the periodic deformation of the

meniscus at the same frequency as the applied oscillation, giving rise to an alternating current component (i_{AC}) in the conductance current flowing through the meniscus. The magnitude of i_{AC} strongly depends on the pipette-to-substrate separation (see section 2.6.4), and can be extracted with the lock-in amplifier and used as a positional feedback signal.

All the signals were collected by a field-programmable gate array (FPGA) card controlled with custom LabVIEW code. The whole setup was placed in a Faraday cage to minimize electronic noise.

2.6.3 Environmental SECCM

To perform experiments without the interference of molecular oxygen, the substrate and pipette were placed in a home-made environmental chamber, as shown in Figure 2.9.[14] A rectangular environmental chamber made of polyether ether ketone was placed under *z*-piezoelectric positioner. Glass windows were glued on the top cover and on the sidewall, allowing optical access with an external camera and illumination by an external light source. Gas inlet and outlet channels are placed next to each other at the back wall. Nitrogen gas was passed through a glass vessel containing water before flowing through the chamber continuously to provide an oxygen-free atmosphere. The chamber is closed with a finger cot, through which the pipette was placed. Before carrying out any electrochemical measurement, nitrogen was normally flowed for at least 30 min to deoxygenate the chamber. Importantly, careful control of the gas flow rate is important in order to minimize the physical disturbance of the electrolyte meniscus during an electrochemical measurement. The efficiency of the chamber was confirmed by CVs recorded on a Pt foil which showed

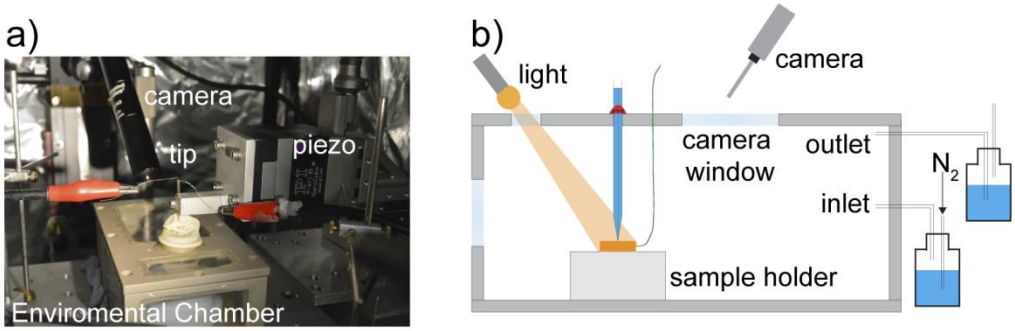

Figure 2.9 a) Top view image of the environmental rig setup. **b)** Schematic of the environmental chamber used in a SECCM setup. The grey bars represent the main part of the chamber made from polyether ether ketone. Two small glass windows were crafted into the walls (one on the top, one on the side) to allow visual access to the pipette for pipette positioning. Nitrogen gas was flushed through a vial containing distilled water. By leading the gas outlet through a vial containing water, a good seal of the chamber was maintained and the gas flow could be monitored visually to assess to flow rate as well as verify there was no leakage.

a negligible oxygen reduction reaction (ORR) current. This environmental chamber was employed in all the SECCM measurements which required a deoxygenated solution.

2.6.4 Working principles

During a SECCM measurement, the *z*-position of the pipette is oscillated at a fixed frequency and amplitude. When the pipette is suspended, the electrolyte meniscus is not in contact with the surface, and i_{DC} across the meniscus is constant and independent of the applied oscillation. Conversely, when the electrolyte meniscus is in contact with the substrate, the oscillation leads to a periodic

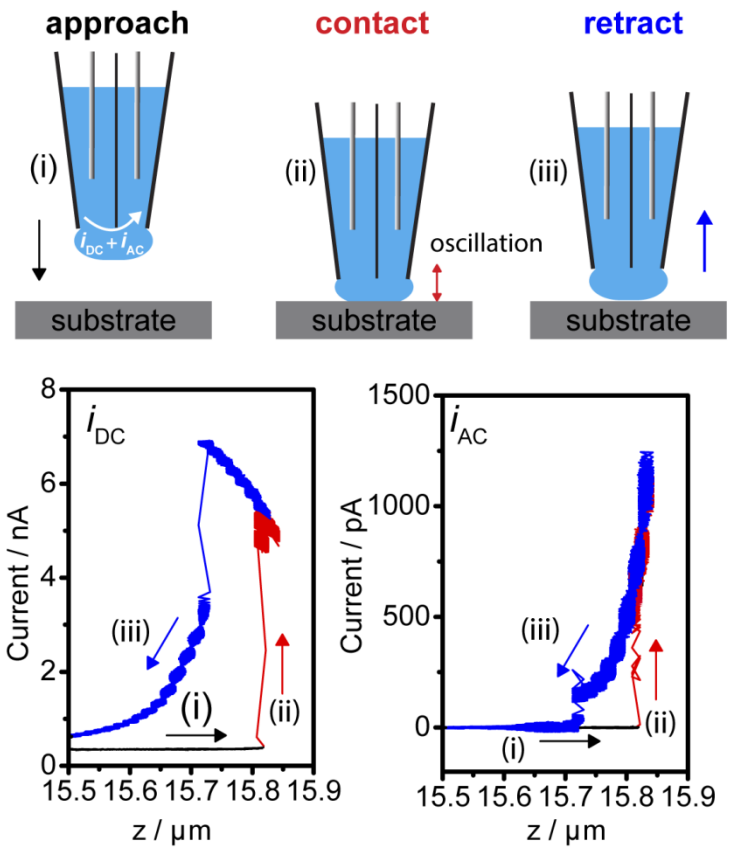

Figure 2.10 i_{DC}, and i_{AC} profiles versus pipette positions. Three regions are identified with different colour: (i) pipette in air, i_{DC} and i_{AC} are stable; (ii) meniscus in contact with a substrate, leading to big jumps in i_{DC} and i_{AC}; and (iii) pipette retracts back to air and meniscus breaks. i_{DC} increases first (wetting) and then decreases, i_{AC} decreases quickly to a small value.

deformation of the meniscus. This deformation introduces i_{AC} component in the i_{DC} with the same frequency as the applied oscillation. Importantly, the amplitude of i_{AC} strongly depends on the height of the meniscus and can be used to control and maintain a constant tip-to-substrate separation. This principle is illustrated in Figure 2.10: while approaching the substrate with the pipette (black lines), i_{DC} is constant, and i_{AC} is negligible small. Once the meniscus contacts the substrate (at ~15.8 µm), there is a snap-to-contact of the meniscus, and leading to a sharp increase in i_{DC}.

Simultaneously, i_{AC} increases by several orders of magnitude. This increase in i_{AC} is used to sense contact between the pipette and the substrate. Retracting the pipette at this point (blue lines) shows that the amplitude i_{AC} is very sensitive to meniscus height, and thus can be used to control the tip-to-substrate separation. Finally, after retracting sufficiently far to break the electrolyte meniscus (~ at 15.7 μm), i_{AC} returns to a negligible value.

2.6.5 Imaging procedure

In this thesis, two different imaging procedures are mainly employed, namely constant distance imaging and hopping voltammetric imaging. Constant distance imaging mode was used in Chapter 3 and 4, where potentiostatic information at a number of key potentials was obtained. In Chapter 5, a hopping voltammetric imaging procedure is introduced and employed to obtain dynamic electrochemical images, providing information over a much wide potential range.

Constant distance imaging mode

In constant distance imaging, once the meniscus contacts the surface, a constant tip-to-substrate distance is maintained by adjusting the pipette height to maintain a constant i_{AC} set point. Figure 2.11a illustrates the pipette movement and the corresponding measurements at the *x*-*y* plane for constant distance imaging. The i_{AC} set point magnitudes for the studies in this thesis were in the range of 1.0 % - 2.0 % of the i_{DC} value.

Two different methods for adjusting pipette height were employed for

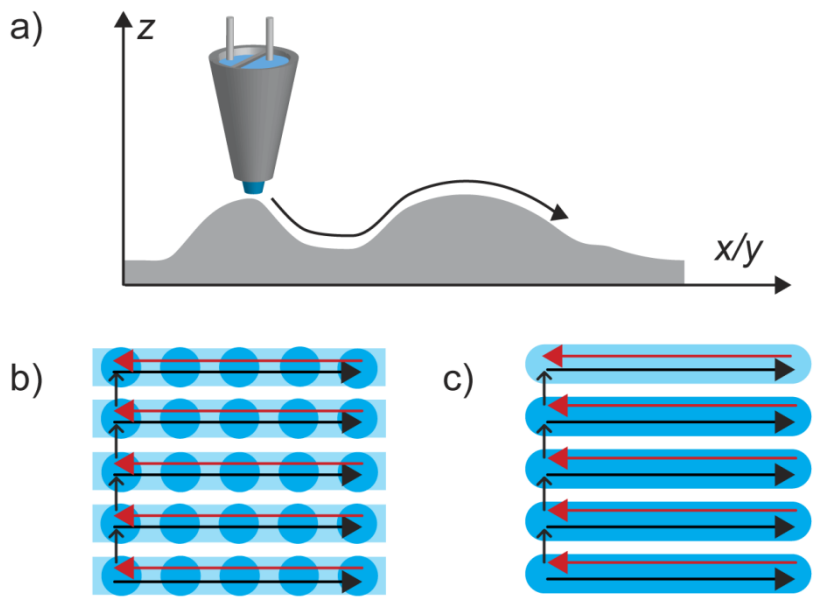

Figure 2.11 Schematic overview of the constant distance imaging procedures. **a)** In constant distance imaging, the meniscus is kept in contact with the surface as the pipette scans across the surface. **b)** Distance-based method. The droplet was kept in contact with the surface continuously but measurements only take placed at predefined pixels. Solid blue circle: area where a measurement took place; light blue strip: trace of a pipette movement. **c)** Time-based imaging procedure. The pipette is moved along the surface at a constant speed and the current is recorded continuously.

constant distance SECCM imaging in this thesis. The first method is a distance-based method (move-stop-measure), as shown in Figure 2.11b. In this procedure, the overall movement of a pipette is divided into separate steps: first, the pipette moves at predefined lateral distance steps while keeping pipette at constant height; then, it pauses, adjusting pipette height by measuring i_{AC} and comparing it to the set point. Finally, after adjusting the height, the pipette can be moved to the next point, or the electrochemical and conductance current can be recorded after a waiting time. This pattern is repeated as the pipette moves laterally across the surface.

An alternative method for adjusting pipette height is a time-based method, see Figure 2.11c. In this mode, the pipette moves laterally along the surface at a constant speed. During this continuous movement, i_{AC} is measured and the pipette height adjusted at a predefined time interval, typically a few milliseconds. Simultaneously, the current signals are recorded continuously during lateral movement of the pipette. This scanning mode can provide images with much higher resolution and reduce the time required to record an image.

In both constant distance imaging procedures, the images are constructed from data obtained in parallel lines. Typically, a pipette scans forward along a line (in the *x*-direction) and then reverses, moving back to the starting position of the line. After one line, the pipette is moved one step in the *y*-direction to the starting point of the next line. This line is then scanned, and the pattern is repeated until the full scan is obtained. The resolution of a constant distance imaging is defined by step size in the scan direction and the spacing between each line perpendicular to the scan direction. In a single scan, two sets of images, from the forward and reverse scan, can be obtained. In each set, maps of i_{DC}, i_{AC}, i_s and z are recorded simultaneously. Typical images and line traces for the two imaging modes are shown in Figure 2.12. In this figure, the map obtained with the distance-based imaging mode is composed by 38 lines in *y* direction, with each line containing 28 point measurements in *x* direction. The line trace shows clearly that measurements only took place at a limited number of pixels. For the time-based imaging, the current was recorded continuously with pipette moving. While the number of lines is still limited in the *y* direction, it is clear that much more data points (9341) were obtained along a line in the *x* direction. Thus, this imaging mode is very useful for obtaining detailed information on small surface features, such as step edges of highly ordered pyrolytic graphite.[13]

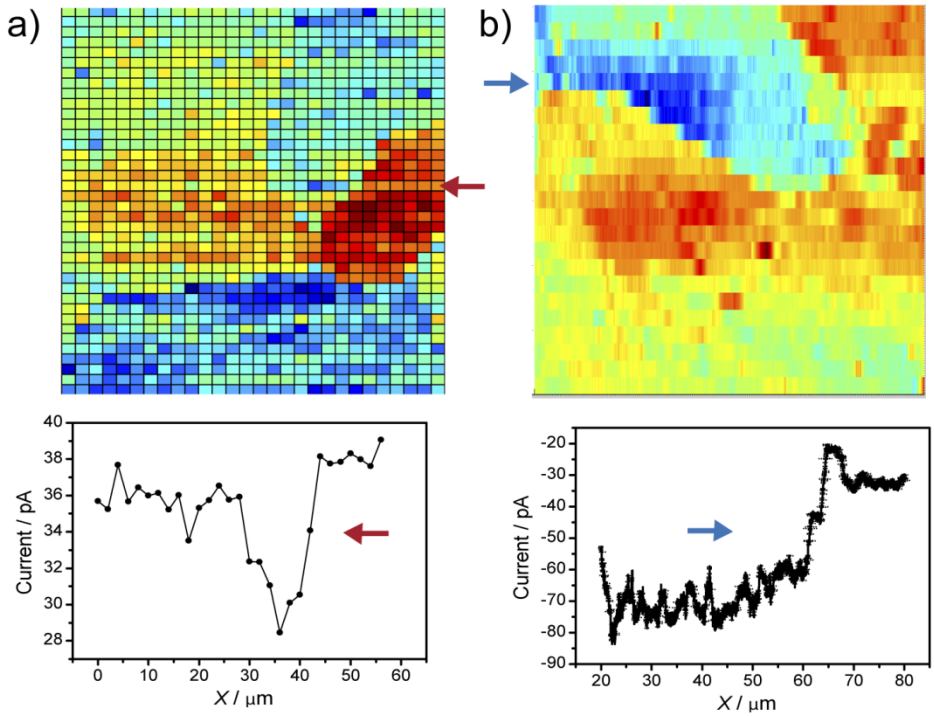

Figure 2.12 SECCM raw images and the corresponding line traces of the electrochemical surface current for a **a)** distance-based imaging and **b)** time-based imaging procedure. The bottom panels show data traces at a single line (indicated by arrows).

Although i_{AC} provides a good feedback parameter for maintaining the tip-to-substrate separation, it is challenging to perform imaging at rough substrates due to the small distance between the end of the tip and the substrate. Furthermore, in constant distance imaging, only one fixed potential is applied during one imaging procedure. To obtain electrochemical current at different potentials, separate scans need to be obtained at every potential which can be very time-consuming, especially for large samples. In addition, for some reactions, the surface can be blocked due to electrolyte fouling, which makes the substrate unavailable for multiple scanning. Thus, to obtain more information at a wide potential, voltammetric SECCM is introduced.

Hopping voltammetric SECCM imaging

In hopping voltammetric SECCM, the pipette moves in a hopping mode and CV (rather than fixed potential) measurements are performed at the contact area. Figure 2.13 illustrates the tip-to-substrate separation, as a function of time, *t*, during imaging, together with the corresponding potential- and current- time profile applied to the substrate working electrode.

As shown from the Figure 2.13, in hopping voltammetric SECCM imaging, the complete tip movement and scanning process consists of the following steps: i) a

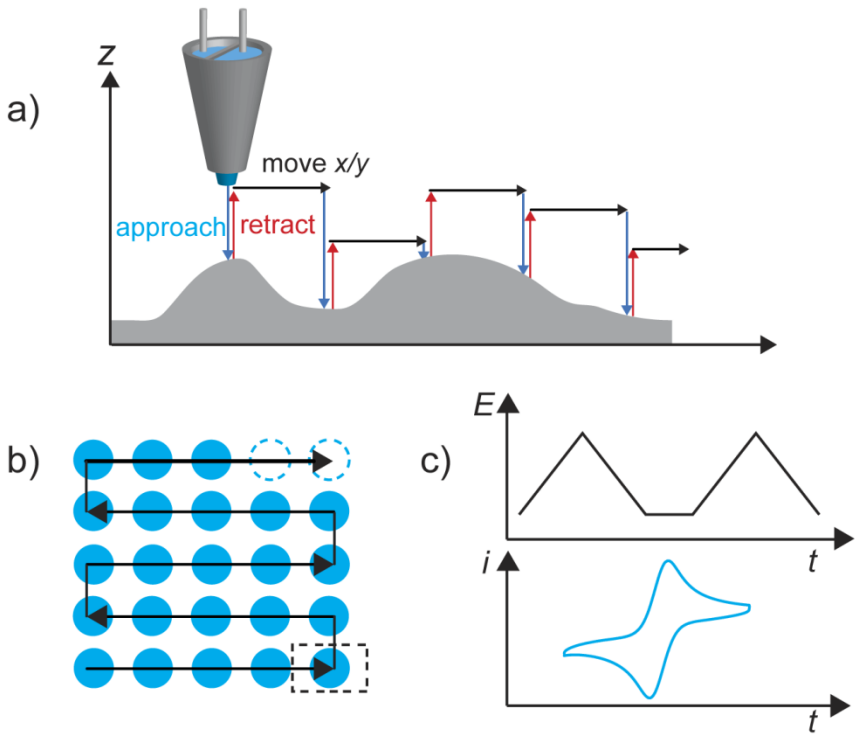

Figure 2.13 Schematic illustration of voltammetric SECCM imaging procedures. **a)** Pipette movements on top of a substrate. The approach (blue arrow) distance depends on the topography of a substrate. Pipette retraction (red arrow) and *x*-*y* movement (black arrow) are fixed at a pre-defined distance. **b)** The pipette movement pattern at *x*-*y* plane. **c)** The potential and current profiles recorded at every positon. At each data point, the CV segment numbers and sweep rates can be adjusted.

slow approach of the pipette to the substrate; ii) meniscus contact; iii) pipette movement is paused, and waiting time is implemented for the meniscus to stabilize; iv) the potential is swept to record one or more CVs; v) quick retraction of the pipette to break the meniscus; and vi) movement in the *x*,*y*-plane to repeat the process for the next pixel. Notably, during meniscus contact time, any potential profiles can be applied to the working electrode, opening up more possibilities for studying complicated reactions. In this imaging procedure, i_{AC} is used to maintain a constant tip-to-substrate distance at every time the meniscus makes contacts with the surface. There was no positional feedback during potential sweeps. As the pipette can retract far away enough while performing the *x*,*y*-lateral movement, it efficiently reduces the chance of pipette crashing.

As potential sweeps are applied to every pixel, with the associated current response measured, multiple electrochemical images can be constructed. For example, electrochemical images can be plotted for every recorded potential as a

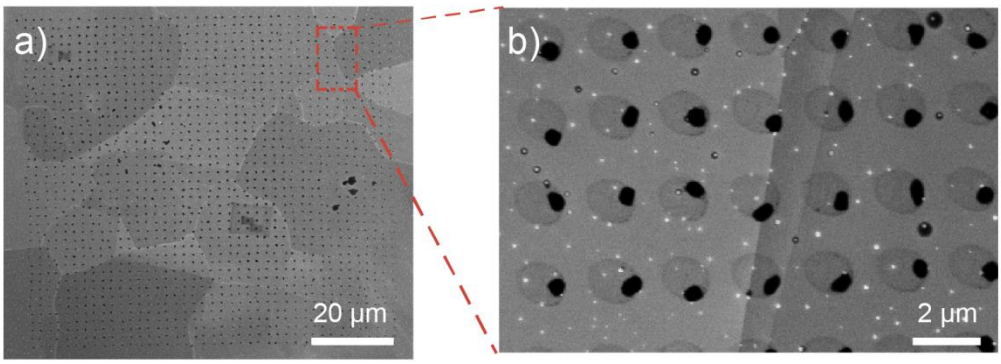

Figure 2.14 SEM images of droplet residues left on a Pt foil after a voltammetric SECCM imaging. **a)** A scanned area contains 1600 measurements (40 × 40 pixels) recorded every 1.5 µm. Each dot represents a CV measurement. **b)** Zoom-in figure of individual droplets, illustrating consistent droplet wetting at different grains.

function of *x*,*y*-position. For a potential sweep at which the current is recorded every 1 mV in a 1.0 V window, 1000 electrochemical images can be plotted and these images can be constructed as potentiodynamic movies. These electrochemical movies provide extensive information about the electrochemical reactivity change across the surface with time and applied potential.

Due to the quick break of droplet while retracting the pipette, residues from electrolyte are often left on the surface. These residues can be used as a map for the probed area, providing exact location for measurements at each individual pixels. A typical SEM for a scanned area after a hopping voltammetric SECCM experiment is shown in Figure 2.14, illustrating the consistency in contact area of the hopping voltammetric scanning mode.

2.6.6 Marking an area after scanning

After SECCM imaging, the scanned area was marked for further surface characterization. One method of marking is by controlled breaking of pipette on the substrate. After all the images are recorded, the pipette used for imaging is retracted about 25 μm away from the substrate. Then, it is approached again manually. Instead of stopping the approach when the meniscus contact was established, the approach was continued until the pipette itself contacts the surface, leading to breaking of the glass and leaving residues (glass debris). Typically, four spots were marked which are sufficiently far away from the scanned area to not leave debris on the area of interest. For example, for a 50×50 μm^2 scan centred at (x, y) = (50,50), the pipette can be broken at (x, y) = (0,0), (0,100), (100, 0) and (100, 100). These debris from the controlled breaking could easily be located with SEM and optical microscopy, thus assisted in locating the imaged area. A careful comparison of SEM, EBSD and

electrochemical images were performed later to further confirm the area. This method was used in Chapter 3 and 4 for locating the scanned area. For images in chapter 5, FIB etching was used to mark sample as described above.

2.7 Self-assembled monolayer (SAM) preparation

The general procedure for preparing self-assembled monolayer (SAM) at Au substrates is shown in Figure 2.15. Au substrates were prepared by evaporating an Au film on a Si/SiO_2 wafer using a using an electronic thermal beam evaporator (MiniLab 060 System, Moorfield). The whole process was carried out under high vacuum control, typically $\leq 1 \times 10^{-6}$ mbar. A 2.5 nm Cr layer was first evaporated at a rate of ~ 0.2 Å s^{-1}. This Cr layer is used to promote the adhesion of Au onto SiO_2. Then, an Au film was deposited at a rate of ~1.0 Å s^{-1} to form a ~ 60 nm film. Some of the prepared Au substrates were used immediately to form SAMs. For the Au samples kept in air for some time, before SAM formation, these samples were cleaned in oxygen plasma at 7×10^{-4} bar and 100 W for 1 min.

Three different types of alkanethiols were employed to form SAMs, with different terminal groups. Two of them have hydrophilic terminal groups, namely 11-mercapto-1-undecanol, ($HS-(CH_2)_{11}-OH$) and 11-mercaptoundecanoic acid ($HS-(CH_2)_{10}-COOH$) and one with a hydrophobic terminal group (dodecanethiol ($HS-(CH_2)_{11}-CH_3$). Alkanethiol SAMs were prepared on the clean Au substrates (Figure 2.15) following literature procedures.[15] First, Au substrates were immersed into ethanol solutions containing 2 mM thiols. After leaving in the solution for more than 24 hours, they were rinsed with copious amounts of absolute ethanol, to remove

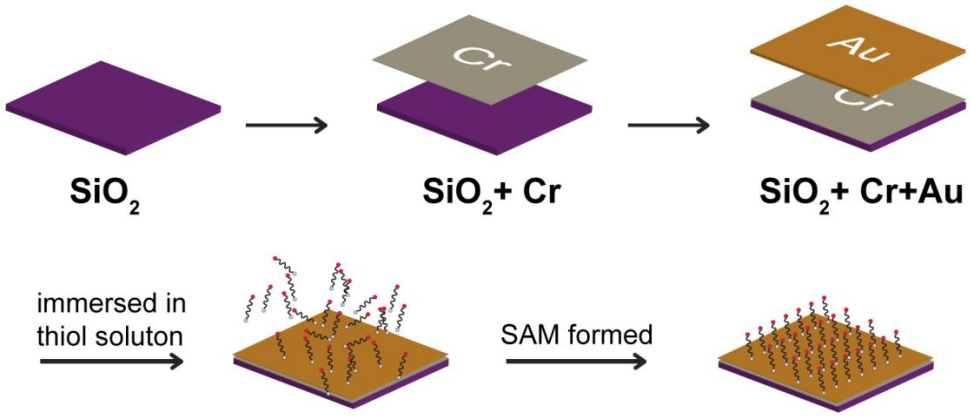

Figure 2.15 A schematic view of the formation of an SAM on a Au substrate.

excess unbound alkanethiols. Then, these samples were dried under a nitrogen gas flow and stored in clean petri-dishes. The quality of SAMs was checked by performing CVs on the substrates using a droplet cell configuration. All substrates were prepared on the day of the experiment to avoid the contamination from air.

2.8 AFM force measurements

All force measurements were performed with a Bruker-Nano Multimode atomic force microscope (MULTIMODE8) controlled by Nanoscope controllers, utilising a small flow cell. A schematic of the AFM force measurement is shown in Figure 2.16.

AFM tips were purchased from Bruker (SNL-10) with triangular, silicon nitride cantilevers of 205 μm length. These tips were prepared by depositing a 2.5 nm Cr adhesion layer followed by a 60 nm gold layer using a thermal beam evaporator, giving tips with 60 nm radius of curvature. The adsorption of citrate ions

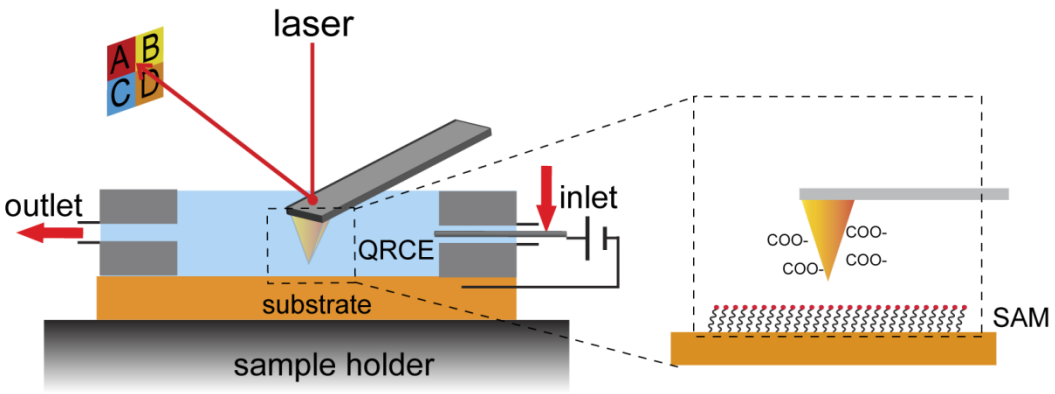

Figure 2.16 A schematic view of the AFM setup for performing force measurements with potential control. The alkanethiol modified Au substrates were used as working electrode. An Ag/AgCl wire of 50 μm was placed in the inlet channel of the flow cell and served as a QRCE. The potential of the working electrode was varied by using an external potentialstat.

on these tips was carried out using a literature procedure[16] by immersing the gold coated AFM tips in 1 mM sodium citrate solution for at least 12 hrs.

All the AFM force curves were recorded under potential-control in a two-electrode system using a CH Instruments potentiostat. The SAM/Au substrate of interest was the working electrode and a thin Ag/AgCl wire placed in the inlet channel of the cell, served as a QRCE. All measurements were performed in an aqueous solution containing 1 mM $K_4Fe(CN)_6$ and 0.4 mM sodium citrate, to ensure the ionic strength was the same as that in NP-impact experiments (Chapter 6). During AFM measurements, a constant potential of 400 mV was applied to the working electrode. The background currents at these potentials were negligible, justifying the use of a two-electrode system and QRCE.

The spring constant of each tip used was measured using the thermal tune method integrated into the Nanoscope software, with a mean value of 0.118 ± 0.010

nN nm^{-1} for the tips used. Raw data were converted to obtain force *vs*. piezo displacement plots, using the measured deflection sensitivities and tip spring constants. For each substrate, more than 200 force-distance curve measurements were performed at multiple substrate areas.

2.9 References

(1) Climent, V.; Feliu, J. M. *J. Solid State Electrochem.* **2011**, *15*, 1297.

(2) Clavilier, J.; Faure, R.; Guinet, G.; Durand, R. *J. Electroanal. Chem.* **1980**, *107*, 205.

(3) Clavilier, J.; Durand, R.; Guinet, G.; Faure, R. *J. Electroanal. Chem. Interfacial Electrochem.* **1981**, *127*, 281.

(4) Bard, A. J.; Mirkin, M. V. *Scanning electrochemical microscopy*; CRC Press, 2012.

(5) Vasile, M. J.; Enke, C. G. *J. Electrochem. Soc.* **1965**, *112*, 865.

(6) Mingard, K. P.; Roebuck, B.; Bennett, E. G.; Gee, M. G.; Nordenstrom, H.; Sweetman, G.; Chan, P. *Int. J. Refract. Met. Hard Mater.* **2009**, *27*, 213.

(7) Humphreys, F. J. *Journal of Materials Science* **2001**, *36*, 3833.

(8) Ebejer, N.; Güell, A. G.; Lai, S. C. S.; McKelvey, K.; Snowden, M. E.; Unwin, P. R. *Annu. Rev. Anal. Chem.* **2013**, *6*, 329.

(9) Snowden, M. E.; Güell, A. G.; Lai, S. C. S.; McKelvey, K.; Ebejer, N.; O'Connell, M. A.; Colburn, A. W.; Unwin, P. R. *Anal. Chem.* **2012**, *84*, 2483.

(10) Ebejer, N.; Schnippering, M.; Colburn, A. W.; Edwards, M. A.; Unwin, P. R. *Anal. Chem.* **2010**, *82*, 9141.

(11) Güell, A. G.; Ebejer, N.; Snowden, M. E.; McKelvey, K.; Macpherson, J. V.; Unwin, P. R. *Proc. Natl. Acad. Sci. U. S. A.* **2012**, *109*, 11487.

(12) Lai, S. C. S.; Dudin, P. V.; Macpherson, J. V.; Unwin, P. R. *J. Am. Chem. Soc.* **2011**, *133*, 10744.

(13) Lai, S. C. S.; Patel, A. N.; McKelvey, K.; Unwin, P. R. *Angew. Chem. Int. Ed.* **2012**, *51*, 5405.

(14) Aaronson, B. D. B.; Lai, S. C. S.; Unwin, P. R. *Langmuir* **2014**, *30*, 1915.

(15) Love, J. C.; Estroff, L. A.; Kriebel, J. K.; Nuzzo, R. G.; Whitesides, G. M. *Chem. Rev.* **2005**, *105*, 1103.

(16) Zhang, H.; He, H.-X.; Wang, J.; Liu, Z.-F. *Langmuir* **2000**, *16*, 4554.

Chapter Three

Pseudo-single-crystal electrochemistry on polycrystalline electrodes: Visualising activity at grains and grain boundaries on platinum for the Fe^{2+}/Fe^{3+} redox reaction

Abstract

The influence of electrode surface structure on electrochemical reaction rates and mechanisms is a major theme in electrochemical research, especially as electrodes with inherent structural heterogeneities are used ubiquitously. Yet, probing local electrochemistry and surface structure at complex surfaces is challenging. In this chapter, high spatial resolution scanning electrochemical cell microscopy (SECCM) complemented with electron backscatter diffraction (EBSD) is demonstrated as a means of performing 'pseudo-single-crystal' electrochemical measurements at individual grains of a polycrystalline platinum electrode, while also allowing grain boundaries to be probed. Using the $Fe^{2+/3+}$ couple as an illustrative case, a strong correlation is found between local surface structure and electrochemical activity. Variations in electrochemical activity for individual high-index grains, visualised in a weakly adsorbing perchlorate medium, show that there is higher activity on grains with a significant (110) orientation contribution, compared to those with (100) and (111) contribution, consistent with findings on single-crystal electrodes. Interestingly, for Fe^{2+} oxidation in a sulfate medium a different pattern of activity emerges. Here, SECCM reveals only minor variations in

activity between individual grains, again consistent with single-crystal studies, with a greatly enhanced activity at grain boundaries. This suggests that these sites may contribute significantly to the overall electrochemical behaviour measured on the macroscale.

Chapter 3

3.1 Introduction

Identifying correlations between the electrochemical activity and morphology (in particular, the crystallographic orientation) of electrode surfaces is of major fundamental importance towards achieving a better understanding heterogeneous electron transfer (ET) processes. Moreover, the rational development of electrocatalysts,[1,2] for a variety of applications, from energy conversion and storage[3-7] to electrosynthesis[8,9] and electrochemical sensors,[10] requires knowledge of electrode structure-activity relationships. A major area of interest is the structure-dependent reactivity of platinum and other platinum-group metals, which have proven to be among the most efficient electrocatalysts for a wide variety of reactions.[11,12]

A common approach to investigating the relationship between surface structure and electrochemical activity is to employ well-defined single-crystal electrodes.[3,13,14] However, while valuable information can be obtained, such studies are challenging, as well as expensive and time-consuming, as each electrode needs to be carefully prepared, characterised and handled so that only a single surface orientation is assured. Furthermore, the effect of boundaries between different crystallographic grains cannot be probed on such surfaces, even though they may play a significant (or possibly even dominant) role in surface reactivity.[15,16] These challenges could be circumvented if one could directly probe the local structure of a polycrystalline sample, for example with electron backscatter diffraction (EBSD),[17] and correlate this with localised electrochemical measurements.[17,18]

One approach for performing localised electrochemistry on a polycrystalline surface is to prepare an array of individually addressable micrometre scale electrodes

through lithographic processing.[17] However, due to the irregular shape and size of crystalline grains, the employment of lithographic techniques to expose specific grains is technically very demanding. Furthermore, lithographic processing is rather involved and can leave residual contaminations which may impact the reactivity of the electrode.[19,20] Another approach is to limit the contacted area of the working electrode by employing droplet based techniques.[18,21-23] However, methods of this type have tended to be restricted to static point-by-point measurements (usually on a large scale), and the mapping of an area of an electrode has proved to be time consuming and difficult technically.

In Chapter 1, scanning electrochemical cell microscopy (SECCM) has been introduced as a scanning probe technique to visualise ET processes quantitatively at the microscale and nanoscale.[21,24-29] An attractive feature of SECCM is that each location on the electrode is only exposed to the electrolyte solution briefly, minimising electrode fouling[21] and other undesired processes. In contrast to scanning electrochemical microscopy (SECM),[30,31] which is also powerful for visualising heterogeneous electrode substrates,[21,32-34] SECCM measures the electrochemical processes of interest directly, in a manner that is similar to conventional dynamic electrochemistry, and readily achieves higher spatial resolution.

This chapter studied the one-electron oxidation of Fe^{2+} to Fe^{3+} in aqueous media on a polycrystalline platinum surface with SECCM, and correlated the local activity with the corresponding microscale crystallographic orientation of the surface determined by EBSD. The $Fe^{2+/3+}$ redox couple is especially interesting, as it is an ostensibly simple one-electron process, although showing strong kinetic limitations and often considered to be a model inner-sphere process based on macroscopic measurements on polycrystalline metal electrodes.[35] Previous work on

polycrystalline boron doped diamond, showed electron transfer for this redox couple to be very strongly surface-sensitive.[21] Similar findings have been reported for other carbon electrode materials[36,37] as well as metal electrodes.[38] However, the origin of the structure-sensitivity is unclear and has been a topic of debate, with explanations ranging from differences in surface coordination of the $Fe^{2+/3+}$ species,[39] variations in the local density of electronic states of the electrode,[38] changes in double layer structure with the surface structure,[40-42] different crystallographic facets of an electrode having different potential of zero charge[40,41] and/or effects due to surface sensitive anion adsorption.[43,44] Fe^{2+} oxidation on platinum is further complicated by the fact that it takes place at potentials at which oxidation of the platinum surface also occurs.[45] Platinum surface oxidation consists of a number of steps whose significance are timescale and potential dependent.[45,46] Initially, surface oxidation occurs through the fast formation of Pt-OH.[47] Further oxidation to form PtO and PtO_2 occurs slowly over the course of seconds to tens of seconds. Thus, the electrochemical response for many redox reactions can be strongly impacted by the timescale of the measurement for potentials in the oxide formation region. This is particularly true for the $Fe^{2+/3+}$ redox process.[45,48] Based on the previous work,[21,24-29,49] SECCM provides a powerful method to investigate whether structural effects hold for the oxidation of Fe^{2+} on polycrystalline platinum.

This work further demonstrates that SECCM coupled with EBSD is a powerful approach to perform 'pseudo-single-crystal' experiments on a polycrystalline (platinum) substrate. In particular, owing to the short contact time of SECCM, information on surface reactivity can be obtained before (irreversible) surface oxidation sets in, allowing probing the structure-activity relationship for Fe^{2+} oxidation at significant overpotentials. Notably, distinct patterns of spatial ET

activity and anion effects have been identified, which provide a new view of heterogeneous redox reactions at polycrystalline platinum. This evidently has significant implications for kinetic and mechanistic studies at polycrystalline electrodes, generally, which are usually studied by macroscopic techniques, such as cyclic voltammetry, without the ability to assess whether reactions can be considered to be uniform across a substrate.

3.2 Results and Discussion

3.2.1 Macroscopic characteristics of the Fe^{2+}/Fe^{3+} redox couple on a polycrystalline platinum foil

The one-electron oxidation of Fe^{2+} on a macroscopic scale was studied in both perchlorate and sulfate media on a polycrystalline platinum foil using cyclic voltammetry. Typical cyclic voltammograms (CVs) of 2 mM Fe^{2+} (from $FeClO_4)_2$) in 10 mM $HClO_4$ and of 2 mM Fe^{2+} (from $FeSO_4$) in 10 mM H_2SO_4 (both *ca.* pH 2) are shown in Figure 3.1a. CVs in only the supporting electrolyte (*i.e.* without the Fe-salt), are shown in Figure 3.1b for comparison. All CVs were measured in aerated solution. The oxidation of ferrous overlaps with the reduction of oxygen at potentials lower than 0.6 V in both Figure 3.1a and b. In this chapter, all potentials reported are relative to reversible hydrogen electrode (RHE).

The onset potential for Fe^{2+} oxidation (Figure 3.1a) is nearly 100 mV lower in sulfate than in perchlorate, although beyond this the current density-potential waves are rather similar. The difference in onset potential between the two electrolytes is not due to any difference in the $Fe^{2+/3+}$ formal potential ($E^{0'}$): this was the same in each medium (+ 0.90 V *vs* RHE). Rather, the CVs in electrolyte alone

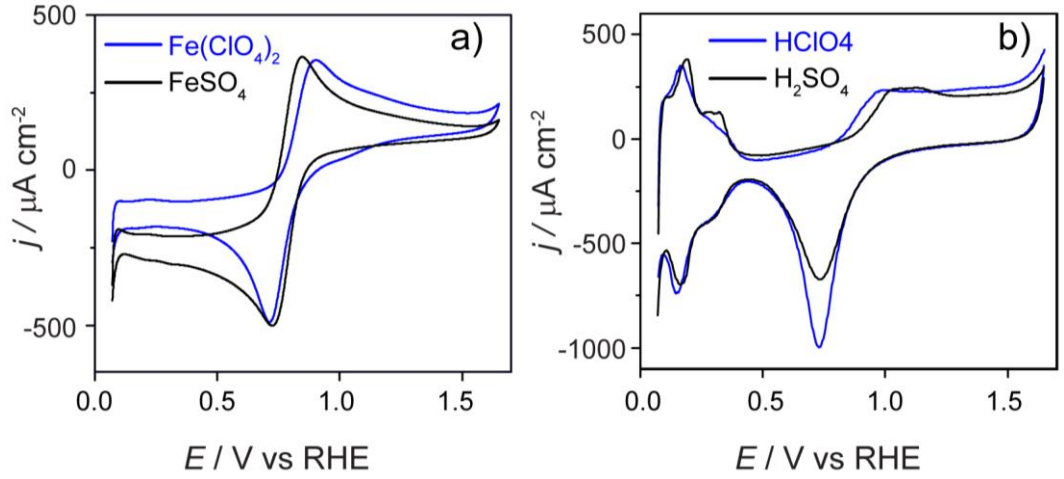

Figure 3.1 a) Cyclic voltammograms of 2 mM $Fe(ClO_4)_2$ in 10 mM $HClO_4$ (blue line) and 2 mM $FeSO_4$ in 10 mM H_2SO_4 (black line); the sweep rate was 25 mV s^{-1}. **b)** Background voltammograms of 10 mM $HClO_4$ (blue line) and 10 mM H_2SO_4 (black line); the sweep rate was 500 mV s^{-1}. All CVs were measured in aerated aqueous solution.

(Figure 3.1b), demonstrate significant differences in the surface oxidation state in each of the two media in the potential range close to $E^{0'}$ for $Fe^{2+/3+}$. The oxidation of platinum in the perchlorate medium starts about 100 mV more cathodic than in the sulfate medium. This can be attributed to the strong adsorption of the sulfate ions, inhibiting surface oxidation, compared to the weakly adsorbing perchlorate ions.[44,50] Generally, it can be seen that, in both sulfuric acid and perchloric acid, the oxidation of Fe^{2+} largely overlaps with the platinum surface oxidation region. These CVs were used to select potentials for SECCM imaging, ranging from the onset of oxidation towards the diffusion-limited region.

As highlighted above, one of the challenges in studying the one-electron Fe^{2+} oxidation on platinum is that the measured current could represent a contribution of both Fe^{2+} oxidation and surface oxide formation processes. Two measures were taken in order to distinguish between Fe^{2+} oxidation and surface oxidation processes in the

SECCM setup: (i) allowing a short waiting time (20 ms), to minimize the current due to double layer charging and Pt-OH formation; and (ii) limiting the time of the measurement at each data point to reduce the influence of slow surface oxidation processes (PtO and PtO_2 formation).

3.2.2 SECCM background image in sulfuric acid electrolyte

To investigate the role of surface oxide formation during SECCM imaging, an electrochemical image of the platinum foil at a potential of 1.15 V in only the oxide region in blank electrolyte (sulfuric acid without Fe^{2+}) was recorded and shown in Figure 3.2. This image and all other SECCM images in this chapter were constructed from parallel line scans with a spacing of 2 µm between each line. A data point (pixel) was recorded every 1.5 µm over a period of 40 ms at a frequency of 25 kHz (corresponding to the average of 1000 measurements), after a 20 ms waiting time. Different from the other images, the image is plotted as raw pixels without interpolating between the pixels.

From Figure 3.2, it can be seen that the current is essentially zero over the entire area, indicating that the contribution of various surface oxidation processes to the measured currents (see below) is negligible compared to tens of pA obtained in the presence of Fe^{2+} (see below). Significantly, it should be mentioned that this image was recorded with a current amplifier settings (100 pA/V) and is the same as for the Fe^{2+} oxidation images (see below), so the small variations in current are indicative of the noise level for the study reported herein. This can be seen in Figure 3.2b, where the surface current is plotted in line profiles, clearly showing that all

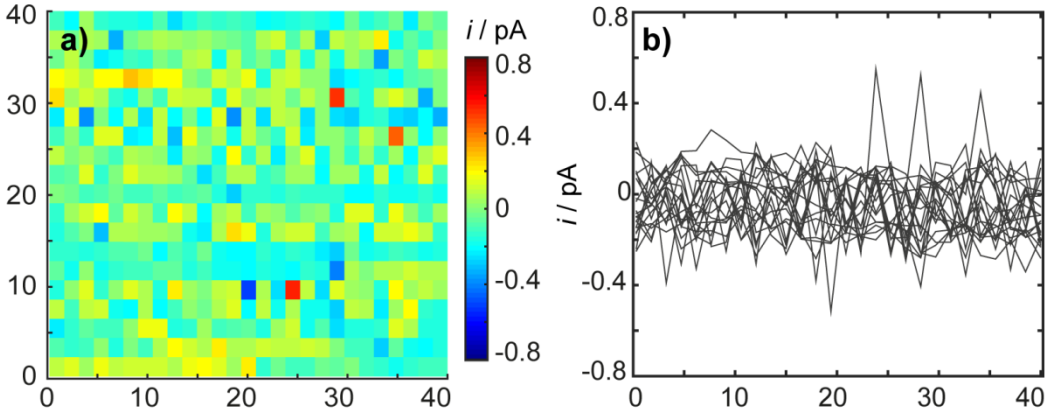

Figure 3.2 a) SECCM image of polycrystalline platinum in 10 mM H2SO4 at 1.15 V vs RHE. **b)** The lines plot of surface current. Each line represents the current along the x direction in the image.

currents are within three times standard deviation (3σ = 0.42 pA). Importantly, the few outliers that are present are distributed randomly, and the small variation in surface current cannot explain the patterns we observe for the Fe^{2+} oxidation (see below).

3.2.3 Fe^{2+} oxidation on platinum in perchloric acid solution

In order to probe the inherent electrochemical activity of polycrystalline platinum towards the oxidation of Fe^{2+}, without the added complexity of a strongly adsorbing anion, a perchloric acid solution was initially employed as electrolyte.

Multiple SECCM activity images for the oxidation of 2 mM $Fe(ClO_4)_2$ in 10 mM $HClO_4$ on the polycrystalline platinum were obtained in the same area of the substrate, while holding the working electrode surface at potentials ranging from 0.80 V (close to the onset potential) to 1.45 V (mass transport limited potential) based on the macroscopic CVs in Figure 3.1a.

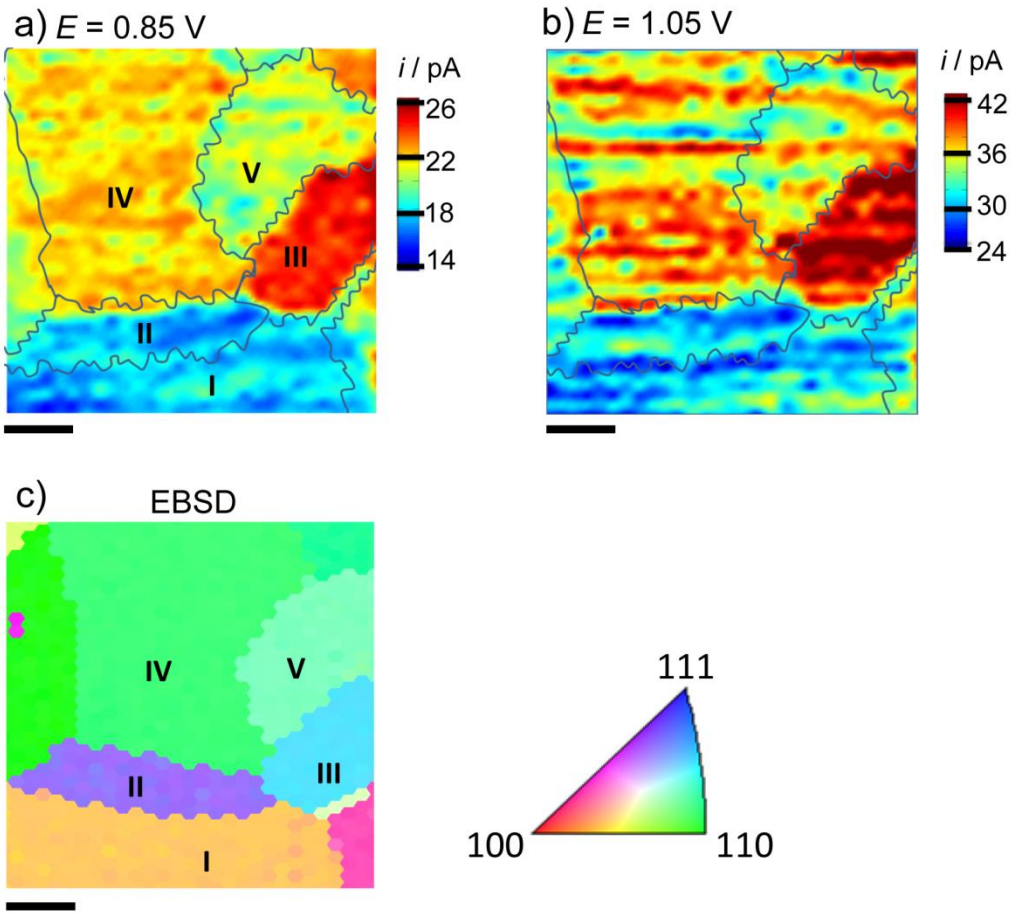

Figure 3.3 a-b) Representative SECCM images of the oxidation of 2 mM Fe^{2+} to Fe^{3+} in 10 mM $HClO_4$ at 0.85 V and 1.05 V vs. RHE. The five grains in the scanned regions are labelled "I", "II", "III", "IV" and "V". The boundaries between the grains deduced from EBSD are marked with blue lines to guide the eye. **c)** Corresponding EBSD image (tilted roughly 10° in the *xy* plane compared to the SECCM images) with the colour coded orientation map of the scanned area. The scale bars are 10 μm.

Two representative SECCM activity images of one area of the platinum surface at 0.85 and 1.05 V are shown in Figure 3.3a and Figure 3.3b, with the corresponding EBSD image of the same area in Figure 3.3c. Five regions, each with different activity, can be identified in the SECCM image, and are labelled in

Table 3-1. Surface orientations of areas marked in Figure 3.3

Grain	Approximate Miller index	Description
I	(13 5 1)	Mixed (100) and (110) character
II	(211)	(100) sites separated by short (111) terraces
III	(221)	(110) sites separated by short (111) terraces
IV	(771)	Mainly (110) character
V	(651)	Mainly (110) character

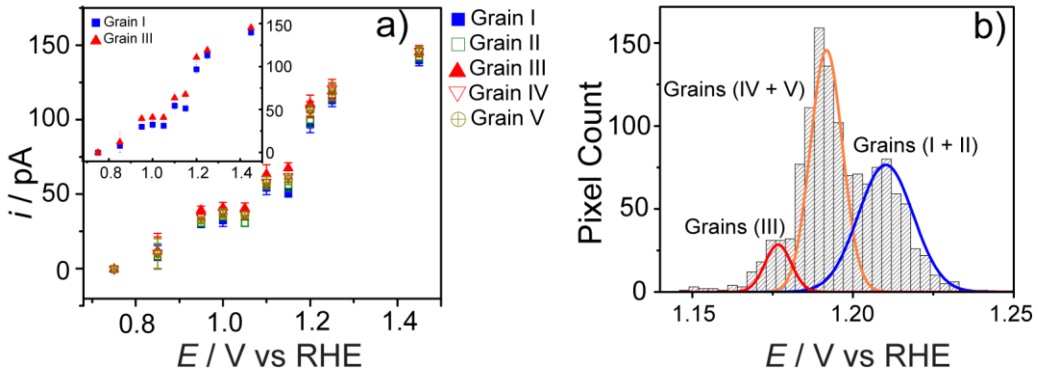

Figure 3.4 a) *I-E* curves of electrochemical current as a function of applied surface potential for 2 mM $FeClO_4$ in 10 mM $HClO_4$. The current is the average from regions of the SECCM images where grains were identified. Inset shows the *I-E* curves for grain "I" and grain "III" for clarity. **b)** Histogram of apparent half-wave potentials from spatially resolved *I-E* data at individual pixels in a series of SECCM images. Corresponding grains are labelled on the image.

Figure 3.3a (I-V). The relative activity of these regions (based on the surface current magnitude) is as follows: III > IV > V > II ≈ I. In addition, some variation in activity can be observed within individual regions.

Comparing the EBSD and SECCM maps, it is evident that the regions of distinctly different electrochemical activity correspond to particular grain structure

by EBSD (Table 3-1). Notably, grains which have substantial (110) character (grains III, IV, and V) generally appear more active than grains having more (100) and (111) character (grains I and II).

Upon closer inspection, there are variations in activity for the grains having mainly (110) character (III-V), with the most active grain (grain III) having some (111) character. This structure-dependent relative activity was evident at all investigated potentials and highlights that, on polycrystalline platinum, the Fe^{2+}/Fe^{3+} reaction rate is strongly structure-dependent at the microscopic level.

The impact of structure on electrochemical reaction rate is summarised quantitatively in Figure 3.4a, which shows the average surface current of the designated grain areas marked in Figure 3.3a, extracted from a series of SECCM activity maps, as a function of the electrode potential. From these current-potential (*I-E*) plots, it is evident that the surface current for all grains increases with the increasing potential (increasing driving force) as expected, based on macroscopic CV measurements on polycrystalline platinum (Figure 3.1a), but is evidently grain-dependent. Note, particularly, that the relative activities between different grains are consistent throughout the entire potential range. Grain III, which has (110) sites, exhibits the highest activity at all potentials while grain II, which has (100) sites separated by short (111) terraces, exhibits the lowest activity at all potentials. Grains IV and V show intermediate activity between these two extremes, as highlighted above.

Single-crystal study of Fe^{2+} oxidation in perchloric acid medium

Reactivity trends deduced from SECCM on the microcrystalline grains might reflect the relative reactivity of single-crystal electrodes. In order to verify this, CVs

on low index platinum basal plane single-crystal electrodes in the absence and presence of $Fe(ClO_4)_2$ in perchloric acid solution were recorded. All single-crystal measurements were performed on bead-type single-crystal electrodes between 1 mm and 3 mm diameter, prepared according to Clavilier's method.[51] Prior to each experiment, the electrodes were flame annealed and allowed to cool down in a hydrogen/argon mixture (*ca.* 3:1) after which they were transferred to the electrochemical cell under the protection of a droplet of deoxygenated ultra-pure water. A piece of platinum foil and a reversible hydrogen electrode (connected via a Luggin capillary) were employed as counter and reference electrode, respectively. All glassware was cleaned by boiling in a 1:1 mixture of nitric acid and sulfuric acid, followed by repeated boiling in ultra-pure water.

Typical CVs for three basal Pt facets are shown in Figure 3.5. To limit damage to the single-crystal electrodes, due to irreversible oxide formation and reduction, the positive potential limit was restricted to 0.95 V and 1.2 V in the Figure 3.5a and b, respectively.

The CV characteristics in perchloric acid for Pt basal planes have been described extensively in literature.[52] For the electrodes used in this work, Pt(111)has two distinct voltammetric features. The broad peak, 0.1 ~ 0.4 V, corresponds to the hydrogen adsorption/desorption and the peaks at 0.6 ~ 0.8 V are the reversible adsorption/desorption of hydroxyl species. Pt(100) has clear hydrogen adsorption features at potentials between 0.2 and 0.4 V and the peak at 0.6 V corresponding to OH adsorption. For Pt(110), hydrogen adsorption give two sharp peaks and the oxide formation is formed at a higher potential. The features are consistent with CVs for

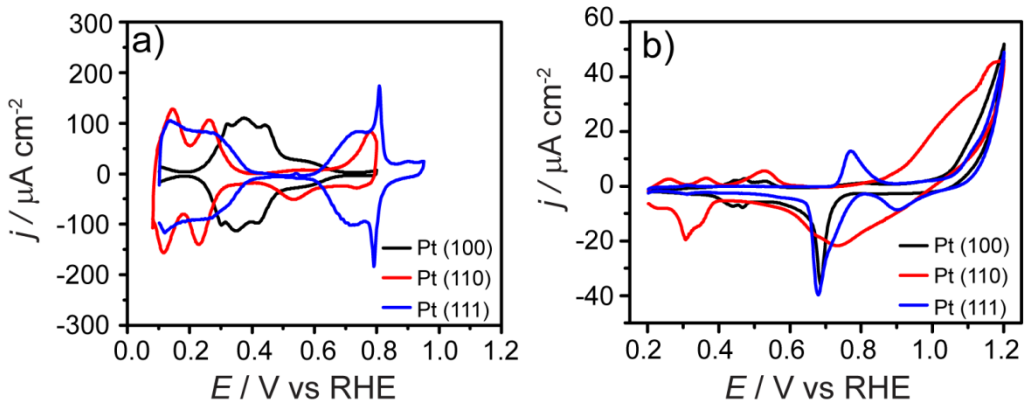

Figure 3.5 Cyclic voltammograms on Pt(111) (blue line), Pt(100) (black line) and Pt(110) electrode (red line) in **a)** only 10 mM $HClO_4$ and **b)** 2 mM $Fe(ClO_4)_2$ and 10 mM $HClO_4$. Sweep rates were 100 (left) and 10 mV s^{-1} (right) respectively.

these electrodes in literature,[52,53] confirming the quality of these single-crystals. Using these electrodes, CVs for Fe^{2+} oxidation were recorded and shown in Figure 3.5b.

In the presence of Fe^{2+}, the upper-potential limit is increased to 1.2 V. The focus is features appearing at potentials above 0.9 V, where Fe^{2+} oxidation is the main reaction. Within the potential window shown in Figure 3.5b, Fe^{2+} oxidation on Pt(110) is clearly visible with an onset potential of *ca.* 0.75 V. On Pt(111) and Pt(100) the oxidation of Fe^{2+} starts at *ca.* 0.95 V, right below the anodic potential limit. Interestingly, this variation in onset potentials for Fe^{2+} oxidation closely mirrors the variations in the potentials of zero total charge (pztc) for the basal planes of platinum at pH 2, with a pztc of 0.23 V vs. RHE for Pt (110) and 0.44 V and 0.43 V for Pt (111) and Pt (100), respectively.[54] This correspondence may suggest that the structure-sensitive activity for the oxidation of Fe^{2+} originates from variations of pztc, which strongly affects the double layer.[40,41]

Thus, it is evident that the single-crystal findings are qualitatively consistent

with the trend in reactivity obtained from SECCM, confirming the validity of the SECCM approach. However, it is important to note that the variation between the electrochemical activities of single-crystal basal planes is much more pronounced than the variations between the different grains on the polycrystalline substrate. This is because grains on the polycrystalline substrate do not possess true basal-plane orientation, but are high-index facets with contributions of all three basal planes. Some variation in orientation within a single grain (seen as slight colour variations in Figure 3.3c) may also be attributed to the variation of surface current within the individual grains (Figure 3.3a-b). On the other hand, a very positive outcome of the EBSD study, coupled with SECCM is that high-index facets can readily be investigated; such faces are extremely difficult to prepare and maintain as macroscopic single-crystals.

The variations in reactivity in the SECCM images can further be analysed quantitatively on a point-by-point basis. For each of the 1271 measurement points in an image, individual *I-E* curves were constructed (*i.e.* 1271 *I-E* curves, each with 10 points), and the half-wave potential corresponding to 75 pA (half the mass transport limited current) for each *I-E* curve was extracted. The distribution of these apparent half-wave potentials is shown in Figure 3.4b, and can be deconvoluted into three prominent individual Gaussian distributions centred around 1.21, 1.19 and 1.18 V. Although the differences in half-wave potentials is small, they are statistically significant at a 90% confidence level (Z-test, with Z-scores are 1.92 for the first and second distributions and 1.86 for the second and third distributions). Based on the number of counts in each distribution, as well as the relative activity of the grains, the distribution centred on 1.21 V was assigned to grains I and II, the distribution around 1.19 V to grains IV and V, and the distribution around 1.18 V to grain III. It is

worthwhile noting that the variation in apparent half-wave potentials, spans for 0.03 V, which might be considered relatively small, but is readily detected in the SECCM experiments.

Estimation of k^0 Values for Individual Grains

The standard electron transfer rate constants (k^0) for $Fe^{2+/3+}$ in perchlorate at the individual grains can be estimated by considering the apparent half-wave potential and the mass transport rate in the SECCM measurement. The mass transport coefficient (k_t) is related to the mass transport limiting current (i_{lim}) according to equation (3-1):

$$i_{\text{lim}} = nFAk_t c^0 \tag{3-1}$$

where n is number of electrons (n = 1), A is the area of the electrode ($A = 1.77 \times 10^{-8}$ cm^{-2}, based on a pipette diameter of 1.5 μm), F is the Faraday constant ($F = 9.649 \times 10^4$ C mol^{-1}) and c^0 is the bulk concentration of reactant species (c^0 = 2 μmol cm^{-3}). For Fe^{2+} oxidation in perchlorate, the mass transport limited current is 150 pA (Section 3.2.3, Figure 3.4a), corresponding to k_t = 0.044 cm s^{-1}.

For a steady-state electron transfer process, the net flux of reactant species towards the electrode is balanced by the reaction rate at the surface, as given by equation (3-2):

$$k_t(c^0 - c_s) = k_r c_s \tag{3-2}$$

In this equation, the net flux of reactant species is given by the product of the mass transport rate constant and the difference between the bulk concentration (c^0) and the

concentration near the electrode surface (c_s). Similarly, the reaction rate at the surface is the product of the (potential-dependent) reaction rate constant (k_r) and c_s.

Finally, the potential dependency of k_r for an irreversible electron transfer process can be described through a simplified Butler-Volmer relationship (equation (3-3)):

$$k_r = k^0 e^{((1-\alpha)F(E-E^{0'})/RT)} \quad (3\text{-}3)$$

where k^0 is the electron transfer rate constant, $(1-\alpha)$ is the transfer coefficient ($(1-\alpha) = 0.5$),[55] E is the applied potential, $E^{0'}$ is the formal potential of the redox couple ($E^{0'} = 0.9$ V vs RHE for $Fe^{2+/3+}$; see above), F is Faraday constant (96,485 C mol^{-1}), R is the gas constant ($R = 8.314$ J K^{-1} mol^{-1}) and T is temperature ($T = 298$ K).

At the half-wave potential, the surface concentrations of Fe^{2+} and Fe^{3+}can reasonably considered equal, and thus c_s is considered to be half of the bulk concentration, or 1.0 μmol cm^{-3}. In section 3.2.3, half-wave potentials of 1.18 V, 1.19 V and 1.21 V were reported for the different grains (see above). By combining equations (3-2) and (3-3), and solving for k^0, electron transfer rate constants of 1.9×10^{-4} cm s^{-1}, 1.6×10^{-4} cm s^{-1}, and 1.1×10^{-4} cm s^{-1}, are deduced for grains III , IV + V and I + II, respectively.

These values fall within the wide range of k^0 values previously reported for the $Fe^{2+/3+}$ couple on platinum in perchloric acid electrolyte, which vary from ~10^{-5} cm s^{-1} [56] to ~10^{-3} cm s^{-1}.[55] This wide range has been ascribed to the strong sensitivity of the $Fe^{2+/3+}$ couple towards the state of the electrode surface, which can be impacted by variations in surface roughness and the presence of trace contaminants (such as strongly adsorbing anions).[56,57]

It is important to point out that the local variation in activity visualised by

SECCM would have some impact on macroscopic CV measurements of heterogeneous ET on polycrystalline platinum. Electrode kinetic measurements on polycrystalline platinum tend to implicitly assume a uniform electrode surface[43,44,58,59] and evidently, at least for the case of Fe^{2+}/Fe^{3+} (and, as shown in later chapters, other reactions), this is not always appropriate.

Atomic force microscopy (AFM) image of platinum foil

In order to exclude the possibility that surface currents observed in the SECCM images were due to changes in wettability of the scanning droplet across the grains, the surface roughness of the Pt foil was analysed, used in the study, with AFM. A typical AFM image of the platinum foil used in this study is shown in Figure 3.6. The average roughness across the surface (R_a) is 5.5 ± 0.5 nm (1 σ) with

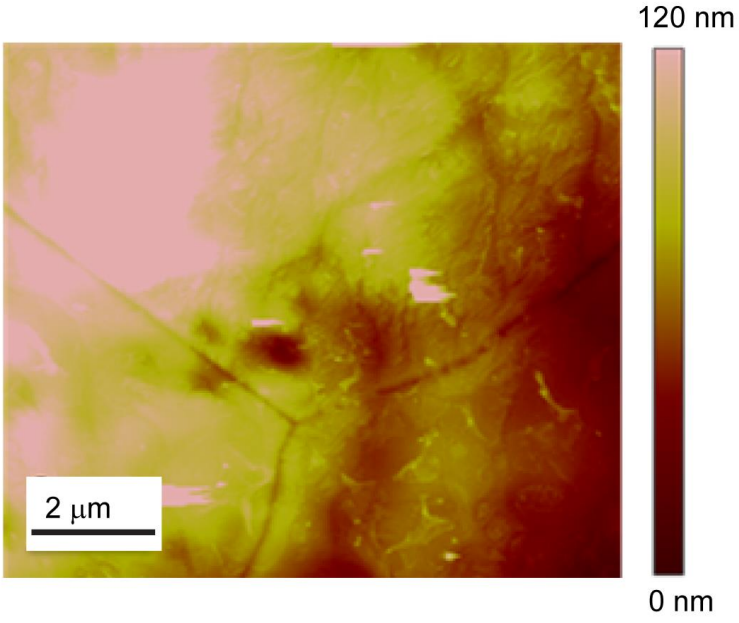

Figure 3.6 AFM image of a platinum foil containing three grains and grain boundaries.

negligible difference of surface roughness among different grains. While the exact measurement of the grain boundary width is complicated due to possible tip convolution effects in AFM, analysis of Figure 3.6 yields an upper limit of ~50 nm for the grain boundary width, which was used for the analysis below.

SECCM Image of $FcTMA^+$ Oxidation in Sulfuric Acid

To further verify that variations in wetting were negligible in the SECCM results, a control experiment was performed on a polycrystalline Pt foil for the oxidation of 1 mM $FcTMA^+$ (ferrocenylmethyltrimethylammonium$^+$), a classical outer-sphere redox mediator. Figure **3.7** shows a typical SECCM image of $FcTMA^+$ oxidation on the polycrystalline platinum foil at a surface potential of + 0.85 V vs. RHE (half-wave potential). The pipette dimensions were similar to those for the Fe^{2+} oxidation studies (~ 1.5 μm diameter). It can be seen that the surface is essentially uniformly active (75 ± 1.4 pA (1 σ)), with little variation in the surface current

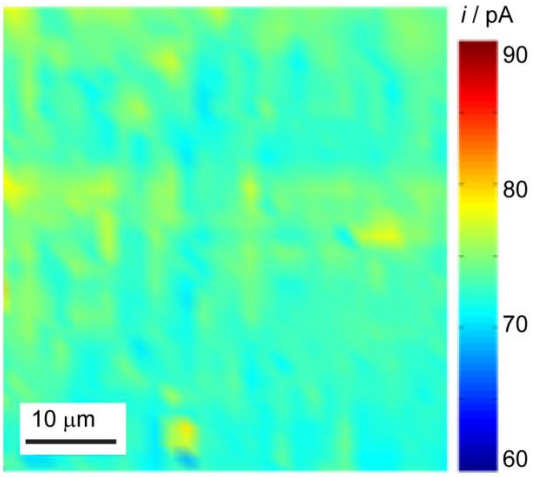

Figure 3.7 SECCM image of the oxidation of 1 mM $FcTMA^+$ in 10 mM H_2SO_4 held at a potential of + 0.85 V relative to RHE.

across the sample. Importantly no grain-structure dependent features can be observed, confirming that the electrochemical current detected in ferrous system does not relate to variations in wetting.

3.2.4 Fe^{2+} oxidation in sulfate medium

SECCM imaging of Fe^{2+} oxidation in sulfate medium

To investigate the possible role of anion adsorption, the Fe^{2+} oxidation on polycrystalline platinum in sulfuric acid was examined, in which sulfate anions absorb specifically.[60] It has been suggested previously that sulfate, or other specifically adsorbed anions (such as Cl^- and Br^-), can facilitate Fe^{2+} oxidation by acting as a bridge for electron transfer, or by modifying the electrical double layer.[61] Given that sulfate adsorption on platinum surfaces is facet sensitive,[62,63] one might expect that the activity for Fe^{2+} oxidation could be affected accordingly.

Eight SECCM electrochemical activity maps for the oxidation of 1 mM Fe^{2+} in 10 mM H_2SO_4 were obtained by holding the surface at potentials ranging from 0.80 V to 1.35 V, based on macroscopic CVs (Figure 3.1a). Figure 3.8a and b show two representative SECCM activity maps at 0.85 and 1.05 V. The corresponding EBSD map for the area imaged with SECCM is shown in Figure 3.8c. From the EBSD map, it can be seen that most of the grains within the area investigated have a significant contribution of (110) orientation with a fraction of grains with a main contribution from (100) orientation. Although the imaged area does not include all basal planes, some striking features are exhibited. By comparing the EBSD and SECCM maps, it is clearly evident that a correlation exists between structure and

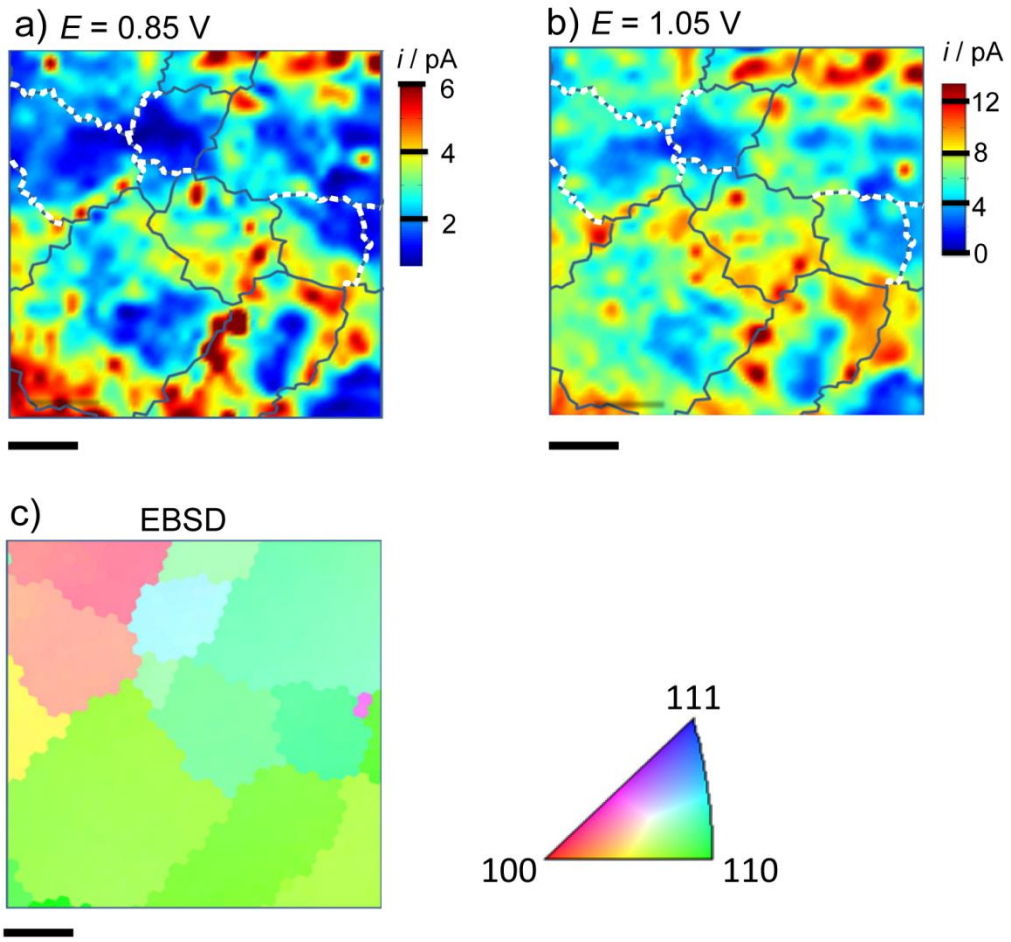

Figure 3.8 a-b) SECCM images of the oxidation of 1 mM Fe^{2+} to Fe^{3+} in 10 mM H_2SO_4 at 0.85 V and 1.05 V vs. RHE. Grain boundaries (from EBSD) are marked with either black lines (boundaries at which an enhanced current was observed) or white dotted lines (with no enhanced current) to guide the eye. **c)** Corresponding EBSD image and surface orientation of the same area. The scale bars are 10 μm.

activity in sulfuric acid, but it is that the activity of the surface is strongly dominated by grain boundaries, with the grains themselves also having some lower activity. This pattern of activity is in stark contrast with the results in the non-adsorbing perchlorate medium where no enhanced activity was detectable at the boundaries between the crystalline grains.

Closer inspection of the maps in Figure 3.8 further highlights that while some

grain boundaries exhibit a strongly enhanced activity, this is not generally true of all grain boundaries. Indeed, grain boundaries deduced from the EBSD map, and marked with white dotted lines on the SECCM maps, do not display enhanced activity in any of the eight images at the wide range of potentials covered. These electrochemically 'invisible' boundaries encompass grains closer to the (100) orientation while the more active grain boundaries are those that encompass grains close to the (110) orientation, indicating that there may be an effect of the character of the grain boundary itself.

Single-crystal study of Fe^{2+} oxidation in sulfate medium

Similarly with study in perchloric acid, CVs of the three Pt basal planes in sulfuric acid were shown in Figure 3.9a, and a brief discussion is provided herein. Starting with Pt(111), the CV at this electrode has three well-defined potential regions, corresponding to H_{upd} (0.1 ~0.4 V), sulfate adsorption (0.4 ~ 0.6 V) and OH adsorption (0.8 ~ 1.1 V), respectively. The CV for Pt(100) has two main peaks at 0.25 and 0.4 V, ascribed to the coupled process of hydrogen and bisulfate adsorption. For Pt(110), the main feature is the hydrogen adsorption peak. Again, these CVs illustrate clean and well-defined Pt basal plane surfaces. CVs in the presence of Fe^{2+} were shown in Figure 3.9b. At all three electrodes, Fe^{2+} oxidation give new notable peaks centred at ~ 1.0 V. Despite the different current densities (due to the different scan rates) compared to the blank experiment, the CVs in the presence of Fe^{2+} kept all features presented in the control experiment (without Fe^{2+}). Clearly, the presence of Fe^{2+} does not affect the adsorption of other species. More importantly, different

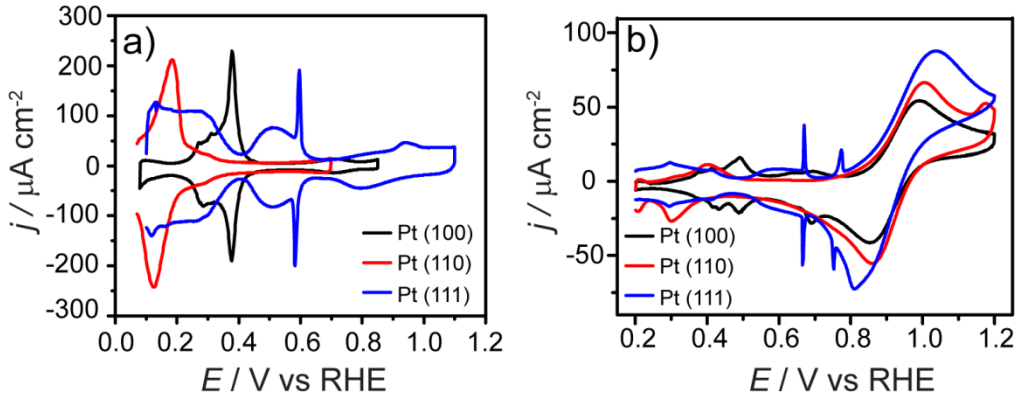

Figure 3.9 Cyclic voltammograms of Pt(111) (blue line), Pt(100) (black line) and Pt(110) electrode (red line) *vs* RHE in **a)** only 10 mM H_2SO_4 and **b)** 2 mM $FeSO_4$ and 10 mM H_2SO_4. Sweep rates were 100 mV s^{-1} (left) and 10 mV s^{-1} (right) respectively.

from results in perchloric acid medium, CVs of the $Fe^{2+/3+}$ redox reaction in sulfate medium on basal plane single-crystal electrodes (Figure 3.9) show minimal differences in activity between basal planes in the potential region for the oxidation of Fe^{2+}, which is in agreement with the SECCM findings for the areas within the grains, which show more or less similar activities. The differences in peak currents for the single-crystal measurements may be attributed to the variations in oxide formation on different facets which inhibit the oxidation of Fe^{2+}.[45] The important point here, however, is that single-crystal measurements cannot reveal any electrochemical information on the grain boundaries, emphasizing a key advantage of SECCM for probing the electrochemical response of complex materials at high resolution, in this case the boundaries between crystalline grains.

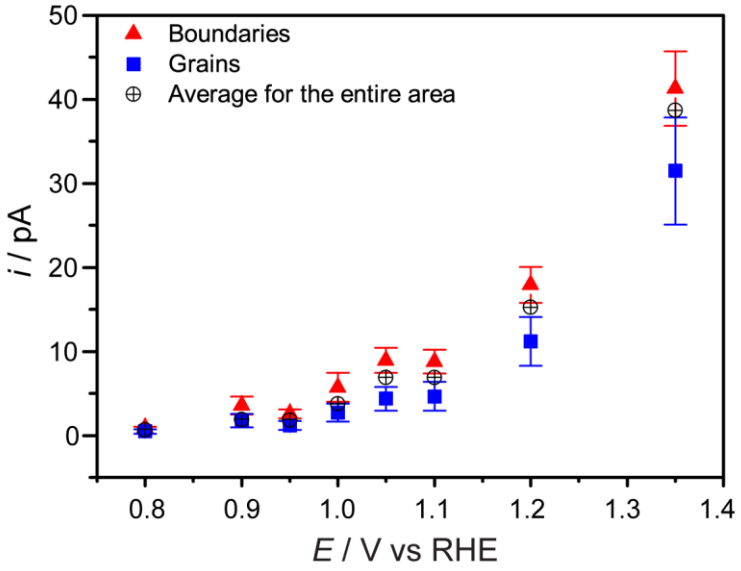

Figure 3.10 *I-E* curves for 1 mM $FeSO_4$ in 10 mM H_2SO_4. The current was obtained by averaging the current from regions of the SECCM images where grain boundaries (▲) and regions within the boundaries (■) were identified. Similarly, an *I-E* curve for the average current over the entire scanned region (including all grains and boundaries) is also shown (⊕) for comparison.

The differences between the activity of grains and grain boundaries can be seen in the *I-E* plots in Figure 3.10, constructed for these different areas from analysis of images at various potentials, from the onset potential to approaching the mass transport limited potential. As in the case of perchlorate, the trend of surface current increase with the increase of the potential (driving force) is clearly seen for both grain boundary areas and areas within grains, but grain boundary areas show higher activity at all potentials. These findings highlight clearly that certain grain boundaries exhibit a strongly enhanced activity towards Fe^{2+} oxidation. A further understanding of the structure of these boundaries and their role in surface reactivity would be beneficial, not only for Fe^{2+} oxidation, but for other surface dependent reactions as well.

Although uncertainty in the size of the grain boundary prevents a full kinetic analysis, an estimate of the grain boundary activity can be made. Between 0.85 V and 1.20 V, the SECCM current when probing at active boundaries is about twice of that in the neighbouring grains. This increase in current can be ascribed to the presence of a grain boundary. However, because the grain boundary is smaller than the meniscus size (1.5 μm diameter), for measurements performed at a boundary, the resulting current is a combination of the activities of the grain boundary and the simultaneously probed grains, resulting in a weighted average of the two. Analysis of the AFM image (Figure 3.6) of a polycrystalline Pt foil yielded an estimated upper limit of grain boundary width of ~ 50 nm (Section 0, Figure 3.6), which accounts for about 4 % of the area encompassed under the 1.5 μm diameter SECCM pipette. This suggests that the grain boundaries are at least 30 fold more active than the areas within the grain.

An important feature of SECCM is that the facilitated migration current across the meniscus at the end of the tip, between the two QRCEs, also enhances mass transport of charged species to and from the substrate of investigation. The mass transport coefficient for an electrode in SECCM is estimated[25] to be about 10-20 times higher than in macroscale measurements and this leads to a much more drawn out current-voltage response in SECCM (Figure 3.10). The same effect on the shape of the wave can be seen for the perchlorate medium when inspecting the macroscale CV. However, the SECCM assisted mass transport rate depends on the charge of the species in solution and on the magnitude of the migration current. Thus, when examining the SECCM results for perchlorate and sulfate media side by side, differences in mass transport of the systems and Fe^{2+} concentration (1 mM and 2 mM for the sulfate and perchlorate, respectively) need to be taken into consideration.

The transport limited current in perchlorate (Figure 3.4a at 1.45 V) is about four times higher than observed in sulfate medium (Figure 3.10 at 1.35 V). This is due to the different concentrations used and differences in mass transport coefficients for the two electrolytes, which depends on speciation (e.g. ion pairing) and the potential bias between the QRCEs. In the sulfate medium, the dominant species is $FeHSO_4^+$ (with some Fe^{2+}, $FeSO_4$ and $FeH_2SO_4^-$), whereas in the perchlorate medium Fe^{2+} and Fe^{3+} remain largely free.[64,65] Regardless, the main point is the significantly different patterns of local activity for the $Fe^{2+/3+}$ couple in the two media at polycrystalline platinum, that are readily revealed for the first time by SECCM.

3.3 Conclusions

Conventional macroscopic electrochemical measurements at polycrystalline metal electrodes, such as platinum, have tended to implicitly assume a uniformly active surface. The studies presented herein show that this is not a reasonable assumption for polycrystalline platinum, at least for the $Fe^{2+/3+}$, a simple one electron transfer system. Indeed, considering heterogeneous electron transfer (ET) rates to be uniform across a polycrystalline surface may not only lead to misinterpretation of kinetic data, but also ignores subtle electrode structure effects which are essential to gaining a deeper understanding of fundamental electrochemical processes. Such effects are readily revealed by SECCM, which provides a powerful approach for visualising electrode activity.

By comparing the activity of individual grains, deduced by SECCM, to grain structure from EBSD images, it is found that the electrochemical oxidation of Fe^{2+} is sensitive to the platinum surface orientation, regardless of the supporting electrolyte.

Moreover, this work established that grain boundaries can play an important role in this rather complex electrochemical process.

The main features of the SECCM technique in the present application are that: (i) it allows 'pseudo-single crystal' experiments (in individual grains of a polycrystalline sample with high-index facets and grain boundaries) owing to the spatial confinement of the electrochemical cell; (ii) it allows access to fast surface kinetic effects owing to the higher mass transport rates generated; and (iii) it enhances the resolution with respect to competing processes (such as surface oxidation) with the ability to fine-tune the time regime in which measurements are made. Thus, Fe^{2+} oxidation in perchlorate medium was found to exhibit variations in rate (current) depending on the crystallographic orientation of the microcrystalline grain, with a trend that could be rationalised to a large extent based on CVs obtained on basal plane (low index) single-crystal electrodes. In contrast, in sulfate medium, boundaries between grains exhibited significantly higher reactivity (at least an order of magnitude) compared to the areas within grains.

The studies herein provide a platform for further investigation of polycrystalline electrode materials, particularly for those of electrocatalytic relevance. More generally, the data presented have major implications for the investigation and analysis of electrochemical processes by macroscopic techniques, which evidently average the reactivity over many different types of surface sites. SECCM provides a means of probing individual sites effectively and unambiguously.

3.4 References

(1) Bard, A. J. *J. Am. Chem. Soc.* **2010**, *132*, 7559.

(2) Somorjai, G. A. *Science* **1985**, *227*, 902.

(3) Marković, N. M.; Ross Jr, P. N. *Surf. Sci. Rep.* **2002**, *45*, 117.

(4) Laoire, C. O.; Mukerjee, S.; Abraham, K. M.; Plichta, E. J.; Hendrickson, M. A. *J. Phys. Chem. C* **2009**, *113*, 20127.

(5) Kato, H.; Asakura, K.; Kudo, A. *J. Am. Chem. Soc.* **2003**, *125*, 3082.

(6) Arico, A. S.; Bruce, P.; Scrosati, B.; Tarascon, J.-M.; van Schalkwijk, W. *Nature Mater.* **2005**, *4*, 366.

(7) Lee, S. W.; Chen, S.; Suntivich, J.; Sasaki, K.; Adzic, R. R.; Shao-Horn, Y. *J. Phys. Chem. Lett.* **2010**, *1*, 1316.

(8) Couper, A. M.; Pletcher, D.; Walsh, F. C. *Chem. Rev.* **1990**, *90*, 837.

(9) Lee, I.; Morales, R.; Albiter, M. A.; Zaera, F. *Proc. Natl. Acad. Sci. U. S. A.* **2008**, *105*, 15241.

(10) Sherigara, B. S.; Kutner, W.; D'Souza, F. *Electroanalysis* **2003**, *15*, 753.

(11) Rabis, A.; Rodriguez, P.; Schmidt, T. J. *ACS Catal.* **2012**, *2*, 864.

(12) Antolini, E. *Energy Environ. Sci.* **2009**, *2*, 915.

(13) Climent, V.; Feliu, J. M. *J. Solid State Electrochem.* **2011**, *15*, 1297.

(14) Koper, M. T. M. *Nanoscale* **2011**, *3*, 2054.

(15) Cherstiouk, O. V.; Gavrilov, A. N.; Plyasova, L. M.; Molina, I. Y.; Tsirlina, G. A.; Savinova, E. R. *J. Solid State Electrochem.* **2008**, *12*, 497.

(16) Maillard, F.; Savinova, E. R.; Stimming, U. *J. Electroanal. Chem.* **2007**, *599*, 221.

(17) König, U.; Davepon, B. *Electrochim. Acta* **2001**, *47*, 149.

(18) Schultze, J. W.; Pilaski, M.; Lohrengel, M. M.; Konig, U. *Faraday Discuss.* **2002**, *121*, 211.

(19) Dudin, P. V.; Snowden, M. E.; Macpherson, J. V.; Unwin, P. R. *ACS Nano* **2011**, *5*, 10017.

(20) Heller, I.; Kong, J.; Heering, H. A.; Williams, K. A.; Lemay, S. G.; Dekker, C. *Nano Lett.* **2004**, *5*, 137.

(21) Patten, H. V.; Meadows, K. E.; Hutton, L. A.; Iacobini, J. G.; Battistel, D.; McKelvey, K.; Colburn, A. W.; Newton, M. E.; Macpherson, J. V.; Unwin, P. R. *Angew. Chem. Int. Ed.* **2012**, *51*, 7002.

(22) Day, T. M.; Unwin, P. R.; Macpherson, J. V. *Nano Lett.* **2006**, *7*, 51.

(23) Williams, C. G.; Edwards, M. A.; Colley, A. L.; Macpherson, J. V.; Unwin, P. R. *Anal. Chem.* **2009**, *81*, 2486.

(24) Ebejer, N.; Schnippering, M.; Colburn, A. W.; Edwards, M. A.; Unwin, P. R. *Anal. Chem.* **2010**, *82*, 9141.

(25) Snowden, M. E.; Güell, A. G.; Lai, S. C. S.; McKelvey, K.; Ebejer, N.; O'Connell, M. A.; Colburn, A. W.; Unwin, P. R. *Anal. Chem.* **2012**, *84*, 2483.

(26) Miller, T. S.; Ebejer, N.; Güell, A. G.; Macpherson, J. V.; Unwin, P. R. *Chem. Commun.* **2012**, *48*, 7435.

(27) Güell, A. G.; Ebejer, N.; Snowden, M. E.; McKelvey, K.; Macpherson, J. V.; Unwin, P. R. *Proc. Natl. Acad. Sci. U. S. A.* **2012**, *109*, 11487.

(28) Lai, S. C. S.; Dudin, P. V.; Macpherson, J. V.; Unwin, P. R. *J. Am. Chem. Soc.* **2011**, *133*, 10744.

(29) Lai, S. C. S.; Patel, A. N.; McKelvey, K.; Unwin, P. R. *Angew. Chem. Int. Ed.* **2012**, *51*, 5405.

(30) Mirkin, M. V.; Nogala, W.; Velmurugan, J.; Wang, Y. *Phys. Chem. Chem. Phys.* **2011**, *13*, 21196.

(31) Wittstock, G.; Burchardt, M.; Pust, S. E.; Shen, Y.; Zhao, C. *Angew. Chem. Int. Ed.* **2007**, *46*, 1584.

(32) Amemiya, S.; Bard, A. J.; Fan, F.-R. F.; Mirkin, M. V.; Unwin, P. R. *Annu. Rev. Anal. Chem.* **2008**, *1*, 95.

(33) Basame, S. B.; White, H. S. *J. Phys. Chem.* **1995**, *99*, 16430.

(34) Bath, B. D.; Lee, R. D.; White, H. S.; Scott, E. R. *Anal. Chem.* **1998**, *70*, 1047.

(35) Albery, J. *Electrode Kinetics*; Oxford University Press, June 5, 1975.

(36) McCreery, R. L. *Chem. Rev.* **2008**, *108*, 2646.

(37) Chen, P.; Fryling, M. A.; McCreery, R. L. *Anal. Chem.* **1995**, *67*, 3115.

(38) Samec, Z. *J. Electrochem. Soc.* **1999**, *146*, 3349.

(39) Nagy, Z.; Curtiss, L. A.; Hung, N. C.; Zurawski, D. J.; Yonco, R. M. *J. Electroanal. Chem.* **1992**, *325*, 313.

(40) Fawcett, W. R. *Electrochim. Acta* **1997**, *42*, 833.

(41) Fawcett, W. R.; Fedurco, M.; Kováčová, Z. *J. Electrochem. Soc.* **1994**, *141*, L30.

(42) Hromadova, M.; Fawcett, W. R. *J. Phys. Chem. A* **2001**, *105*, 104.

(43) Bochmann, H. G.; Vielstich, W. *Electrochim. Acta* **1988**, *33*, 805.

(44) Rodriguez-Lopez, J.; Bard, A. J. *J. Am. Chem. Soc.* **2010**, *132*, 5121.

(45) Rodríguez-López, J.; Minguzzi, A.; Bard, A. J. *J. Phys. Chem. C* **2010**, *114*, 18645.

(46) Angerstein-Kozlowska, H.; Conway, B. E.; Sharp, W. B. A. *J. Electroanal. Chem. Interfacial Electrochem.* **1973**, *43*, 9.

(47) Schouten, K. J. P.; van der Niet, M. J. T. C.; Koper, M. T. M. *Phys. Chem. Chem. Phys.* **2010**, *12*, 15217.

(48) Imai, H.; Izumi, K.; Matsumoto, M.; Kubo, Y.; Kato, K.; Imai, Y. *J. Am. Chem. Soc.* **2009**, *131*, 6293.

(49) Güell, A. G.; Ebejer, N.; Snowden, M. E.; Macpherson, J. V.; Unwin, P. R. *J. Am. Chem. Soc.* **2012**, *134*, 7258.

(50) Inzelt, G.; Berkes, B. B.; Kriston, Á. *Pure Appl. Chem.* **2011**, *83*, 269.

(51) Clavilier, J.; Armand, D.; Sun, S. G.; Petit, M. *J. Electroanal. Chem. Interfacial Electrochem.* **1986**, *205*, 267.

(52) Marković, N. M.; Adžić, R. R.; Cahan, B. D.; Yeager, E. B. *J. Electroanal. Chem.* **1994**, *377*, 249.

(53) Marković, N. M.; Ross, P. N., Jr *Surf. Sci. Rep.* **2002**, *45*, 117.

(54) Garcia-Araez, N.; Climent, V.; Feliu, J. *J. Phys. Chem. C* **2009**, *113*, 9290.

(55) Angell, D. H.; Dickinso.T *J. Electroanal. Chem.* **1972**, *35*, 55.

(56) Weber, J.; Samec, Z.; Marecek, V. *J. Electroanal. Chem.* **1978**, *89*, 271.

(57) Galizzio, D.; Trasatti, S. *J. Electroanal. Chem.* **1973**, *44*, 367.

(58) Bockris, J. O. M.; Mannan, R. J.; Damjanovic, A. *J. Chem. Phys.* **1968**, *48*, 1898.

(59) Łosiewicz, B.; Jurczakowski, R.; Lasia, A. *Electrochim. Acta* **2012**, *80*, 292.

(60) Kunimatsu, K.; Samant, M. G.; Seki, H. *J. Electroanal. Chem. Interfacial Electrochem.* **1989**, *258*, 163.

(61) Johnson, D. C.; Resnick, E. W. *Anal. Chem.* **1977**, *49*, 1918.

(62) Nart, F. C.; Iwasita, T.; Weber, M. *Electrochim. Acta* **1994**, *39*, 2093.

(63) Mostany, J.; Herrero, E.; Feliu, J. M.; Lipkowski, J. *J. Phys. Chem. B* **2002**, *106*, 12787.

(64) Gil, A. F.; Salgado, L.; Galicia, L.; González, I. *Talanta* **1995**, *42*, 407.

(65) Sutton, J. *Nature* **1952**, *169*, 71.

Chapter Four

High Resolution Mapping of Oxygen Reduction Reaction Kinetics at Polycrystalline Platinum Electrodes

Abstract

The scanning droplet-based technique, scanning electrochemical cell microscopy (SECCM), combined with electron backscatter diffraction (EBSD), is demonstrated as a powerful approach for visualizing surface structure effects on the rate of the oxygen reduction reaction (ORR) at polycrystalline platinum electrodes. Elucidating the effect of electrode structure on the ORR is of major interest in connection to electrocatalysis for energy-related applications. The attributes of the approach herein stem from: (i) the ease with which the polycrystalline substrate electrode can be prepared; (ii) the wide range of surface character open to study; (iii) the possibility of mapping reactivity within a particular facet (or grain), in a *pseudo-single-crystal* approach, and acquiring a high volume of data as a consequence; (iv) the ready ability to measure the activity at grain boundaries; and (v) an experimental arrangement (SECCM) that mimics the three-phase boundary in low temperature fuel cells. The kinetics of the ORR was analysed and a finite element method model was developed to explore the effect of the three-phase boundary, in particular to examine pH variations in the droplet and the differential transport rates of the reactants and products. A significant variation of activity across the platinum substrate was found, inherently linked to the crystallographic orientation, but do not

detect any enhanced activity at grain boundaries. Grains with (111) and (100) contributions exhibit considerably higher activity than those with (110) and (100) contributions. These results, which can be explained by reference to previous single-crystal measurements, enhance the understanding of ORR structure-activity relationships on complex high-index platinum surfaces, and further demonstrate the power of high resolution flux imaging techniques to visualise and understand complex electrocatalyst materials.

Chapter 4

4.1 Introduction

The oxygen reduction reaction (ORR) is a key reaction in low temperature fuel cells[1-3] and lithium-air batteries,[4,5] and is arguably a major limiting factor, at least from a scientific point of view, to the widespread adoption of these technologies. However, even on the best catalysts (Pt and Pt-based materials), the ORR suffers from sluggish kinetics and requires a high overpotential. The mechanism and kinetics of the ORR on Pt have been studied[6-8] to understand the cause of the sub-optimal performance and to identify strategies to optimise the catalytic properties of Pt surfaces.[9-11] A common strategy is to identify the most efficient surface structure for the ORR and then try to expose these micro- or nano-structures in the catalysts.[10] To do this, knowledge of the structure-dependence of the ORR activity is required. Previous research on a variety of Pt-based materials, spanning bulk polycrystalline electrodes,[12,13] single-crystal electrodes[14,15] and nanoparticles,[2,16] has shown that the ORR kinetics and mechanism are strongly affected by the nature and the structure of electrodes. Importantly, research on atomically well-defined single-crystal electrodes has revealed a strong crystallographic orientation dependence of the ORR activity.[9,14,17,18]

The catalytic activity of the ORR on the three basal planes of Pt has been investigated widely in different electrolytes.[19-23] In sulfuric acid, the reactivity of the Pt basal planes decreases in the order (110) > (100) > (111),[20] following the relative adsorption strength of the sulfate anion. These studies have been augmented by research on stepped Pt surfaces in the $[0\,1\,\bar{1}]$ and $[1\,\bar{1}\,0]$ zones, showing that these have higher activity than the basal planes. Recently, this has been rationalised by using the OH binding energy as a descriptor for activity, yielding a volcano-relationship.[24]

Similar relative reactivity patterns have been found in non-specific adsorbing perchlorate electrolyte, although the variation in activities is much smaller.[17,18]

While single-crystal electrodes provide valuable information on systematic trends, the availability of surfaces can be limited, with high-index surfaces particularly challenging to prepare and maintain. Furthermore, the activity of grain boundaries, which are present in real catalysts and on polycrystalline electrodes, cannot be studied on single-crystal surfaces, even though these features have been suggested to play a large role in real catalysts.[25,26] For example, as shown in Chapter 3, the $Fe^{2+/3+}$ redox process on polycrystalline platinum electrodes in sulfuric acid is dominated by grain boundaries.[27] To evaluate whether similar effects operate for the ORR, localised electrochemical measurements are needed, as reported herein.

In contrast to the extensive studies on Pt basal surfaces, and, to some extent, stepped surfaces, less is known about the ORR on high-index surfaces. However, real surfaces, as presented in bulk electrodes and nanoparticles, are usually heterogeneous in the crystallographic structure and combine different facets and surface features, such as atomic steps and kinks.[28] Moreover, some high-index surfaces, which have high densities of steps and kinks,[28] are reported to exhibit higher electrocatalytic activity than basal planes.[29,30] Therefore, more research on high-index Pt surfaces is essential to gain a better understanding of the structure sensitivity of the ORR.

The studies in this chapter draw on the *pseudo-single-crystal* approach described in Chapter 3, in which scanning electrochemical cell microscopy (SECCM)[27,31-38] is used to probe local electrochemical activity that is correlated with the local surface structure provided by electron backscatter diffraction (EBSD).[39] This approach has several key attributes. First, minimal sample preparation is

required. Second, grains of high-index orientation, which are not easily prepared as single-crystal electrodes, can be studied, and activity can be mapped within a grain, in a *pseudo-single-crystal* approach. Third, any enhanced activity at grain boundaries can be detected directly based on the scanning mode of SECCM.[27] Finally, for the ORR, SECCM provides a relevant configuration with a three-phase boundary between the solid electrode, liquid electrolyte and gaseous oxygen (air), which mimics the geometry present at the cathode of low temperature fuel cells. This configuration leads to greatly enhanced mass transport of oxygen to the electrode surface, as oxygen is not only provided through the electrolyte solution but also across the liquid-air interface to the electrode surface, while (solution-phase) reaction products can only be transported away from the electrode surface through the electrolyte solution at a slower rate. The impact of this differential mass transport between reactants and products on the ORR kinetics has only rarely been investigated,[40] but is open to study with the approach herein**.**

4.2 Results and Discussion

4.2.1 Macroscopic cyclic voltammograms (CVs) of ORR

Macroscopic cyclic voltammograms (CVs) of a polycrystalline Pt electrode recorded in aerated and nitrogen purged solutions were recorded and shown in Figure 4.1. The experiment was performed in a conventional three electrode system using a piece of Pt wire as the working electrode, with a Pd-H_2 and Pt wire as reference and counter electrode, respectively. All Pt wires were cleaned following

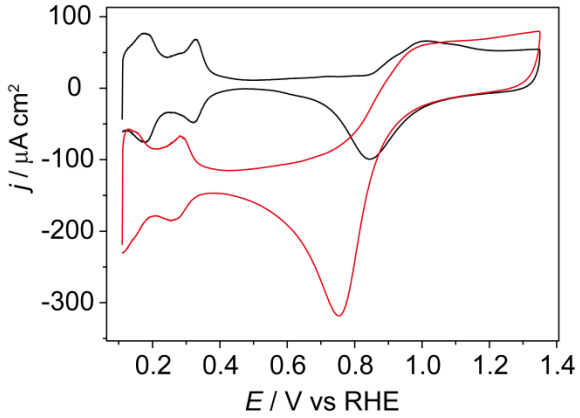

Figure 4.1 Cyclic voltammograms of platinum in nitrogen purged (black) and air saturated (red) 50 mM sulfuric acid solutions at a sweep speed of 50 mV s^{-1}.

the procedure described in Chapter 2. The solution was deaerated by flowing nitrogen through 10 mL of 50 mM sulfuric acid solution for 30 min. Furthermore, a nitrogen flow was sustained over the solution during the CV measurement. As shown in Figure 4.1, the CV under deaerated conditions shows the characteristic features of a polycrystalline electrode in sulfuric acid solution (see Chapter 1).[41] After recording the CV, the solution was aerated for 1 h. The change in the CV morphology on the cathodic scan (starts at 0.85 V) in this solution (red line) is due to the ORR. All the potentials reported in this chapter are relative to reversible hydrogen electrode (RHE).

4.2.2 Microscopic CVs of ORR recorded in a SECCM setup

Figure 4.2a shows a schematic of the setup for SECCM (in air), illustrating the meniscus at the end of the pipette which results in a three-phase boundary configuration, so that there is diffusion of oxygen down the two barrels of the pipette as well as from the edge of the droplet across the air-water interface. Figure 4.2b

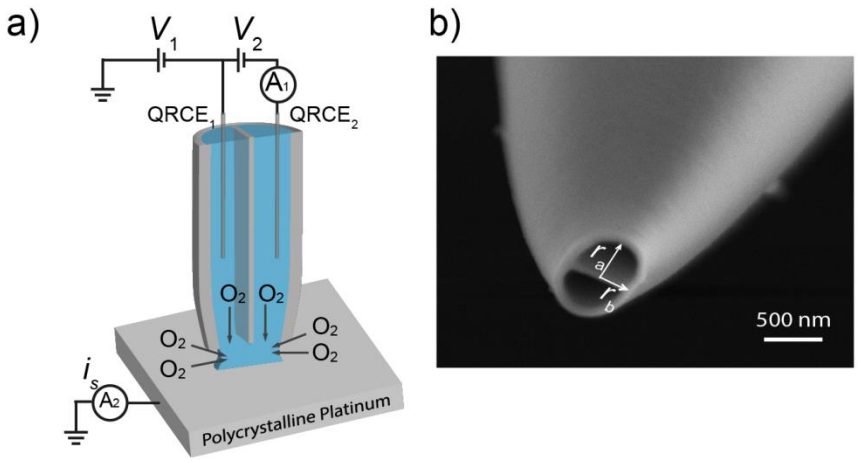

Figure 4.2 a) Schematic of the SECCM setup. Pd-H_2 quasi-reference counter electrodes (QRCEs) were inserted into two channels of a pipette, filled with 50 mM H_2SO_4. A bias potential, V_2, was applied between the two QRCEs and the resulting ion conductance current (i_{DC}) between the two channels was measured. A potential, V_1, relative to ground, was applied to $QRCE_1$; and the effective working electrode potential (at ground) was - (V_1 + V_2 / 2) vs. Pd-H_2, against which the working electrode current, i_s, was measured. Of particular interest to this chapter is the mass transport of oxygen from solution as well as through the air/electrolyte interface. **b)** SEM image of a pipette used for SECCM imaging. r_a and r_b are the major and minor inner radii of the pipette opening.

shows a representative scanning electron microscopy (SEM) image of the pipette used in the SECCM measurements in this chapter. All the pipettes used herein were pulled from double-barrelled (theta) capillaries, creating openings at the end of the pipettes that were 700-800 nm in diameter.

Typical CVs recorded in the SECCM setup in the presence and absence of oxygen using a pipette filled with 50 mM H_2SO_4 at a polycrystalline platinum foil electrode are shown in Figure 4.3. To perform the measurement without oxygen, the substrate and pipette were placed in an environmental chamber (Chapter 2) where

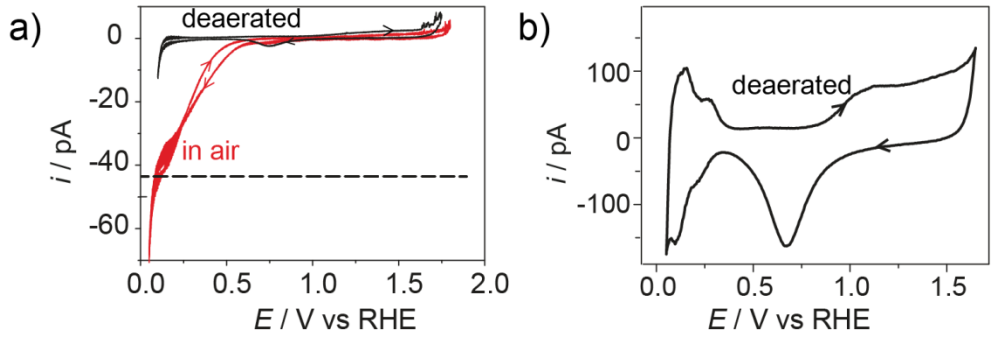

Figure 4.3 a) SECCM cyclic voltammograms of a polycrystalline Pt electrode in a deaerated (nitrogen-purged) solution (black line) and in air for the ORR (red line) at a sweep speed of 50 mV s^{-1}. The diffusion-limited current (approximately 40-45 pA) is indicated by the horizontal black dashed line for ease of reference. **b)** A blank CV recorded in a deaerated solution at a sweep speed of 5 V s^{-1}. Electrolyte solution: 50 mM H_2SO_4.

nitrogen gas (passed through a glass vessel containing water) was flowed through continuously to remove the dissolved oxygen in the meniscus.[42] In Figure 4.3a, the black line is a CV recorded under nitrogen flow between 0.05 V (starting and end potential) and 1.75 V (reverse potential) at a sweep speed of 50 mV s^{-1}. The red line refers to the ORR CV recorded at the same starting potential but slightly higher reverse potential (1.8 V) at the same sweep speed in air. In the ORR CV, there is a small hysteresis between the forward and reverse waves because the forward wave starts at a cathodic potential (0.05 V) where the surface is covered with adsorbed hydrogen (and is evolving hydrogen) whereas for the reverse wave, the surface is oxide covered before the ORR commences. Comparing the two CVs, it is clear that significant currents due to the ORR are observed at potentials below ca. 0.7 V, a potential region at which oxide reduction processes typically occur. Figure 4.3b is a CV recorded in the SECCM setup under nitrogen flow at a higher sweep speed of 5 V s^{-1}. A high sweep rate is used to ensure that a clear hydrogen underpotential

deposition (H_{upd}) feature can be resolved, as the high mass transport rate of oxygen leads to significant ORR currents for even residual amounts of oxygen. The characteristic platinum features can been seen,[41] similar to CVs obtained under conventional conditions (see Figure 4.1), validating the SECCM experimental setup and highlighting that the as-prepared substrate remains clean.

Notably, the ORR CV recorded in the SECCM setup is recorded under high mass transport conditions (k_t ~ 0.1 cm s^{-1}), which is about an order of magnitude higher than conventional electrochemical measurement, e.g. using a rotating disk electrode. The high mass transport of SECCM serves to push the ORR diffusion-limited current to more cathodic potentials. Recently, Kucernak and co-workers have reported similar cathodic shifts for the ORR measurement on Pt nanoparticles under high mass transport conditions.[43,44]

In SECCM, for the ORR, the flux of oxygen is provided by diffusion down the barrels of the pipette into the electrolyte meniscus as well as across the air-water interface of the meniscus (Figure 4.2a), which is a rapid process.[45] Consequently, the diffusion-limited current (approximately 40 - 45 pA as marked by dashed line in Figure 4.3a) is much higher than would be expected if diffusion was only due to O_2 initially in solution (ca. 27 pA based on meniscus height of 150 nm, *vide infra*). This is an interesting feature of SECCM, opening up studies of the ORR in the presence of a three-phase boundary, and with the possibility of controlling mass transport rates by changing the meniscus height, as discussed herein.

4.2.3 Meniscus geometry effects on the ORR

The impact of the meniscus geometry on the ORR current was investigated through experiments in which the meniscus height was varied while measuring the

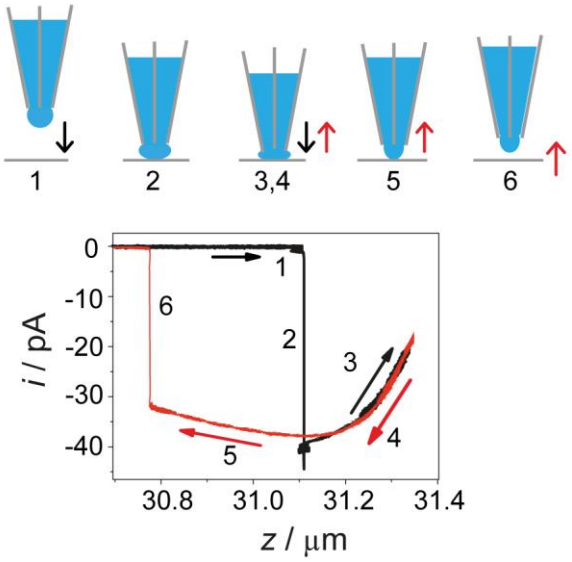

Figure 4.4 Typical surface electrochemical current response for the ORR on a polycrystalline Pt electrode in 50 mM H_2SO_4 at 0.20 V *vs.* RHE (close to the diffusion-limit for the ORR) as: 1, the pipette approached the surface; 2, the meniscus contacted the surface; 3, the meniscus was squeezed; 4 and 5, pipette retracted from the surface; 6, the meniscus detached. The cartoon illustrates the pipette and droplet position at these different stages.

diffusion-limited oxygen current, as illustrated in Figure 4.4. Initially, the droplet at the end of the pipette was brought into contact with the surface held at 0.2 V (close to the mass transport-limited potential) at a speed of 1.5 µm s^{-1} (label 1 in Figure 4.4). Once surface meniscus contact was established (label 2), as a jump to contact, there was rapid establishment of the ORR diffusion-limited current. Once this was sensed, the tip translation speed towards the substrate changed automatically to a much slower value as the tip was further lowered (20 nm s^{-1}, label 3), decreasing the tip-to-substrate separation, or similarly, squeezing the meniscus height, for a total distance of 250 nm. Clearly, squeezing the meniscus decreases the area of the air-water interface and consequently diminishes the flux of O_2 to the Pt surface as evident in the gradual decrease of the mass transport-limited current. Before the pipette made

physical contact with the surface, the motion was reversed, increasing the tip-to-substrate separation (meniscus height). It can be seen that the ORR current during the retraction of the pipette initially closely follows that during squeezing with little hysteresis (label 4). However, detachment (label 6) does not occur at the same *z* position as attachment (label 2). Rather, the pipette has to be pulled back an additional 300 nm (label 5) before liquid meniscus detachment from the surface. This is reminiscent of AFM force curves in air where there is a strong attractive interaction between the tip and the substrate due to capillary forces.[46,47] During this pull-off period, there was a small decrease in the limiting current, which might be a consequence of a small decrease in the contact area of the meniscus with the surface.

4.2.4 SECCM line scan

For the present studies, up to about one hour could elapse between preparing the sample (albeit with protection from the electrolyte for part of the time) and finally landing the meniscus for SECCM imaging. Since the ORR could be susceptible to contamination, additional checks were performed that there was no significant change in the surface quality from atmospheric contamination. To do this, SECCM line scan experiments were performed on different areas of the Pt foil, in which each line was scanned four times with the meniscus at different potentials.

Typical sets of current profiles on two different areas are shown in Figure 4.5. After the electrolyte meniscus was brought into contact with the as-prepared surface as usual, a meniscus linescan across 40 μm at a speed of 0.5 μm s^{-1} was carried out four times over the same area of the surface. For the first (label a) and last pass (label d), the potential was held at the value of interest (0.45 V, well removed from the

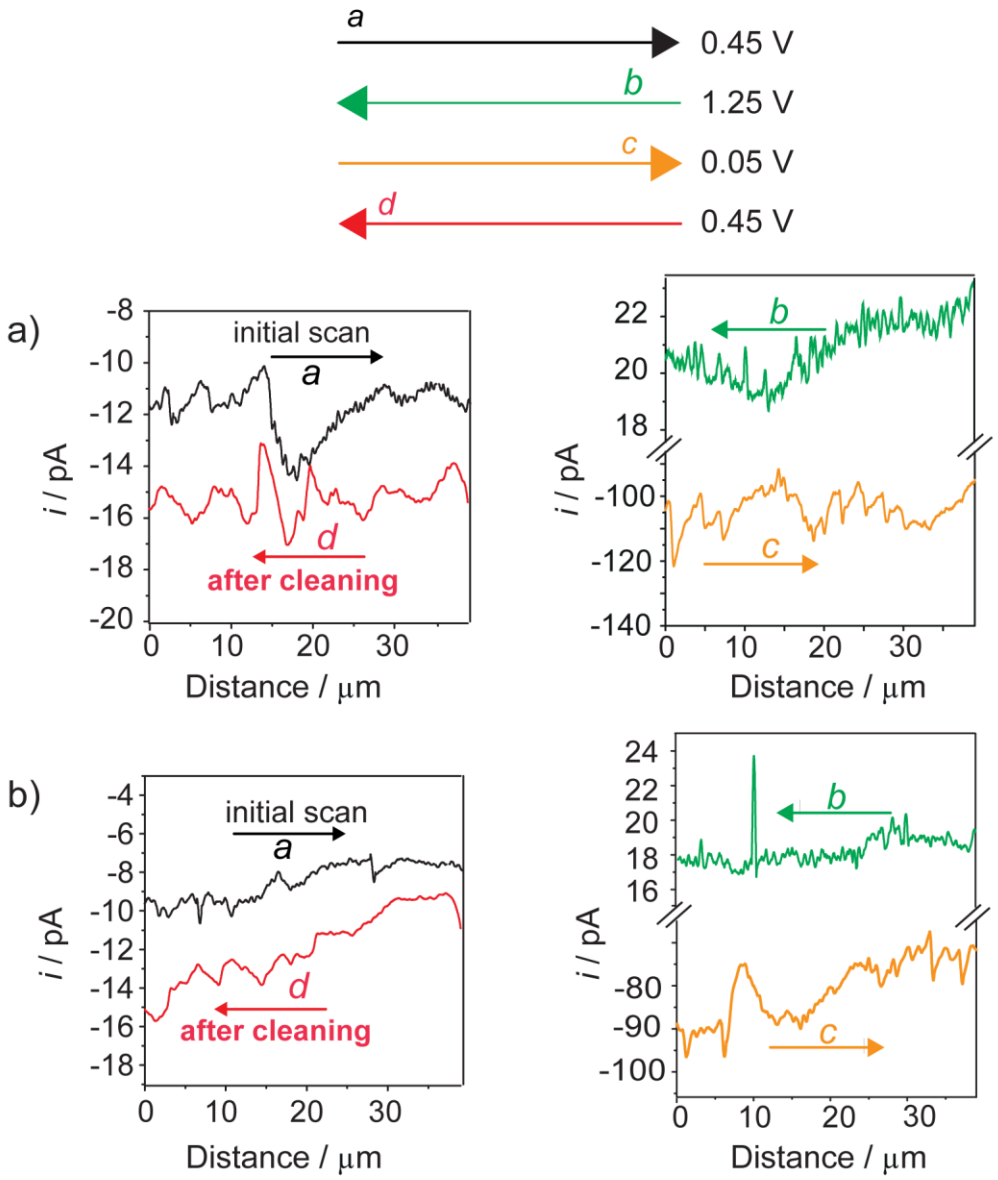

Figure 4.5 Experimental data of two separate series of line scans in 50 mM H_2SO_4 (shown in top and bottom figures respectively). Each line was scanned four times at different potentials relative to RHE: a, 0.45 V; b, 1.25 V; c, 0.05 V; and d, 0.45 V. Letters in the figures and the arrows with different colours represent the sequence and direction of scanning.

diffusion-limited potential to ensure that any impact of changes in the surface kinetics would be seen). In the second pass (label b), a potential of 1.25 V was

applied which would readily oxidised any surface contaminants. On the third pass (label c), the potential was held at 0.05 V to reduce the surface oxides formed on the second pass. By comparing the ORR current for the first pass (sample as prepared) and the fourth pass (sample as prepared plus *in situ* electrochemical cleaning), the effect of the two areas at 0.45 V was found to be about 20-30 %, which is small compared to the several-fold change in activity observed between grains (*vide infra*). It was found that similar current features were observed without and with additional cleaning. This indicates that the method of surface preparation and SECCM analysis yields a relatively clean surface with minimal impact of surface contamination on electrochemical activity over the duration of the imaging measurements. Importantly, this aspect was further evident from the images reported herein in which there was no obvious deterioration in surface electrochemical current during the course of a scan (*vide infra*).

4.2.5 SECCM imaging

To investigate the influence of structure on ORR activity, SECCM imaging experiments were performed. For this experiment, the dimensions of the pipette and the footprint of the droplet were measured precisely by SEM. The SEM measurement (Figure 4.2b) showed that the pipette used for SECCM imaging had an elliptical end opening, with a major inner radius r_a = 370 nm and minor inner radius r_b = 260 nm. The footprint measurement showed a droplet contact with major and minor semiaxes, r_{ma} and r_{mb}, of 650 nm and 520 nm, respectively, resulting in a contact area of 1.06×10^{-8} cm^2. The meniscus size is within the size range reported for SECCM.[31,34] SECCM activity images of an area of interest on the Pt foil held at

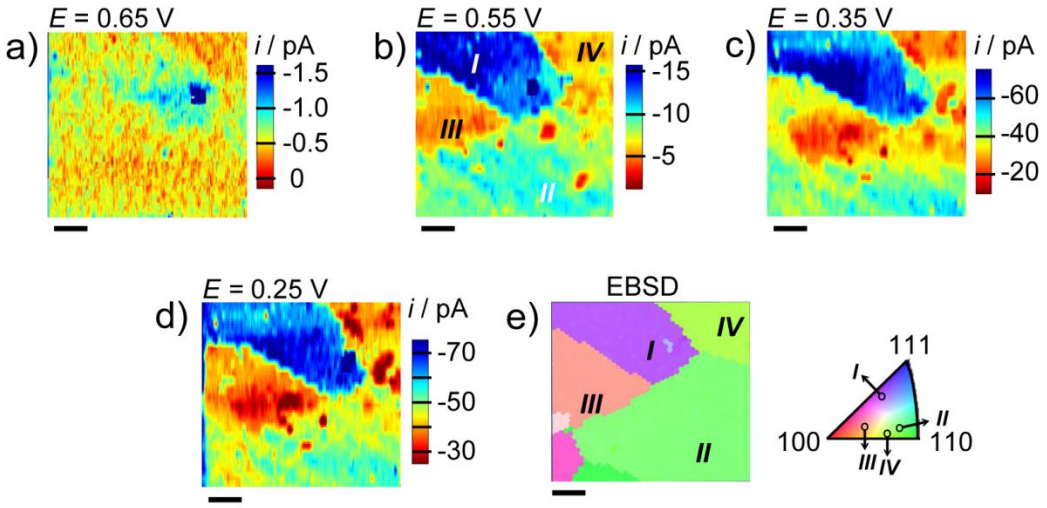

Figure 4.6 SECCM surface current images **a-d)** and the corresponding EBSD image **(e)** of one area of a Pt electrode. Electrochemical current images at **a)** 0.65 V, **b)** 0.55 V, **c)** 0.35 V, and **d)** 0.25 V vs. RHE in 50 mM H_2SO_4. Labels "*I*", "*II*", "*III*" and "*IV*" (in (b) and (e)) highlight four characteristic grains. The scale bar is 10 µm.

four different substrate potentials, 0.65 V, 0.55 V, 0.35 V and 0.25 V in 50 mM H_2SO_4 are shown in Figure 4.6a-d, respectively. Note that the data were acquired in a random order (in the sequence of 0.55 V, 0.25 V, 0.65 V and 0.45 V) to avoid any systematic error. For this area, data were acquired every 6.5 nm along a particular line with a spacing of 2.5 µm between lines. The crystallographic orientation of the same area was obtained by EBSD and is shown as an inverse pole plot in Figure 4.6e. In the colour legend, the three corners of the triangle represent the three basal planes of Pt. The facets which are located on the side-lines are vicinal (or stepped) planes, while the inside of the triangle represents high-index (or kinked) planes. The EBSD image indicates that all of the grains in the scanned area are high-index orientations of distinctly different structure. Comparing the SECCM images with the EBSD results, four main grains can be identified, labelled as grain *I*, *II*, *III* and *IV*. The correlation between the electrochemistry and surface structure is discussed below.

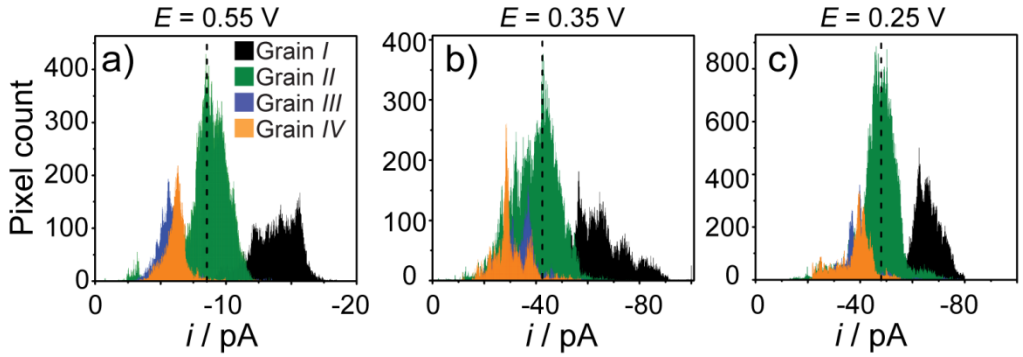

Figure 4.7 Histograms of electrochemical current distribution for the ORR on the four labeled grains in Figure 3 at a Pt electrode potential of **a)** 0.55 V, **b)** 0.35 V, and **c)** 0.25 V vs. RHE in 50 mM H_2SO_4. The dashed line in each figure indicates the average current at that potential. These histograms were obtained by analyzing the data at individual pixels from regions where grains were identified on the SECCM images.

The data obtained from SECCM allows further quantitative analysis of the images. Histograms of the electrochemical current for the grains in Figure 4.6 at 0.55 V, 0.35 V and 0.25 V are shown in Figure 4.7a, b and c, respectively. At each potential, the electrochemical current distribution was plotted by extracting data from the individual grains in the SECCM images. The black vertical dashed line in each histogram indicates the average current over the entire scanned area at that potential. The relative activity for the four main grains is always in the order *I* > *II* > *III* ≈ *IV*. Moreover, the current distribution for each grain is rather broad, which can be attributed to the complex structure of the grains, which have contributions from all three basal planes in different proportions, rather than being perfect single-crystal surfaces. It is important to point out that variations in activity due to the variations in wetting can be ruled out, as can be seen from the complementary ion conductance

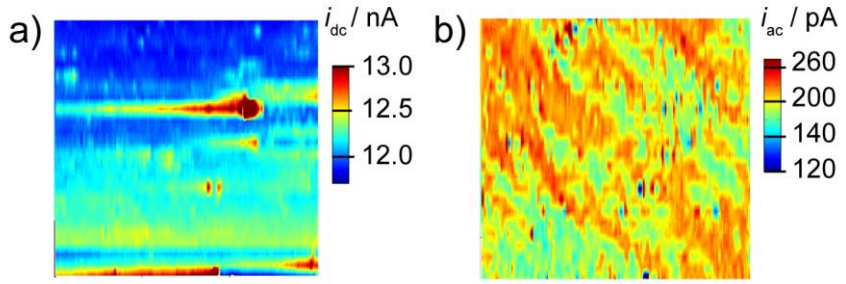

Figure 4.8 Typical **a)** SECCM ion conductance current and **b)** ac component of the ion conductance current image obtained while carrying out the ORR on a polycrystalline platinum electrode at 0.65 V vs. RHE.

direct and alternating current images in Figure 4.8. The ion conductance current across the surface is stable, within a range of 12 ~ 13 nA, indicating a stable meniscus during scanning. A slightly higher current spot is found in Figure 4.8. This is due to a change in topography at that site. Despite this, the ion conductance is stable for most of the scanned area and it is independent of the surface current patterns. The ac component map is shown in Figure 4.8b and has values ranging between 140 ~ 260pA. This illustrates that a good contact is maintained throughout imaging. Both ion conductance and alternating current map demonstrate the stability of the meniscus size and the constancy of the pipette-substrate separation during scanning. Importantly, it shows that the droplet wetting is featureless and grain-independent. In addition, the activity features observed, are not due to variations in the roughness of the platinum foil, which is negligible, as discussed in Chapter 3.[27]

To support the data above, and obtain more detail, higher resolution images were acquired, again with a resolution of 6.5 nm for each pixel in the line, but with a spacing of 1 μm between each line. Images of the electrochemical activity at 0.45 V and 0.25 V are presented in Figure 4.9a-b, while the crystallographic orientations of

the grains in this area are shown in Figure 4.9c. In this case, SECCM images combined with EBSD maps allowed us to identify five regions with different activities and assign these to individual grains (*I'*, *II'*, *III'*, *IV'* and *V'*). Here the experiment employed a thicker meniscus, as evidenced by the higher ion conductance current (~ 27.5 nA), which means more influence of oxygen transport through the water-air interface (following from Figure 4.4), and so higher electrochemical substrate currents, especially in the limiting current region. In Figure 4.6 and Figure 4.9, comparison of SECCM images and EBSD maps shows a strong correlation between variations in electrochemical activity and the grain structure. Specifically, grain *I* (Figure 4.6) and grain *I'* (Figure 4.9), which have (100) and (111) characteristics, exhibit the highest activity among all the grains. In the map recorded at a low driving potential, 0.65 V (Figure 4.6a), grain *I* can still clearly be distinguished, even when the currents from the other grains are negligible. In general, amongst the other grains, which are located close to (but not on) the bottom side of the colour legend triangle there are two categories: those close to the (110) basal plane exhibit higher activities than those close to the (100) plane. Thus, in Figure 4.6, grain *II* is more active than grain *III* and grain *IV*, while in Figure 4.9, grain *II'* and grain *III'* exhibit higher activity than grain *IV'* and grain *V'*. Finally, grains close to the (100) orientation exhibit the lowest activity among all the investigated grains and the difference amongst them is much smaller.

In summary, SECCM images combined with EBSD data demonstrate that ORR activity varies strongly with the crystallographic orientations of high-index Pt grains. The relative activity trend holds throughout the entire (wide) potential range investigated. Notably, the current value varies by several-fold for different grains

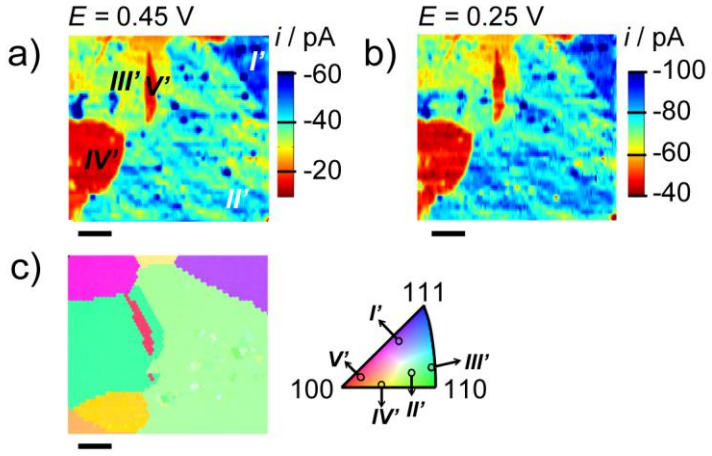

Figure 4.9 Electrochemical current images at **a)** 0.45 V and **b)** 0.25 V *vs.* RHE in 50 mM H_2SO_4 and **c)** the corresponding EBSD image for an area of a Pt electrode. The orientations of the five labelled grains are also marked on the colour coded orientation map to guide the reader. The scale bar is 10 µm.

across a small area of the surface (60 µm × 60 µm). Based on research on single-crystal basal planes, the adsorption of (bi)sulfate on (111) long range terraces strongly hinders the ORR, while the introduction of mono-atomic steps on the surface, enhances the activity by breaking the long range order and thereby the anion adsorption strength.[10,48] The results herein are consistent with this analysis, showing that facets close to (111) orientation with (100) contributions are the most active.

Although a possible role of grain boundaries for the ORR has been discussed in a few papers on nanocrystalline particles,[25,26] no obvious enhanced activities at grain boundaries was observed. SECCM is capable of visualizing such enhancements in activity[27], as discussed in Chapter 3, although the grain boundary activity needs to be much higher than that of the grain in order for it to be detected.

4.2.6 Kinetics analysis

To further assess the SECCM data and validate the approach in comparison to other techniques, a simple kinetic analysis was performed at 0.55 V, where the current is mostly under kinetic control and where perturbations of the solution composition in the meniscus are also less severe than at more driving potentials.

Although the ORR current is essentially under kinetic control, minor mass transport effects are corrected. The relationship between the measured current density (j), the kinetic current density (j_k), and the mass transport-limited current density (j_t) is reasonably given by:

$$\frac{1}{j} = \frac{1}{j_k} + \frac{1}{j_t} \tag{4-1}$$

which yields the following for j_k,

$$j_k = \frac{jj_t}{j_t - j} \tag{4-2}$$

Current densities were obtained by dividing measured currents by the contact area of the electrolyte meniscus (*vide supra*). j_t is calculated to be 6.2 mA cm^{-2}, based on the average current in the major active grain I in Figure 4.6 (65.4 pA) at a potential of 0.25 V which corresponds to the mass transport-limited potential. At 0.55 V, the average j is 810 µA cm^{-2} (based on the average current, i = 8.6 pA, across the entire scanned area). By solving equation (4-2), an average j_k of 932 µA cm^{-2} was obtained. Evidently, the current values depicted in Figure 4.6b approximate well to kinetic values, with minimal mass transport contribution.

From the kinetic current density, the exchange current density (j_0) can be estimated, with knowledge of the Tafel relationship (equation (4-3)) [49]:

$$\log j_k = \log j_0 + \eta/b \quad (4\text{-}3)$$

where b is the Tafel slope (in mV per decade), η is the overpotential ($\eta = E_{applied} - 1.23$ V,[8] For the ORR on Pt, the Tafel slopes depend on the potential region. At high anodic potentials (low current density region), where the ORR takes place on a (partially) oxidised Pt surface, a Tafel slope of 60 mV per decade is typically found, while at high current densities region (ORR on metallic Pt), the Tafel slope is 120 mV per decade[43,50]. At more cathodic potentials still, and for high mass transport conditions, the effective Tafel slope is ca. 240 mV/decade.[43] These latter conditions are appropriate to the experiments in this chapter, yielding an average exchange current density of 1.38 μA cm^{-2}.

The exchange current density obtained is broadly in line with, although a little lower than, previous studies as shown in Table 4-1.[43] In large part, this can be attributed to the three-phase system that results in differential mass transport of the reactant O_2 (which is provided down the barrels of the pipette and across the electrolyte-air interface) versus the flux of solution-phase reactants and products

Table 4-1 Exchange current density values, j_0, of the ORR at Pt electrode in H_2SO_4

References	j_0 (μA cm^{-2})	Electrode
Feliu[17]	~1.0	Pt(100) RDE
Feliu[17]	0.45	Pt(15,13,13) RDE
Feliu[17]	4.5	Pt (211) RDE
Feliu[18]	~5.0	Pt(110)
Kucernak[43]	1.2 ~3.7	Pt NP
This work	1.38	Polycrystalline Pt

(such as H^+ and H_2O_2, which can only diffuse to and from the electrode in barrels of the pipette). To gain some insights into the impact of the three-phase system on mass transport, a finite element method (FEM) model was developed. With this model, the electrochemical currents (with specific electrode kinetics), and the resulting average proton concentration in the solution near the electrode surface can both be predicted.

4.2.7 Finite element method (FEM) modelling

The SECCM setup was modelled using COMSOL Multiphysics 4.3 (COMSOL AB, Sweden) as described in detail elsewhere.[34,36,38] Briefly, the concept of the model is as follows. The pipette and the electrolyte meniscus are considered as truncated cones, as shown in Figure 4.10. Although a 3D simulation is necessary, a plane of symmetry perpendicular to the theta pipette inner wall means that only half of the pipette needs to be considered, which improves the computational efficiency.[34] The dimensions of the pipette opening, defined by r_a and r_b, were obtained from a SEM image in Figure 4.2b.

The contact area of the meniscus was determined by filling a pipette, of the same size as used for imaging, with 50 mM KCl solution and bringing it into contact with the platinum surface. The pipette was held in place for several minutes and then retracted, leaving a droplet of solution that upon drying produced a residue of KCl crystals. The meniscus footprint was then measured by SEM, and showed major and minor semi axes, r_{ma} and r_{mb}, of 650 nm and 520 nm, respectively. For the simulation, a taper angle of the pipette of $\theta = 8°$ was used, measured accurately by SEM and within the typical measured range of values.[34]

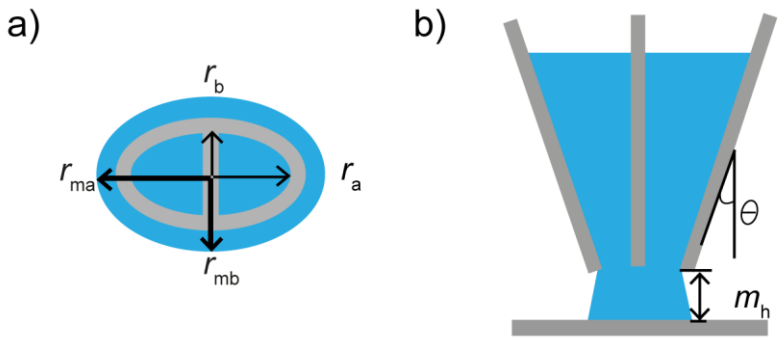

Figure 4.10 Schematics of the pipette (grey) and meniscus (blue) geometry used for FEM simulations. **a)** r_a and r_b (thin arrows) represent the major and minor inner radius of the pipette; r_{ma} and r_{mb} (thick arrows) indicate the major and minor radius of the meniscus. **b)** θ and m_h are the angle of the pipette and the height of the meniscus, respectively.

Based on the average values of ion conductance current (12 nA, Figure 4.8a) and the alternating current set point (200 pA, Figure 4.8b), the meniscus height, m_h, was determined to be 150 nm, for the experiment where a kinetic analysis was carried out.

The model included four molecular species: H^+, SO_4^{2-}, HSO_4^- and O_2. The diffusion coefficients for all species and the molar conductivity values for the ions were obtained from literature and are summarised in Table 4-2.

Table 4-2 Values for the ionic conductivity and diffusion coefficients of solution species, with their source (reference in superscripts).

Species	Λ_j (S cm^2 mol^{-1})	D (10^{-5} cm^2 s^{-1})
H^+	349.65[51]	7.90[52]
HSO_4^-	52[51]	1.39[51]
1/2 SO_4^{2-}	80[51]	1.07[51]
O_2		2.1[45]

The concentration of sulfuric acid was 50 mM. The speciation was evaluated with the known pK_a values of H_2SO_4 corrected for activity. The distribution of concentrations and the electric field in the pipette and meniscus were computed under steady-state conditions by solving the Nernst-Plank equation with electroneutrality. Due to the rapid gaseous O_2 transport[45] from air to the meniscus walls, a Dirichlet boundary conditions on the meniscus was imposed:

$$c_{O_2}(walls) = c_{O_2}^0 \tag{4-4}$$

where $c_{O_2}^0$ designates the concentration of oxygen in air-saturated solution (2.5×10^{-7} mol cm^{-3}).[45] This means that, besides the diffusion of O_2 down to the pipette, there is also a constant flux of O_2 from the meniscus "walls" (across the air/solution interface).

Since the simulations was mainly used to investigate mass transport effects in the SECCM ORR experiment, an effective rate constant for the ORR, k_r (variable) was applied, see equation (4-5). It was included in the model as a boundary condition at the electrode surface (equation (4-6) and (4-7)). The faradaic current, i, was computed from equation (4-8).

$$O_2 + 4H^+ + 4e^- \xrightarrow{k_r} 2H_2O \tag{4-5}$$

$$J_{O_2} = -k_r c_{H^+} c_{O_2} \tag{4-6}$$

$$J_{O_2} = \frac{1}{4} J_{H^+} \tag{4-7}$$

$$i = 8F \int_S D_{O_2} \left(\frac{\partial c_{O_2}}{\partial z} \right)_{z=0} dS \tag{4-8}$$

Here, *dS* represents the surface element, the factor 8 results from the four electron reaction and the symmetry of the simulation mentioned above. The integration in equation (4-8) was performed over the surface of the meniscus contact area S. [34]

By applying a range of reaction rate constants, k_r, at the surface and solving equations (4-6), (4-7) and (4-8), a working curve of electrochemical current (*i*) vs. k_r can be produced (Figure 4.11a), together with a plot of proton concentration near the working electrode versus current (Figure 4.11b). By matching experimental current values, one can extract k_r and the proton concentration for a potential of interest. At 0.55 V, the average current across the entire scanned area is 8.6 pA, corresponding to a k_r of 9.0×10^{-3} cm s^{-1}. By applying the same kinetic analysis as in section 4.2.6, an exchange current density of 1.49 μA cm^{-2} was obtained. This value is close to the exchange current density (1.38 μA cm^{-2}) calculated from the experimental data, confirming the validity of the simulation.

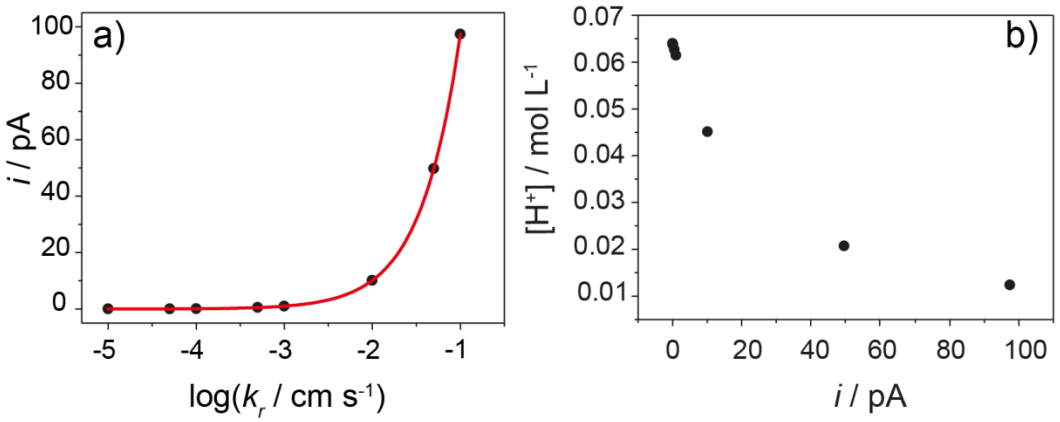

Figure 4.11 a) Working curve of electrochemical current vs. effective rate constant for the ORR. **b)** Proton concentration near the electrode surface vs. surface electrochemical current for the ORR from FEM simulations.

To further investigate the relative contributions of diffusion of O_2 down the barrels compared to that across the meniscus, a zero-flux boundary condition (equation (4-9)) was applied on the meniscus "walls" and the limiting current was obtained by applying equation (4-10) on the working electrode surface.

$$J_{O_2}(walls) = 0 \tag{4-9}$$

$$(c_{O_2})_{z=0} = 0 \tag{4-10}$$

This leads to a value for the limiting current of 27 pA which is about one third of the limiting current obtained in SECCM imaging (Figure 4.3). This result clearly shows the impact of the meniscus in enhancing oxygen mass transport in the SECCM setup.

Notably, Figure 4.11b shows that the proton concentration near the electrode decreases sharply with increasing electrochemical current (kinetics). The depleted proton concentration decreases the effective applied overpotential at the electrode-electrolyte interface (through a shift in the equilibrium potential), thereby reducing the driving force and the observed current. This mismatch between oxygen and proton transport pathways, resulting in proton depletion at the three-phase boundary can also be a major issue in fuel cells, particularly as proton transport in proton exchange membranes is much slower than in aqueous electrolytes.[53] The SECCM technique described provides an effective way to investigate such an effect. Importantly, the work demonstrates that it is possible to obtain approximate kinetic parameters for individual high-index grains in a semi-quantitative manner with a simple kinetic analysis.

4.3 Conclusions

SECCM combined with EBSD has allowed us to study electrode structure effects on the ORR at high-index facets of polycrystalline Pt with a three-phase boundary configuration. SECCM has provided information on variations in ORR activity across grains of different orientation at high spatial resolution. Grains having mixed (111) and (100) character exhibit higher activity than those with (100) and (110) features, in line with studies on pure single-crystals, confirming the validity of the approach, while highlighting the versatility of the *pseudo-single-crystal* approach as a means of investigating high-index crystal facets. Generally, the results on polycrystalline Pt highlight the importance of considering microstructural effects in order to understand the activity of practical electrocatalysts. In addition to illustrating the critical importance of grain structure, the results rule out major contributions to electrocatalytic activity from grain boundaries.

The approach described herein opens up new avenues for studying structure-activity relationships on complex surfaces. A key strength of the methodology is that it is underpinned by a quantitative treatment of mass transport,[27,31] in this particular case the influence of the three-phase boundary and differential mass transport of oxygen and the products on the kinetics can be elucidated. In the future, we plan to integrate sensor electrodes into the SECCM probe that could be used to detect intermediates of electrode reactions. This could be particularly beneficial for the ORR reaction where the detection of H_2O_2 and other intermediates would provide deeper insight into microscopic kinetics, marrying the attributes of SECCM and scanning electrochemical microscopy.

4.4 References

(1) Rabis, A.; Rodriguez, P.; Schmidt, T. J. *ACS Catal.* **2012**, *2*, 864.

(2) Lim, B.; Jiang, M.; Camargo, P. H. C.; Cho, E. C.; Tao, J.; Lu, X.; Zhu, Y.; Xia, Y. *Science* **2009**, *324*, 1302.

(3) Steele, B. C. H.; Heinzel, A. *Nature* **2001**, *414*, 345.

(4) Laoire, C. O.; Mukerjee, S.; Abraham, K. M.; Plichta, E. J.; Hendrickson, M. A. *J. Phys. Chem. C* **2009**, *113*, 20127.

(5) Lu, Y.-C.; Gasteiger, H. A.; Shao-Horn, Y. *J. Am. Chem. Soc.* **2011**, *133*, 19048.

(6) Wroblowa, H. S.; Yen Chi, P.; Razumney, G. *J. Electroanal. Chem.* **1976**, *69*, 195.

(7) Yeager, E. *Electrochim. Acta* **1984**, *29*, 1527.

(8) Gewirth, A. A.; Thorum, M. S. *Inorg. Chem.* **2010**, *49*, 3557.

(9) Stamenkovic, V. R.; Fowler, B.; Mun, B. S.; Wang, G.; Ross, P. N.; Lucas, C. A.; Marković, N. M. *Science* **2007**, *315*, 493.

(10) Komanicky, V.; Iddir, H.; Chang, K.-C.; Menzel, A.; Karapetrov, G.; Hennessy, D.; Zapol, P.; You, H. *J. Am. Chem. Soc.* **2009**, *131*, 5732.

(11) Nesselberger, M.; Ashton, S.; Meier, J. C.; Katsounaros, I.; Mayrhofer, K. J. J.; Arenz, M. *J. Am. Chem. Soc.* **2011**, *133*, 17428.

(12) Hsueh, K. L.; Chin, D. T.; Srinivasan, S. *J. Electroanal. Chem.* **1983**, *153*, 79.

(13) Paulus, U. A.; Wokaun, A.; Scherer, G. G.; Schmidt, T. J.; Stamenkovic, V.; Markovic, N. M.; Ross, P. N. *Electrochim. Acta* **2002**, *47*, 3787.

(14) Marković, N. M.; Ross, P. N., Jr *Surf. Sci. Rep.* **2002**, *45*, 117.

(15) Marković, N. M.; Schmidt, T. J.; Stamenković, V.; Ross, P. N. *Fuel Cells* **2001**, *1*, 105.

(16) Guo, S.; Zhang, S.; Sun, S. *Angew. Chem. Int. Ed.* **2013**, *52*, 8526.

(17) Maciá, M. D.; Campiña, J. M.; Herrero, E.; Feliu, J. M. *J. Electroanal. Chem.* **2004**, *564*, 141.

(18) Kuzume, A.; Herrero, E.; Feliu, J. M. *J. Electroanal. Chem.* **2007**, *599*, 333.

(19) Marković, N. M.; Adžić, R. R.; Cahan, B. D.; Yeager, E. B. *J. Electroanal. Chem.* **1994**, *377*, 249.

(20) Marković, N. M.; Gasteiger, H. A.; Ross, P. N. *J. Phys. Chem.* **1995**, *99*, 3411.

(21) Marković, N. M.; Gasteiger, H. A.; Ross, P. N. *J. Phys. Chem.* **1996**, *100*, 6715.

(22) El Kadiri, F.; Faure, R.; Durand, R. *J. Electroanal. Chem.* **1991**, *301*, 177.

(23) Kita, H.; Lei, H. W.; Gao, Y. *J. Electroanal. Chem.* **1994**, *379*, 407.

(24) Bandarenka, A.; Hansen, H. A.; Rossmeisl, J.; Stephens, I. *Phys. Chem. Chem. Phys.* **2014**, *16*, 13625.

(25) Cherstiouk, O. V.; Gavrilov, A. N.; Plyasova, L. M.; Molina, I. Y.; Tsirlina, G. A.; Savinova, E. R. *J. Solid State Electrochem.* **2008**, *12*, 497.

(26) Savinova, E. R.; Hahn, F.; Alonso-Vante, N. *Surf. Sci.* **2009**, *603*, 1892.

(27) Aaronson, B. D. B.; Chen, C.-H.; Li, H.; Koper, M. T. M.; Lai, S. C. S.; Unwin, P. R. *J. Am. Chem. Soc.* **2013**, *135*, 3873.

(28) Blakely, D. W.; Somorjai, G. A. *Surf. Sci.* **1977**, *65*, 419.

(29) Hoshi, N.; Kawatani, S.; Kudo, M.; Hori, Y. *J. Electroanal. Chem.* **1999**, *467*, 67.

(30) Banholzer, W. F.; Masel, R. I. *J. Catal.* **1984**, *85*, 127.

(31) Ebejer, N.; Güell, A. G.; Lai, S. C. S.; McKelvey, K.; Snowden, M. E.; Unwin, P. R. *Annu. Rev. Anal. Chem.* **2013**, *6*, 329.

(32) Lai, S. C. S.; Dudin, P. V.; Macpherson, J. V.; Unwin, P. R. *J. Am. Chem. Soc.* **2011**, *133*, 10744.

(33) Patten, H. V.; Meadows, K. E.; Hutton, L. A.; Iacobini, J. G.; Battistel, D.; McKelvey, K.; Colburn, A. W.; Newton, M. E.; Macpherson, J. V.; Unwin, P. R. *Angew. Chem. Int. Ed.* **2012**, *51*, 7002.

(34) Snowden, M. E.; Güell, A. G.; Lai, S. C. S.; McKelvey, K.; Ebejer, N.; O'Connell, M. A.; Colburn, A. W.; Unwin, P. R. *Anal. Chem.* **2012**, *84*, 2483.

(35) Ebejer, N.; Schnippering, M.; Colburn, A. W.; Edwards, M. A.; Unwin, P. R. *Anal. Chem.* **2010**, *82*, 9141.

(36) Güell, A. G.; Ebejer, N.; Snowden, M. E.; Macpherson, J. V.; Unwin, P. R. *J. Am. Chem. Soc.* **2012**, *134*, 7258.

(37) Lai, S. C. S.; Patel, A. N.; McKelvey, K.; Unwin, P. R. *Angew. Chem. Int. Ed.* **2012**, *51*, 5405.

(38) Güell, A. G.; Ebejer, N.; Snowden, M. E.; McKelvey, K.; Macpherson, J. V.; Unwin, P. R. *Proc. Natl. Acad. Sci. USA* **2012**, *109*, 11487.

(39) *Electron Backscatter Diffraction in Materials Science*; Schwartz, A. J.; Kumar, M.; Adams, B. L.; Field, D. P., Eds.; Springer 2010.

(40) Li, M. F.; Liao, L. W.; Yuan, D. F.; Mei, D.; Chen, Y.-X. *Electrochim. Acta* **2013**, *110*, 780.

(41) Climent, V.; Feliu, J. M. *J. Solid State Electrochem.* **2011**, *15*, 1297.

(42) Aaronson, B. D. B.; Lai, S. C. S.; Unwin, P. R. *Langmuir* **2014**, *30*, 1915.

(43) Chen, S.; Kucernak, A. *J. Phys. Chem. B* **2004**, *108*, 3262.

(44) Zalitis, C. M.; Kramer, D.; Kucernak, A. R. *Phys. Chem. Chem. Phys.* **2013**, *15*, 4329.

(45) Slevin, C. J.; Ryley, S.; Walton, D. J.; Unwin, P. R. *Langmuir* **1998**, *14*, 5331.

(46) Zitzler, L.; Herminghaus, S.; Mugele, F. *Phys. Rev. B* **2002**, *66*, 155436.

(47) Jang, J.; Schatz, G. C.; Ratner, M. A. *J. Chem. Phys.* **2004**, *120*, 1157.

(48) Komanicky, V.; Menzel, A.; You, H. *J. Phys. Chem. B* **2005**, *109*, 23550.

(49) Markovic, N.; Gasteiger, H.; Ross, P. N. *J. Electrochem. Soc.* **1997**, *144*, 1591.

(50) Sepa, D. B.; Vojnovic, M. V.; Vracar, L. M.; Damjanovic, A. *Electrochim. Acta* **1987**, *32*, 129.

(51) *CRC Handbook of Chemistry and Physics*; Lide, D. R., Ed.; CRC Press: Boca Raton.

(52) Macpherson, J. V.; Unwin, P. R. *Anal. Chem.* **1997**, *69*, 2063.

(53) Choi, P.; Jalani, N. H.; Datta, R. *J. Electrochem. Soc.* **2005**, *152*, E123.

Chapter Five

Voltammetric scanning electrochemical cell microscopy: dynamic imaging of hydrazine electro-oxidation on platinum electrodes

Abstract

Voltammetric scanning electrochemical cell microscopy (SECCM) incorporates cyclic voltammetry measurements in the SECCM imaging protocol, by recording electrochemical currents in a wide potential window at each pixel in a map. This provides much more information compared to traditional fixed potential imaging. Data can be represented as movies (hundreds of frames) of current (over a surface region) at a series of potentials and are highly revealing of subtle variations in electrode activity. Furthermore, by combining SECCM data with other forms of microscopy, e.g. scanning electron microscopy and electron backscatter diffraction data, it is possible to directly relate the current-voltage characteristics to spatial position and surface structure. In this chapter a 'hopping mode' is employed, where the SECCM pipette probe is translated towards the surface at a series of positions until meniscus contact. Small amounts of residue left on the surface, upon probe retraction, demark the precise area of each measurement. This technique is used to study hydrazine oxidation on a polycrystalline platinum substrate both in air and in a deaerated environment. In both cases, the detected faradaic current shows a structural dependence on the surface crystallographic orientation. Significantly, in the presence of oxygen (aerated solution) the electrochemical current decreases

strongly for almost all grains (crystallographic orientations). The results highlight the flexibility of voltammetric SECCM for electrochemical imaging and present important implications for hydrazine electroanalysis.

Chapter 5

5.1 Introduction

Electrochemical imaging is of interest for visualising (electro)chemical processes at interfaces and provides valuable information about the associated kinetics, mass transport and localised activity. In traditional electrochemical imaging approaches, the electrochemical current is recorded at a fixed potential of interest and, typically, only one or a few images are recorded.[1-3] Dynamic imaging was reported by Wipf[4,5] and Schuhmann[6] by combining scanning electrochemical microscopy (SECM) with time-dependent techniques, such as cyclic voltammetry (CV) and potential pulse methods, although this type of approach has not been widely adopted and has not been used to gain information on heterogeneous electrode surface activity, having employed rather large probe electrodes.

Scanning electrochemical cell microscopy (SECCM) is particularly powerful in revealing electrode surface activity, as demonstrated by a number of applications.[7-11] In Chapters 3 and 4, a pseudo-single-crystal approach was introduced, which combines SECCM and electron backscatter diffraction (EBSD), for investigating the structure-activity relationship at polycrystalline Pt, which comprises high-index Pt facets and grain boundaries.[12,13] However, in previous studies, SECCM was limited to imaging experiments at a few fixed potentials. In this chapter, voltammetric SECCM imaging, in a hopping mode, which combines CV and SECCM, is developed. In this imaging mode, a full CV is recorded at a number of locations (pixels) on the substrate, which are arranged in a (rectangular) grid. A wealth of information can obtained from these measurements that can then be visualised in different ways (e.g. equipotential maps or spatially resolved CVs).

This work focuses on spatially-resolved studies of the electrocatalytic oxidation of hydrazine on a polycrystalline Pt electrode, and these results are

compared to those obtained on traditional macro- and microscale electrodes. Hydrazine (N_2H_4) is of practical interest due to its wide application in the fields of electroanalysis and electrocatalysis. Liquid hydrazine is easily transferred and its oxidation offers relatively high power density with carbon-free products, making it a promising fuel for low temperature fuel cells.[14-16] Hydrazine is also important in the pharmaceutical industry, as a common starting material in the synthesis of many pharmaceutical compounds.[17,18] However, it is often a key impurity in pharmaceutical products, and its high toxicity has led to the development of (electrochemical) hydrazine sensors.[19-21] Voltammetric and amperometric hydrazine analysis is usually performed in air and the role of oxygen in hydrazine detection is rarely taken into account.[22] This is an important consideration, because hydrazine can (catalytically) reduce oxygen on various surfaces, a process that is exploited for corrosion protection.[23-26] Thus, the faradaic response for hydrazine electro-oxidation (especially at trace levels) might be expected to change in the presence of O_2 in a manner that depends on the electrode structure, as considered herein.

Pt and Pt-based electrodes are relatively active for hydrazine electro-oxidation and the mechanism and kinetics of hydrazine oxidation on Pt have received ample attention.[27-29] The overall reaction oxidises hydrazine to molecular nitrogen and depends on the pH of the solution:

$$N_2H_5^+ \rightarrow N_2 + 5H^+ + 4e^- \quad (\text{low pH}) \qquad (5\text{-}1)$$

$$N_2H_4 + 4OH^- \rightarrow N_2 + 4H_2O + 4e^- \quad (\text{high pH}) \qquad (5\text{-}2)$$

Various possible intermediates and (pH-dependent) reaction pathways have been proposed. In general, no oxygen-containing compounds are detected by on-line electrochemical mass spectrometry (OLEMS)[28] and the N-N bond is found to remain

intact through isotopic labelling.[30] As this is a catalytic reaction, the role of surface structure is of interest and has been investigated using Pt single-crystal electrodes.[31-33] For Pt in a weakly adsorbing electrolyte (perchloric acid), the reactivity (in terms of peak potential) for the basal planes decreases in the order of Pt(100) > Pt(111) > Pt(110).[32] While single-crystal research provides valuable information for basal planes, less is known about high-index surfaces and grain boundaries, of practical importance in polycrystalline or nanoparticle-based sensors, which is the focus of this chapter.

In this chapter, voltammetric SECCM is used to study hydrazine oxidation at a polycrystalline platinum electrode in air and in a nitrogen atmosphere. Equipotential images and dynamic movies obtained from pixel-resolved CV measurements allow direct visualisation of hydrazine oxidation across Pt surfaces at multiple different potentials and surface orientations. In the absence of oxygen, the structure-dependent reactivity of hydrazine oxidation for high-index surfaces is established. In air, the electrochemical current for hydrazine oxidation was found to decrease dramatically for most Pt facets, with important implications for hydrazine electroanalysis.

5.2 Voltammetric SECCM measurement

Voltammetric SECCM has been described in Chapter 2. Bias voltages of 200 or 500 mV were applied to QRCEs. Tip modulation of the *z*-position of the tip has a frequency of 66 Hz for experiments in deaerated environment and 266 Hz for experiments in air. The oscillation peak amplitudes were within 25-50 nm. A

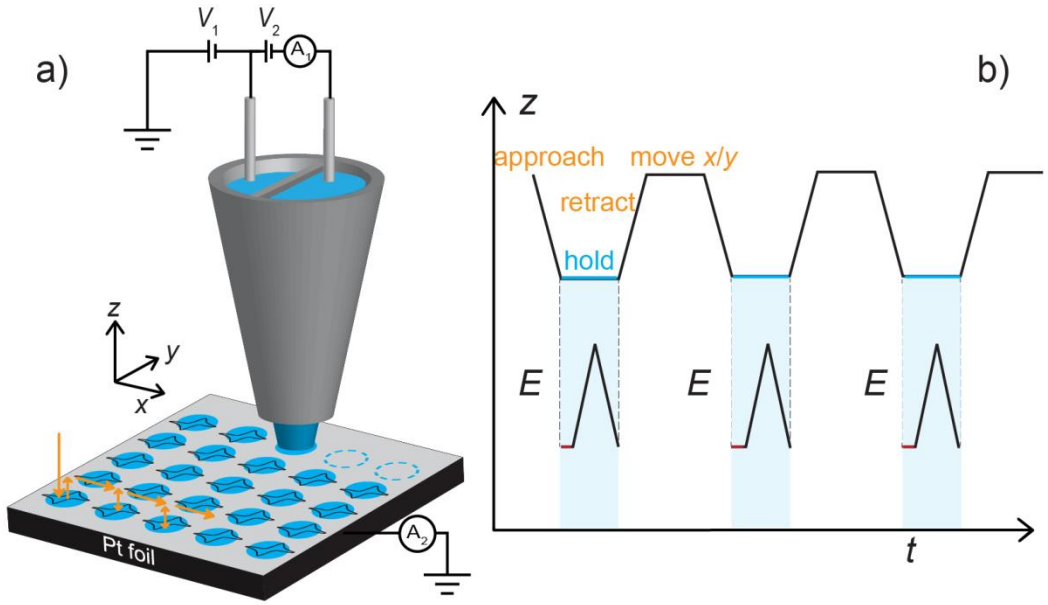

Figure 5.1 a) Schematic overview of the voltammetric hopping SECCM mode. V_2 and V_1 are the bias voltage and substrate voltage applied to one of the QRCEs, respectively. A_1 and A_2 are current amplifiers to measure i_{DC} and the substrate working electrode current (i_s), respectively. The blue circles indicate the probed areas of the working electrode and the arrows indicate the movement of the pipette. **b)** Schematic profiles of pipette-to-substrate separation (top) and the corresponding potential profile (bottom) applied to the substrate with time. The red lines in the potential profile indicate the hold time before recording a CV, typically 1 s.

constant tip-to-substrate distance was maintained by using the magnitude of i_{AC} as feedback.[7-13]

Figure 5.1b illustrates the tip-to-substrate separation, as a function of time, *t*, during imaging, together with the corresponding potential-time profile applied to the substrate working electrode. The complete scanning process parameters are as following: slow approach of the pipette (0.5 μm s^{-1}); 1 s waiting time to stabilise the meniscus; potential sweeps (0.1 V s^{-1}) to obtain the CV; quick retraction (2.0 μm s^{-1});

and movement in the *xy*-plane (2-3 μm between each pixel at a speed of 2.0 μm s^{-1}). For the CV measurement, current data were recorded at least every 1 mV, so that potentiodynamic movies containing many hundreds of frames could be produced. Movies can be found at:

http://pubs.acs.org/doi/suppl/10.1021/acs.analchem.5b00988

The distance between adjacent pixels (2-3 μm) was chosen such that there was no overlap between each probed area (diameter ~1 μm). Another important factor to determine the pixel spacing was the total imaging time which was typically several hours. The retract distance was chosen based on the tip size and the roughness/flatness of the substrate and was typically 1-1.5 μm. As a 'fresh' surface (i.e. a region of the surface that had not yet been in contact with the electrolyte solution) was encountered for each pixel, all CVs recorded in the SECCM imaging are the first CV at that particular position.

5.3 Results and discussion

5.3.1 Voltammetry of hydrazine oxidation at Pt electrodes

To study the electrochemistry of hydrazine and provide a comparison for the SECCM results, CV measurements were carried out at polycrystalline platinum electrodes at different length scales. Typical CVs for hydrazine oxidation recorded on a mm-scale platinum wire, on a Pt ultramicroelectrodes (UME), and on a polycrystalline Pt foil using a 1 μm diameter SECCM pipette are shown in Figure 5.2. The cleaning procedure of these electrodes can be found in Chapter 2. CVs at the Pt wire and UME were carried out in deaerated electrolyte solutions, which

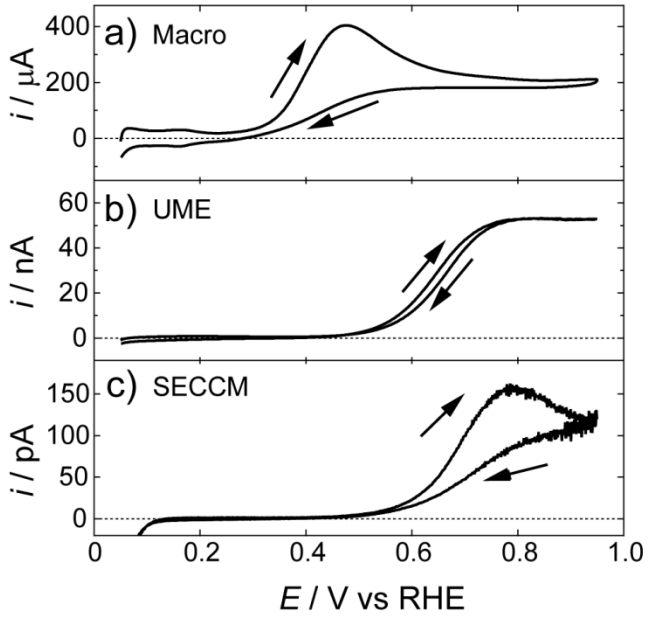

Figure 5.2 Typical CVs of hydrazine oxidation at **a)** a Pt wire, **b)** a 25 μm diameter Pt UME, and **c)** a polycrystalline Pt foil in a SECCM setup. Note the different current scales. In all cases the CVs were recorded in deaerated electrolyte solutions containing 2 mM N_2H_4 in 0.1 M $HClO_4$. The sweep rates were 100 mV s^{-1}.

were flushed with N_2 for 30 minutes before the measurements. SECCM experiments in deaerated conditions were carried out in an environmental cell (Chapter 2), which was placed over the Pt foil and the pipette and was flushed with humidified N_2 before starting the experiment and during imaging. All CVs were recorded in a deaerated solution of 2 mM N_2H_4 in 0.1 M $HClO_4$ at 100 mV s^{-1}.

At the macroscopic Pt electrode, hydrazine oxidation in an acidic electrolyte starts at potentials more positive than the hydrogen desorption region and then quickly reaches peak current at ca. 0.48 V. In the case of the UME, (diffusional) mass transport is much faster than for the macroelectrode. In competition with the surface kinetics for hydrazine electro-oxidation this leads to an apparent shift in the onset potential to ca. 0.45 V. A steady-state current is observed at potentials above 0.80 V. Similar with CVs reported in literature, hydrazine oxidation is a reasonably

facile process at both the macro- and the microscale, leading to mass transport limited reactivity at intermediate overpotentials.[29,34] Figure 5.2c shows a typical CV for hydrazine oxidation at a platinum foil recorded in the SECCM setup. The oxidation of hydrazine has a similar onset potential as on the UME, but there is a small transient peak in the current at 0.80 V before a steady-state at more anodic potentials. Importantly, Figure 5.2c shows no features due to oxygen reduction (which would be manifested in observable reduction currents well above the present cathodic onset of ~0.1 V), confirming the performance of the environmental cell, as the fast diffusion of O_2 from the surroundings across the meniscus to the surface would lead to a noticeable current (see Chapter 4).[13] Furthermore, as it will be showed below, the presence of oxygen leads to significantly distorted features in the voltammetric profile for the oxidation of hydrazine.

The diffusion coefficient of hydrazine can be (D) calculated from the UME experiments using the limiting current equation for an inlaid UME: [35]

$$i_{\text{lim}} = 4nFDcr \tag{5-3}$$

where n is the number of electrons transferred per hydrazine molecule (n = 4), F is the Faraday constant, c is the bulk hydrazine concentration (c = 2 mM) and r is the UME radius (r = 12.5 μm). The calculated D, 1.4×10^{-5} cm^2 s^{-1}, is consistent with values reported in the literature.[36,37] In SECCM, the steady-state diffusion-limited current, i_{lim}, beyond the peak is 100 pA. The mass transport coefficient, k_t, can be calculated based on the equation:

$$k_t = i_{\text{lim}} / nFAc \tag{5-4}$$

where A is the meniscus footprint area for 1 μm diameter spot size (A = 7.85 ×10^{-9} cm^2). Based on i_{lim} in SECCM, k_t is 1.65 × 10^{-2} cm s^{-1}. It is about 5 % of that for an inlaid UME (k_t = 4D/πr) of the same size, which is within the typical range reported for a micrometer-sized SECCM pipette,[9] and similar to that of the 12.5 μm diameter UME. That the SECCM voltammogram shows a slight transient response (quasi-steady state) compared to the UME (Figure 5.2b and c) is because of a very different current distribution in SECCM. For $N_2H_5^+$, which is the predominant species herein, there is a large difference in mass transport rate down the two channels of the theta pipette in SECCM.[9] Further, note that some of the differences between the CVs in Figure 5.2 will be due to the different electrodes used, and methods of preparation, because as it is showed herein, hydrazine oxidation is very surface sensitive.

In some recent work, a significant 'activation' of a Pt UME after scanning towards high oxidative potentials was reported, attributed to the formation of catalytic residual surface oxides in sequential voltammetric scans.[34] To study the surface oxide residual effects on hydrazine oxidation, some CVs were recorded in this study where the potential was scanned up to 1.45 V and shown in Figure 5.3.

As shown in the figure, CVs from the Pt UME (top) and in the SECCM setup (bottom) show very similar characteristics. Despite the number of cycles, under both conditions, hydrazine oxidation shows a pre-wave peak at around 0.70 V and a diffusion-controlled plateau at high potential range. While there are small changes in the voltammetric signature, the responses were generally similar to the 'stabilized' CV reported[34] without the need of any initial activating scan. It should be kept in

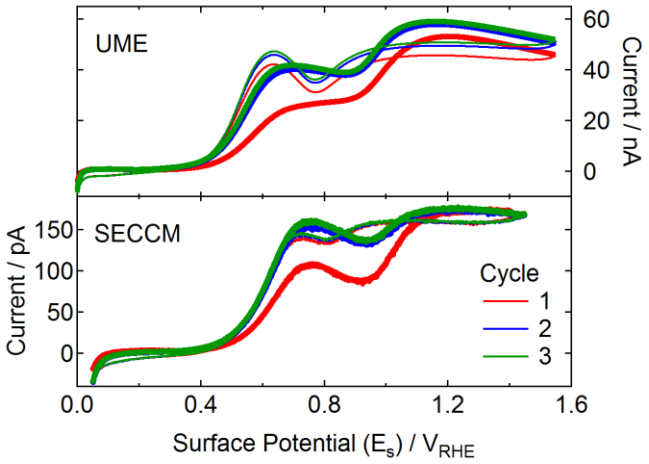

Figure 5.3 First three CVs (colour indicated) of hydrazine oxidation at a Pt UME (top) and at a Pt foil (bottom) in a SECCM setup. For both experiments, nitrogen was flowed to deaerate the electrolyte solution. Electrolyte: 2 mM N_2H_4 in 0.1 M $HClO_4$. Sweep rate: 100 mV s^{-1}.

mind, however, that the surface preparation herein is an oxidative process (flame-annealing) which could introduce such residual oxides. Nonetheless, to avoid possible complications due to further extensive Pt oxide formation and reduction, all the CVs in SECCM imaging experiments were recorded from 0.05 V to 0.95 V, focusing on the main response.

5.3.2 Voltammetric SECCM imaging in deaerated environment

Figure 5.4a shows an EBSD image of a typical probed area of polycrystalline platinum foil. In this case SECCM focused on a 41 μm × 86 μm area, with data recorded every 3 μm within this area. The analysis focuses on the voltammetry of the four numbered grains as they present the limiting cases of the orientations present.

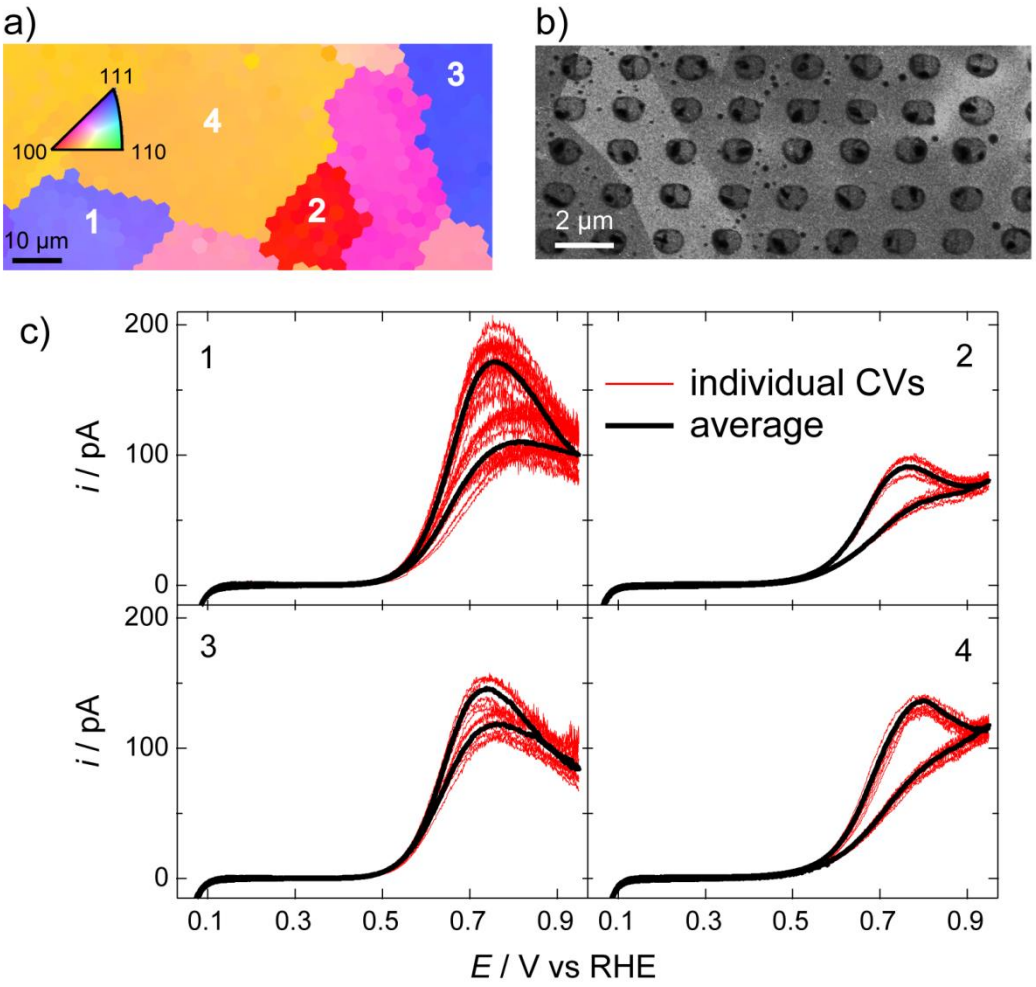

Figure 5.4 a) EBSD image of the Pt foil used in the SECCM imaging experiments. Data resolution: 2.5 μm per pixel. The grain orientations are indicated in the triangle. **b)** A typical SEM image of a part of a scanned area after SECCM imaging. **c)** Individual CVs (red, 7-10 for each grain) and grain-averaged CVs (black) for different grains.

EBSD results show that all the grains are high-index surfaces, but grain 1 and 3 have orientations approaching (111), while grain 2 has an orientation approaching (100). Grain 4 lies between (100) and (110).

Optical microscopy and SEM images after SECCM imaging showed droplet residues on the surface due to the quick breaking of the meniscus during probe

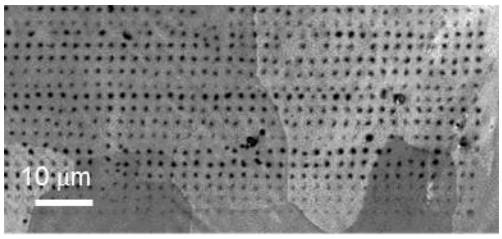

Figure 5.5 A SEM image showing the droplet residues after a SECCM imaging experiment. The black dots shown in this image are meniscus residues due to the quick retraction of the pipette.

retraction. Figure 5.4b is a typical zoomed-in SEM image after an SECCM measurement. These droplet residues are fairly consistent in shape and size at the different grains, confirming the stability and reproducibility of the technique and the absence of a dependence of droplet wetting on the surface structure. This is shown in a more extensive region in Figure 5.5. The black dots are the droplet residues left on the surface due to the quick break of droplets during pipette retracting. It can be seen that the footprints of most droplets are consistent in size, indicating the stability of droplets in voltammetric SECCM imaging and, most importantly, grain structure-independent droplet wetting.

Additionally, the residues helped us to determine the exact scanned area and droplet size (meniscus footprint) after SECCM imaging. Before each new experiment, all residues from any previous imaging were cleaned by immersing the foil in a 50 mM H_2SO_4 solution overnight.

By combining the results from SECCM, SEM, and EBSD, the position of each individual CV can be determined. Figure 5.4c shows CVs from 7-10 pixels obtained on each of the four numbered grains. On top of the individual CVs, an averaged CV is plotted for each grain to show the representative CV feature of that area. It is clear that the variation within a particular grain is fairly small, particularly

for grain 2 and grain 4, but the character of the grain has a significant impact on the voltammetric response. This is not due to changes in the meniscus contact area as the footprint is reasonably consistent (see above). Moreover, the corresponding i_{DC} images (http://pubs.acs.org/doi/suppl/10.1021/acs.analchem.5b00988 Movie si_002) show no structural dependent features. Although all the grains are high-index surfaces, grains 1 and 3, which have contributions mainly from the (111) orientation, have very similar CVs. Grains 2 and 4, which are mainly (100) oriented, show lower peak currents and higher peak potentials. Furthermore, closer inspection reveals that on grains 1 and 3 (mainly of (111) orientation), the current decrease after the peak is reversible (increasing again after reversal of the potential sweep direction). This is likely related to the initial stages of surface oxide formation on Pt(111) in perchloric acid, which is highly reversible (*i.e.* surface oxide formation occurs at the same potential as reduction).[38] In contrast, on grains 2 and 4 (mainly (100) orientation), the current continues to decrease after reversal of the sweep direction, mirroring the irreversibility of surface oxidation on Pt(100).[38] Thus, we believe surface oxidation/reduction kinetics is (one of) the factors determining the shape of the voltammogram. Significantly, this effect would have remained unnoticed in (conventional) fixed-potential imaging, highlighting a considerable strength of voltammetric scanning SECCM. Importantly, these results illustrate that hydrazine oxidation at high-index Pt surfaces is strongly structure dependent.

In addition to individual and averaged CVs, the spatially resolved reactivity can be visualised through activity maps of various types. For example, as current values were recorded at least every 1 mV during the pixel-resolved CV

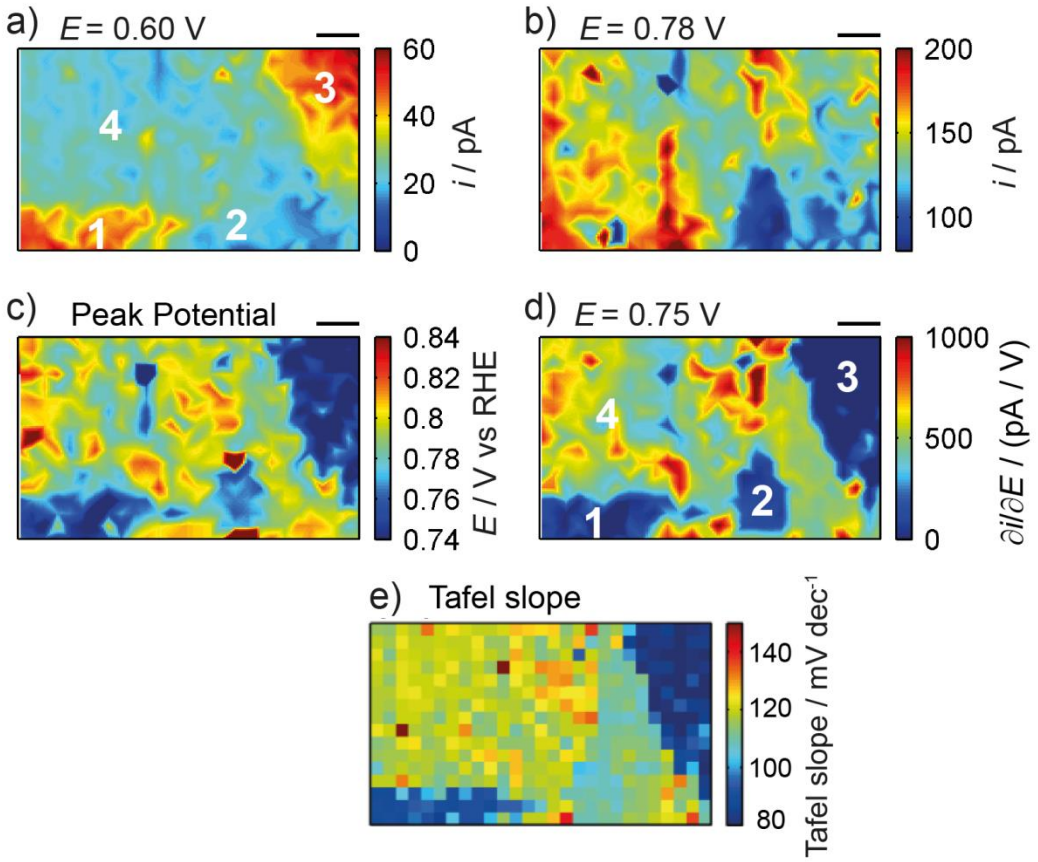

Figure 5.6 Various map representations of the SECCM data of a single region; **a-b)** activity, expressed as substrate current maps for E = 0.60 V and 0.78 V; **c)** peak potential; **d)** $\partial i/\partial E$ at E = 0.75 V. Note the different colour scales. **e)** Tafel slope in mV per decade determined using the data from 0.45 > E > 0.65 V. The scale bar is 10 µm in all images.

measurements, a series of equipotential maps can be constructed by plotting the electrochemical activity current (i_s) of all pixels at a given potential as a function of spatial position. The full series can then be compiled as a movie, (available at http://pubs.acs.org/doi/suppl/10.1021/acs.analchem.5b00988 Movie si_003), which illustrates the localised evolution of the surface current during a cyclic potential sweep. In the movie, with increasing potential, the activity of different grains starts to show up, providing a direct view of the electrochemical activity across the surface. Figure 5.6a and b are two frames of data from the i_s movie during the forward scan at

potentials of 0.60 V and 0.78 V respectively, but with the colour scales adjusted to highlight the full current range at each potential. These maps are conceptually similar to maps which could have been obtained with fixed potential SECCM imaging, but with voltammetric SECCM approach these are only 2 maps of 1800 maps that can be constructed from the data at different potentials. The chosen potentials for Figure 5.6a and b are close to the onset of the oxidation current (Figure 5.6a, $E = 0.60$ V) and the peak potential (Figure 5.6b, $E = 0.78$ V). In Figure 5.6a, grains 1 and 3 can be recognized as having higher activity, while grains 2 and 4 are visible in Figure 5.6b.

As evident in Figure 5.4c, SECCM CVs on this timescale typically show a peak during the oxidative potential sweep, and the potential at which this peak occurs is related semi-quantitatively to the driving force required for the reaction. This is shown in Figure 5.6c, from which it is clear that if the peak occurs at lower overpotential, then the current is higher in the surface activity maps in Figure 5.6a and b. Using another approach, a high order polynomial was fitted through each pixel-resolved CV to calculate $\partial i/\partial E$, with the result at $E = 0.75$ V shown in Figure 5.6d. This quantity again gives a measure of the ease of reaction, and the result is a map showing the distinct behaviour of the different grains. Finally, a Tafel analysis was performed for all four grains, using the potential interval from 0.45 V to 0.65 V (at the foot of the wave, where mass transport and concentration polarization can be neglected) and is shown in Figure 5.6e. For the whole area, the apparent Tafel slope is mainly within the range of 80 to 140 mV per decade. This range is within that of the previously reported Tafel slope values, 82 mV per decade to 110 mV per decade, for polycrystalline Pt electrodes in acidic solution.[29,39] However, the data herein are very illuminating showing that the precise slope is very grain-orientation dependent.

The average Tafel slopes for grains from 1 to 4 are 100 ± 12, 130 ± 2, 88 ± 3 and 139 ± 3 mV per decade, respectively. Comparing Figure 5.6a-b to 4c-e, it is demonstrated through the use of voltammetric SECCM it becomes possible to visualise/identify differences (especially in the $\partial i/\partial E$ maps) in electrochemical activity which would be invisible using fixed potential imaging.

5.3.3 Voltammetric SECCM of hydrazine oxidation in air

Besides the faradaic oxidation of hydrazine, there are also studies reporting catalytic (non-faradaic) decomposition of hydrazine.[25,40] Although the non-faradaic oxidation of hydrazine in air is slow at room temperature, it can be accelerated in the presence of catalysts, such as platinum, copper, and manganese.[25,30,40] As demonstrated recently that the three phase boundary in SECCM[13] provides high mass transport of oxygen, SECCM is an interesting technique to study the role of O_2 in the total oxidation reaction. Thus, imaging experiments were performed in the same area as shown in Figure 5.4a, but on a newly cleaned surface, without using the environmental cell. CVs were recorded every 2 μm between 0.45 V and 0.95 V. Figure 5.7a shows an equipotential i_s map extracted from the SECCM imaging experiment in air, at 0.78 V. Movies of i_s and i_{DC} for the CV measurements are provided online (http://pubs.acs.org/doi/suppl/10.1021/acs.analchem.5b00988 Movies si_004 and si_005). Compared with Figure 5.4c, Figure 5.7a shows that except for grain 1, the electrochemical activity of all the grains is almost completely suppressed. Similar to the approach in Figure 5.4c, CVs recorded at grains 1 to 4 at single pixels (red) and the averaged ones (black) are shown in Figure 5.7b. It is clear that hydrazine oxidation CVs in air exhibit different shapes and much lower current

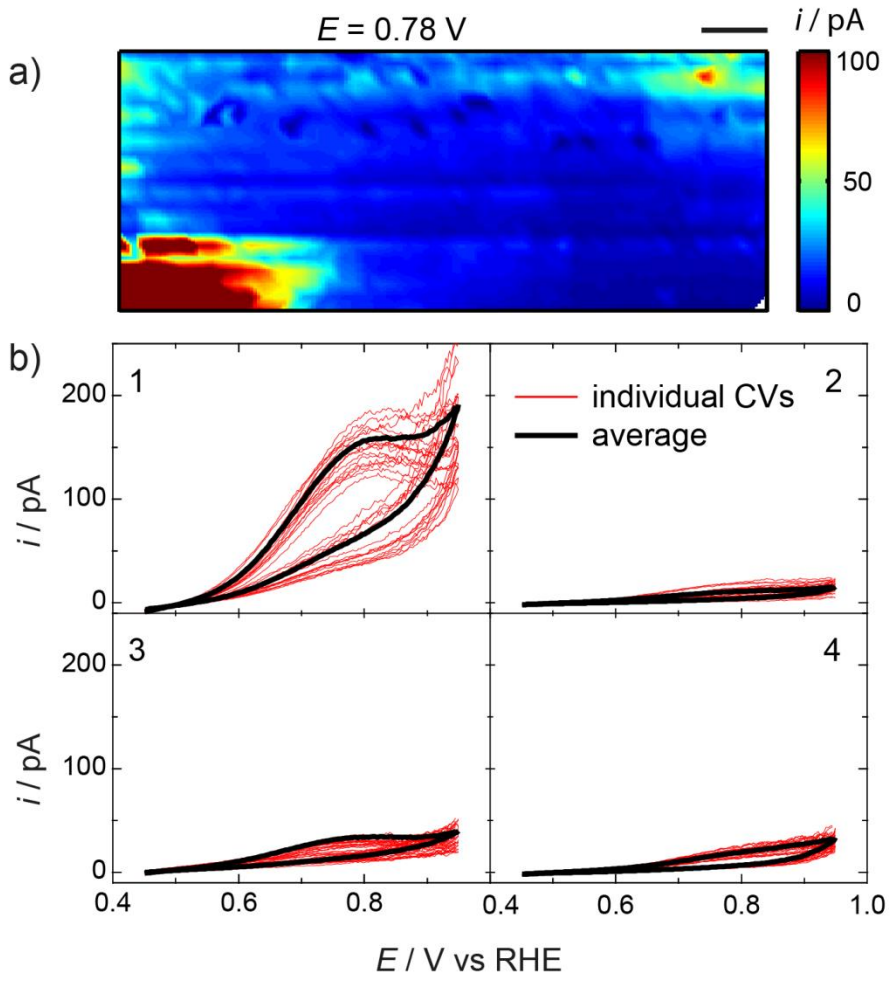

Figure 5.7 a) Equipotential is map of hydrazine oxidation in air at E = 0.78 V. The scale bar is 10 µm. **b)** Individual (red, 10-20 for each grain) and averaged (black) CVs for different grains in air. Numbers in b) correspond to grain areas marked in Figure 5.4a.

values compared with CVs in the absence of O_2, with the peak current, when discernible, shifted to higher overpotential.

To further understand the role of oxygen and the cause of the large differences in activity, a blank SECCM experiment in air was performed using just the supporting electrolyte. The potential was scanned between 0.45 V and 1.35 V at a sweep rate of 0.5 V s^{-1}. Averaged CVs in each of the four grains for all three imaging experiments (hydrazine oxidation in a deaerated solution, hydrazine oxidation in the presence of dissolved oxygen and blank CVs) are summarised in

Figure 5.8. Comparing the three measurements, it is clear that, generally, the presence of oxygen leads to a decrease in the currents observed for the oxidation of hydrazine. There are two main causes of this effect. First, it can be seen in the blank CVs that at potentials below 0.65 V, there is a significant (reduction) current due to the oxygen reduction reaction (ORR), in agreement with the previous findings (Chapter 4).[13] Thus, at potentials between 0.45 V and 0.65 V, the oxidation of hydrazine (positive current) overlaps with the reduction of oxygen (negative current) in an aerated solution, and the overall observed current in this potential range represents the sum of the two processes. As a result, the apparent current for the oxidation of hydrazine in air in this potential range is much smaller than that of the oxidation of hydrazine in deaerated conditions (and, similarly, the reduction current of oxygen with hydrazine present is smaller (in absolute terms) than that of the reduction of oxygen in the absence of hydrazine). Second, as mentioned above, hydrazine can react with oxygen through the following reaction at a catalyst (such as platinum) surface:

$$N_2H_4 + O_2 \rightarrow N_2 + 2H_2O \qquad (5\text{-}5)$$

This non-faradaic (*i.e.* no 'current-producing') reaction consumes hydrazine, thereby lowering the interfacial concentration of hydrazine. In fact, this reaction is most likely exacerbated in the experimental setup, as is the ORR effect mentioned above, due to the enhanced mass transport of oxygen at the three-phase boundary.[13] Consequently, a lower current for the (electrochemical) oxidation of hydrazine is observed compared to a deaerated solution, as the current is directly proportional hydrazine concentration.

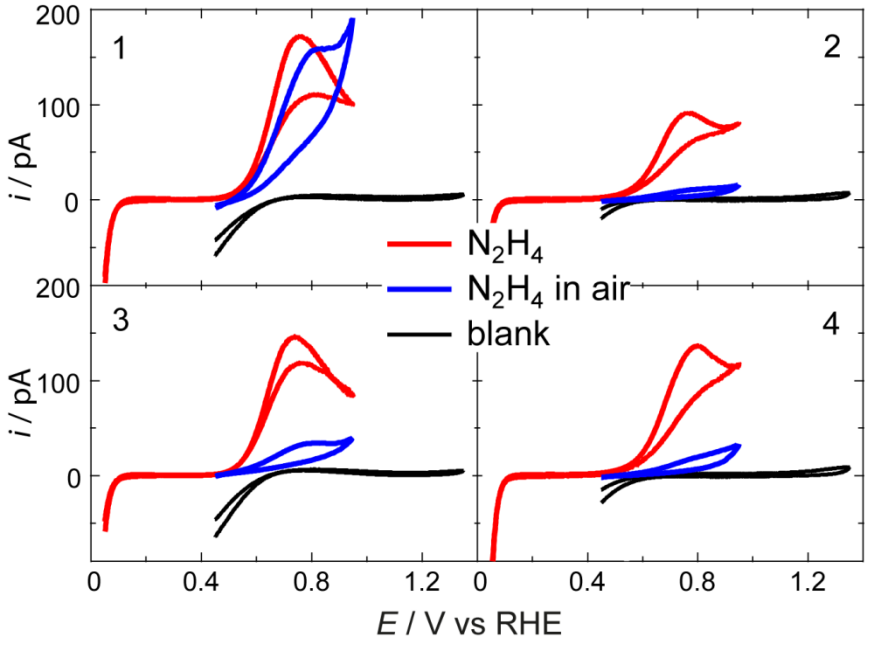

Figure 5.8 Comparison of N2H4 oxidation (red) in deaerated enviroment, N_2H_4 oxidation in air (blue), and blank (in air, black) averaged CVs for different grain orientations (numbers indicated).

In fact, this second mechanism to obtain the structural dependency can be exploited (at least in a semi-quantitative manner) of the non-faradaic reaction between oxygen and hydrazine. By using the observed current in the presence of oxygen as a probe for the residual hydrazine concentration (that is, the hydrazine concentration after the non-faradaic consumption of hydrazine), the extent to which the non-faradaic reaction takes place can be deduced. Specifically, substrate regions where there is a small decrease in current (such as grain 1) indicate a low activity towards the non-faradaic reaction, whereas a large decrease (such as grains 2, 3 and 4) represents a high activity. Using this approach, it is found that the activity towards the non-faradaic reaction of hydrazine and oxygen to follow the relative order: grain 2 > grain 4 > grain 3 > grain 1. Interestingly, this is the inverse of the electrochemical activity (see Figure 5.4c), and, at least in part, this rationalises the

trend because the faradaic and non-faradaic processes are in competition. Importantly, these results provide a novel method to probe local structure effects in non-faradaic catalytic reactions through electrochemical measurements, an avenue which will further explore in the future. There are also clearly implications for the optimal design of hydrazine voltammetric sensors in aerated solution.

5.4 Conclusions

This chapter highlighted the considerable power of voltammetric SECCM, which combines SECCM with CV measurements, as a methodology for electrochemical imaging. Compared to traditional fixed potential imaging,[8,11,13,41] this approach has significant attributes. First, as CVs are recorded at every pixel of the scanned area, it is possible to probe local electrochemical currents at multiple potentials (1800 separate potentials in the deaerated hydrazine CVs herein) and thus increases imaging efficiency. Furthermore, as the meniscus breaks and droplet residues are left on the substrate, as the pipette moves to a new position on the substrate for the next measurement, it is possible to determine the exact position and surface area of each pixel. Finally, it allows for potentiodynamic information to be obtained, complementing potentiostatic information from fixed potential imaging, which both have their uses in certain situations (cf. cyclic voltammetry and chronoamperometry).

In this chapter, using voltammetric SECCM, hydrazine oxidation at high-index Pt surfaces in air and in a deaerated environment was studied. Results showed CV characteristics of hydrazine oxidation at Pt electrode are strongly surface structure dependent. The reactivity of hydrazine at different surfaces can be

compared from equipotential maps and dynamic movies. For all grains studied here, grains having more (111) features show higher activity than grains having more (100) features. This might appear to counter studies with single-crystal electrodes, but it should be noted that the studies herein are on high-index and high defect facets, highlighting the importance of such features in the electrocatalytic oxidation of hydrazine oxidation on practical surfaces.

Significant changes in hydrazine oxidation activity were observed in air, where oxygen transfers through the three-phase boundary of the SECCM with high rates. It is found the presence of oxygen strongly decreased the detected electrochemical current for hydrazine oxidation at most of the Pt grains. The variation in activity between different grains was also much more pronounced than in the absence of air. These changes were ascribed to the overlap between the potentials for hydrazine oxidation and ORR as well as the non-faradaic decomposition of hydrazine with oxygen at certain Pt facets. These results emphasise the importance of considering oxygen in the voltammetric detection of hydrazine, which could greatly affect the response of the hydrazine sensors in a manner dependent on the Pt substrate used.

5.5 References

(1) Bard, A. J.; Mirkin, M. V. *Scanning Electrochemical Microscopy*; Marcel Dekker: New York, 2001.

(2) Bard, A. J.; Fan, F. R. F.; Kwak, J.; Lev, O. *Anal. Chem.* **1989**, *61*, 132.

(3) Amemiya, S.; Bard, A. J.; Fan, F. R. F.; Mirkin, M. V.; Unwin, P. R. *Annu. Rev. Anal. Chem.* **2008**, *1*, 95.

(4) Díaz-Ballote, L.; Alpuche-Aviles, M.; Wipf, D. O. *J. Electroanal. Chem.* **2007**, *604*, 17.

(5) Schrock, D. S.; Wipf, D. O.; Baur, J. E. *Anal. Chem.* **2007**, *79*, 4931.

(6) Nebel, M.; Grützke, S.; Diab, N.; Schulte, A.; Schuhmann, W. *Faraday Discuss.* **2013**, *164*, 19.

(7) Ebejer, N.; Schnippering, M.; Colburn, A. W.; Edwards, M. A.; Unwin, P. R. *Anal. Chem.* **2010**, *82*, 9141.

(8) Ebejer, N.; Güell, A. G.; Lai, S. C. S.; McKelvey, K.; Snowden, M. E.; Unwin, P. R. *Annu. Rev. Anal. Chem.* **2013**, *6*, 329.

(9) Snowden, M. E.; Güell, A. G.; Lai, S. C. S.; McKelvey, K.; Ebejer, N.; O'Connell, M. A.; Colburn, A. W.; Unwin, P. R. *Anal. Chem.* **2012**, *84*, 2483.

(10) Lai, S. C. S.; Patel, A. N.; McKelvey, K.; Unwin, P. R. *Angew. Chem. Int. Ed.* **2012**, *51*, 5405.

(11) Güell, A. G.; Ebejer, N.; Snowden, M. E.; Macpherson, J. V.; Unwin, P. R. *J. Am. Chem. Soc.* **2012**, *134*, 7258.

(12) Aaronson, B. D. B.; Chen, C.-H.; Li, H.; Koper, M. T. M.; Lai, S. C. S.; Unwin, P. R. *J. Am. Chem. Soc.* **2013**, *135*, 3873.

(13) Chen, C.-H.; Meadows, K. E.; Cuharuc, A.; Lai, S. C. S.; Unwin, P. R. *Phys. Chem. Chem. Phys.* **2014**, *16*, 18545.

(14) Serov, A.; Kwak, C. *Appl. Catal., B* **2010**, *98*, 1.

(15) Yamada, K.; Asazawa, K.; Yasuda, K.; Ioroi, T.; Tanaka, H.; Miyazaki, Y.; Kobayashi, T. *J. Power Sources* **2003**, *115*, 236.

(16) Rees, N. V.; Compton, R. G. *Energy & Environmental Science* **2011**, *4*, 1255.

(17) Elder, D. P.; Snodin, D.; Teasdale, A. *J. Pharm. Biomed. Anal.* **2011**, *54*, 900.

(18) Liu, D. Q.; Sun, M.; Kord, A. S. *J. Pharm. Biomed. Anal.* **2010**, *51*, 999.

(19) Metters, J. P.; Tan, F.; Kadara, R. O.; Banks, C. E. *Anal. Methods* **2012**, *4*, 1272.

(20) Liu, J.; Li, Y.; Jiang, J.; Huang, X. *Dalton transactions* **2010**, *39*, 8693.

(21) Chakraborty, S.; Raj, C. R. *Sensors and Actuators, B: Chemical* **2010**, *147*, 222.

(22) Hu, G.; Zhou, Z.; Guo, Y.; Hou, H.; Shao, S. *Electrochem. Commun.* **2010**, *12*, 422.

(23) Moussa, M.; Taha, F.; Gouda, M.; Singab, G. *Corros. Sci.* **1976**, *16*, 379.

(24) Andries, V.; Couturier, D. *Mater. Perform.* **2000**, *39*, 58.

(25) Cuy, E.; Bray, W. *J. Am. Chem. Soc.* **1924**, *46*, 1786.

(26) Moon, J.-S.; Park, K.-K.; Kim, J.-H.; Seo, G. *Applied Catalysis, A: General* **1999**, *184*, 41.

(27) Bard, A. J. *Anal. Chem.* **1963**, *35*, 1602.

(28) Rosca, V.; Koper, M. T. M. *Electrochim. Acta* **2008**, *53*, 5199.

(29) García, M. D.; Marcos, M. L.; Velasco, J. G. *Electroanalysis* **1996**, *8*, 267.

(30) Arnolds, K. *Zeitschrift fuer Naturforschung, Teil A: Physik, Physikalische Chemie, Kosmophysik* **1974**, *29*, 359.

(31) Nishihara, C.; Raspini, I. A.; Kondoh, H.; Shindo, H.; Kaise, M.; Nozoye, H. *J. Electroanal. Chem.* **1992**, *338*, 299.

(32) Álvarez-Ruiz, B.; Gómez, R.; Orts, J. M.; Feliu, J. M. *J. Electrochem. Soc.* **2002**, *149*, D35.

(33) Gómez, R.; Orts, J. M.; Rodes, A.; Feliu, J. M.; Aldaz, A. *J. Electroanal. Chem.* **1993**, *358*, 287.

(34) Aldous, L.; Compton, R. G. *Phys. Chem. Chem. Phys.* **2011**, *13*, 5279.

(35) Saito, Y. *Rev. Polarogr.* **1968**, *15*, 177.

(36) Dudin, P. V.; Unwin, P. R.; Macpherson, J. V. *PCCP* **2011**, *13*, 17146.

(37) Eisner, U.; Gileadi, E. *J. Electroanal. Chem. Interfacial Electrochem.* **1970**, *28*, 81.

(38) Rodes, A.; Zamakhchari, M. A.; El Achi, K.; Clavilier, J. *J. Electroanal. Chem. Interfacial Electrochem.* **1991**, *305*, 115.

(39) Harrison, J. A.; Khan, Z. A. *J. Electroanal. Chem. Interfacial Electrochem.* **1970**, *28*, 131.

(40) Gaunt, H.; Wetton, E. A. M. *J. Appl. Chem.* **1966**, *16*, 171.

(41) Lai, S. C. S.; Dudin, P. V.; Macpherson, J. V.; Unwin, P. R. *J. Am. Chem. Soc.* **2011**, *133*, 10744.

Chapter Six

Impact of Surface Chemistry on Nanoparticle-Electrode Interactions in the Electrochemical Detection of Nanoparticle Collisions

Abstract

The electrochemical detection of a single nanoparticle (NP) at a support electrode can provide key information on surface chemistry and fundamental electron transfer (ET) properties at the nanoscale. This study employs scanning electrochemical cell microscopy (SECCM) as a fluidic device to both deliver individual citrate-capped gold nanoparticles (AuNPs) and study the interactions between them and a range of alkanethiol-modified Au electrodes with different terminal groups, namely, -COOH, -OH and -CH_3. Single NP collisions were detected through the AuNP-mediated ET reaction of $Fe(CN)_6^{4-/3-}$ in aqueous solution. The collision frequency, residence time and current-time characteristics of AuNPs are greatly affected by the terminal groups of the alkanethiol. Methods to determine these parameters, including the effect of the instrument response function, and derive ET kinetics are outlined. To further understand the interactions of AuNPs with these surfaces, atomic force microscopy (AFM) force measurements were performed using citrate-modified Au-coated AFM tips and the same alkanethiol-modified Au substrates in aqueous solution at the same potential bias as for the AuNP collision experiments. Force curves on OH-terminated surfaces showed no repulsion and negligible adhesion force. In contrast, a clear repulsion (on approach) was seen for

COOH- terminated surface and adhesion forces (on retract) were observed for both COOH- and CH_3-terminated surfaces. These interactions help to explain the residence times and collision frequencies in AuNP collisions. More generally, as the interfacial properties probed by AFM appear to be amplified in NP collision experiments, and new features also become evident, it is suggested that such experiments provide a new means of probing surface chemistry at the nanoscale.

Chapter 6

6.1 Introduction

Metal nanoparticles (NPs) find many applications in numerous fundamental and applied fields, with electrochemical studies particularly prominent.[1,2] The electrochemical activity of a NP not only depends on the intrinsic electron transfer (ET) properties of the NP, but also on the interaction between the NP and the support electrode surface.[3,4] While tremendous efforts have been made to understand correlations between NP properties and NP electroactivity,[5] interactions between NPs and electrode surfaces have been studied much less.

To investigate the interaction between a NP and an (electrode) surface, well-defined and thoroughly characterised model systems are needed. Self-assembled monolayers (SAMs), particularly alkanethiol monolayers on gold electrodes, which were used herein, are useful in this respect, as they form well-defined films with the possibility of a high degree of control over the thickness (within ~ 1 Å, one CH_2 group), and a wide range of accessible terminal group chemical functionalities.[6,7] The ET probability across an insulating layer, such as a SAM, separating an electrode and a redox species in solution is proportional to $\exp(-\beta d)$, where d is the thickness of the insulating monolayer and β is the tunnelling decay constant (β ~ 1 $Å^{-1}$ for a saturated hydrocarbon chain).[8] Consequently, SAMs with carbon chains longer than 10 carbon atoms (~ 1 nm) are expected to effectively block ET between a species in solution and the electrode surface, with little faradaic current flow. Interestingly, the Fermín[9,10] and Gooding[11] groups found that electron tunnelling from redox species to electrodes could be restored by NP adsorption on top of the insulating layer. This phenomenon was further interpreted by a theoretical framework proposed by Chazalviel and Allongue.[12] The basis of this model is that electronic coupling between a NP and a support electrode may be sufficiently strong

to allow the NP to facilitate ET between the support electrode and solution redox species. While this model has been validated for NP-mediated ET on a macroscopic scale, much less is known about a single NP in this configuration.

To electrochemically detect single NPs, the main approaches rely on separating the responses of individual NPs, either spatially and/or temporally.[5] For the latter, Bard's group introduced a novel strategy by performing NP-impact experiments on bare ultramicroelectrodes (UMEs).[13-15] In this approach, a conductive support electrode is held at a potential at which it is kinetically inert towards an (electrocatalytic) reaction of interest. As a single NP in solution collides with the electrode, the contact sets up a reaction at the NP, giving rise to a change in the faradaic current. Since its introduction, this methodology has been employed by several research groups to study different combinations of electrode materials and redox mediators.[16-21] Two general types of signals, staircase or blip, have been reported so far in these NP-impact experiments. Staircase signals are found in systems where particles sequentially adhere to the electrode and continuously catalyse the reaction, so that with each NP addition, the current-time curve is a series of current jumps (new NP arrived) and plateaus.[22-24] Blip responses are produced when NPs only interact with electrodes for a short amount of time.[25]

Besides using bare UMEs, there are a few recent reports of using chemically-modified UMEs to perform NP-impact experiments.[26,27] For example, Bard's group[26] performed Pt NP collisions at a Pt UME passivated with a thin TiO_2 film, in solutions containing $K_3Fe(CN)_6$ and rationalized their findings in a recent model model taking mass transport of the redox species, electron transfer kinetics at the NP surface and electron tunnelling through the insulating layer into account.[28] The TiO_2 film blocked the conductive Pt UME surface but allowed electron tunnelling through

the film when Pt NPs landed on the surface, in (qualitative) agreement with the Chazalviel-Allongue model described above.[12] The Crooks' group[27] studied Pt NP collisions at an Au UME modified with polyelectrolyte multilayer films (up to 5 nm thick) for the electrooxidation of N_2H_4. For Pt NPs with a diameter of ~ 57 nm, there was sufficient electronic coupling through the films for electrocatalysis to occur upon Pt NP collision with the UME. Pt NP collision frequencies were controlled by manipulating the electrostatic charge presented by the polyelectrolyte multilayer films.

This chapter investigated the effect of the surface functionality of the collector (support) electrode on NP interactions by using scanning electrochemical cell microscopy (SECCM). This technique has several advantages over NP-impact experiments with UMEs. First, due to the small size of the pipette (1.5 to 3.0 μm in this study), which is used to form an electrochemical cell with a substrate (electrode) of interest by meniscus contact, the background current is significantly decreased. Second, electrode materials which cannot be fabricated as UMEs can be used as the collector electrode in SECCM.[29] Third, one can select an area of interest on a substrate to carry out measurements, a feature used herein to identify areas with very high quality SAM organization (low background current). Forth, although not exploited in this work, one can easily use an electronic field to control the delivery of particles and for particle counting.[30] The principles of this technique for NP detection are shown in Figure 6.1. A meniscus at the end of a double barrel pipette forms a small electrochemical cell with an alkanethiol modified Au (SAM/Au) substrate that is used as the working electrode. This electrode is inert towards ferrocyanide ($Fe(CN)_6^{4-}$) oxidation, and in the absence of AuNPs, there is essentially

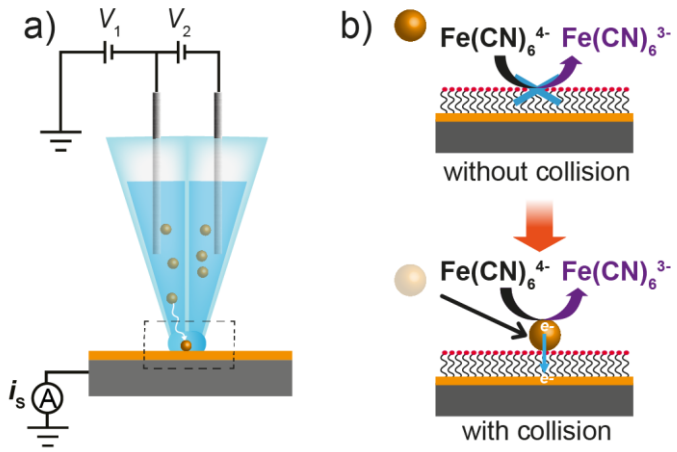

Figure 6.1 a) Schematic of the SECCM setup. V_1 is the potential at which SECCM conductive cell is floated with respect to ground and V_2 is the bias potential between the QRCEs in the pipette. The current flowing through the working electrode is denoted by i_s. **b)** Principle of the electrochemical detection of a single AuNP collision on an alkanethiol modified substrate. Top: an alkanethiol monolayer effectively inhibits electron transfer between a redox species ($Fe(CN)_6^{4-}$) in solution and an electrode surface. Bottom: an AuNP collision opens up a new electronic pathway and mediates electron transfer.

no interfacial electron transfer. However, AuNP collisions on the surface form an AuNP/SAM/Au structure and electron transfer between $Fe(CN)_6^{4-}$ and the Au substrate (mediated by the AuNP) occurs.

These interactions were further investigated by performing AFM force measurements, using citrate-coated AFM tips and substrates modified by SAMs with the same terminal group functionalities (-OH, -COOH and $-CH_3$). These interactions were discussed in terms of surface wetting, hydrogen bonding and surface charge, and assess their implications for NP-impact experiments. The results presented here provide new insights into the nature of NP-substrate interactions and their impact on ET processes. A further outcome of the work is that NP collisions provide a sensitive means of probing surface chemistry.

6.2 Results and discussion

6.2.1 Electrochemical characterisation of substrates

Macroscopic CV characterisation of bare Au and SAM/Au electrodes

Typical CVs (scan rate 100 mV s^{-1}) for the oxidation of 1 mM $K_4Fe(CN)_6$ in 100 mM KCl at a macroscopic gold electrode with and without the different SAMs are shown in Figure 6.2.

The voltammetric response at a bare Au electrode (black line) shows the expected reversible redox behaviour, with a peak-to-peak separation of ~ 60 mV, characteristic of a facile outer-sphere redox mediator such as $Fe(CN)_6^{4-/3-}$ on a metal electrode surface. Modification of the electrode by an alkanethiol SAM strongly inhibits the electrochemical reaction, as evident from the much decreased current magnitudes in Figure 6.2, indicative of well-ordered closely packed SAMs.[9,31] Upon

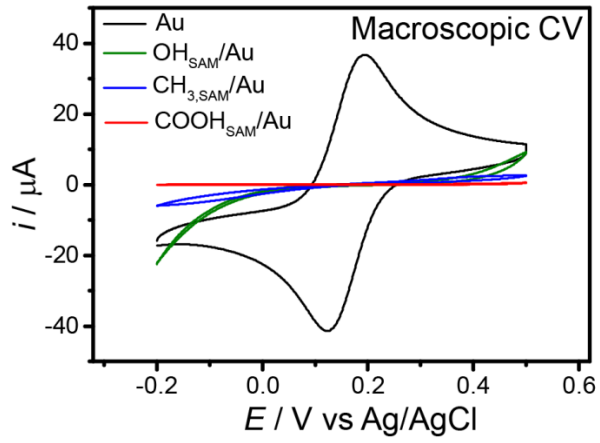

Figure 6.2 Macroscale cyclic voltammograms (CVs) for 1 mM $K_4Fe(CN)_6$ in 100 mM KCl on bare Au and the three different SAM/Au electrodes (see figure). All CVs shown in this figure are the second cycles.

closer inspection, it can also be observed that the extent to which the SAM inhibits ET depends, to some degree, on the terminal groups. The electrochemical activity decreases in the order of OH_{SAM}/Au > $CH_{3,SAM}$/Au > $COOH_{SAM}$/Au, which is determined by the electrostatic forces associated with the terminal groups and the (negatively-charged) redox species.[32] Nonetheless, irrespective of the end-termination, the blocking of ET by all the SAMs is sufficient for these electrodes to be regarded as electrochemically 'inert' for the NP-impact experiments that follow.

Microscopic CV characterisation of bare Au and SAM/Au electrodes in the SECCM

To further verify the quality of SAMs at the microscopic scale, as well as to validate the approach, micro-scale CVs of Au and SAM/Au electrodes were recorded using the SECCM setup, with a pipette of ~ 3 μm diameter, shown in Figure 6.3a and b. Clearly, all of the SECCM CVs of SAM/Au electrodes showed considerable blocking towards $Fe(CN)_6^{4-}$ oxidation. The extremely low current response of the SAM/Au electrode in Figure 6.3b indicates that the SECCM setup is close to ideal for the proposed studies. It is important to note that pinholes can be present in the SAMs (as inferred from the macro-CVs discussed above). This could also be seen sometimes with SECCM, with CVs produced that had a relatively high current (Figure 6.3c). However, a key feature of SECCM is that surface current can be used as an indicator of local SAM quality, by landing the pipette on different areas of the substrate and performing chronoamperometric measurements. By doing this,

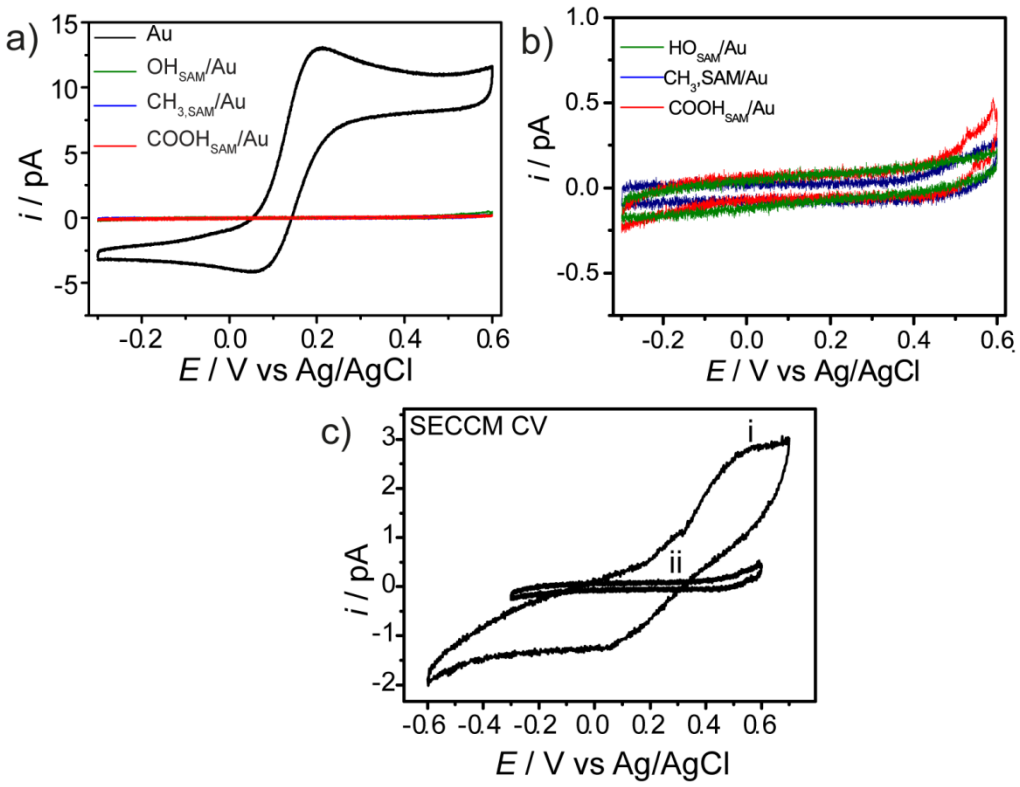

Figure 6.3 a) Microscale CVs recorded for bare Au (black line) and various SAM/Au electrodes (coloured lines) by using a pipette of 3 μm diameter in the SECCM setup. b) Zoom-in of the CVs at SAM/Au electrodes. **c)** Microscale CVs in the SECCM setup for the case where the voltammetric response indicates that (i) pinholes are apparent; and (ii) the surface is well blocked, in the region of the SAM targeted by SECCM. Potential sweep speed: 100 mV s^{-1}. Electrolyte solution: 1 mM $K_4Fe(CN)_6$ and 20 mM KCl.

a 'low background' current area can be selected (indicative of a closely-packed SAM layer) to carry out NP-impact experiments. Based on the CVs, all NP-impact experiments were performed at a collector electrode potential of 400 mV, a potential well in the mass transport-limited regime for $Fe(CN)_6^{4-}$ oxidation at both macroscopic Au surface and SECCM configuration on the CV timescale, but as shown below, where kinetics effects have to be considered (and can be revealed) for

$Fe(CN)_6^{4-}$ oxidation at AuNPs, due to the much higher mass transport rates at isolated NPs.

6.2.2 NP-impact experiments at SAM/Au electrodes

NP-impact experiments were performed using the SECCM setup with electrolyte solutions containing 1 mM $K_4Fe(CN)_6$ and 5 nM citrate-stabilized AuNPs, with no additional supporting electrolyte. The average size of the AuNPs was determined by analysis of transmission electron microscopy (TEM) images and they were found to be 5 nm in radius as shown in Figure 6.4. The AuNP concentration chosen ensured that sufficient collision events could be observed and the relatively low ionic strength served to minimise AuNP agglomeration.

For SECCM NP-impact experiments, the pipette slowly approached the substrate at a speed of 100 nm s^{-1} while holding the substrate potential at -200 mV. Meniscus contact resulted in the formation of an electrochemical cell with the substrate, as evidenced by a spike current at the substrate due to double layer charging. The meniscus thickness as estimated from the conductance current was a

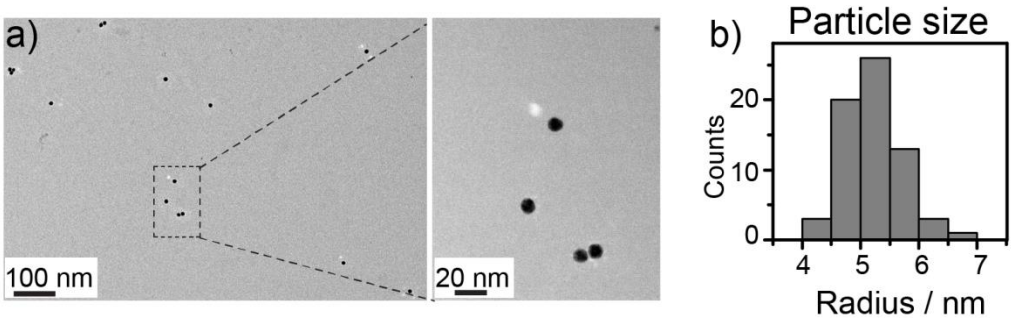

Figure 6.4 a) TEM images of AuNPs used in NP-impact experiment. **b)** Particle size distribution of AuNPs obtained from TEM images.

few hundred nm.[33] This signalled the pipette movement to stop. The potential was then switched to +400 mV and current-time traces were recorded continuously, using a highly sensitive home-built autoranging current amplifier. The bandwidth of the current amplifier was set to 100 Hz, for the current range used, 10 fA/V to 10 pA/V. The measured signal was passed through a first order low pass filter at 1 kHz to reduce high frequency noise. Data points were collected every 650 μs, with each point being the average of 64 readings, *i.e.* with a reading acquired every 10 μs. Herein, all potentials are reported with respect to an Ag/AgCl QRCE for SECCM. All signals that were higher than 2 times the standard deviation of the background were counted automatically as a peak and, after this process, all the peaks found in this way were checked manually.

6.2.3 AuNP collisions at OH_{SAM}/Au electrodes

Typical current-time traces recorded at an OH_{SAM}/Au electrode with a 3 μm diameter pipette is shown in Figure 6.5. Before AuNP-impact experiments, a control experiment was performed using a pipette of the same size with solution containing only 1 mM $K_4Fe(CN)_6$ (*i.e.* no AuNPs) and the 'blank' current-time trace is provided in Figure 6.5a. As seen from the trace, after stepping the working electrode potential from -200 mV to +400 mV (as for the NP-impact experiment), there is a charging current, which quickly decays to a current of negligible magnitude. At long-time, the trace is featureless and the current value is small (~ 0.1 pA), indicating negligible electron transfer between $Fe(CN)_6^{4-}$ and the Au electrode, making this a very attractive platform for detecting NP collisions.

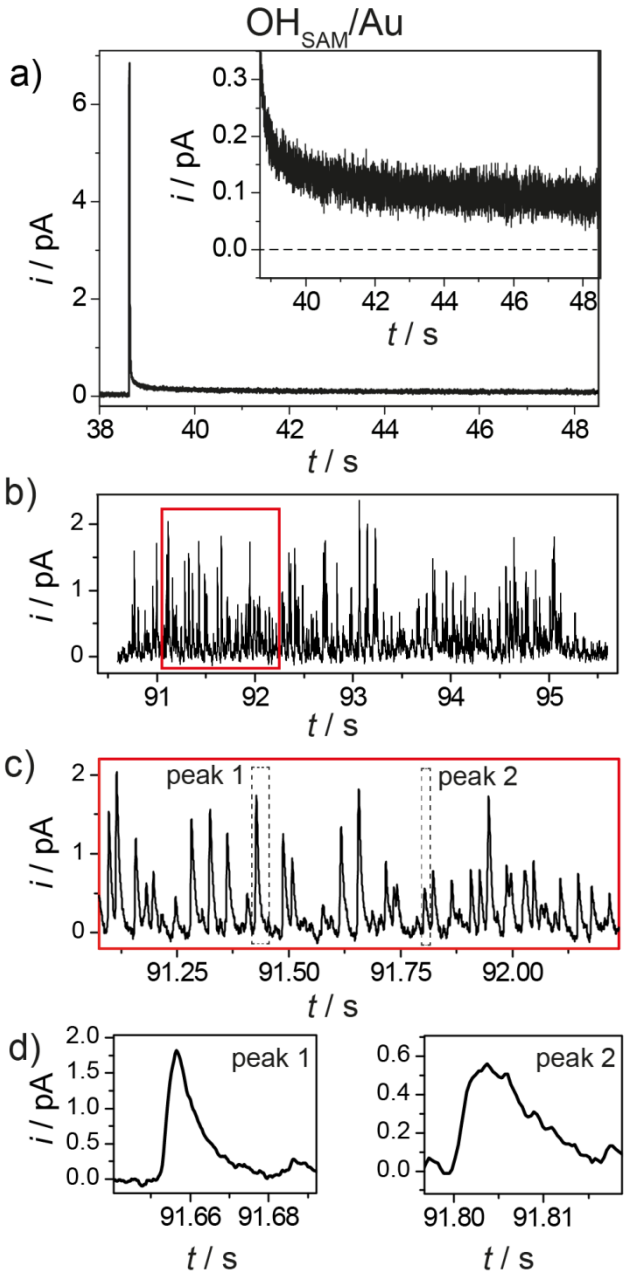

Figure 6.5 Current-time traces recorded at an OH_{SAM}/Au electrode bias at 400 mV using a 3 μm diameter pipette in the **a)** absence (only 1 mM $K_4Fe(CN)_6$) and **b)** presence of AuNPs (1 mM $K_4Fe(CN)_6$ + 5 nM AuNP). **c)** Zoom-in of the AuNP collision current trace within a time range of ~1 s. **d)** Expanded view of the current transients for peak 1 (high peak current) and peak 2 (low peak current).

In the presence of AuNPs in the pipette, clear distinctive current peaks in the time-trace are observed, as shown in Figure 6.5b, indicating the occurrence of discrete electrochemical reactions on the substrate, due to AuNP collisions. Figure 6.5b (inside the red box) provided a detailed view of the transients for each NP collision, over a time range of ~ 1 s, and plot the data in Figure 6.5c. This shows that the current spikes are discrete signals, with some variation in the peak current values. Two examples of current-time responses with different peak currents are shown in Figure 6.5d. Clearly, they both have a relatively fast rise time (a few ms) to the peak, followed by a slower decay down to the baseline level. Current spikes for NP collisions have been reported extensively,[16,22] but not with this clarity. In general terms, three distinct mechanisms have been proposed which can yield a spike-shaped transient. First, spikes can be caused by 'elastic' NP collisions.[25] Here, a NP comes into contact (*i.e.* within electron tunnelling distance) with the substrate electrode for a brief period of time, before diffusing away. Second, the NPs can be deactivated, either due to 'poisoning' of the reaction by products or intermediates of the probe redox system, or poisoning by the substrate electrode material.[34,35] Finally, the probe redox process can be self-limiting, such as in the case of NP dissolution or underpotential deposition on the NP.[20,36]

The redox species used in this work, $Fe(CN)_6^{4-/3-}$, is not expected to cause AuNP poisoning. There are several examples of NPs on SAMs showing high electrochemical activity to support this idea.[9,37,38] Thus, NP poisoning and self-limiting reactions can be reasonably ruled out as causes for the spike shape, and attribute this to a 'semi-elastic' collision of AuNPs on the surface. As the AuNP

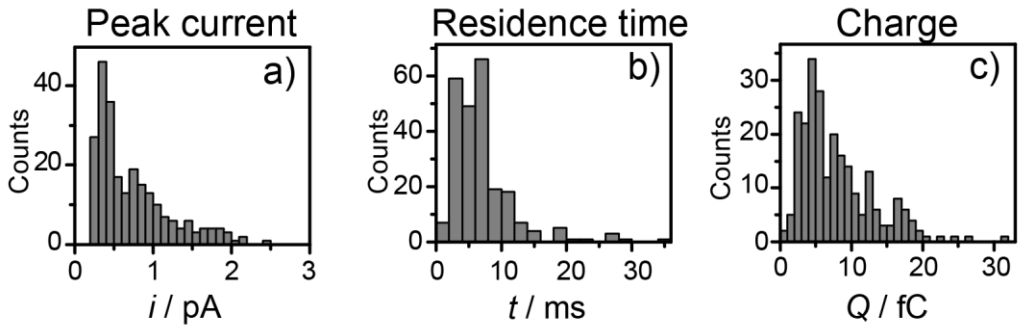

Figure 6.6 Statistical distributions of **a)** peak current, **b)** residence time, and **c)** charge of AuNP collisions at an OH_{SAM}/Au substrate from the current-time trace in Figure 6.5b.

comes into contact with the SAM/Au electrode, electron tunnelling takes place, setting off the redox reaction and giving rise to a rapid increase in electrochemical current. The NP can become trapped (transiently) in the tunnelling region or stabilised on the surface for a certain time. Once the NP leaves the tunnelling region, the current starts to decay with time.[39] To obtain more information on these AuNP collisions, statistical analysis was carried out using the data in Figure 6.5b. The results are summarised in Figure 6.6a-c, which shows the peak current, NP residence time on the electrode and charge of each collision event, respectively. Further analysis is given in Table 6-1 and those data was explained in more detail below.

Estimation of AuNP collision frequency

The theoretical AuNP collision frequency (assuming one pass of a NP with the electrode) is typically estimated based on the diffusion-based mass transport of AuNPs to the collector electrode. The landing frequency is then determined by the diffusion-limited flux equation. For an inlaid ultramicroelectrode (UME), the flux is given by equation (6-1): [5,22]

$$f = 4D_{NP}c_{NP}N_A r_{UME} \quad (6\text{-}1)$$

where f is the landing frequency, D_{NP} is the NP diffusion coefficient , c_{NP} is the NP bulk concentration, N_A is the Avogadro constant (6.022×10^{23} mol^{-1}), and r_{UME} is the disk radius of the UME, herein the radius of the meniscus.

The diffusion coefficient of AuNP can be estimated from the Stokes–Einstein Equation:

$$D_{NP} = k_B T / 6\pi\eta r_{NP} \quad (6\text{-}2)$$

in which k_B is the Boltzmann constant ($k_B = 1.381 \times 10^{-23}$ J K^{-1}), T is the temperature (298 K), and η is the dynamic viscosity of water ($\eta = 8.90 \times 10^{-4}$ Pa s at 25 °C). For a 5 nm radius AuNP, $D_{NP} = 4.9 \times 10^{-7}$ cm^2 s^{-1} is obtained. Combining the two equations and considering that the flux down a pipette is about 10 % of the flux of a UME of the same size,[29,33] the calculated collision frequency at a 3 μm diameter pipette is 0.018 s^{-1} pM^{-1} (or 25×10^4 s^{-1} pM^{-1} cm^{-2}). The experimental AuNP collision

Table 6-1. AuNP collision frequencies and the median values of peak current, residence time and charge at three different SAM/Au electrodes. Potential: +400 mV *vs.* Ag/AgCl

Electrode	shape	f	i_p	$i_{p,c}$	τ_p	Q
		10^4 s^{-1} pM^{-1} cm^{-2}	pA	pA	ms	fC
OH_{SAM}/Au	spike	12.80	0.55	0.77	6.2	6.30
$COOH_{SAM}$/A	spike/plateau	4.30	0.47	0.49	17.6	10.03
$CH_{3,SAM}$/Au	spike	0.16	0.21	0.37	7.0	2.00

f, collision frequency;
i_p, peak current;
$i_{p,c}$, corrected peak current (see text);
τ_p, residence time;
Q, charge.
All values of i_p, $i_{p,c}$ τ_p, and Q in Table 6-1 are median values.

frequency (f) at an OH_{SAM}/Au electrode was determined to be 12.8 $\times 10^4$ s^{-1} pM^{-1} cm^{-2} (Table 6-1), which is in the same order of magnitude as the theoretical value and roughly the same range as reported by other groups (typically ~ 10^4 s^{-1} pM^{-1} cm^{-2}).[5]

Estimation of diffusion-limited current for a single AuNP

The experimental peak current (i_p) distribution (Figure 6.6a), shows a broad range of values from 0.25 pA to 2.5 pA with a median value of 0.55 pA. An indication of the current expected from a NP collision can be estimated by calculating the steady-state diffusion-limited current generated at an individual spherical NP in contact with a planar electrode using equation (6-3),[13,14]

$$i_{lim} = 4\pi(\ln 2)nFDcr_{NP} \quad (6\text{-}3)$$

where n is the number of electrons transferred (1), F is the Faraday constant (96485 C mol^{-1}), D is the diffusion coefficient of $Fe(CN)_6^{4-}$ (6.67 $\times$ 10^{-6} cm^2 s^{-1}),[40] c is the concentration of $Fe(CN)_6^{4-}$ (1 mM), and r_{NP} is the radius of AuNP (5 nm). From equation (6-3), i_{lim} is 2.8 pA. It can be seen that the overwhelming majority of the responses are smaller than this value. This difference in terms of heterogeneous ET kinetics was discussed below.

The effect of the instrument response function

A discussion of the observed residence time is now warranted. For these studies, in order to probe the small currents arising from NP collisions (often < 1 pA), a high sensitivity (charge sensitive) current amplifier was employed with a bandwidth of 100 Hz (corresponding to a ~ 20 ms response time). Importantly, this is

orders of magnitude slower than the diffusional timescale of freely diffusing NPs ($\tau_D = L^2/D$, where L is the diffusion length and D the diffusion constant). Considering that the NP needs to remain within tunnelling distance (a few nanometres at most) of the electrode surface, and the diffusion coefficient of the NP employed is 4.9×10^{-7} $cm^2\ s^{-1}$ (See above), τ_D is tens of ns. Thus, in order to detect a NP in these studies, the NP must stay near the electrode for a reasonable period of time (several ms and longer) and the SECCM measurement recorded such events.

On this timescale, a NP collision can be considered as a binary event (the NP is either in contact or 'far' away from the electrode surface). This would result in an ideal 'on-off' signal as illustrated by the black *square wave* signal in Figure 6.7,

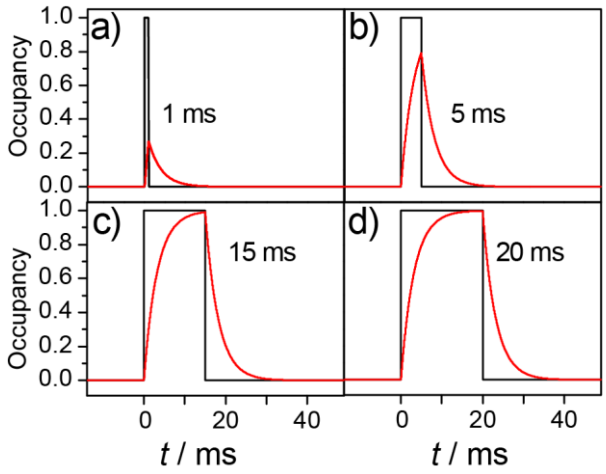

Figure 6.7 Plots of the occupancy as a function of time (black line) and its convolution (red line) with the electronic impulse function for event time, *t*, values of **a)** 1 ms, **b)** 5 ms, **c)** 15 ms and **d)** 20 ms.

where occupancy of 0 indicates NP away from the surface and 1 means NP on the surface. However, the square signal is lost due to the limited time response of electronics. The impulse response of the electronics follows an *exponential decay* and can be written as $(2\pi/\tau)\cdot exp(-2\pi t/\tau)$,[41] where τ is the time constant of current amplifier (20 ms) and t is the time of an event (in this case, residence time of the particle at the support electrode surface). By convolving the occupancy plot (black wave) with the electrometer response (exponential decay), transient signals (shown in red line) corresponds to the experimentally observed signal can be obtained, in which the instrument effect can be fully taken into account. The peak occupancy values in these transient signals indicate the fraction of the observed current relative to the unattenuated signal (i.e. signal would be measured if the electronics are infinitely fast).

Using τ = 20 ms, as employed for the studies herein, the convolutions of 'ideal' (binary 'on-off') signals were calculated with the impulse response of the electronics for events of different time scales, t, ranging from 1 to 20 ms, and shown in Figure 6.7a-d. These convolutions values demonstrate the fraction of the observed value compared to the 'real' value, which is 1 herein.

These figures illustrate a few intuitively simple, but important effects. First, the response time of the electronics leads to a signal with a different shape than the real (square-wave) occupancy signal. In particular, the sharp increase (and decrease) of the square-wave signal are drawn out to a slow rise (and decay) time. Second, the observed signal requires 20 ms to reach the plateau of the real occupancy signal. Consequently, for events shorter than 20 ms (Figure 6.7a and b), the observed (convoluted) peak value is only a fraction of the 'real' (deconvoluted) value. For example, in Figure 6.7a, for a t value of 1 ms, the fraction is 27 %. For a t of 15 ms

(Figure 6.7c), 99 % of the real occupancy magnitude is recovered. Third, and significantly, the residence time of a NP (τ_p) on the surface is given by the time between the start of the observed signal increase until the start of the decrease of the signal (and not by the total width of the signal). On this basis, residence times for the OH_{SAM}/Au system are summarized in Figure 6.6b.

For AuNP collision at the OH_{SAM}/Au electrode, the median time is 6.2 ms, corresponding to an occupancy of 85 %, which means the observed current in the experiments is attenuated to about 85 % of the 'real' value had the measurement electronics responded fully. This partially explains the lower current observed, but is not the main factor for the lower than diffusion-limited values, as discussed below. Importantly, because the occupancy for each signal can be determined, corrected peak currents ($i_{p,c}$), representing what would be the non-attenuated response, can be obtained and they are shown in Table 6-1. For the OH_{SAM}/Au system, the corrected median current peak value is 0.77 pA.

It is importantly to point it out that although the peak current is attenuated (see discussion above), as the measurements are made using a charge-sensitive detector, the total charge of an event is conserved (i.e. the magnitudes of the integral of the black square wave signal and red convoluted signal in Figure 6.6 are equal). By integrating each current time trace, the total charge (Q) for each collision can further be obtained, as shown in Figure 6.6c. In this case, the median charge of 6.3 fC corresponds to an event of just 3.7×10^4 electrons. As colloidal NPs are likely to have a different charge than a bulk electrode which is under potential control, some charge transfer is needed to equilibrate the potentials when an NP comes into contact with a bulk electrode. For an AuNP of 5 nm radius, approximately a few hundred electrons are needed to equilibrate the potential of the NP in solution with the

support electrode upon contact from 0.8 V to reach 0 V vs. SHE, corresponding to a charge of up to ~ 10^{-17} C.[42] Considering this, a change of 600 mV in this work will correspond to about the same charge (~ 10^{-17} C), which is negligible compared to the charge observed (10^{-15} C). Therefore, the observed current cannot be attributed to NP charging alone, and must be almost entirely the result of the redox reaction at the NP surface.

6.2.4 AuNP collisions at $COOH_{SAM}$ /Au electrodes

To gain further insight into the effect of the surface functionality on NP electrocatalytic impacts, 11-mercaptoundecanoic acid ($COOH_{SAM}$) were also used, which provides a different hydrophilic surface. Figure 6.8 shows current-time traces in the absence (a) and presence (b-c) of AuNPs recorded at a $COOH_{SAM}$/Au, using a 1.5 μm diameter pipette. Due to the low collision frequency of this substrate, partly due to the use of a smaller pipette, data were collected and analysed over a longer time period compared that for OH_{SAM} substrate. Again, the control experiment (Figure 6.8a) showed a featureless background. A zoomed-in current-time trace in Figure 6.8c gives a clearer view of distinctive collision signals. In contrast to AuNP collisions at an OH_{SAM}/Au electrode (section 6.2.3), AuNP collisions at $COOH_{SAM}$/Au electrodes can be separated into two distinct types of signals, as marked by '°' and '*' in Figure 6.8c-d. The first type of signal, marked by '°', consists of spike, with the current rising to peak value and then decaying, similar to the signal observed for AuNP collisions at the OH_{SAM}/Au electrode. In contract, the second type of signal (marked by '*') shows a current plateau of a few tens of milliseconds. These two different signal traces suggest two distinct types of interactions of AuNPs with the substrate, which will be discussed in detail later.

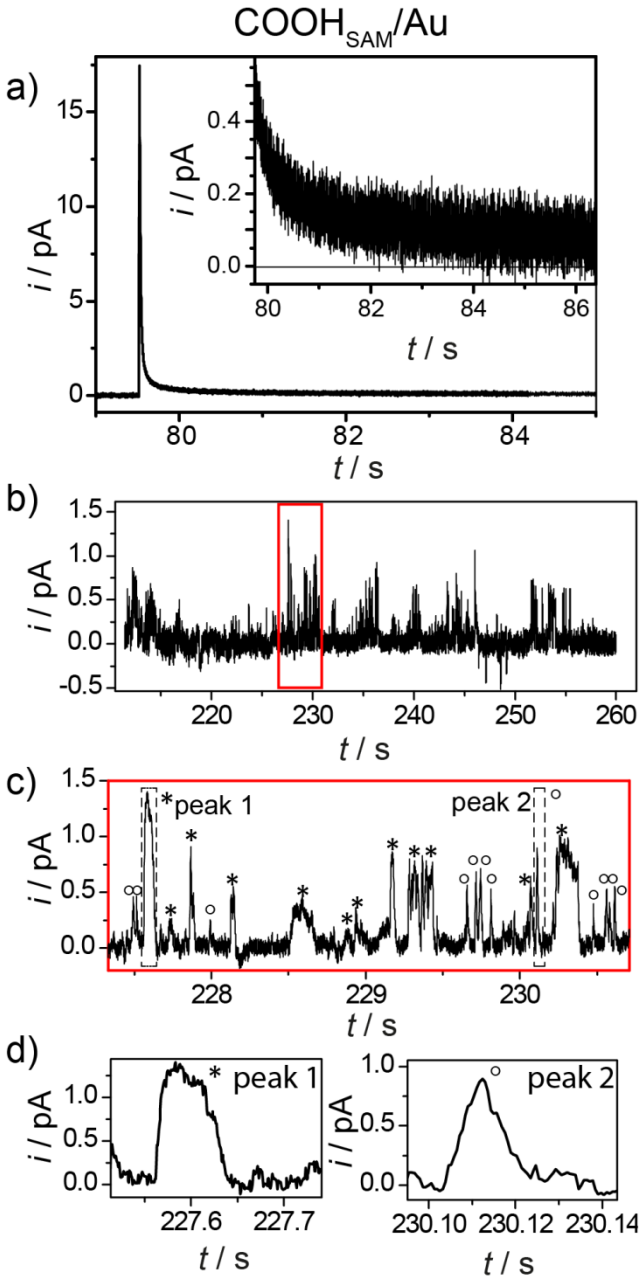

Figure 6.8 Current-time traces recorded at a $COOH_{SAM}$/Au substrate using a 1.5 μm diameter pipette in the **a)** absence and **b)** presence of AuNPs. **c)** Zoom-in of current transients within a time range of ~3.0 s. The transients display two types of peaks. Peaks displaying a plateau current are marked with '*', while sharp spikes are marked with '°' **d)** Typical current transients of a plateau peak (peak 1, '*') and a spike peak (peak2, '°').

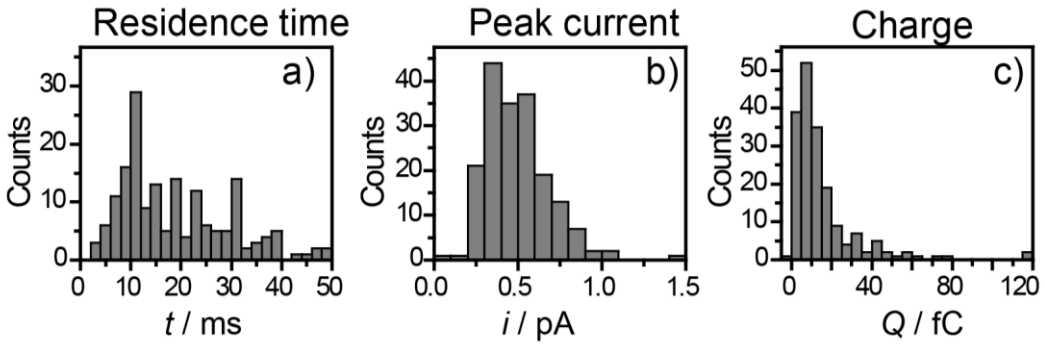

Figure 6.9 Histograms of **a)** residence time, **b)** peak current, and **c)** charge for AuNP collisions at a $COOH_{SAM}$/Au substrate. The median values obtained from each histogram are summarised in Table 6-1.

Similar to the analysis for OH_{SAM}/Au electrodes, histograms of peak current, residence time, and charge are shown in Figure 6.9 and summarised in Table 6-1. The frequency of AuNP collisions on $COOH_{SAM}$/Au electrodes, *ca.* 4.3×10^4 s^{-1} pM^{-1} cm^{-2} (Table 6-1), is approximately three times smaller than that for the OH_{SAM}/Au (12.8×10^4 s^{-1} pM^{-1} cm^{-2}). This decrease in collision frequency can be attributed to the electrostatic repulsion between the (partially) negatively charged surface due to deprotonated carboxylate groups at the pH of the measurement,[43,44] *ca.* 7.3, and the negatively charged colloidal AuNPs (from the stabilizing citrate). Similar effects have been reported previously to explain the low collision frequency of Pt NPs at a 3-mercaptopropionic acid modified Au UME for hydrazine oxidation.[22]

The median residence time for AuNPs on a $COOH_{SAM}$/Au electrode is longer than for an OH_{SAM}/Au (17.6 ms *vs.* 6.2 ms) substrate. As a consequence, by deconvoluting the measured signal from the instrumental response, as described above for OH_{SAM}/Au, it is found that the majority of the peak current magnitudes (> 90 %) were within 90 % of the real, deconvoluted signal. The corrected median peak current value was found to be 0.49 pA (Table 6-1), essentially the same as the raw

data, 0.47 pA. This indicates that most of the NP collisions detected at this substrate are long enough for the current amplifier to detect a fully amplified signal. A notable result from these studies is that the median current at this substrate is similar to that for the OH_{SAM}/Au substrate, indicating that ET at the AuNPs is essentially independent of the surface termination groups for the two hydrophilic substrates.

6.2.5 AuNP collisions at $CH_{3,SAM}$/Au electrodes

Finally, to explore a wide range of surface chemistry, hydrophobic dodecanethiol-modified Au electrodes were employed. Figure 6.10b shows a typical current-time trace recorded for AuNP impacts on a $CH_{3,SAM}$/Au electrode with a pipette of 3.0 μm diameter. Again, distinctive current spikes can be observed compared to the background current in Figure 6.10a. Figure 6.10c is an expanded view of the current transients over a time range of 2 s. Figure 6.10d shows two typical current-time transients with different peak current magnitudes. Similar to AuNP collisions at the OH_{SAM} covered surfaces, all the collisions were found to give 'spike' type signals.

Similar to the two systems above, histograms of peak current, residence time, peak charge and collision frequency are plotted in Figure 6.11, with a summary of the data provided in Table 6-1. The collision frequency on $CH_{3,SAM}$/Au was found to be 0.16 s^{-1} pM^{-1} cm^{-2}, approximately one order of magnitude smaller than the values obtained for the hydrophilic surfaces ($COOH_{SAM}$ and OH_{SAM} surfaces). The median residence time for AuNP collisions at this electrode was 7.0 ms, similar to that for an OH_{SAM}/Au, while the raw median peak current was 0.21 pA and the value after correction for the instrument response function was 0.37 pA. This latter value is a little lower than that for the two hydrophilic substrates (see above and Table 6-1).

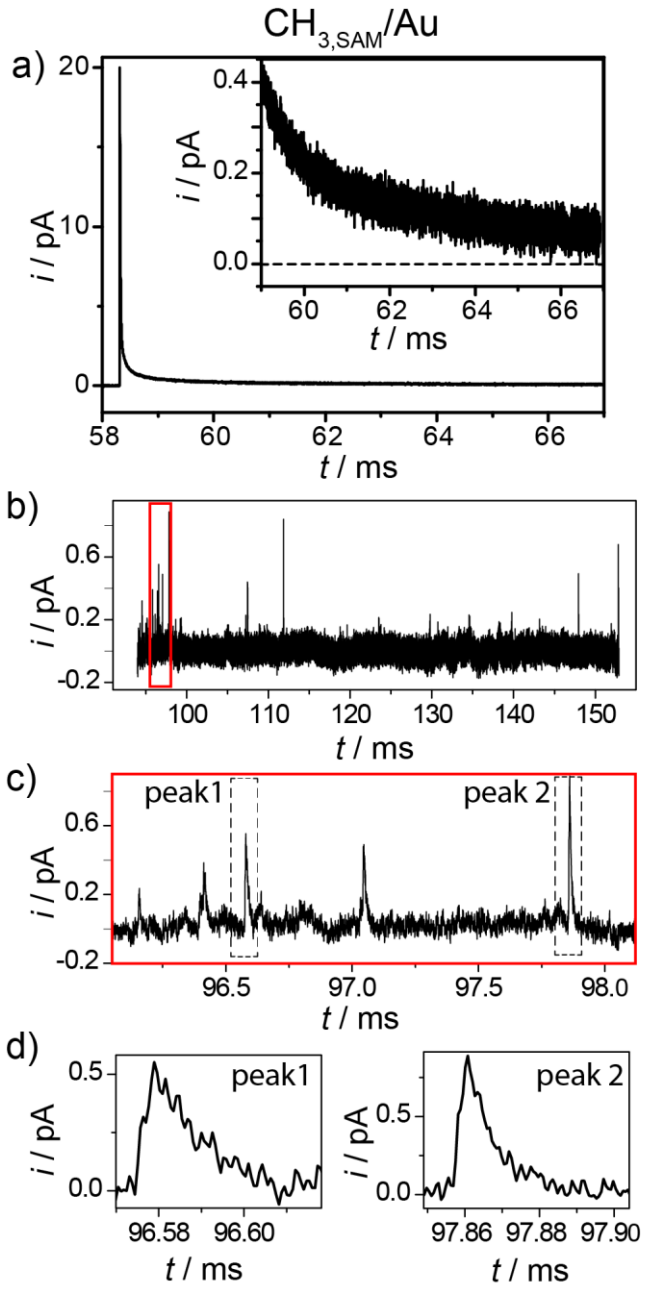

Figure 6.10 Current-time traces recorded at $CH_{3,SAM}$/Au electrode in the **a)** absence and **b)** presence of AuNPs. **c)** Zoom-in of current events within a time range of 2 s. **d)** Typical current transients of events with a low (peak 1) and a high (peak 2) peak current value.

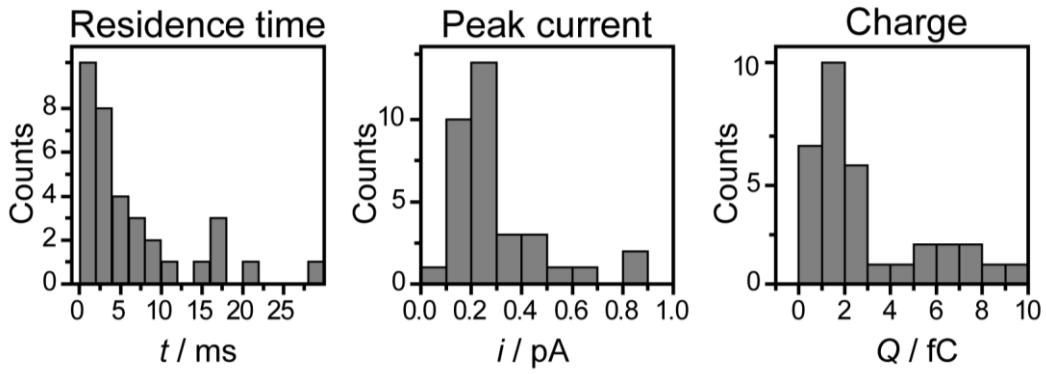

Figure 6.11 Histograms of residence time, peak current, and charge for AuNP collisions at a $CH_{3,SAM}$/Au substrate.

6.2.6 Kinetic analysis

To gain more insights into the kinetics of the electron transfer through SAMs, a finite element method model was developed to calculate the steady state current for the $Fe(CN)_6^{4-}$ oxidation process at a AuNP on a film at the potential of the electrode as a function of the standard heterogeneous ET rate constant, k^0 (Butler-Volmer kinetics). A spherical reactive NP of 5 nm radius (see Figure 6.4) was positioned on an electrochemically inert surface. The flux conservation equation (equation 6-4):

$$\nabla(D\nabla c) = 0 \tag{6-4}$$

was solved, assuming purely diffusional mass-transport of redox species from the solution bulk towards the NP surface (D and c denote diffusion coefficient and local species concentration of the redox molecules, respectively).

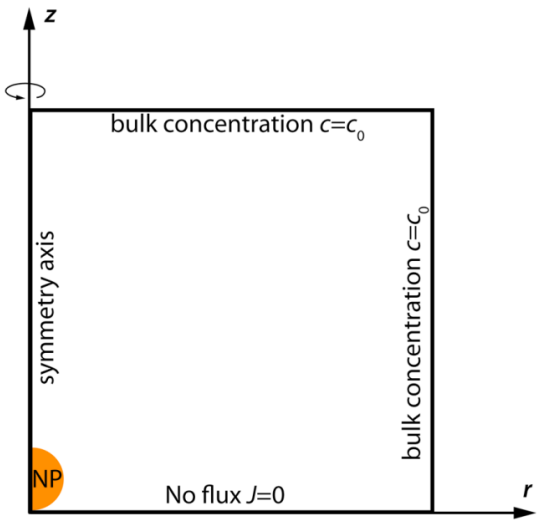

Figure 6.12 Schematic (not to scale) representation of a computational domain and boundary conditions used in a finite element model.

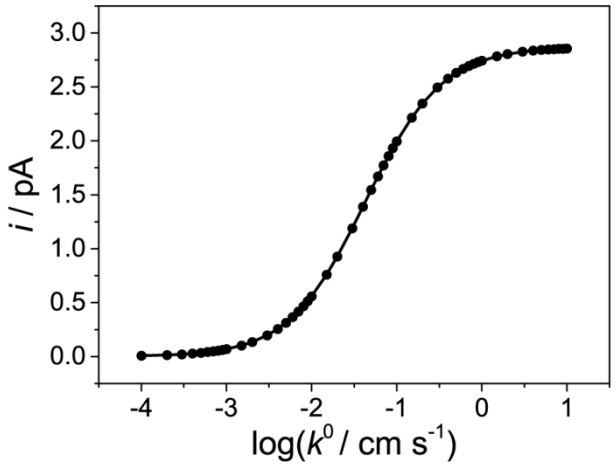

Figure 6.13 Working curve of the electrochemical current at 400 mV (*vs*. Ag/AgCl, overpotential 250 mV) as a function of the standard heterogeneous electron transfer rate constant, k^0, for 1 mM $Fe(CN)_6^{4-}$ at a single AuNP (r = 5 nm).

The flux of redox species on the NP surface was modelled using a Butler-Volmer formulation (equation 6-5):

$$J = -k^0\left(c\exp\left[\alpha\frac{F}{RT}(E-E^{0'})\right]-(c^0-c)\exp\left[-(1-\alpha)\frac{F}{RT}(E-E^{0'})\right]\right) \quad (6\text{-}5)$$

where k^0, α, F, R, T, E, $E^{0'}$, c^0 denote heterogeneous standard rate constant, transfer coefficient, Faraday constant, gas constant, temperature, applied potential, formal potential and bulk concentration of species, respectively. The model was solved in a two-dimensional axisymmetric cylindrical coordinate system (see the schematic on Figure 6.12) to reduce the computational effort.

The model was computed using Comsol Multiphysics 4.4 finite element software package running on MacBook Pro with 2.8 GHz Intel Core i7 processor and equipped with 16 GB of RAM. The mesh was refined down to 0.1 nm at the NP surface. Simulations were run for $Fe(CN)_6^{4-}$ oxidation, assuming equality of diffusion coefficient (D = 6.7×10^{-6} cm^2 s^{-1}) for both oxidised and reduced forms, with the oxidised form initially present in the solution bulk at a concentration c^0 = 1 mM. The steady-state current at the NP was computed at 250 mV overpotential (appropriate to the measurements in the work) at different values of k^0, ranging from 10^{-4} to 10 cm s^{-1}. Figure 6.13 depicts the relation between the faradaic current at the NP and log(k^0). The corrected median peak currents for the OH_{SAM}/Au, $COOH_{SAM}$/Au and $CH_{3,SAM}$/Au substrates are 0.77, 0.49, and 0.37 pA, corresponding to k^0 values of 15.3×10^{-3}, 8.5×10^{-3} and 6.1×10^{-3} cm s^{-1}.

The k^0 values obtained herein are consistent with k^0 values reported in the literature for NP mediated electron transfer to $Fe(CN)_6^{4-/3-}$ across insulating layers,[10] and are also reasonably in line with the rate constants reported for this redox couple at polycrystalline Au electrodes.[10,45,46] Although there is a trend in the rate constants, the values are reasonably close and it is difficult to make definitive statements as to

the origin of any differences in apparent electron transfer kinetics between the systems. However, it needs to be pointed out that, for the conditions of these measurements, where the Debye length (~ 3 nm) is of the order of the diffusion layer around the NP (~ 5 nm radius), nanoscale surface charge and double layer effects will be important[47-53] for both the kinetics and the mass transport. These effects will be sensitive to the local environment of AuNPs on the different SAMs. In particular, the partially negatively charged groups from the $COOH_{SAM}$ may lead to a local decrease in $Fe(CN)_6^{4-}$ concentration as well as inhibit mass transport, which is seen in kinetics (lower current), when comparing the data for OH_{SAM}/Au and $COOH_{SAM}$/Au. The water and double layer structure at the $CH_{3,SAM}$ (for hydrophobic surfaces generally)[54] will be very different to that at the hydrophilic SAMs, which again will impact mass transport and apparent kinetics (currents). Some of these issues were picked up in the next section.

6.2.7 AFM force measurements

To obtain further understanding of AuNP-substrate interactions, AFM force measurements were performed, which can be highly revealing of the interaction forces between an AFM tip and a substrate of interest.[55,56] Herein, gold coated-AFM tips were used that had radii of curvature of ~ 60 nm, and were modified with citrate (see Chapter 2) to serve as a model for citrate-capped AuNPs. Force-distance curves were recorded in several areas on all three SAM/Au substrates, to determine whether there was any inhomogeneity in the surface functionalization. The force-distance curves are plotted in Figure 6.14. The corresponding adhesion forces from 200

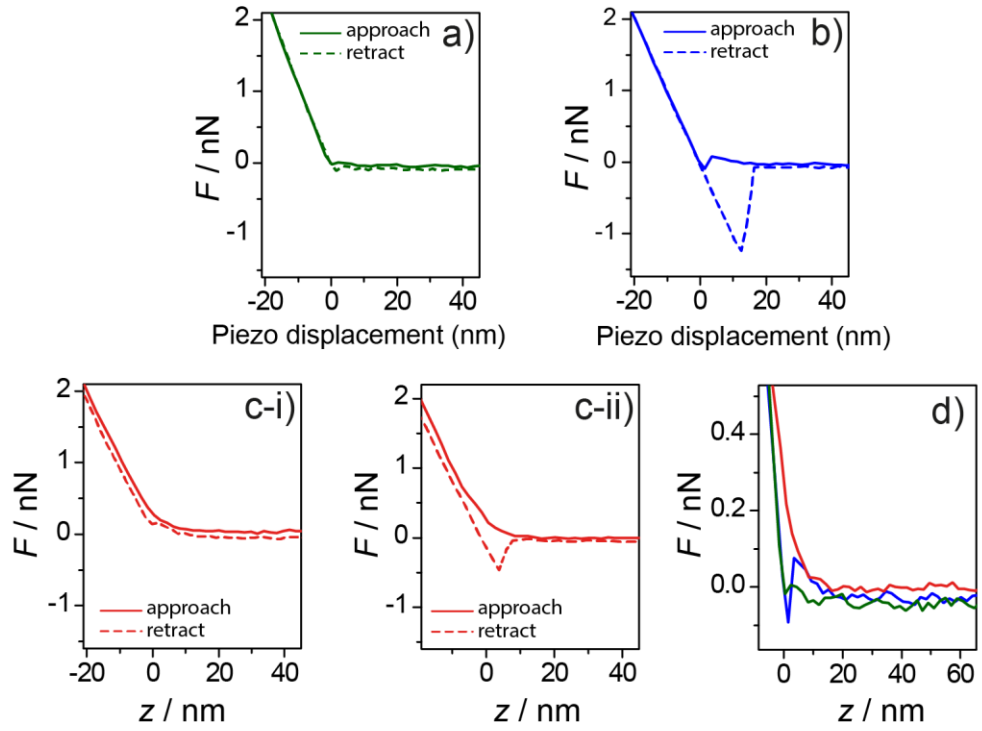

Figure 6.14 a-d) Representative force-piezo displacement curves (in aqueous solution containing 1 mM $K_4Fe(CN)_6$ and 0.4 mM sodium citrate) obtained for citrate-modified AFM tips with substrates modified by three different alkanethiols: **a)** OH-terminated; **b)** CH_3-terminated; and **c-i)** COOH-terminated first curve, **c-ii)** COOH-terminated second curve. **d)** Comparison of the approach curves for the three different substrates. The origin corresponds to the initial contact between the tip and the substrate, as determined by the onset of the linear regime of each approach curve. Measurements were made under electrochemical control, with each of the substrates bias at 400 mV *vs*. Ag/AgCl QRCE.

measurements are plotted in histograms in Figure 6.15. Figure 6.14a-c shows typical force-distance curves (here as force vs. displacement of the piezoelectric actuator) obtained on the three SAM/Au substrates (see caption and Chapter 2 for details). Three characteristic regions can be distinguished in these force-displacement curves. At large distances (the 'zero-region'), there is no effective interaction between the tip

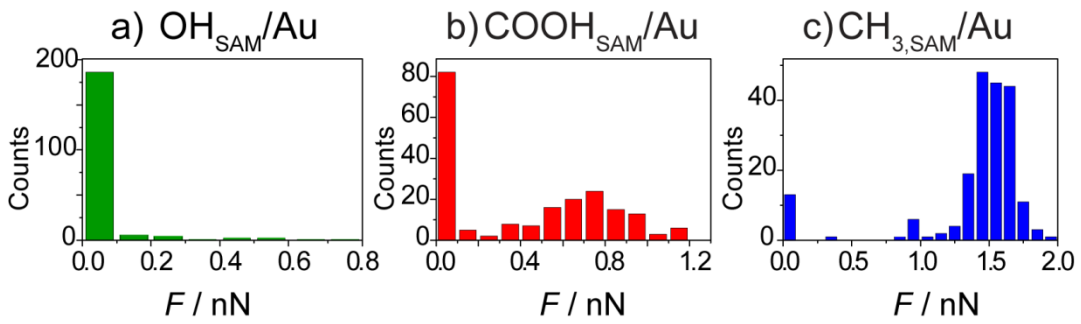

Figure 6.15 Histograms showing the adhesion forces in 200 repetitive measurements for **a)** OH_{SAM}/Au, **b)** $COOH_{SAM}$/Au, and **c)** $CH_{3,SAM}$/Au substrate, respectively.

and the substrate, and the force is zero. Upon moving the tip towards the surface (decreasing the piezo-displacement), the forces start to deviate from zero ('interacting region'). After the tip physically contacts the surface (at zero displacement), a linear force-displacement relation is observed with a slope equal to the spring constant of the cantilever, typical for hard (*i.e.* non-deformable) contact (the 'contact region').[56]

Firstly, two hydrophilic substrates were discussed. For the OH_{SAM}/Au (Figure 6.14a), the zero-region is directly followed by the contact region, and no interaction (attractive or repulsive) during approach or adhesion during retraction of the tip is observed. In comparison, for the $COOH_{SAM}$/Au (Figure 6.14c-i and c-ii), a weak but clear repulsive force was observed at short distances (< 10 nm), as can be seen from the non-linear deviation of the force-distance curve from the zero-force baseline. This is attributed to the electrostatic repulsion between the partially negatively charged carboxylate groups at the substrate and on the tip, as the solution used had a bulk pH ~ 7.3, while typical pK_a for surface-confined COOH groups range from 5.5-10.3,[43,44,57] with complete deprotonation ranging from pH 7-10 depending on the ionic strength. In addition to the solution pH, the surface acid/base properties of the

SAMs can be controlled by the electrode potential.[58,59] The short-range nature of this interaction is in agreement with the Debye screening length in this solution (~3 nm).[60] This repulsion can reasonably be correlated with the lower NP collision frequency on $COOH_{SAM}$ (relative to OH_{SAM}), as a colloidal AuNP needs to come within electron tunnelling distance of the electrode surface to be detected electrochemically. In further support of the arguments, it should be noted that earlier cavity-ring down spectroscopy studies of similar citrate-protected AuNPs on clean (negatively charged) glass surfaces found no evidence of long-term accumulation of AuNPs.[61]

On the retraction of the tip, two types of curves are observed for the $COOH_{SAM}$. The first type (Figure 6.14c-i) is essentially the reverse of the approach curve. The second type (Figure 6.14c-ii) shows an apparent adhesion (with a maximum adhesion force of ~ 0.68 ± 0.23 nN, Figure 6.15b) between the tip and the substrate. This adhesion can be attributed to some hydrogen bonding between the citrate COOH-groups on the AFM tip and the surface-COOH groups. The heterogeneity in the force curve characteristics implies some variation on the extent of surface protonation/deprotonation across the surface at the nanoscale, in which the potential applied plays a complicated role.[62] Note that due to the pH of the solution (~7.3) used herein, the $COOH_{SAM}$-citrate adhesion force is much lower than the reported value for completely protonated COOH-COOH groups at pH < 5 (7.0 ± 0.2 nN) for a similar tip radius.[55]

Interestingly, for the NP collisions on the $COOH_{SAM}$, two types of electrochemical response were observed (*vide supra*). The existence of two types of signals in the NP impact experiments ('spike' *vs.* 'plateau') and in the force

measurements (no adhesion *vs*. adhesion) suggests that there may be a correlation

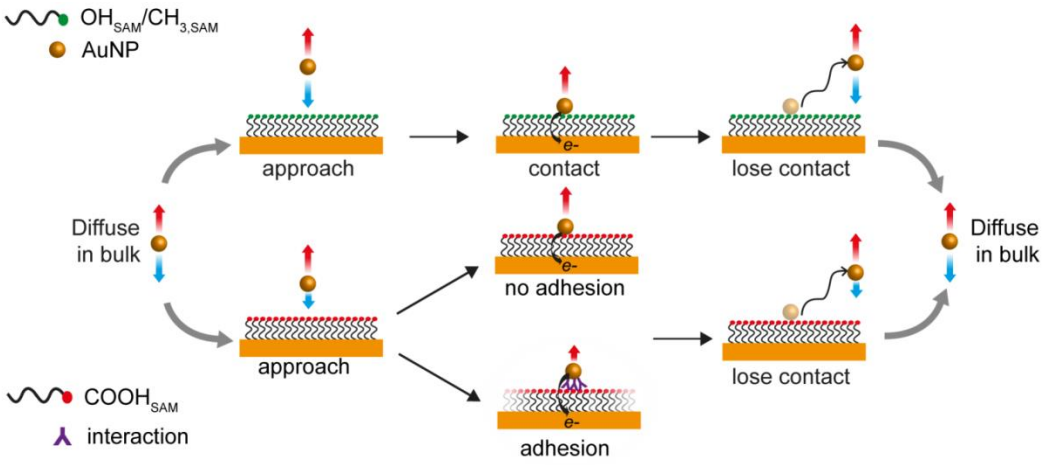

Figure 6.16 Schematic view of AuNP collisions and their interactions with OH_{SAM}/Au, $CH_{3,SAM}$/Au, and $COOH_{SAM}$/Au substrates. The two arrows on a single AuNP indicate that it can move towards (blue) or away (red) from the surface. The length of arrows illustrates the relatively probability of movement in that direction (when the NP is close to the surface). For the sake of clarity, only movement perpendicular to the electrode surface is displayed. For OH_{SAM}/Au and $CH_{3,SAM}$/Au, there is no strong interaction between the surface and the particles. For $COOH_{SAM}$/Au, the surface repels NPs which tend to move away (long arrow). Once in contact, some NPs interact strongly with the surface.

between the NP collision and force curve characteristics. Thus, it can be hypothesised that the 'spike' signals correspond to case where no-adhesion force is detectable (as these types of signals were the only type observed on the OH_{SAM}), whereas the 'plateau' signals correlate with the stronger adhesion case. From a physical view, the following mechanism to occur for NP collisions on the two hydrophilic surfaces can be described, as shown in Figure 6.16: at a random point in time, a freely diffusing colloidal NP comes into close vicinity of the modified electrode surface. For the OH_{SAM}, the NP-surface interaction forces are weak, and as a result of the random movement of the NP, contact is established and broken ('kiss-and-run'), probably many times and with high frequency (compared to the

electrochemical measurement response time) so that a continuous signal is seen,[63] before the NP eventually diffuses into bulk solution again. For the $COOH_{SAM}$, there is a small repulsive interaction between the colloidal NP and the surface, so that upon approach to the surface, a NP may be repelled from the electrode, before any detectable electrochemistry is seen, leading to a lowered collision frequency. If the NP overcomes the repulsive barrier and comes into contact with the electrode, there are two scenarios. Contact is quickly established and broken (as for OH_{SAM}), leading to 'spike' signal. Alternatively, with stronger hydrogen bond formation, the NP is 'trapped' within tunnelling distance for a longer period of time, and a plateau signal with a longer residence time is observed. In all cases, the NP will eventually diffuse into the solution, marking the end of the signal. This process may be aided by the electrochemical process: an uneven distribution redox reaction rate across the NP surface, may lead to some electrochemical propulsion as seen for large 'swimmer' particles in solution.[64]

Finally, a brief discussion of the $CH_{3,SAM}$ surface is provided. A typical force curve for the $CH_{3,SAM}$/Au substrate (Figure 6.14b) shows a number of features. Upon approach, a small repulsive force (< ~20 nm, comparable to $COOH_{SAM}$, Figure 6.14b) is observed. This is followed by an apparent snap-to-contact at small distances. During the retraction of AFM tips, a significant adhesion was observed, extending over almost 20 nm of piezo displacement with a maximum adhesion force of ~ 1.2 nN. Such force-distance traces have been observed for hydrophobic surfaces in aqueous solutions, and are typically correlated with a hydrophobic interaction.[56] The origin of this hydrophobic interaction is still under debate and a few hypotheses exist, including a change in water structure at (hydrophobic) interfaces,[65] the electrostatic interactions in water or on the surface[66] and the presence of vapour cavities or

surface nanobubbles at hydrophobic surfaces.[56,67] Surface nanobubbles have been observed with AFM imaging on a number of different hydrophobic surfaces, particularly in non-degassed solutions (such as the air saturated solutions in this research).[68,69] Such nanobubbles, which are either formed spontaneously or due to initial contact of AFM tips, cause strong attractions while also bridging with each other,[70] leading to a long range adhesion force in AFM force curves due to capillarity effects. Importantly, for significantly hydrophobic surfaces (contact angles > 100°), it is found that up to 90 % of a hydrophobic surface may be covered by surface nanobubbles.[69] Such an extensive coverage of the surface with nanobubbles would be consistent with the studies herein, as all force-distance measurements displayed a similar trace, implying that the interaction between the AFM tip and the nanobubbles is probed (rather than the interaction between the tip and the 'bare' SAM-covered surface). This high coverage implies that in electrochemical measurements, the surface is covered by insulating nanobubbles with patches of the bare electrode surface between the bubbles less than the size of the modified AFM tip (~ 60 nm radius of curvature), resulting in a partially blocked electrode. It is believed that this is the main cause of the low AuNP collision frequency on the hydrophobic $CH_{3,SAM}$/Au substrate compared to $COOH_{SAM}$ and OH_{SAM} surfaces as only NPs (10 nm diameter; smaller than the AFM tip) colliding with the bare surface will lead to a electrochemical signal, whereas NP collisions on a nanobubble will be separated by a thick insulating layer. In fact, the apparently small proportion of the surface that is bare and the strong adhesion between a citrate-covered gold surface and the nanobubble-covered hydrophobic surface (as evident from Figure 6.14b) would trap AuNPs at the nanobubble-modified parts of the surface. This would lead to a much lower electrochemical collision frequency, as seen in the experiments. Finally, the

short interaction time in these particle collision experiments demonstrates that there is little stabilization between the AuNP and the bare (electrochemically active) substrate, a new finding that which were unable to obtain from the AFM measurements due to the size of the AFM probe. This serves to highlight how electrochemical NP collision experiments can reveal new aspects and features on surface chemistry that are not possible from other existing nano-tools.

6.3 Conclusions

This work investigated the interaction between single AuNPs and a support electrode with different chemical functionality using an SECCM-based technique. SAM-modified Au electrodes with different surface properties serve as 'inert' electrodes towards an electrochemical reaction with a solution redox-couple, $Fe(CN)_6^{4-}/Fe(CN)_6^{3-}$. The collision of AuNPs opens up a new electrochemical pathway, where electron tunnelling can occur between the passivated Au electrode and the AuNPs where the redox reaction occurs. Both the small contact area in SECCM and the insulating SAM film-modified electrode allow us to achieve extremely low background currents, and therefore detect electrochemical responses for a single AuNP across an insulating layer with exquisite sensitivity. The results demonstrate that the substrate properties have a significant influence on AuNP collision behaviour. To further understand the behaviour, these interactions were studied using AFM force measurements.

The results of both the NP-impact experiments and AFM force measurements with a citrate-modified gold tip give rise to similar conclusions. i) AuNPs interact weakly with OH_{SAM} modified surfaces. This is demonstrated by the lack of adhesion

force seen for this substrate from AFM force measurements, and the low residence times in NP-impact experiments. However, the higher collision frequencies seen for this surface can be explained by the lack of repulsion seen in the force measurements. ii) Some repulsion is observed between AuNPs and $COOH_{SAM}$ surfaces during AFM approach curves, with small adhesion forces observed on the retract. This leads to some repulsion in the collision experiments, but if a NP overcomes this and makes contact with the substrate, it is somewhat stabilized. The result is lower collision frequencies but higher residence times for this substrate. iii) For hydrophobic surfaces with CH_3 surface groups, the lowest collision frequencies are observed in AuNP-impact experiments, which are tentatively ascribed to the surface having an extensive coverage by nanobubbles, as seen for hydrophobic surfaces in aqueous solution.[68,69]

In general, this work has demonstrated the applicability of SECCM-based NP-impact experiments for probing intermolecular interactions, especially if combined with AFM force measurements. Notably, subtle variations in the small molecular forces between a NP and a support electrode on a molecular level can have significant effects on NP collision behaviour and ET properties at individual NPs. In addition, some subtle differences that are manifest in AFM measurements are amplified in electrochemical NP collision parameters, such as collision frequencies and residence times. This suggests that NP collision can be used to probe surface chemistry. At the same time, the AFM and the NP-impact techniques approaches are complementary, as they rely on measuring different physical properties (ET activity *vs*. interacting forces), providing a synergistic approach for exploring NP-substrate intermolecular interactions. Thus, although on the whole, the electrochemical measurements of NP collisions are consistent with AFM force

measurements, NP collisions provide a new, alternative method for investigating interfaces and the interactions of NPs with surfaces. Such measurements are of key importance for understanding and developing NP applications in many research fields and technologies.

6.4 References

(1) Cox, J. T.; Zhang, B. *Annu. Rev. Anal. Chem.* **2012**, *5*, 253.

(2) Hernández-Santos, D.; González-García, M. B.; García, A. C. *Electroanalysis* **2002**, *14*, 1225.

(3) Xiao, X.; Pan, S.; Jang, J. S.; Fan, F.-R. F.; Bard, A. J. *J. Phys. Chem. C* **2009**, *113*, 14978.

(4) Hayden, B. E. *Acc. Chem. Res.* **2013**, *46*, 1858.

(5) Kleijn, S. E. F.; Lai, S. C. S.; Koper, M. T. M.; Unwin, P. R. *Angew. Chem. Int. Ed.* **2014**, *53*, 3558.

(6) Love, J. C.; Estroff, L. A.; Kriebel, J. K.; Nuzzo, R. G.; Whitesides, G. M. *Chem. Rev.* **2005**, *105*, 1103.

(7) Chidsey, C. E. D.; Loiacono, D. N. *Langmuir* **1990**, *6*, 682.

(8) Adams, D. M.; Brus, L.; Chidsey, C. E. D.; Creager, S.; Creutz, C.; Kagan, C. R.; Kamat, P. V.; Lieberman, M.; Lindsay, S.; Marcus, R. A.; Metzger, R. M.; Michel-Beyerle, M. E.; Miller, J. R.; Newton, M. D.; Rolison, D. R.; Sankey, O.; Schanze, K. S.; Yardley, J.; Zhu, X. *J. Phys. Chem. B* **2003**, *107*, 6668.

(9) Zhao, J.; Bradbury, C. R.; Huclova, S.; Potapova, I.; Carrara, M.; Fermín, D. J. *J. Phys. Chem. B* **2005**, *109*, 22985.

(10) Zhao, J.; Bradbury, C. R.; Fermín, D. J. *J. Phys. Chem. C* **2008**, *112*, 6832.

(11) Shein, J. B.; Lai, L. M. H.; Eggers, P. K.; Paddon-Row, M. N.; Gooding, J. J. *Langmuir* **2009**, *25*, 11121.

(12) Chazalviel, J.-N.; Allongue, P. *J. Am. Chem. Soc.* **2010**, *133*, 762.

(13) Bard, A. J.; Zhou, H.; Kwon, S. J. *Isr. J. Chem.* **2010**, *50*, 267.

(14) Xiao, X.; Bard, A. J. *J. Am. Chem. Soc.* **2007**, *129*, 9610.

(15) Tel-Vered, R.; Bard, A. J. *J. Phys. Chem. B* **2006**, *110*, 25279.

(16) Dasari, R.; Robinson, D. A.; Stevenson, K. J. *J. Am. Chem. Soc.* **2013**, *135*, 570.

(17) Fosdick, S. E.; Anderson, M. J.; Nettleton, E. G.; Crooks, R. M. *J. Am. Chem. Soc.* **2013**, *135*, 5994.

(18) Alligrant, T. M.; Anderson, M. J.; Dasari, R.; Stevenson, K. J.; Crooks, R. M. *Langmuir* **2014**, *30*, 13462.

(19) Guo, Z.; Percival, S. J.; Zhang, B. *J. Am. Chem. Soc.* **2014**, *136*, 8879.

(20) Pearson, A.; O'Mullane, A. P. *Chem. Commun.* **2015**, *51*, 5410.

(21) Dasari, R.; Tai, K.; Robinson, D. A.; Stevenson, K. J. *ACS Nano* **2014**, *8*, 4539.

(22) Xiao, X.; Fan, F.-R. F.; Zhou, J.; Bard, A. J. *J. Am. Chem. Soc.* **2008**, *130*, 16669.

(23) Kleijn, S. E. F.; Serrano-Bou, B.; Yanson, A. I.; Koper, M. T. M. *Langmuir* **2013**, *29*, 2054.

(24) Jung, A. R.; Lee, S.; Joo, J. W.; Shin, C.; Bae, H.; Moon, S. G.; Kwon, S. J. *J. Am. Chem. Soc.* **2015**, *137*, 1762.

(25) Zhou, H.; Fan, F.-R. F.; Bard, A. J. *J. Phys. Chem. Lett.* **2010**, *1*, 2671.

(26) Kim, J.; Kim, B.-K.; Cho, S. K.; Bard, A. J. *J. Am. Chem. Soc.* **2014**, *136*, 8173.

(27) Castañeda, A. D.; Alligrant, T. M.; Loussaert, J. A.; Crooks, R. M. *Langmuir* **2015**, *31*, 876.

(28) Hill, C. M.; Kim, J.; Bard, A. J. *J. Am. Chem. Soc.* **2015**, *137*, 11321.

(29) Kleijn, S. E. F.; Lai, S. C. S.; Miller, T. S.; Yanson, A. I.; Koper, M. T. M.; Unwin, P. R. *J. Am. Chem. Soc.* **2012**, *134*, 18558.

(30) O'Connell, M. A.; Snowden, M. E.; McKelvey, K.; Gayet, F.; Shirley, I.; Haddleton, D. M.; Unwin, P. R. *Langmuir* **2014**, *30*, 10011.

(31) Diao, P.; Jiang, D.; Cui, X.; Gu, D.; Tong, R.; Zhong, B. *J. Electroanal. Chem.* **1999**, *464*, 61.

(32) Takehara, K.; Takemura, H.; Ide, Y. *Electrochim. Acta* **1994**, *39*, 817.

(33) Snowden, M. E.; Güell, A. G.; Lai, S. C. S.; McKelvey, K.; Ebejer, N.; O'Connell, M. A.; Colburn, A. W.; Unwin, P. R. *Anal. Chem.* **2012**, *84*, 2483.

(34) Dasari, R.; Walther, B.; Robinson, D. A.; Stevenson, K. J. *Langmuir* **2013**, *29*, 15100.

(35) Kwon, S. J.; Fan, F.-R. F.; Bard, A. J. *J. Am. Chem. Soc.* **2010**, *132*, 13165.

(36) Zhou, Y. G.; Rees, N. V.; Compton, R. G. *Angew. Chem., Int. Ed.* **2011**, *50*, 4219.

(37) Zhao, J.; Wasem, M.; Bradbury, C. R.; Fermín, D. J. *J. Phys. Chem. C* **2008**, *112*, 7284.

(38) Bradbury, C. R.; Zhao, J.; Fermín, D. J. *J. Phys. Chem. C* **2008**, *112*, 10153.

(39) Kang, M.; Perry, D.; Kim, Y.-R.; Colburn, A. W.; Lazenby, R. A.; Unwin, P. R. *Journal of the American Chemical Society* **2015**, *137*, 10902.

(40) Konopka, S. J.; McDuffie, B. *Anal. Chem.* **1970**, *42*, 1741.

(41) Singh, P. S.; Kätelhön, E.; Mathwig, K.; Wolfrum, B.; Lemay, S. G. *ACS Nano* **2012**, *6*, 9662.

(42) Scanlon, M. D.; Peljo, P.; Mendez, M. A.; Smirnov, E.; Girault, H. H. *Chem. Sci.* **2015**, *6*, 2705.

(43) Schweiss, R.; Welzel, P. B.; Werner, C.; Knoll, W. *Langmuir* **2001**, *17*, 4304.

(44) Hu, K.; Bard, A. J. *Langmuir* **1997**, *13*, 5114.

(45) Krysiński, P.; Brzostowska-Smolska, M. *J. Electroanal. Chem.* **1997**, *424*, 61.

(46) Angell, D. H.; Dickinson, T. *J. Electroanal. Chem. Interfacial Electrochem.* **1972**, *35*, 55.

(47) Chen, S.; Liu, Y.; Chen, J. *Chem. Soc. Rev.* **2014**, *43*, 5372.

(48) Morris, R. B.; Franta, D. J.; White, H. S. *The Journal of Physical Chemistry* **1987**, *91*, 3559.

(49) Smith, C. P.; White, H. S. *Anal. Chem.* **1993**, *65*, 3343.

(50) Seibold, J. D.; Scott, E. R.; White, H. S. *J. Electroanal. Chem. Interfacial Electrochem.* **1989**, *264*, 281.

(51) Watkins, J. J.; Zhang, B.; White, H. S. *J. Chem. Educ.* **2005**, *82*, 712.

(52) He, R.; Chen, S.; Yang, F.; Wu, B. *J. Phys. Chem. B* **2006**, *110*, 3262.

(53) Xiaoling, Y.; Guigen, Z. *Nanotechnology* **2007**, *18*, 335201.

(54) Ball, P. *Nature* **2003**, *423*, 25.

(55) Noy, A.; Vezenov, D. V.; Lieber, C. M. *Annu. Rev. Mater. Sci.* **1997**, *27*, 381.

(56) Butt, H.-J.; Cappella, B.; Kappl, M. *Surf. Sci. Rep.* **2005**, *59*, 1.

(57) Kakiuchi, T.; Iida, M.; Imabayashi, S.-i.; Niki, K. *Langmuir* **2000**, *16*, 5397.

(58) Fawcett, W. R.; Fedurco, M.; Kovacova, Z. *Langmuir* **1994**, *10*, 2403.

(59) White, H. S.; Peterson, J. D.; Cui, Q.; Stevenson, K. J. *J. Phys. Chem. B* **1998**, *102*, 2930.

(60) Bard, A. J.; Faulkner, L. R. *Electrochemical Methods: Fundamentals and Applications*; Wiley, 2000.

(61) Mazurenka, M.; Hamilton, S. M.; Unwin, P. R.; Mackenzie, S. R. *J. Phys. Chem. C* **2008**, *112*, 6462.

(62) Burgess, I.; Seivewright, B.; Lennox, R. B. *Langmuir* **2006**, *22*, 4420.

(63) Kwon, S. J.; Zhou, H.; Fan, F.-R. F.; Vorobyev, V.; Zhang, B.; Bard, A. J. *Phys. Chem. Chem. Phys.* **2011**, *13*, 5394.

(64) Sánchez, S.; Soler, L.; Katuri, J. *Angew. Chem. Int. Ed.* **2015**, *54*, 1414.

(65) Eriksson, J. C.; Ljunggren, S.; Claesson, P. M. *J. Chem. Soc., Faraday Trans. 2* **1989**, *85*, 163.

(66) Wood, J.; Sharma, R. *Langmuir* **1995**, *11*, 4797.

(67) Ederth, T.; Liedberg, B. *Langmuir* **2000**, *16*, 2177.

(68) Ishida, N.; Inoue, T.; Miyahara, M.; Higashitani, K. *Langmuir* **2000**, *16*, 6377.

(69) Tyrrell, J. W. G.; Attard, P. *Phys. Rev. Lett.* **2001**, *87*, 176104.

(70) Attard, P. *Langmuir* **2000**, *16*, 4455.

Chapter Seven

Conclusions

The aim of this thesis was to probe electrochemistry locally and understand the structure-activity relationship of the electrochemical (electrocatalytical) reactions at the nanoscale. A number of approaches were employed to study this relationship, including single-crystal electrochemistry, micro-electrode studies and scanning electrochemical cell microscopy (SECCM), combined with structure characterisation techniques, such as scanning electron microscopy (SEM), atomic force microscopy (AFM) and electron backscatter diffraction (EBSD). In addition, electron transfer at single nanoparticles (NPs) across self-assembled monolayers (SAMs) and their interaction with SAMs were investigated. The effect of electrolyte, mass transport, parasitic reactions, and surface chemistry of supporting materials on the electrochemical (electrocatalytic) activity has been studied and discussed.

Chapter three introduced a 'pseudo-single-crystal' approach, which combined SECCM with EBSD to study the effect of local electrode surface structure on the electrochemical reaction rate. This method was demonstrated by studying the oxidation of Fe^{2+} at a polycrystalline platinum foil electrode in sulfuric and perchloric acid. Grain dependent heterogeneous activity for Fe^{2+} oxidation was found in both electrolytes. Interestingly, an enhanced activity at grain boundaries was observed in sulfuric acid but not in perchloric acid medium. These results are consistent with findings on single-crystals. The study demonstrated the capability of SECCM in probing local electrochemistry at polycrystalline metals and provided a powerful approach for studying structure-activity relationship of (electrocatalytical)

reactions at complex surfaces, especially high-index facets and grain boundaries at polycrystalline metal electrodes.

In Chapter four, the structure-activity relationship of the oxygen reduction reaction (ORR) at polycrystalline platinum electrode in a sulfuric acid medium was studied with the 'pseudo-single-crystal method' introduced in Chapter three. The electrochemical activity of the ORR at high-index grains on a polycrystalline Pt foil was mapped by SECCM. The results revealed a strongly structure-dependent activity of the ORR on high-index Pt surfaces. Amongst all the grains investigated, grains having (111) and (100) contributions exhibited considerably higher activity than those with mainly (110) or (100) contributions. These results are again consistent with studies using single-crystal approaches. For the ORR, no enhanced grain boundary effect was found in sulfuric acid. A key attribute in this work is that SECCM provided a configuration of a three-phase boundary between the solid electrode, liquid electrolyte and gaseous oxygen (air), which mimics the geometry of the cathodes in fuel cells. This configuration allows studying the ORR at a greatly enhanced mass transport rate, which can be quantitatively controlled by adjusting the tip-to-substrate separation (meniscus height). One of the future aspects of this work is integrating sensor electrodes into SECCM probes, to detect intermediates or undesired products (hydrogen peroxide) of the reaction and provide deeper insights into the reaction kinetics and mechanisms, particularly under high and differential mass transport conditions.

In Chapters three and four, SECCM electrochemical imaging was performed by holding the substrate at a fixed potential value. Chapter five developed a new scanning mode, named voltammetric SECCM, to achieve a more comprehensive view of an electrochemical reaction. In voltammetric SECCM, the pipette operates in

a hopping mode and cyclic voltammograms (CVs) were recorded at each pixel of an imaged area, producing electrochemical maps at a much wider range of potentials compared to fixed potential imaging. These electrochemical activity images can be plotted as dynamic movies, with frames recorded at a few mVs, provides potentiodynamic information of a reaction. Using voltammetric SECCM, the oxidation of hydrazine at a polycrystalline platinum electrode was studied, both in air and under deaerated conditions. In both cases, CVs of hydrazine oxidation were consistent within a single grain but varied between different grains, indicating the reaction is surface structure dependent. However, CVs recorded in air had much lower electrochemical current. The changes in CVs are attributed to the overlap of the ORR with hydrazine oxidation at the measured potential range and the non-faradic decomposition of hydrazine with oxygen. The work provides important implications for hydrazine oxidation, especially in its detection, where the effect of oxygen is not well studied. Furthermore, it demonstrates that SECCM may be amenable to the study of non-faradic interfacial reactions.

As nanoparticles (NPs) are used widely as electrocatalysts, the electron transfer property of a single NP and its interaction with a supporting substrate is of key importance in understanding its electrocatalytic activity. In Chapter six, the electron transfer property of single Au NPs across SAMs and their interaction with SAMs of different chemical functionalities, namely OH, COOH and CH_3, was studied. Single Au NP collisions were detected by observing the current increase upon Au NP contact with the substrates. Interestingly, results showed that the chemical functionalities of the self-assembled monolayers are important in NP interaction with the substrate, leading to difference in current response and collision frequency. AFM force measurement was used as a complementary approach,

providing further information on the interaction force on a molecular level. The surface effects are rather subtle in AFM, but are amplified in NP collision experiments, highlighting NP collisions as a new approach for studying surface chemistry at the nanoscale.

In summary, the studies herein have demonstrated the capability of SECCM in probing local electrochemistry. Particularly, combining SECCM with other structure characterisation techniques provides a powerful platform for studying structure-reactivity in electrocatalysis.

The 'pseudo-single-crystal method' developed in this thesis opens new avenues for investigating structure-reactivity relationship at complex surfaces. Although this thesis has mainly focused on polycrystalline Pt, the method can be applied to a wealth of other (metal) materials, particularly for those of electrocatalytic relevance. The exemplar reactions studied in this thesis have confirmed the validity of this approach, which can be applied for the study of a wide range of electroanalytical (electrocatalytic) reactions, such as those that are of interest in energy conversion and storage applications. With the voltammetric SECCM, pipette crashing can be efficiently avoided and thus materials with complicated topographical features can be studied. Furthermore, the potentiodynamic movies provide direct view of the reaction over wide potential windows with high imaging speed. A research field in which this could be of particular useful is (electro)catalysts library screening. The structure-reactivity information obtained on polycrystalline materials provides important guidance for the synthesis of applied catalysts. One of the interesting developments of the technique would be incorporating SECCM with other analytical tools, such as

spectroscopic techniques, to provide more information of the reactions intermediates and products.

Finally, the effect of local environment on the electron transfer of NPs is of great interest for electrochemists. The results from single NP collision experiments illustrates that surface chemistry of supporting materials has great effects on the NP interaction with the substrate. The result provides great insights in understanding the role of the supporting material in electrocatalysis and SAM structure in sensor building. Future work can be performed to study the film thickness and NP size effect on the interaction. In addition, a flow cell configuration can be envisaged to control the flux of NPs towards the surface for a more controlled system.

With the studies in the thesis, we have demonstrated that SECCM is a powerful technique for studying electrochemistry, particularly electrocatalysis, at nanoscale. The marriage of SECCM with other structure characterization techniques allows a deep understanding of local structure effects on electrochemical activity. It has been shown in this thesis that the local platinum structure has a significant impact on its activity for the studied electrocatalytic reactions. Although SECCM is a powerful technique in electrochemical imaging, further improvements can be made for electrocatalysis studies. First, as SECCM is operated in a gaseous atmosphere (typically air), the substrate and meniscus are more likely to be exposed to contaminations in the environment. Especially, with the high mass transport through the three-phase boundary between the liquid meniscus-air-and solid substrate, it is difficult to avoid trace contaminations. We have demonstrated that a relatively clean system can be obtained by encasing the setup in an environmental chamber, purged with an inert gas such as nitrogen, but complete environmental control would require the high-quality environmental control and use of ultra-pure gases. Second, as

SECCM measurements are based on the contact area of meniscus with the electrode surface, consistent (and, ideally, substrate-independent) wetting of the droplet is paramount for a quantitative interpretation of measured data. We have shown that SECCM is able to handle moderately hydrophobic and hydrophilic surfaces. For very hydrophobic/hydrophilic surfaces, variations in meniscus wetting will need to be considered. Furthermore, it is challenging to apply SECCM on porous materials (such as microporous supports which are commonly used in applied catalysts) as maintaining a stable meniscus contact without the electrolyte filling the pores irreversibly would present a significant obstacle. In addition, so far, SECCM is still limited to work on relatively flat substrates. A step towards adapting SECCM for surfaces with a higher surface roughness was already taken in voltammetric SECCM, where the pipet movement is operated in a hopping mode. A further challenge lies in the use of smaller tips, allowing higher spatial resolution. Single barrel glass pipettes with diameters of a few nanometres have been reported. Extend this methodology to double-barrelled (theta) tips, while still maintain the easy of rendering only the outer wall would be an interesting development for the measurements at a higher spatial resolution with SECCM. Finally, an exciting future prospect would be combining SECCM with other (electro)analytical techniques, such as SECM for electrochemical product generation/detection, localised sampling with, *e.g.* mass spectrometry or chromotography, or spectroscopic techniques for investigating reaction mechanisms.